BERGISCHE
UNIVERSITÄT
WUPPERTAL

Fakultät für Mathematik und Naturwissenschaften
Fachgruppe Physik

Measurement of the inclusive and fiducial $t\bar{t}$ production cross-sections in the lepton+jets channel in pp collisions at $\sqrt{s} = 8\,\text{TeV}$ with the ATLAS detector

Dissertation zur Erlangung des Grades
Doktor der Naturwissenschaften (Dr. rer. nat.)

vorgelegt von

Arwa Bannoura

Eingereicht am 20. Juli 2018

Tag der mündlichen Prüfung: 11. Januar 2019

The PhD thesis can be quoted as follows:

urn:nbn:de:hbz:468-20190325-131323-9
[http://nbn-resolving.de/urn/resolver.pl?urn=urn%3Anbn%3Ade%3Ahbz%3A468-20190325-131323-9]

Referent: Prof. Dr. Peter Mättig

Korreferent: Dr. Mark Owen

Contents

Introduction

The intention of science is to answer the open questions about our universe, where the role of particle physics lies at the most fundamental level. Particle physics aims to answer basic questions, such as: ‘what are the building blocks of matter?’. The theoretical framework of particle physics is the so-called ‘Standard Model of particle physics’. The Standard Model (SM) describes the elementary particles and the interactions between them. It has been validated by many experiments and shown to be in very good agreement with experimental evidence. However, the SM is incomplete. Some of the phenomena that it cannot explain are: why there are exactly three generations of fermions; the large differences in the masses of the elementary particles; gravity and the asymmetry between matter and anti-matter in our universe. Many theories have been proposed to extend the SM and provide explanations to the SM shortcomings. These theories predict the existence of new particles and are referred to as Beyond the Standard Model (BSM) theories. Therefore, current particle physics research focuses on the one hand on precision measurements of SM parameters and on the other hand on searches for such BSM theories.

The top quark, being the heaviest among the known elementary particles, is one of the main interests of particle physics research. The top-quark mass, which is a free parameter in the SM, is 40 times larger than the second heaviest elementary fermion, the bottom quark. The large mass implies a large Yukawa coupling to the Higgs boson (close to unity), which gives the top quark a special role in electroweak symmetry breaking. In addition, having a large mass indicates that the top-quark may play a key role in searches for new physics. Top quarks are produced in pairs via the strong interaction or as single top-quarks via the weak interaction. The production of top-quark pairs, referred to as $t\bar{t}$ process, is the dominant production process of top-quarks.

The Large Hadron Collider (LHC) is the largest particle accelerator in the world, where protons are brought to collision at very high energies. The LHC provides the opportunity to probe constituents of matter down to very small scales at conditions similar to those shortly after the Big Bang. Particles emerging from these collisions are detected by huge devices, called detectors. Using data collected by these detectors, scientists aim to measure properties of known particles with high precision and search for new particles predicted by BSM theories. One of the main general purpose experiments at the LHC is the ATLAS detector. The ATLAS detector consists of multiple layers of subsystems designed to detect different kinds of particles passing through it and measure their properties.

At the LHC, due its high collision energies, a large sample of top-quark pairs is produced. A precise measurement of the $t\bar{t}$ production cross-section provides an important verification of QCD calculations and helps in the precise determination of the top-quark mass. It is also very important for searches for new physics since several BSM theories predict particles decaying into top-quark pairs. Hence, an excess in the measured $t\bar{t}$ cross-section with respect to the SM prediction would indicate the existence of new physics.

This thesis presents the measurement of the $t\bar{t}$ production cross-section at a centre-of-mass energy of $\sqrt{s} = 8\,\mathrm{TeV}$ using $20.2\,\mathrm{fb}^{-1}$ of data collected in pp collisions in 2012 with the ATLAS experiment at the LHC. The measured cross-section is extracted in the lepton+jets final state for the full phase space and for a fiducial phase space close to the selected dataset.

The chapters of this thesis are organised as follows: Chapter 1 gives an introduction to the Standard Model and top-quark physics. Chapter 2 describes the ATLAS experiment at the LHC. In Chapter 3, the event generation and the simulated samples are explained. The objects reconstruction and selection are given in Chapter 4. Chapter 5 defines the event selection, reconstruction and signal regions, and discusses the backgrounds estimation. A data-driven W+jets method is presented in Chapter 6. In Chapter 7, the discriminating observables used in this analysis are defined. Sources of systematic uncertainties are discussed in Chapter 8 and the statistical analysis techniques are presented in Chapter 9. Chapter 10 summarises the results.

1

Theory

The theoretical background of this thesis is based on a comprehensive theory, referred to as the Standard Model of particle physics, wherein the top quark plays an important role. The Standard Model agrees with all experimental results with very high accuracy. However, it is not a complete theory since it cannot explain some phenomena, like gravity, dark matter, neutrino oscillations or the asymmetry between matter and anti-matter.

A basic overview of the Standard Model is given in Sect. 1.1. Explanations of top-quark pair production and decay, along with theoretical predictions of the production cross-section, are presented in Sect. 1.2. In Sect. 1.3, the principles and definitions of the inclusive and fiducial $t\bar{t}$ cross-section measurements are described.

1.1 The Standard Model

The Standard Model (SM) of particle physics [1–6] is the theory that describes the elementary particles and their interactions. The SM has been extensively tested in experiments and no significant discrepancy has been observed. There are two types of particles that differ in their properties and spin (both are related by the spin-statistics theorem). ‘Fermions’ have half integer spin and follow Pauli-Dirac statistics, ‘bosons’ have integer spin and follow Bose-Einstein statistics. All matter particles happen to be elementary fermions, force-carrying particles are (gauge) bosons. There are two classes of elementary fermions: ‘leptons’ and ‘quarks’, both grouped into three generations. The first generation has the lightest and most stable fermions while the third has the heaviest and least stable ones. The six leptons and six quarks arranged in the three generations are listed in Table 1.1 along with their mass and electric charge. The quarks come in six flavours: the up-type quarks, u, c, t, which have an electric charge of $+2/3$, and the down-type ones, d, s, b, carrying an electric charge of $-1/3$. The leptons come in three flavours: e, μ and τ, all of which carry an electric charge of -1, in addition to their corresponding neutrinos, ν_e, ν_μ and ν_τ, which have no electric charge. Each lepton, ℓ, or quark, q, has its own anti-particle. Anti-particles have exactly the same properties as the corresponding particles, except that their charges have the opposite sign.

Table 1.1: *The elementary particles of the Standard Model and some of their properties [7]. The top-quark mass is taken from Ref. [8].*

Generation	Particle	Charge	Mass
	Leptons		
I	electron, e	-1	0.51 MeV
	electron neutrino, ν_e	0	< 2 eV
II	muon, μ	-1	105.66 MeV
	muon neutrino, ν_μ	0	< 2 eV
III	tau, τ	-1	1776.86 MeV
	tau neutrino, ν_μ	0	< 2 eV
	Quarks		
I	up, u	$+2/3$	2.2 MeV
	down, d	$-1/3$	4.7 MeV
II	charm, c	$+2/3$	1.275 GeV
	strange, s	$-1/3$	95 MeV
III	top, t	$+2/3$	173.34 GeV
	bottom, b	$-1/3$	4.18 MeV

Gauge bosons are particles that mediate interactions between fermions carrying the relevant quantum number. There are four fundamental forces: the strong force, the electromagnetic force (EM), the weak force and gravitation. One of the SM's shortcomings is that it does not include gravitation, but it is the weakest force of all at the quantum scale. The gauge bosons are listed in Table 1.2, which are: photons γ, $W^{\pm}$ bosons, Z^0 boson and gluons g. In addition there is a scalar boson (spin 0), called the Higgs boson, which will be introduced later in this chapter.

The SM is a quantum field theory that is based on gauge invariance under certain symmetry groups. According to Noether's theorem, any continuous symmetry leads to one conserved quantity. This means that each gauge symmetry has an associated conserved charge (colour, electric, weak isospin). The Lagrangian of the Standard Model has a $SU(3) \times SU(2) \times U(1)$ symmetry, where $SU(3)$ is the symmetry group of the strong interaction, $SU(2)$ of the weak interaction and $U(1)$ of the electromagnetic interaction.

Table 1.2: *The gauge bosons and some of their properties [7]*

Boson	Charge	Force	Mass [GeV]
Photon, γ	0	EM	0
$W^{\pm}$	±1	weak	80.379 ± 0.012
Z^0	0	weak	91.1876 ± 0.0021
Gluon, g	0	strong	0

The strong interaction

The strong interaction is described by the theory of Quantum Chromodynamics (QCD) based on the $SU(3)_C$ gauge symmetry, where C refers to the colour charge. It is a quantum number that quarks and gluons carry. Each quark has one of three colour states: red, green or blue and each anti-quark carries one of the anti-colours. A gluon carries a colour and a different anti-colour. Quarks interact with each other through the strong force by exchanging a gluon. The $SU(3)$ local gauge invariance leads to the presence of eight gluons. Since gluons carry colour charges themselves, they can have self-interactions.

Partons (quarks and gluons) have never been observed as free particles, which is referred to as ‘confinement’. Quarks and anti-quarks only exist in the form of colourless objects, called hadrons. Hadrons are either ‘mesons’, quark-antiquark pairs, ‘baryons’, three-quarks bound states or ‘anti-baryons’, three anti-quarks bound states. For example, the pion is a meson consisting of $u\bar{d}$, the proton is a baryon that consists of uud and the neutron consists of udd.

The coupling strength α_s of the strong interaction is given by [9]:

$$\alpha_s(Q^2) = \frac{12\pi}{(33 - 2n_f) \cdot \log(\frac{Q^2}{\Lambda^2})}, \tag{1.1}$$

where n_f is the number of quark flavours, Q^2 is the momentum transfer, Λ is an intrinsic energy scale of QCD.

For large Q^2 (small distances), α_s decreases and the interaction can be described by perturbation theory, which implies that the quarks behave as free particles. This property is called ‘asymptotic freedom’. On the other hand, at large distances or small Q^2, α_s increases and approximation using perturbation theory is not possible. At some point, the potential energy is large enough to create additional quark-antiquark pairs, which form hadrons. This process is called ‘fragmentation’. The particle showers resulting from this process are referred to as ‘jets’. Free partons are not observed at experiments but the resulting jets are detected.

The electromagnetic interaction

The electromagnetic interaction is described by Quantum Electrodynamics (QED) based on the $U(1)$ gauge symmetry group. The photon is the gauge boson exchanged in QED. It is massless and carries no electric charge. Photons couple to particles carrying electric charge, therefore they do not have self-coupling. This means that all charged fermions, including charged leptons and all quarks, can interact by the electromagnetic force through the exchange of photons. The strength of the coupling depends on the energy scale of the interaction. The coupling constant of QED, α_{QED} is of the order of $\frac{1}{137}$ when Q^2 equals zero.

The weak interaction

The weak force is described by the $SU(2)_L$ symmetry of the weak isospin I. All fermions can interact via the weak interaction. The gauge bosons of the weak force are the massive $W^{\pm}$ and the Z^0 bosons. The W^+, W^- bosons are charged while the Z^0 boson is neutral. The weak interaction is the only interaction that can change the flavour of a fermion.

Left-handed fermions and right-handed anti-fermions are represented as doublets, which can interact via the exchange of both $W^{\pm}$ and Z^0 bosons:

$$\begin{pmatrix} \nu_e \\ e^- \end{pmatrix}, \begin{pmatrix} \nu_\mu \\ \mu^- \end{pmatrix}, \begin{pmatrix} \nu_\tau \\ \tau^- \end{pmatrix}, \begin{pmatrix} u \\ d' \end{pmatrix}, \begin{pmatrix} c \\ s' \end{pmatrix}, \begin{pmatrix} t \\ b' \end{pmatrix} \tag{1.2}$$

where, d', s', b' are the weak eigenstates, which are not the same as the mass eigenstates of quarks, d, s, b. Right-handed fermions and left-handed anti-fermions are represented as singlets and can only interact via the exchange of the Z^0 boson. Thus, the weak interaction through a W boson exchange (charged-current) violates parity.

Quarks can couple weakly to quarks from a different generation by a W boson exchange. The transformation of the mass and weak eigenstates is described by the unitary Cabibbo-Kobayashi-Maskawa (CKM) mixing matrix [10, 11]:

$$\begin{pmatrix} d' \\ s' \\ b' \end{pmatrix} = V_{\mathrm{CKM}} \begin{pmatrix} d \\ s \\ b \end{pmatrix} \tag{1.3}$$

where [7],

$$V_{\mathrm{CKM}} = \begin{pmatrix} V_{ud} & V_{us} & V_{ub} \\ V_{cd} & V_{cs} & V_{cb} \\ V_{td} & V_{ts} & V_{tb} \end{pmatrix} = \begin{pmatrix} 0.97446 & 0.22452 & 0.00365 \\ 0.22438 & 0.97359 & 0.04214 \\ 0.00896 & 0.04133 & 0.999105 \end{pmatrix} \tag{1.4}$$

The probability for a quark i transition into a quark j by the exchange of a W boson is proportional to the element $|V_{ij}|$. The matrix is diagonal dominant, i.e. the transition of quarks in the same family is dominant.

The electroweak theory

The electroweak theory is the combination of the weak and electromagnetic interactions. It was developed in the 1960s by Glashow, Salam and Weinberg [1–3]. It is described by the $SU(2)_L \times U(1)_Y$ symmetry group where the conserved quantum numbers are the weak isospin I for the $SU(2)_L$ gauge symmetry and the weak hypercharge Y for the $U(1)_Y$ symmetry. The weak hypercharge is related to the electric charge, Q, and the third component of the weak isospin, I_3: $Y = 2(Q - I_3)$. Neutrinos and up-type quarks have $I_3 = +\frac{1}{2}$, while charged leptons and down-type quarks carry $I_3 = -\frac{1}{2}$.

The three generators of $SU(2)$ and one of $SU(1)$ correspond to four massless gauge bosons: W_1, W_2, W_3 from $SU(2)_L$ and B^0 from $U(1)_Y$. Including mass terms for the gauge bosons violates the gauge invariance, but the gauge bosons of the weak interaction are observed to be massive. In order to solve this problem, a spontaneous symmetry breaking has been introduced. The concept was developed by Brout, Englert and Higgs in 1964, referred to as the Brout-Englert-Higgs mechanism [12, 13], where the $SU(2)_L \times U(1)_Y$ symmetry is spontaneously broken into the $U(1)_Q$ symmetry. The spontaneous symmetry breaking causes the fields of the $W^\pm$, Z^0 bosons and the photon γ to be formed as a mixture of the electroweak gauge boson fields:

$$W^\pm = \frac{1}{\sqrt{2}}(W_1 \mp iW_2) \tag{1.5}$$

$$\begin{pmatrix} \gamma \\ Z^0 \end{pmatrix} = \begin{pmatrix} \cos\theta_W & \sin\theta_W \\ -\sin\theta_W & \cos\theta_W \end{pmatrix} \begin{pmatrix} B^0 \\ W_3 \end{pmatrix} \tag{1.6}$$

where θ_W is the electroweak mixing angle measured to be $\theta_W \approx 28.7°$ [14].

The Brout-Englert-Higgs mechanism is based on introducing a scalar field, referred to as the Higgs field, which gives masses to the gauge bosons of the weak interaction. It also generates masses of fermions via the Yukawa-coupling of the fermions' fields to the Higgs field. This mechanism leads to the existence of an additional massive scalar boson, the Higgs boson, H. The discovery of the Higgs boson was announced by the ATLAS and CMS collaborations in 2012 [15, 16]. The Higgs boson has no electric or colour charge and its mass is measured to be $m_H = 125.09 \pm 0.21(\text{stat.}) \pm 0.11(\text{syst.})$ GeV [17].

1.2 The top quark

The top quark was discovered in 1995 by the CDF and D0 experiments at the Tevatron collider [18, 19]. It is the heaviest elementary particle with a mass of $m_{\text{top}} = 173.34 \pm 0.76$ GeV [8]. The large mass implies a large Yukawa coupling to the Higgs boson (close to unity), which gives the top quark a special role in electroweak symmetry breaking. The top quark has a very short lifetime $\tau_{\text{top}} \approx 5 \times 10^{-25}$ s, which means that it does not form hadrons but it decays, passing its spin information on to its decay products. This feature of the top quark presents a unique opportunity to study the properties of a 'bare' quark. Studying and measuring the properties of the top-quark provides a probe of the SM and a window to searches for potential new physics beyond the Standard Model (BSM). More details can be found in reviews of top-quark physics, some of which are in Refs. [20–24].

Top-quarks at hadron colliders are produced in pairs via the strong interaction. Single-top quarks are produced via the weak interaction in association with a b-quark, a light quark or a W boson. Since this thesis presents the top-quark pair production cross-section, single-top quarks production is treated as a background process and will be mentioned later. In the following, the $t\bar{t}$ production and the top-quark decay is explained.

The top-quark pair production

The production of top-quark pairs via the strong interaction is the dominant production process of top quarks. At the lowest order in perturbation theory (tree-level), referred to as leading-order (LO), the $t\bar{t}$ process is produced either by gluon fusion or quark anti-quark annihilation. At next-to-leading-order (NLO), qg scattering processes also exist, beside virtual corrections to the LO processes and gluon bremsstrahlung. Feynman diagrams for the $t\bar{t}$ production at LO and and some example diagrams at NLO are shown in Fig. 1.1.

In the parton model, protons consist of 'valence' quarks, uud, which are bound together by gluons and 'sea' quarks (quark anti-quark pairs). A hard scattering process in a pp collision occurs between partons of the two colliding protons, each with momentum p_p. The initial momentum p_i of a parton i, which carries the momentum fraction x_i, is $p_i = x_i p_p$.

The inclusive (total) cross-section, σ, of a certain process, here the $t\bar{t}$ production, is calculated using the QCD factorisation theorem as [25]:

$$\sigma(pp \to t\bar{t}) = \sum_{i,j} \int dx_i dx_j f_{i,p}(x_i, \mu^2) f_{j,p}(x_j, \mu^2) \cdot \hat{\sigma}(ij \to t\bar{t}; \hat{s}, \mu^2) \tag{1.7}$$

where, the sum runs over all pairs of partons (i, j) contributing to the process. The hard scattering is separated into short-distance and long-distance contributions. The long-distance contribution is the same for every process and is related to the parton

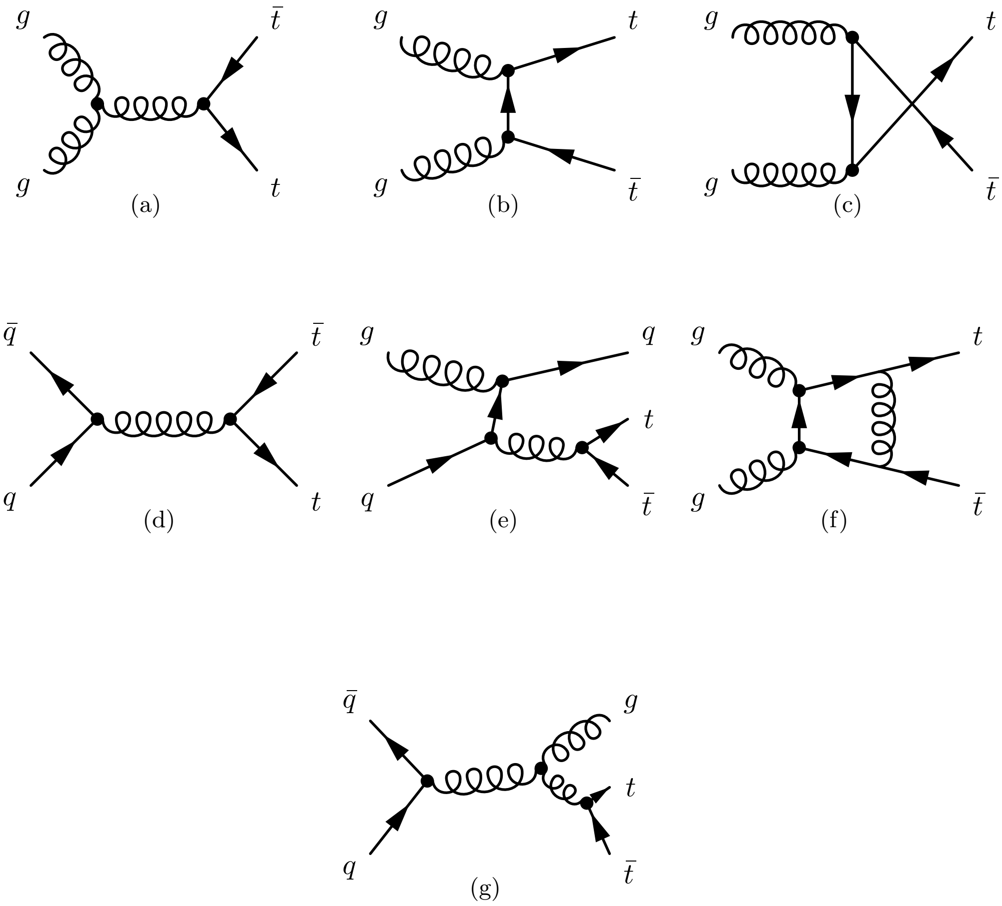

(a) (b) (c)

(d) (e) (f)

(g)

Figure 1.1: *Feynman diagrams for $t\bar{t}$ production via (a)-(c) gluon fusion at LO, (d) quark anti-quark annihilation at LO, (e) qg scattering at NLO, (f) gluon fusion with virtual corrections at NLO and (g) quark anti-quark annihilation with gluon bremsstrahlung at NLO.*

distribution function (PDF), $f_{i,p}(x_i, \mu^2)$, which describes the probability density of finding parton i inside the proton carrying the momentum fraction x_i. A factorisation scale, μ_f, is introduced in the calculations, which describes the scale of the interaction. The short distance is related to the hard scattering of the interacting partons, $\hat{\sigma}(ij \to t\bar{t}; \hat{s}, \mu^2)$, which is calculable in perturbative expansion to a certain order. $\hat{s}$ is the squared centre-of-mass energy of the colliding partons. A renormalisation scale, μ_r is introduced to account for divergence of corrections at higher orders. The factorisation and renormalisation scales, μ_f and μ_r, are arbitrary scales. Their values are normally set to the top-quark mass in the case of the top-quark production, $\mu_f = \mu_r = \mu = m_{\text{top}}$. Since the cross-section calculations depend on the values of μ_f and μ_r, an uncertainty in the theoretical prediction of the cross-section is considered by varying those scales.

The PDFs are determined using fits to experimental data, which are usually from deep inelastic scattering experiments. Various collaborations perform similar fits and provide PDF sets. Fig. 1.2 shows the PDFs for g, u, $\bar{u}$, d, $\bar{d}$, b partons in the proton as a function of their momentum fraction for the CT10 pdf set [26] at $\mu = 173\,\text{GeV}$.

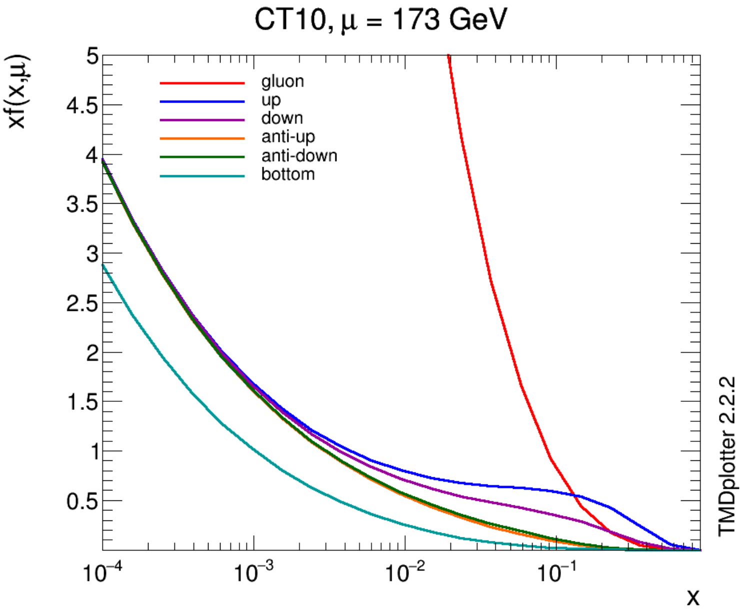

Figure 1.2: *The PDFs for the partons g, u, $\bar{u}$, d, $\bar{d}$, b in the proton as a function of their momentum fraction x for the CT10 pdf set at $\mu = 173\,\text{GeV}$. This plot was done using the TMDplotter tool [27].*

For the production of top-quark pairs, the partonic centre-of-mass energy, $\sqrt{\hat{s}} = \sqrt{x_i x_j s}$, needs to be at least twice the mass of the top quark, $\sqrt{\hat{s}} \geqslant 2 \cdot m_{\text{top}}$. Assuming the two partons carrying the same momentum fraction x, the relation becomes:

$$x \geqslant \frac{2m_{\text{top}}}{\sqrt{s}} \tag{1.8}$$

Applying the relation to the LHC at a centre-of-mass energy of $\sqrt{s} = 8\,\text{TeV}$, leads to $x \geqslant 0.04$. From Fig. 1.2, it can be seen that the gluon PDF is much larger at this value than the PDFs of the quarks. Thus the production of the $t\bar{t}$ process is dominated by gluon fusion. At the Tevatron ($p\bar{p}$ collider), where the centre-of-mass energy is $\sqrt{s} = 1.96\,\text{TeV}$, the relation leads to $x \geqslant 0.18$. In this region, the quark anti-quark annihilation dominates the $t\bar{t}$ production.

Theoretical predictions

The theoretical prediction of the inclusive $t\bar{t}$ production cross-section is calculated at NNLO QCD accuracy including soft gluon resummation at next-to-leading logarithmic (NNLL) accuracy with the `Top++` program [28–33] using the MSTW2008 NNLO PDF set [34]. This is the most precise calculation so far, which is available since 2013.

The predicted inclusive $t\bar{t}$ cross-section at a centre-of-mass energy of $\sqrt{s} = 8\,\text{TeV}$, assuming a top-quark mass $m_{\text{top}} = 172.5\,\text{GeV}$, is

$$\sigma(pp \to t\bar{t}) \;=\; 253^{+13}_{-15} \quad \text{pb.} \tag{1.9}$$

The total scale, PDF and α_{S} uncertainty of the predicted cross-section is about 6 %, which sets the current goal for the experimental precision. The uncertainties due to the PDFs and α_{S} are calculated using the PDF4LHC prescription [35], where the uncertainties of the MSTW2008 68 % CL NNLO [36], CT10 NNLO [26, 37] and NNPDF 2.3 [38] PDF sets are added in quadrature to the α_{S} uncertainty. The scale uncertainty is evaluated by varying μ_f and μ_r independently to half the default scale $0.5m_{\text{top}}$ and twice the default scale $2m_{\text{top}}$.

Using this result as a basis, other calculations were done using different methods for the gluon resummation or Coulomb effects, for example in Ref. [39]. Recently, also approximate N3LO computations (N3LO$_{\text{app}}$) became available [40, 41], which are performed by re-expanding the NNLL resummation. Fig. 1.3 compares various calculations in many approximations from different groups at a centre-of-mass energy of $\sqrt{s} = 8\,\text{TeV}$, assuming a top-quark mass $m_{\text{top}} = 173.3\,\text{GeV}$ [32, 39, 40, 42–44].

Differential predictions for the $t\bar{t}$ production at the LHC at $\sqrt{s} = 8\,\text{TeV}$ are available at NNLO QCD accuracy in Ref. [46]. Fig. 1.4 shows the p_{T} of the top-quark and the rapidity of the top-quark pair in LO, NLO and NNLO QCD accuracy. The predictions are significantly higher in NLO compared to LO QCD accuracy, but still within the scale

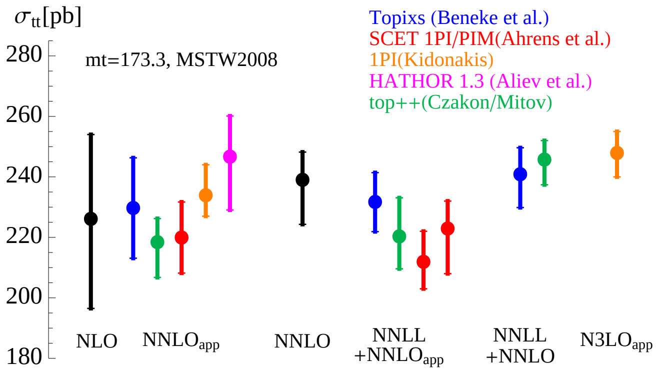

Figure 1.3: *The theoretical prediction of the $t\bar{t}$ cross-section at a centre-of-mass energy of $\sqrt{s} = 8\,\text{TeV}$, assuming a top-quark mass $m_{top} = 173.3\,\text{GeV}$, by different groups in various approximations with the MSTW2008 PDF. Only the scale uncertainty is shown [45].*

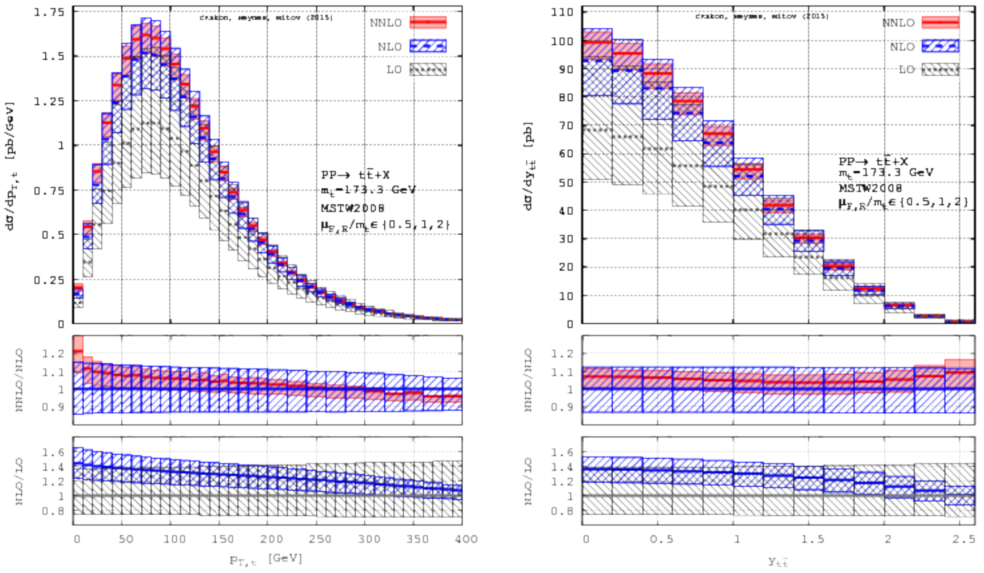

(a)

(b)

Figure 1.4: *(a) The p_T of the top-quark distribution and (b) the rapidity of the top-quark pair distribution, in LO, NLO and NNLO QCD accuracy. Error bands from scale variation only [46].*

uncertainty. NNLO QCD corrections are contained within the NLO error bands. At low p_T, the NNLO QCD prediction is higher than the NLO prediction by $\sim 10\,\%$.

Predictions for $t\bar{t}$ differential distributions for the LHC at $\sqrt{s} = 13\,\mathrm{TeV}$ became recently available at NNLO QCD accuracy, including NLO electroweak corrections (see Ref. [47]).

The top-quark pair decay

The top quark has three decay modes: $t \to Wb$, $t \to Ws$ and $t \to Wd$. The branching ratio for each decay mode is proportional to the square of the corresponding CKM matrix element, where $|V_{tb}| \gg |V_{ts}|, |V_{td}|$. Thus, the decay mode $t \to Wb$ is dominant with a branching ratio $\mathcal{B} \approx 99.9\,\%$. The suppressed $t \to Ws$ ($\mathcal{B} \approx 0.1\,\%$) and $t \to Wd$ ($\mathcal{B} \approx 0.01\,\%$) decay modes are not considered in the following.

The decay width of the top-quark including first order QCD corrections is given by [48, 49]:

$$\Gamma_\mathrm{top} = \frac{G_F m_\mathrm{top}^3}{8\pi\sqrt{2}} |V_{tb}|^2 \left(1 - \frac{m_W^2}{m_\mathrm{top}^2}\right)^2 \left(1 + 2\frac{m_W^2}{m_\mathrm{top}^2}\right) \left[1 - \frac{2\alpha_s}{3\pi} \cdot f(y)\right] \tag{1.10}$$

where G_F is the Fermi constant, m_W and m_top are the masses of the W boson and the top quark, respectively, $y = (m_W/m_\mathrm{top})^2$ and $f(y) = 2\pi^2/3 - 2.5 - 3y + 4.5y^2 - 3y^2 \ln y$.

Using $m_\mathrm{top} = 172.5\,\mathrm{GeV}$ yields $\Gamma_\mathrm{top} = 1.33\,\mathrm{GeV}$. The lifetime of the top quark is $\tau_\mathrm{top} = 1/\Gamma_\mathrm{top} \approx 5 \times 10^{-25}\,\mathrm{s}$. The hadronisation scale is $\approx 3 \times 10^{-24}\,\mathrm{s}$, which means that the top-quark's lifetime is shorter than the hadronisation scale. Thus, top-quarks decay before they can hadronise.

The classification of the $t\bar{t}$ decay is determined according to the decay of the two W bosons $t\bar{t} \to W^+bW^-\bar{b}$. The W boson decays leptonically into a charged lepton and a neutrino with three flavours or hadronically into a pair of quarks ($u\bar{d}$, $c\bar{s}$) with three possible colour states. In total, there are nine possible final states for the W-boson decay. The probability of the hadronic decay $W \to q\bar{q}$ is approximately $6 \times 1/9 = 2/3$ and the probability for a leptonic decay $W \to \ell\nu$ is $3 \times 1/9 = 1/3$.

Thus, the $t\bar{t}$ final states can be classified into three decay modes:

- Dilepton channel: In this channel, the two W bosons decay leptonically, $t\bar{t} \to W^+W^-b\bar{b} \to \ell^+\nu\ell^-\bar{\nu}b\bar{b}$. The final state of this channel consists of two oppositely charged leptons, two b-quarks and two neutrinos. The presence of the two charged leptons and high missing transverse momentum resulting from the two neutrinos leads to a clean signature in this channel. Hence, the expected number of background events is the lowest compared to the other two channels. However, having two neutrinos in the final state makes it difficult to fully reconstruct the event. The branching ratio of this channel is the lowest $\mathcal{B} \approx 10.3\,\%$.

- Single-lepton channel (lepton+jets channel): One of the two W bosons decays leptonically, while the other decays hadronically, $t\bar{t} \rightarrow W^+W^-b\bar{b} \rightarrow \ell\nu q'\bar{q}b\bar{b}$. The final state includes one charged lepton, a neutrino, two light quarks and two b-quarks. The branching ratio for this channel is $\mathcal{B} \approx 43.5\,\%$, which is much higher than the branching ratio of the dilepton channel. However, the expected number of background events in this channel is also higher than in the dilepton channel. The $t\bar{t}$ cross-section measurement presented in this thesis is performed in this channel. An exemplary Feynman diagram for the production and the full decay chain is shown in Fig. 1.5.

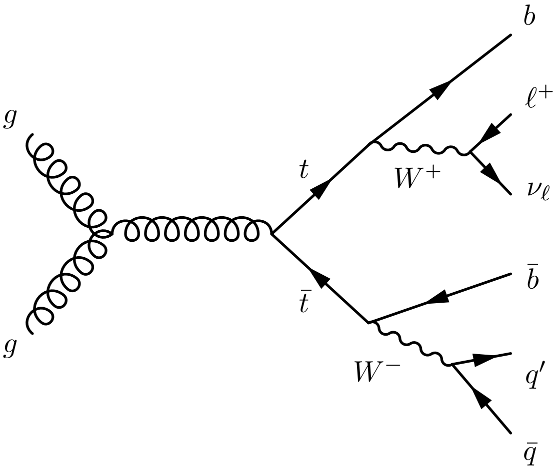

Figure 1.5: *An exemplary Feynman diagram for the $t\bar{t}$ production via gluon fusion and the full decay chain in the lepton+jets channel.*

- All-hadronic channel: Here, the two W bosons decay hadronically, $t\bar{t} \rightarrow W^+W^-b\bar{b} \rightarrow q\bar{q}'q''\bar{q}'''b\bar{b}$. The final state consists of four light quarks and two b-quarks. The branching ratio of this channel is the highest compared to the other two channels, $\mathcal{B} \approx 46.2\,\%$. This channel has a large expected number of background events from multijet production.

The charged leptons can be either e, μ or τ. e-leptons and μ-leptons can be identified in the detector, while τ-leptons cannot be observed directly in the detector. They have a short lifetime $\approx 3 \times 10^{-13}\,$s and decay either leptonically or hadronically. The hadronic decay of a τ lepton is dominant ($\mathcal{B} \approx 64.8\,\%$). Leptonic decays are $\tau \rightarrow e\nu_e\nu_\tau$ ($\mathcal{B} \approx 17.8\,\%$) and $\tau \rightarrow \mu\nu_\mu\nu_\tau$ ($\mathcal{B} \approx 17.4\,\%$). In the definition of the lepton+jets channel for this analysis, the leptonic decay of τ-leptons is included.

The top-quark mass

The top-quark mass is a free parameter in the SM. A first direct measurement of m_{top} was done at Tevatron. In 2014, a world combination of top-quark mass measurements performed at the LHC and Tevatron was done [8]. Fig. 1.6 shows a comparison of several m_{top} measurements from ATLAS and CMS compared with the LHC and world combination result.

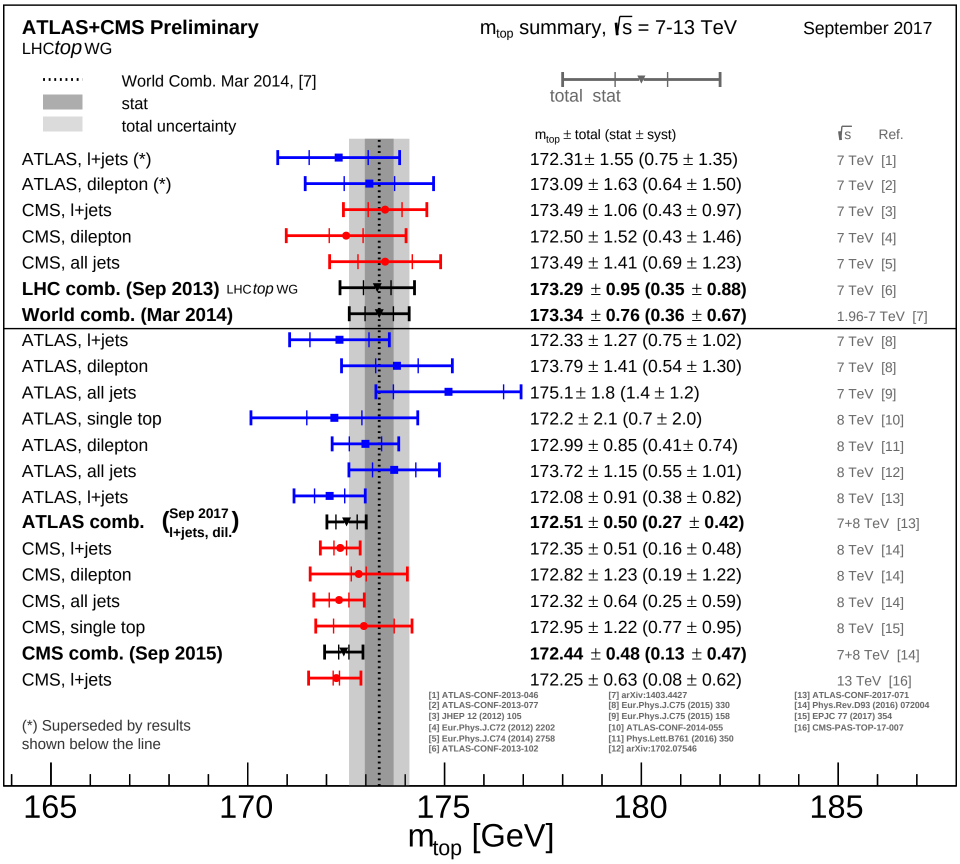

Figure 1.6: *Summary of the ATLAS and CMS direct m_{top} measurements. The results are compared with the LHC and world m_{top} combinations [50].*

The $t\bar{t}$ cross-section depends on the assumed value of the top-quark mass. Therefore, m_{top} can be indirectly extracted when performing a $t\bar{t}$ cross-section measurement.

1.3 The $t\bar{t}$ cross-section measurement

In this thesis, the $t\bar{t}$ production cross-section is measured in the lepton+jets channel at a centre-of-mass energy of $\sqrt{s} = 8\,\text{TeV}$ for both the full phase space and for a fiducial phase space close to the selected dataset.

Measurements of the $t\bar{t}$ cross-section have been published for several centre-of-mass energies between 1.96 and 13 TeV in $p\bar{p}$ and pp collisions. At the Tevatron, the uncertainty in the

$t\bar{t}$ cross-section measured by the D0 and CDF collaborations at a centre-of-mass energy of 1.96 TeV is 5.4 % [51]. The most precise measurement for a centre-of-mass energy of 8 TeV, with a total uncertainty of 3.2 %, was performed by the ATLAS Collaboration in the dilepton channel [52]. Further measurements at 7, 8 and 13 TeV in the same final state were published by the ATLAS and CMS collaborations [53–55].

The most precise cross-section previously measured in the lepton+jets channel at $\sqrt{s} = 8$ TeV was published by the CMS Collaboration and reached an uncertainty of 6.8 % [56]. Additionally, a previous measurement by the ATLAS Collaboration achieved a total uncertainty of 9.4 % using the same dataset as this analysis [57].

Fig. 1.7 shows a summary of LHC and Tevatron measurements of the $t\bar{t}$ production cross-section as a function of the centre-of-mass energy compared with the NNLO+NNLL theoretical prediction.

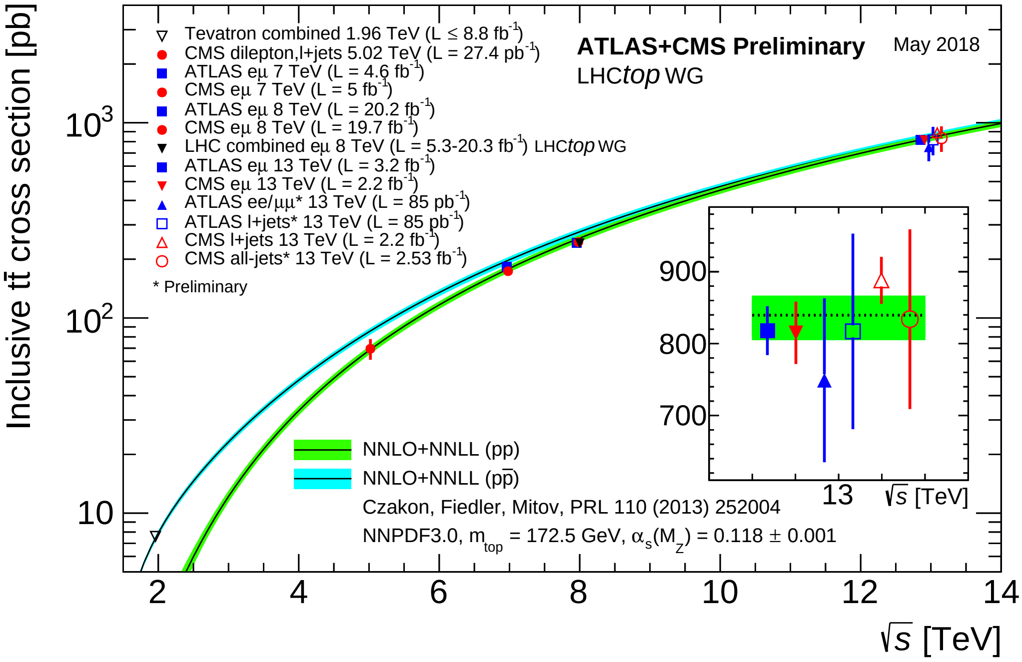

Figure 1.7: *Summary of LHC and Tevatron measurements of the $t\bar{t}$ production cross-section as a function of the centre-of-mass energy compared to the NNLO QCD calculation complemented with NNLL resummation (top++2.0). The measurements and the theory calculation are quoted at $m_{top} = 172.5$ GeV [50].*

Performing the same measurement in different channels is important to check the consistency of the results. Furthermore, uncertainties may affect each channel differently.

The definitions of the inclusive and fiducial $t\bar{t}$ cross-section measurements are explained in the following.

The inclusive $t\bar{t}$ cross-section

The measured inclusive cross-section is given by

$$\sigma_{\text{inc}} = \frac{\hat{\nu}}{\epsilon \cdot \mathcal{L}_{\text{int}}} = \frac{\hat{\beta} \cdot \nu}{\epsilon \cdot \mathcal{L}_{\text{int}}} \quad \text{with} \quad \epsilon = \frac{N_{\text{sel}}}{N_{\text{total}}} \,, \tag{1.11}$$

where $\hat{\nu}$ is the observed number of signal events. The quantity ϵ is the total event-selection efficiency, N_{total} is the number of events obtained from a simulated signal sample before applying any requirement and N_{sel} is the number of events obtained from the same simulated signal sample after applying all selection requirements.

The observed number of signal events, $\hat{\nu}$ is given by

$$\hat{\nu} = \hat{\beta} \cdot \nu \tag{1.12}$$

where $\hat{\beta}$ is an estimated scale factor obtained from the measurement and $\nu = \epsilon \cdot \sigma_{\text{theo}} \cdot \mathcal{L}_{\text{int}}$ is the expected number of events for the signal process. The reference cross-section σ_{theo} is defined by the central value of the theoretical prediction given in Eq. (1.9). By combining Eq. (1.11) with Eq. (1.12), one obtains:

$$\sigma_{\text{inc}} = \hat{\beta} \cdot \sigma_{\text{theo}}. \tag{1.13}$$

Thus, $\hat{\beta}$ is the parameter of interest that is measured in this analysis and using Eq. (1.13), the measured value of the inclusive cross-section is obtained.

The fiducial $t\bar{t}$ cross-section

The measurement of the $t\bar{t}$ cross-section in a fiducial volume close to the selected dataset is advantageous in reducing MC modelling uncertainties since the extrapolation to the full phase-space is avoided.

The fiducial cross-section is given by

$$\sigma_{\text{fid}} = A_{\text{fid}} \cdot \sigma_{\text{inc}} \quad \text{with} \quad A_{\text{fid}} = \frac{N_{\text{fid}}}{N_{\text{total}}} \,, \tag{1.14}$$

with N_{fid} being the number of events obtained from a simulated signal sample after applying a particle-level selection. Here, the fiducial acceptance, A_{fid}, is defined for an inclusive $t\bar{t}$ sample, including all decay modes of the W bosons. Using Eq. (1.11), the fiducial cross-section can be written as:

$$\sigma_{\text{fid}} = \frac{\hat{\nu}}{\epsilon' \cdot \mathcal{L}_{\text{int}}} \quad \text{with} \quad \epsilon' = \frac{N_{\text{sel}}}{N_{\text{fid}}} \,. \tag{1.15}$$

It can be seen from Eq. (1.15), that uncertainties affecting N_{sel} and N_{fid} in a similar way give a reduced uncertainty in σ_{fid} compared to that in σ_{inc}.

Applying Eq. (1.14), the measured value of the fiducial cross-section is obtained using the measured value of the inclusive cross-section.

2

Experimental setup

This chapter aims to explain the experimental setup used to produce and record the data analysed in this thesis. The data is generated in a proton–proton collision at the Large Hadron Collider (LHC) [58] and it is collected by the ATLAS detector [59]. The technical design of the LHC and the components of the ATLAS detector are explained in Sects. 2.1 and 2.2. Additionally, Sect. 2.3 reports the 2012 dataset.

2.1 The LHC

The LHC, located at the European Organization for Nuclear Research (CERN) near Geneva, is the largest and most powerful particle accelerator in the world, with the highest design centre-of-mass energy of 14 TeV for a *pp* collision and an instantaneous luminosity of $10^{34}\,\mathrm{cm}^{-2}\,\mathrm{s}^{-1}$. The tunnel of the LHC was constructed for the Large Electron–Positron collider (LEP). It is 26.7 km long, located about 100 m underground. LHC collides protons as well as heavy lead ions. The protons or the (Pb) ions are steered in beams using superconducting magnets. Two high-energy particle beams circulating in opposite directions are brought to collision at four interaction points where the four main detectors are situated. The detectors are: ATLAS, Compact Muon Solenoid (CMS) [60], Large Hadron Collider beauty (LHCb) [61] and A Large Ion Collider Experiment (ALICE) [62]. ATLAS and CMS are general purpose detectors to explore a wide range of physics with high precision and resolution and search for new physics and particles beyond our current knowledge. LHCb is specialised in B-physics and Charge-Parity (CP) violation. ALICE is designed to study the dense state of matter (quark-gluon plasma) produced during the heavy ions collisions. In addition there are three smaller experiments: Large Hadron Collider forward (LHCf) [63], which uses particles in the very forward region of the LHC collisions to simulate cosmic rays; ToTal cross section, Elastic scattering and diffraction dissociation Measurement (TOTEM) [64], dedicated to measure the *pp* interaction cross section and study elastic and diffractive scattering at the LHC; Monopole and Exotics Detector At the LHC (MoEDAL) [65], which specialises on searching for magnetic monopoles as well as highly ionising Stable Massive Particles (SMPs).

A schematic of the CERN accelerator complex is shown in Fig. 2.1. Before the protons circulate and collide at the LHC, they pass through a chain of pre-accelerators. First, the protons are extracted from the ionisation of hydrogen gas using an electric field. In the second step, these protons are accelerated to 50 MeV by the linear accelerator (LINAC 2). Next, they are injected into the Proton Synchrotron Booster, which accelerates them to an energy of 1.4 GeV. Then, they enter the Proton Synchrotron (PS), where their energy is increased to 25 GeV. After that, they pass through the Super Proton Synchrotron (SPS). The SPS is 7 km in circumference and accelerates the protons to an energy of 450 GeV. Finally, the protons are injected into one of the two pipes of the LHC, where they are accelerated to the final energy, which was 4 TeV per beam in 2012.

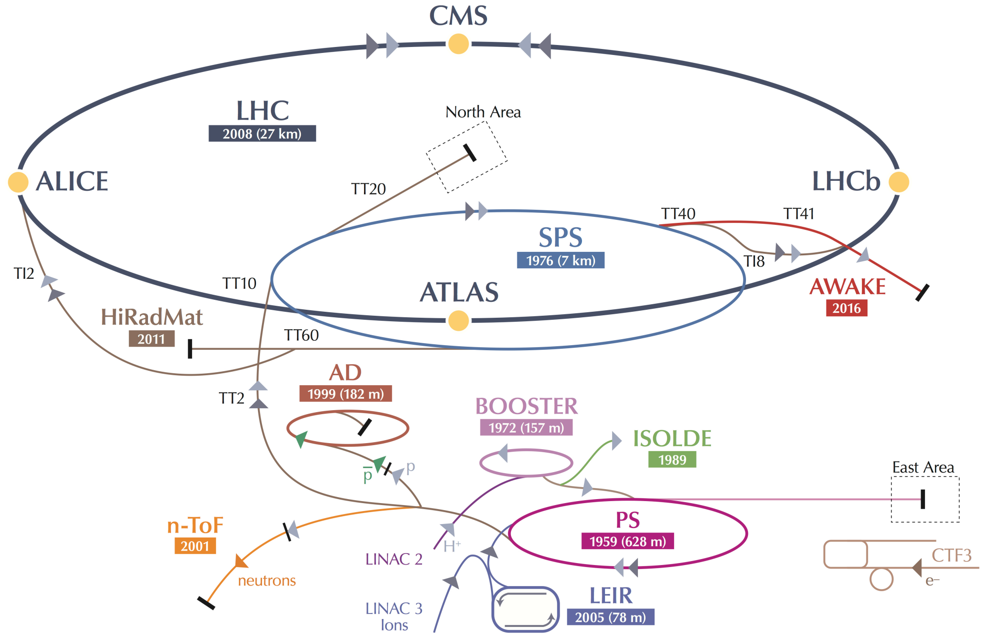

Figure 2.1: *A schematic of the CERN accelerator complex. The four main experiments are marked as yellow dots [66].*

The protons are accelerated in bunches using eight radio frequency (RF) cavities per beam, which provide an accelerating field strength of 5 MV/m. The LHC can be filled with up to 2808 bunches per beam. Each bunch contains about 10^{11} protons. The bunches remain on a circular path by strong magnetic fields provided by superconducting electromagnets.

These electromagnets are made from Niobium-Titanium (NbTi) coils which are cooled down to 1.9 K using super-fluid helium.

To achieve high production rate of rare processes at the LHC, a high integrated luminosity $\mathcal{L}_{\text{int}}$ is needed. The dependence of the number of events for a particular process with cross-section σ_{event} on the integrated luminosity is given by [58]:

$$N_{\text{event}} = \mathcal{L}_{\text{int}} \cdot \sigma_{\text{event}} \tag{2.1}$$

The integrated luminosity can be calculated as:

$$\mathcal{L}_{\text{int}} = \int \mathcal{L} dt \tag{2.2}$$

where $\mathcal{L}$ is the instantaneous luminosity, i.e. the number of interactions per square centimeter per second. It is an important parameter in particle colliders. The instantaneous luminosity can be written as [58]:

$$\mathcal{L} = \frac{N_b^2 n_b f_{\text{rev}} \gamma_r}{4\pi \epsilon_n \beta^*} F \tag{2.3}$$

where N_b is the number of protons per bunch, n_b is the number of bunches per beam, f_{rev} is the revolution frequency, γ_r is the relativistic gamma factor, ϵ_n is the normalised transverse beam emittance, β^* is the beta function at the interaction point (IP) and F is the geometric luminosity reduction factor due to the crossing angle at the IP.

An overview of the LHC performace parameters are given in Table 2.1, where performance values in 2012 are compared to design values.

Table 2.1: *The LHC performance parameters comparing the design values with the values in 2012 [67].*

Parameter	Design value	value in 2012
Beam energy [TeV]	7	4
β^* in IP 1,2,5,8 [m]	0.55	0.6,3.0,0.6,3.0
Bunch spacing [ns]	25	50
Number of bunches n_b	2808	1374
Number of protons per bunch N_b	1.15×10^{11}	$1.6 - 1.7 \times 10^{11}$
ϵ_n at start of fill [mm mrad]	3.75	2.5
Peak luminosity [$\text{cm}^{-2}\,\text{s}^{-1}$]	1×10^{34}	7.7×10^{33}
Max. mean number of events per bunch crossing	19	≈ 40
Stored beam energy [MJ]	362	≈ 140

The LHC started operation in November 2009. At the end of 2011, it reached the centre-of-mass energy of 7 TeV. The data analysed in this thesis was collected in 2012, when a centre-of-mass energy of 8 TeV was achieved and an integrated luminosity[1] of 20.3 fb^{-1} was accumulated. Fig. 2.2 shows the total integrated luminosity during 2012 delivered to and recorded by ATLAS.

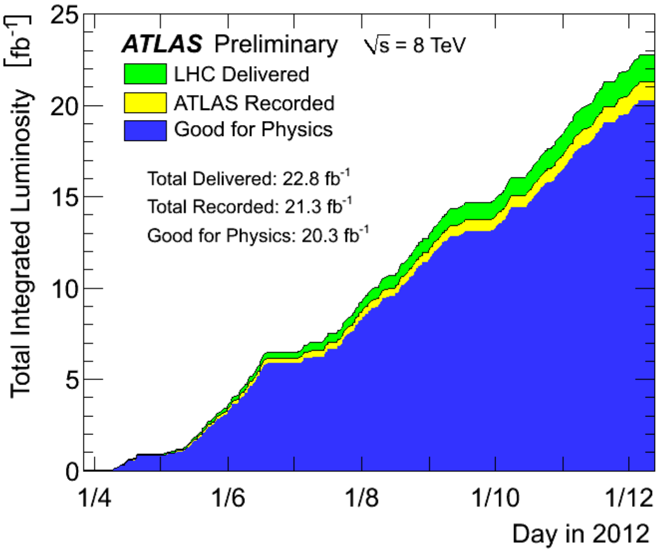

Figure 2.2: *The integrated luminosity versus time delivered to and recorded by ATLAS at* 8 TeV *centre-of-mass energy in 2012 [68].*

2.2 The ATLAS detector

ATLAS is the largest detector at the LHC, with a weight of about 7000 t. Its dimensions are 44 m in length and 25 m in height. A cutaway view of the ATLAS detector is shown in Fig. 2.3. It consists of multiple layers of subsystems arranged in a cylindrical symmetry around the interaction point as well as in two endcaps perpendicular to the beam axis. This setup allows for approximately 4π angular coverage. Each subsystem has its own functionality to detect particles passing through the detector layers and measure their properties. The innermost detector is called the Inner Detector (ID). The ID is composed of three sub-detectors and surrounded by a solenoid magnet. Around it, the electromagnetic and hadronic calorimeters are situated. The outermost part of ATLAS is called the Muon Spectrometer (MS), which is covered by a magnetic field from toroid magnets. More details describing the subsystems and their roles in detecting particles are stated in the next sections of this chapter.

---

[1] $1\,\text{fb}^{-1}=10^{39}\,\text{cm}^{-2}$

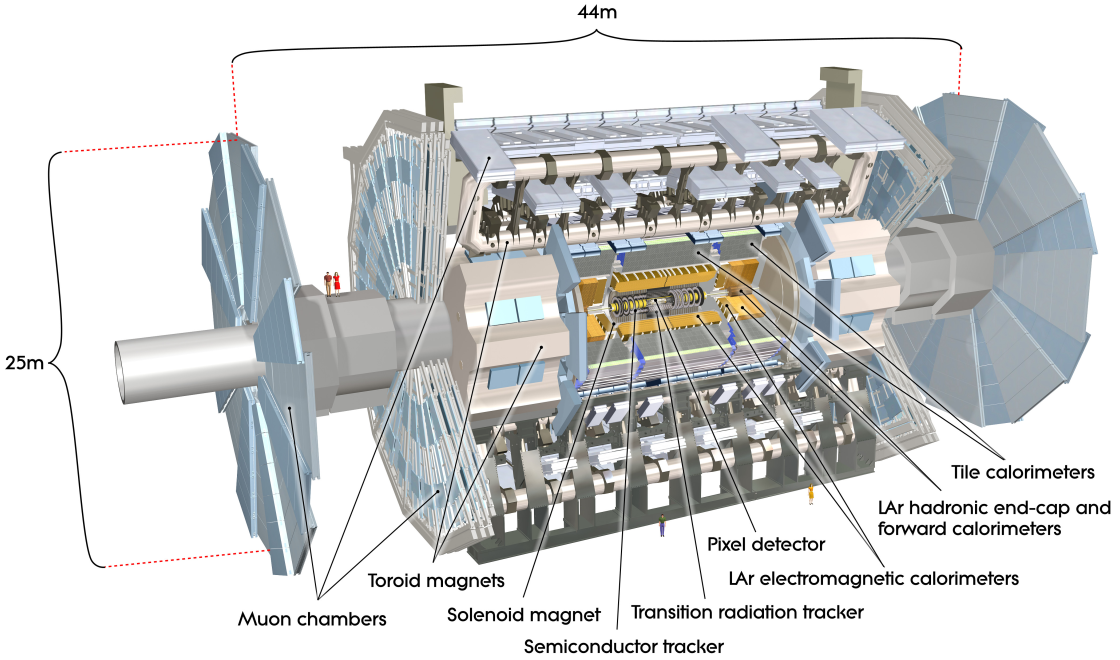

Figure 2.3: *The ATLAS detector with its main layers of subsystems [59].*

ATLAS' coordinate system is a right-handed Cartesian system with the interaction point defined as its origin. The x-axis is pointing to the centre of the LHC ring, while the y-axis is directed upwards and the z-axis is the beam direction, making the xy-plane transverse to the beam. Particle momenta are usually given in terms of their projection onto the transverse plane, referred to as transverse momentum $p_{\mathrm{T}} = \sqrt{p_x^2 + p_y^2}$, and the angles θ and ϕ. The angles θ and ϕ indicate the direction of the particles. θ is the polar angle with respect to the beam axis. ϕ is the azimuthal angle in the transverse plane with respect to the positive x-axis. The rapidity is often used instead of θ. It is defined as:

$$y = \frac{1}{2} \ln \left(\frac{E + p_z}{E - p_z} \right), \tag{2.4}$$

where E is the particle's energy and p_z is its momentum component in the z-direction. The pseudorapidity is an approximation of the rapidity for relativistic particles (with low mass), expressed as:

$$\eta = -\ln \left[\tan \left(\frac{\theta}{2} \right) \right]. \tag{2.5}$$

The angular distance between two particles in the η–ϕ plane is defined as:

$$\Delta R = \sqrt{(\Delta\eta)^2 + (\Delta\phi)^2}. \tag{2.6}$$

The transverse energy is defined for objects measured in the calorimeter as:

$$E_{\mathrm{T}} = E \sin\theta. \tag{2.7}$$

Particles that do not interact with the detector's material, such as neutrinos, cause an imbalance in the transverse momentum. The initial transverse momentum is zero, hence finding missing transverse momentum indicates the existence of such particles. The missing transverse momentum vector is calculated as:

$$\vec{E}_{\mathrm{T}}^{\mathrm{miss}} = -\sum_{i} \vec{p}_{\mathrm{T}}(i), \tag{2.8}$$

where the sum runs over all visible particles. The magnitude of the missing transverse momentum vector is defined as:

$$E_{\mathrm{T}}^{\mathrm{miss}} = |\vec{E}_{\mathrm{T}}^{\mathrm{miss}}|. \tag{2.9}$$

2.2.1 The inner detector

The inner detector is the subsystem closest to the interaction point. The main purpose of the ID is to detect tracks of charged particles traversing the detector and measure their momenta in a high track density environment. The ID is 6.2 m long with a diameter of 2.1 m and coverage in the region of $|\eta| < 2.5$. A solenoid magnet surrounding the ID provides a 2 T magnetic field facilitating the momentum measurement by causing a curvature in the path of the charged particles. Another purpose of the ID is to help distinguishing electrons from pions and to determine the position of primary vertices of the *pp* collisions as well as secondary vertices originated from long lived particles. The ID consists of cylindrical layers in the barrel region and disks perpendicular to the beam pipe in the endcaps region. It is composed of three sub-detectors: the Pixel detector, the SemiConductor Tracker (SCT) and the Transition Radiation Tracker (TRT), see Fig. 2.4. The pixel detector and the SCT are high-resolution semiconductor trackers, while the TRT is a straw tube detector with lower spacial resolution, but higher hit multiplicity. Together they allow for high precision pattern recognition of tracks.

The pixel detector

The pixel detector provides the highest spatial resolution for track reconstruction and consists of three layers at radii 5.05 cm, 8.85 cm and 12.25 cm in the barrel region and three disks at each side in the endcaps region. The minimal pixel size is 50×400 µm^2 in R–$\phi \times z$. It offers in total 80.4 million readout channels and has an intrinsic accuracy of 20 µm in the R–ϕ plane and 115 µm in z. When charged particles pass through the pixel sensors, electron-hole pairs are created in the semi-conductor material and the resulting electrical current is detected by the readout chips, allowing to determine the position of the particles. Typically, a hit is recorded in each layer of the pixel detector allowing track reconstruction. The pixel detector is also important for finding the location of secondary vertices and for b-tagging algorithms, where jets originating from b-hadrons are identified.

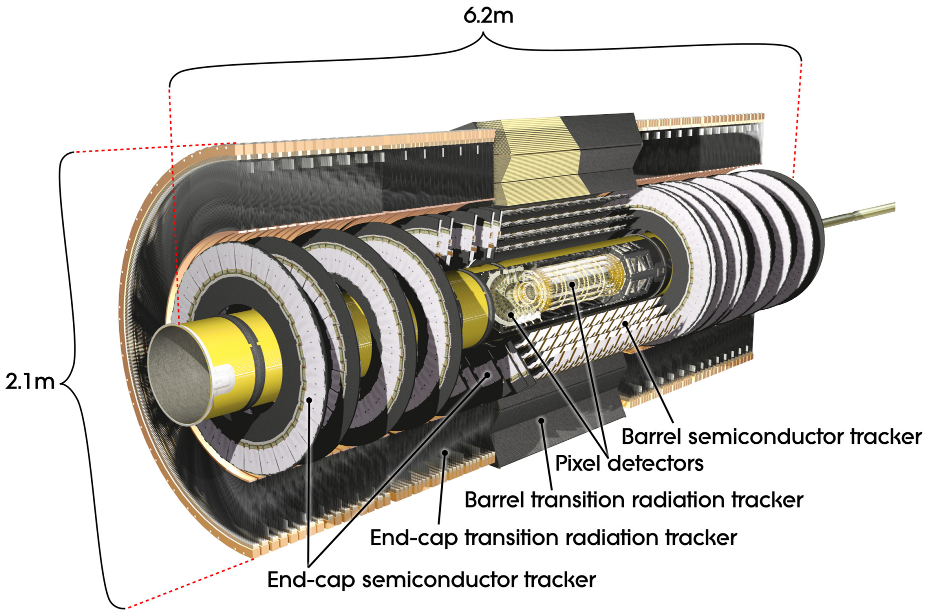

Figure 2.4: *A cutaway view of the ATLAS inner detector with its components [59].*

The semiconductor tracker

The SCT is made up of silicon microstrip sensors ordered in four layers in the barrel region with radii from 30 cm to 50 cm and nine disks in each endcap region. There are 6.3 millions readout channels. The SCT works similar to the pixel detector by ionisation of the silicon material. To increase the spatial resolution of the SCT, each layer has back-to-back modules aligned with an angle of 40 mrad between them to enable 3D measurements of the hit position. The SCT has an intrinsic resolution of 17 µm in the R–ϕ plane and 580 µm in z.

The transition radiation tracker

The TRT comprises the outer part of the ID. It consists of straw tubes filled with a Xenon-based gas mixture. In the barrel region, the straw tubes are situated parallel to the beam axis, while in the endcap region, they are arranged radially in wheels. The TRT covers the region of $|\eta| < 2.0$. Each straw is 4 mm in diameter. In addition to momentum measurements, material of different indices of refraction, placed between the tubes, assists in electron identification. Transition radiation is emitted from highly relativistic particles crossing the border of inhomogeneous media. Transition radiation is proportional to the Lorentz factor γ of the particle, making it possible to distinguish electrons from hadrons. Like in the silicon trackers, charged particles interact with gas molecules and free electrons, which drift to an anode wire running through the center of the tubes, where the current is measured. The intrinsic resolution of the TRT is 130 µm, which is lower than the silicon trackers, but the TRT has a high hit multiplicity per track; a typical track leaves 36 hits in the TRT.

2.2.2 The calorimeter

The ATLAS calorimeter system measures the energy of charged and neutral particles, it also assists in the measurement of missing transverse momentum $E_{\mathrm{T}}^{\mathrm{miss}}$ of events. It employs sampling calorimeters, which separate absorber and active materials. Particles traversing the absorber material interact with it and create electromagnetic or hadronic showers, depending on the incoming particle, which are measured by the active material. The calorimeter system comprises an electromagnetic calorimeter surrounded by a hadronic calorimeter, see Fig. 2.5. The whole system covers a range of $|\eta| < 4.9$ and the full ϕ range.

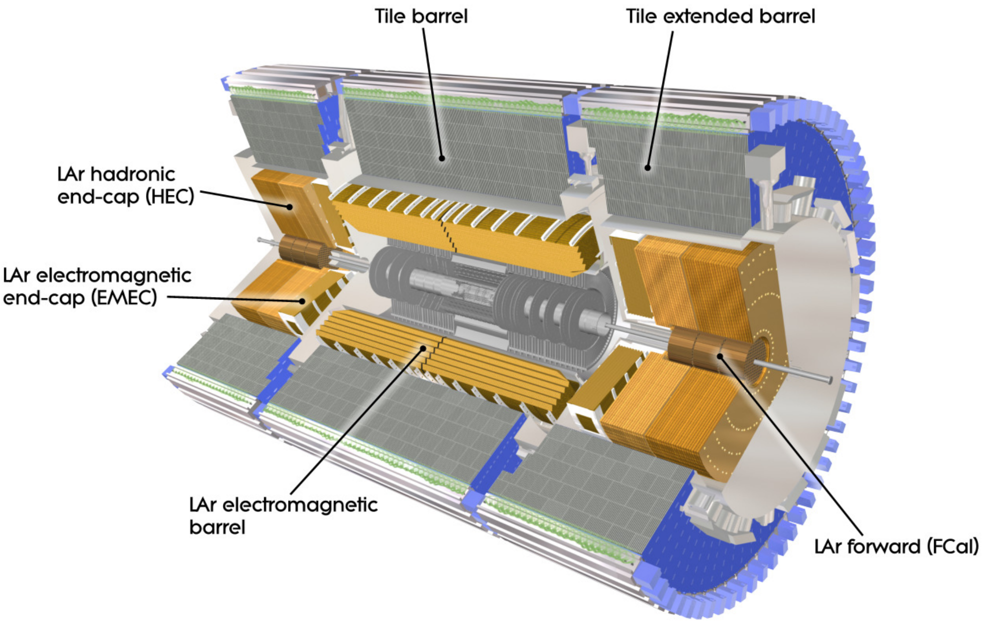

Figure 2.5: *The ATLAS calorimeter [59].*

The electromagnetic calorimeter

The electromagnetic calorimeter is divided into three parts, each contained in its own cryostat: the barrel region with $|\eta| < 1.475$, the two endcaps regions with $1.375 < |\eta| < 3.2$ and the forward region with $3.1 < |\eta| < 4.9$. In all regions, liquid Argon (LAr) is used as the active material. Lead serves as the absorber medium in the barrel and endcaps regions, while copper is the absorber material for the forward calorimeter. Electrons and photons interact with the absorber material through bremsstrahlung or pair production (e^+e^-) and create electromagnetic showers. They deposit all their energy and are absorbed in the electromagnetic calorimeter, while hadrons deposit only small fraction of their energy and pass through to the hadronic calorimeter. An important design parameter when building calorimeters is the thickness of the absorber material such that electrons and photons are contained completely in the electromagnetic calorimeter. This is expressed in radiation lengths[2] X_0. The thickness is $> 22X_0$ in the barrel region and $> 24X_0$ in the endcaps. The electromagnetic calorimeter has a very good energy resolution. The design resolution is $\frac{\sigma_E}{E} = \frac{10\,\%}{\sqrt{E}} \oplus 0.7\,\%$.

The hadronic calorimeter

The hadronic calorimeter operates similarly to the electromagnetic calorimeter, but it measures the energies of jets resulting from hadrons instead of electrons and photons. It is composed of the Tile barrel calorimeter which covers the region of $|\eta| < 1.7$, the hadronic endcap calorimeter covering $1.5 < |\eta| < 3.2$ and the second and third layers of the forward calorimeter covering the range of $3.1 < |\eta| < 4.9$. The Tile calorimeter is subdivided into two parts, the Tile barrel with $|\eta| < 1.0$ and the Tile extended barrel covering $0.8 < |\eta| < 1.7$. The Tile calorimeter utilizes steel as the absorber material and scintillating tiles as the active material. For the endcaps and the forward calorimeters, LAr is used again as the active material. Copper is the absorber medium for the endcaps, while Tungsten is used in the forward calorimeter. The thickness of the hadronic calorimeter is expressed in interaction lengths λ[3]. The total thickness is about 10 λ, which ensures a good energy resolution. The design energy resolution is $\frac{\sigma_E}{E} = \frac{50\,\%}{\sqrt{E}} \oplus 3\,\%$ for the barrel and endcaps regions and $\frac{\sigma_E}{E} = \frac{100\,\%}{\sqrt{E}} \oplus 10\,\%$ for the forward region.

2.2.3 The muon spectrometer

The outer part of the entire ATLAS detector is the muon spectrometer. It is a tracking system for muons, which are not stopped in the detector parts but they penetrate the whole detector. Toroid magnets provide a magnetic field that bends the path of muons and allows for measuring muon momenta. The strength of the delivered magnetic field is 0.5 T in the barrel region and 1 T in the endcaps. Four components operate to measure the momentum within $|\eta| < 2.7$ and trigger high-energetic muons events within $|\eta| < 2.4$, as

---

[2] The radiation length X_0 is the mean distance over which an electron looses all but $1/e$ of its energy by bremsstrahlung.

[3] The interaction lengths λ is the mean path length to reduce the flux of relativistic primary hadrons to a fraction $1/e$ [69].

shown in Fig. 2.6. The Monitored Drift Tubes (MDT) consist of aluminum tubes containing a gas mixture and a tungsten wire which works as an anode. Muons passing through the detector, ionise the gas and the freed electrons drift to the anode. The drift time is used to measure the position of the muons. The Cathode Strip Chambers (CSC) are multi-wire proportional chambers that are placed in the innermost endcap layer to handle the high particles rate covering a pseudorapidity range of $2.0 < |\eta| < 2.7$. The Resistive Plate Chambers (RPC) in the barrel region and the Thin Gap Chambers (TGC) in the endcaps are two trigger chambers which provide information about muon tracks to the level-1 trigger system (L1).

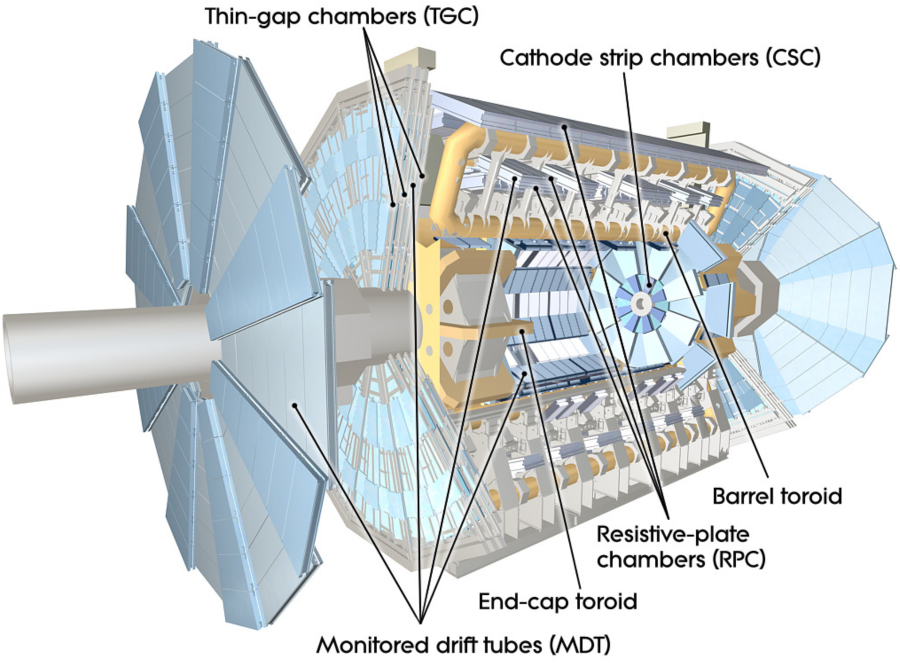

Figure 2.6: *Cutaway view of the ATLAS muon spectrometer [59].*

2.2.4 The trigger system

The LHC is designed to collide protons with a bunch spacing of 25 ns, which corresponds to a collision rate of 40 MHz. Storing this huge amount of data is not achievable. The trigger system filters interesting events and reduces the amount of data that is stored and used later in analyses [70]. The trigger system is split into three levels. Each level passes its selected data to the next level for further filtering. The Level-1 (L1) trigger is a hardware-based trigger utilising the calorimeter and the RPC and the TGC of the muon system to identify events with high p_{T} leptons, jets and photons, as well as high missing transverse momentum $E_{\mathrm{T}}^{\mathrm{miss}}$. L1 reduces the event rate to 75 kHz. The time needed for a decision at L1 is 2.5 µs. L1 defines Regions-of-Interest (RoI) where possible trigger objects are found. The Level-2 (L2) trigger is software-based and uses the RoI information, reducing the event rate to 3.5 kHz. The L2 trigger decision takes about 40 ms. The Event Filter (EF) trigger is a second software-based trigger. It employs offline algorithms and methods to bring the event rate down to about 400 Hz. The EF trigger decision takes about 4 s.

2.2.5 Luminosity detectors

A precise measurement of the luminosity is crucial for cross-section measurements, since the uncertainty in the luminosity determination is usually significant in the measurement. The instantaneous luminosity is related to the pp inelastic cross-section σ_{inel} by [71]:

$$\mathcal{L} = n_b \langle \mathcal{L}_b \rangle = n_b \frac{\langle \mu \rangle f_{\text{rev}}}{\sigma_{\text{inel}}} \tag{2.10}$$

where $\langle \mathcal{L}_b \rangle$ is the mean bunch luminosity and $\langle \mu \rangle$ is the bunch-averaged pile-up parameter. ATLAS measures the visible interaction rate per bunch crossing, μ_{vis} using several detectors and algorithms, where $\mu_{\text{vis}} = \epsilon \mu$, ϵ is the efficiency of the detector. The total inelastic cross section is related to the visible cross-section, $\sigma_{\text{vis}} = \epsilon \sigma_{\text{inel}}$. Thus, the bunch luminosity can be written as [71]:

$$\mathcal{L}_b = \frac{\mu_{\text{vis}} f_{\text{rev}}}{\sigma_{\text{vis}}} \tag{2.11}$$

There are two primary luminosity sub-detectors in ATLAS. LUminosity measurement using a Cherenkov Integrating Detector (LUCID) [72] and Beam Conditions Monitor (BCM) [73]. LUCID is a gas Cherenkov detector located at a distance of 17 m on both sides of the IP, covering the pseudorapidity range $5.6 < |\eta| < 6.0$. BCM consists of four diamond sensors, which surround the beam pipe at a distance of 1.84 m from the IP and a radius of 55 mm. Both detectors provide online monitoring of the beam and the running conditions.

The calibration of the luminosity scale is performed using Van der Meer scans of the beam, where the bunch luminosity is extracted from beam parameters. The interaction rate is measured for each colliding bunch-pair in the two orthogonal directions x and y. Using the luminosity extracted from the scans and the measured μ_{vis} by each detector, σ_{vis} is determined.

2.3 The 2012 dataset

Data samples used in this analysis were delivered and recorded by the ATLAS detector from April 4th to December 6th, 2012 from the LHC pp collision at a centre-of-mass energy of 8 TeV. To make sure that data was taken with full operation of all sub-components of the ATLAS detector, data quality flags are gathered in a Good Run List (GRL). Only events passing the GRL are filtered and utilised in physics analyses. Single-electron [74] and single-muon [75] triggers are operated to filter events. The overall integrated luminosity of the 2012 dataset is $\mathcal{L}_{\text{int}} = 20.2\,\text{fb}^{-1}$.

3

Event generation and simulated samples

Understanding the physics processes generated in the *pp* collisions at the LHC is very challenging especially with the complexity of the experimental setup of the ATLAS detector. The production of simulated samples is a method of imitating real data using theoretical prediction and phenomenological approach of physics processes. The simulated samples are generated to be similar to real data, which allows them to be compared to observed data. After the generation of simulated events, the interaction of particles with the detector's material and the detector responses are simulated. The same reconstruction algorithms are used for data and simulated events.

Sect. 3.1 gives an overview of the simulation of *pp* collisions and the detector simulation. The samples of simulated events used in this analysis for the signal and background processes are introduced in Sect. 3.2.

3.1 Event generation

The tools employed to simulate physics events are called Monte Carlo (MC) event generators. The generation is done in several steps as shown in Fig. 3.1.

The hard interaction occurs between partons of two colliding protons (shown as a large red blob in Fig. 3.1). The momentum fractions of the interacting initial partons are derived from PDFs. To simulate the hard process, the matrix elements are calculated using Feynman diagrams at leading order (LO) or next-to-leading order (NLO) accuracy in perturbation theory. The generated partons from the hard process consist of quarks, gluons and leptons. The showering is then modelled, where gluons can split into quark

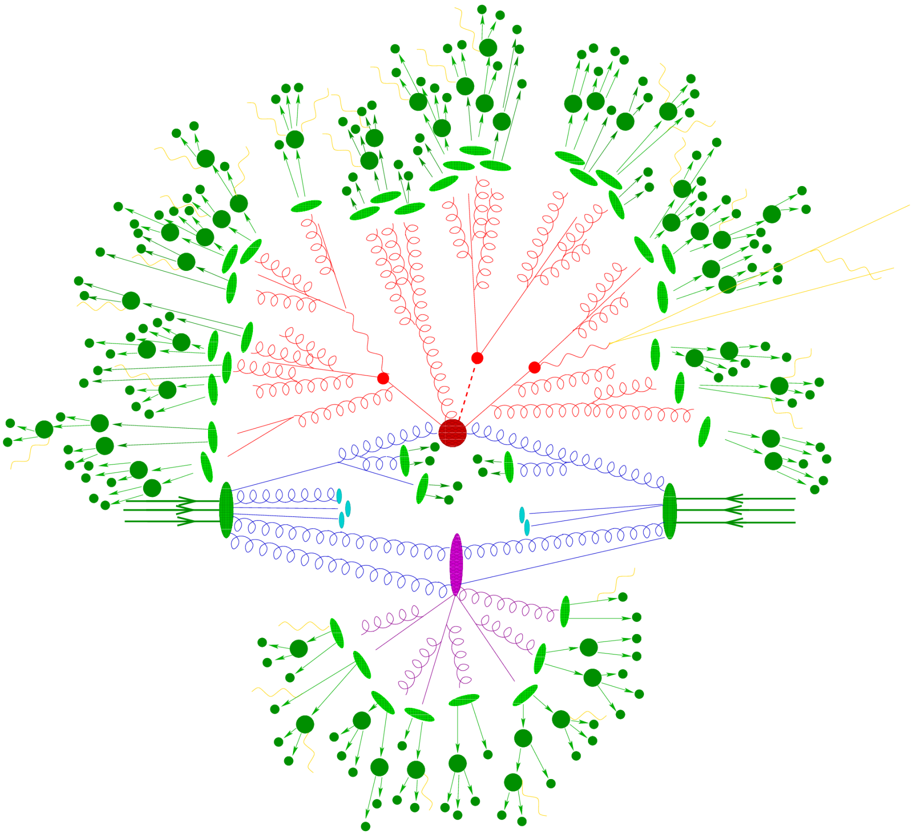

Figure 3.1: *Sketch of a hard pp collision simulated by an event generator [76].*

anti-quark pairs or partons radiate gluon bremsstrahlung (red lines). Initial- and final-state radiations (ISR/FSR) are associated with incoming or outgoing particles, respectively. ISRs are shown in Fig. 3.1 as blue curly lines connected to the hard interaction red blob. Once the decreasing energy scale reaches below a cut-off scale ($\approx 1\,\mathrm{GeV}$), the evolution of parton shower is terminated. The resulting partons merge together to form colour-singlet hadrons, a process referred to as hadronisation (shown as light-green blobs). These hadrons decay further into stable particles (dark-green blobs). The hadronisation cannot be calculated using perturbation theory, therefore the simulation relies on phenomenological models. Interactions and activities of the proton remnants, called ‘the underlying event’, are added. These activities include showering and hadronisation and are not part of the hard interaction (shown as purple blob and lines).

Multiple other pp interactions occur within each bunch-crossing, referred to as ‘pile-up’. Additional collisions occurring in the same bunch-crossing as the hard process of interest are called in-time pile-up [77]. On the other hand, out-of-time pile-up are additional collisions occurring in bunch-crossings just before and after the collision of interest. Minimum-bias events generated with PYTHIA 8 [78] were used to simulate the production of pile-up events. The distribution of the number of pile-up interactions in the simulation is re-weighted according to the instantaneous luminosity spectrum in the data.

Monte Carlo event generators

The event generators used in this thesis are shortly explained here. Some of them are multi-purpose generators that can perform all steps of the event generation, while others are specialised to carry out part of the steps. Matrix element (ME) generators simulate the hard process but need to be interfaced to other models for showering and hadronisation. The matching of the ME calculation with the parton shower (PS) has to consider overlapping partons generated by the ME and the PS, which lead to the same n-parton configuration. Different matching methods in event generators are employed to remove the overlapping partons.

Event generators used in the scope of this analysis are:

- POWHEG-BOX [79, 80]: It is a ME event generator with NLO accuracy in perturbative QCD calculations. It generates events with positive weights and does not depend on the showering generator. Hence, it can be interfaced to any modern shower generator. In the scope of this thesis, it has been interfaced to PYTHIA and HERWIG PS generators.
- MC@NLO [81, 82]: Like POWHEG-BOX, MC@NLO is a NLO ME generator. It provides a method of matching the NLO calculations to the PS using a subtraction procedure. The method generates a fraction of events (10 % to 20 %) with negative weights. The parton shower and hadronisation are simulated using HERWIG.

- ALPGEN [83]: It is a hard process event generator with the emphasis on final states with large jet multiplicities. The ME calculation is performed with LO accuracy. It has been interfaced to PYTHIA and HERWIG as shower models. The overlapping between the ME and PS are removed using the MLM method [84].
- SHERPA [85]: It is a multi-purpose complete event generator. It provides LO ME calculation of hard scattering processes and a PS model for the emission of additional partons. The fragmantation of partons into hadrons is described using a phenomenological cluster-hadronisation model. A simple model of multiple interactions is used to account for the underlying event. The CKKW method [86] is employed to match the ME to the PS.
- PYTHIA [87]: It is a multi-purpose event generator. The hard scattering process is calculated to LO accuracy in QCD. A PS model is provided and the Lund string model is used for hadronisation. Additionally, a model is provided to simulate the underlying event. Hard scattering events can be generated using another program and then fed to PYTHIA for the PS and hadronisation.
- HERWIG [88]: Like PYTHIA, HERWIG is a multi-purpose event generator. It includes the simulation of the hard scattering at LO accuracy and simulates the PS and hadronisation. The PS model takes into consideration colour coherence effects and azimuthal correlations both within and between jets. The cluster model is used for hadronisation. HERWIG is usually interfaced to the JIMMY model [89] to simulate the underlying event.

Event generators come with a set of parameters, which are tuned and tested with data. These parameters are mostly related to the simulation of hadronisation and underlying events since they are based on phenomenological models. Optimisation of the parameters is performed to give a better description of the data.

Detector simulation

The simulation of the particles' interaction with the detector material and of the detector response is performed using the GEANT4 framework [90]. The generated particles pass through a simulation of the ATLAS geometry and their hypothetical energy deposits are recorded as 'hits' with position and time. The hits are then converted to detector responses (voltages and currents) during a step of digitisation. The output of the simulation is identical to that of the ATLAS detector [91]. Thus, the same trigger and reconstruction algorithms can be used for simulated events as for real data.

Most of the 'full simulation' time is spent simulating particles traversing the calorimeters. The ATLFAST2 simulation is provided with pre-simulated showers stored in memory in order to reduce the CPU time of the simulation.

Parton-, particle- and detector-level

Particles generated after the hard interaction, i.e. before the showering and the hadronisation, are referred to be at ‘parton-level’. Quarks and gluons at parton-level, e.g. the top-quark, are not visible in the detector but only their decay products. Particles at parton-level depend on the features of the event generator. After showering and hadronisation, final-state particles are referred to be at ‘particle-level’. Particle-level objects are less dependent on the implementation of the generators and are used in this analysis in performing the fiducial measurement. Particles that went through the detector simulation are called ‘detector-level’ objects, which are used in performing the inclusive $t\bar{t}$ cross-section measurement.

3.2 Simulated samples

Simulated samples are needed for the signal process ($t\bar{t}$) to understand the modelling and to estimate systematic uncertainties. Backgrounds are physics processes with a similar final state signature to the signal process, that pass the event selection applied in the signal region under study. In order to understand and estimate their contributions, simulated samples are generated for each of the background processes. Detailed lists of simulated samples used in this analysis are given in App. A.

Signal samples

Signal $t\bar{t}$ events were simulated using the Powheg-Box event generator [79, 80] with the CT10 PDF set [26]. The renormalisation and factorisation scales in the matrix element calculation were set to the value $\mu = \sqrt{m_{\text{top}}^2 + p_{\text{T}}^2(t)}$ where $p_{\text{T}}(t)$ is the top-quark transverse momentum, evaluated for the underlying Born configuration, i.e. before radiation. The h_{damp} parameter, which controls the p_{T} of the first emission beyond the Born configuration, was set to m_{top}. The main effect of this is to regulate the high-p_{T} gluon emission against which the $t\bar{t}$ system recoils. Parton shower, hadronisation and the underlying event were simulated with Pythia and the Perugia2011C set of tuned parameters [92].

As all event generators rely on different models and parameters, alternative generators and samples are used to study the modelling of $t\bar{t}$ events and to estimate systematic uncertainties:

- Powheg-Box event generator and setting the h_{damp} parameter to infinity, interfaced to Herwig.
- Powheg-Box event generator and setting the h_{damp} parameter to infinity, interfaced to Pythia.

- MC@NLO event generator interfaced to Herwig and Jimmy.
- Powheg-Box event generator, interfaced to Pythia, with a variation of the factorisation and renormalisation scales by a factor of 2 combined with the Perugia2012radLo parameters.
- Powheg-Box event generator, interfaced to Pythia, with a variation of the factorisation and renormalisation scales by a factor of 0.5 combined with the Perugia2012radHi parameters and setting the h_{damp} parameter to $2 \times m_{\text{top}}$.

All $t\bar{t}$ samples were simulated with a top-quark mass of 172.5 GeV and a width of 1.32 GeV modelled using a Breit–Wigner distribution. The top quark is assumed to decay via $t \to Wb$ 100 % of the time.

W+jets and Z+jets

The production of a W boson via the electroweak interaction with additional jets, referred to as W+jets, is the main background for the $t\bar{t}$ process in the lepton+jets channel. When the W boson decays leptonically, $W \to \ell\nu$, and the event has four jets, the final state signature is the same as the $t\bar{t}$ signature. The production of the Z boson with additional jets, Z+jets, is a main background for $t\bar{t}$ in the dilepton channel since the Z boson decays into two leptons $Z \to \ell^+\ell^-$. Nevertheless, in case one of the leptons is not detected, the event can pass the selection cuts for $t\bar{t}$ in the lepton+jets channel. However, this is largely suppressed by the small $E_{\text{T}}^{\text{miss}}$ in the Z+jets events since there is no neutrino in the final state signature.

Fig. 3.2 shows the production of the V bosons ($V = Z, W$) with 0 partons and with 1 parton. Additional jets are produced through gluon bremsstrahlung and gluon splitting into $q\bar{q}$.

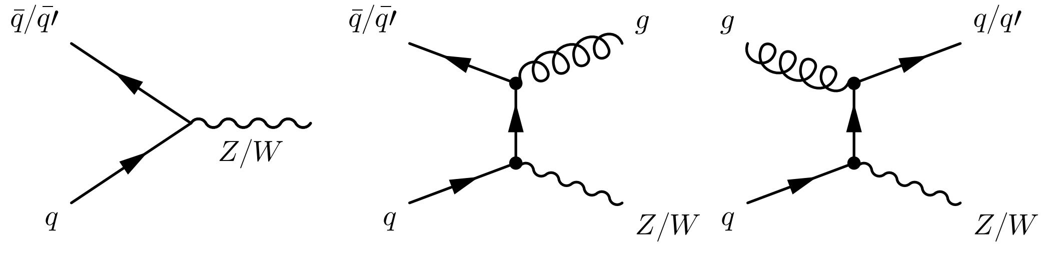

Figure 3.2: *Examples of Feynman diagrams for $V + 0$ partons and $V + 1$ parton production.*

The simulated W+jets samples were produced with the Alpgen event generator using the CTEQ6L1 set of PDFs [93]. Pythia was used for the showering using the Perugia2011C set of tuned parameters. Events of W+jets and Z+jets were produced with up to five additional partons. Dedicated samples are generated for events with at least one heavy flavour quark i.e., $W + b\bar{b}, W + c\bar{c}, W + c$ and $Z + b\bar{b}, Z + c\bar{c}$. The "MLM" matching scheme was employed to remove overlaps between the ME and the PS. The overlapping events between the inclusive W+jets and Z+jets samples and the dedicated samples with heavy-flavour jets were removed using the ΔR matching.

The cross-sections for inclusive W- and Z-boson production are calculated with NNLO precision using the FEWZ program [94, 95] and are estimated to be 12.1 nb and 1.13 nb, respectively. The uncertainty is 4 %, including the contributions from the PDF and scale variations.

Single top-quark

The production of a single top-quark via the electroweak interaction includes three channels: t-channel, s-channel and Wt-channel. Feynman diagrams of the single-top production in the three channels are shown in Fig. 3.3. In the t-channel, the top quark is produced by the interaction of a b-quark with a light quark via the exchange of a virtual W boson. This channel has at least three jets in the final state, two of which are b-jets, in addition to a lepton and neutrino from the leptonic W decay ($W \rightarrow \ell\nu$). In the s-channel, two b-quarks are in the final state together with the W boson decay products. In the Wt-channel, in case that one of the W bosons decays leptonically and the other hadronically, the final state signature is a lepton, a neutrino, one b-jet and two light-jets. For the three channels, more jets can be produced via ISR/FSR, which leads to a final-state signature similar to $t\bar{t}$ in the lepton+jets channel.

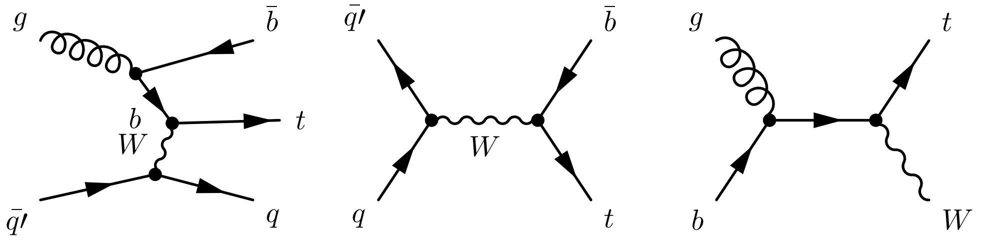

Figure 3.3: *Examples of Feynman diagrams for single top production in (from left to right) t-channel, s-channel and Wt-channel.*

The simulated samples were produced by the Powheg-Box event generator with the CT10 PDF set interfaced to Pythia using the Perugia2011C set of tuned parameters.

The Wt process has a predicted production cross-section of 22.3 pb [96], calculated to approximate NNLO accuracy with an uncertainty of 7.6 % including scale and PDF uncertainties. The cross-sections for single top-quark production in the s- and t-channel are calculated with the Hathor tool [97] to NLO precision, see Ref. [98]. Uncertainties from variations of scales used in the ME and PDFs are estimated using the same methodology as for $t\bar{t}$ production. For t-channel production, this leads to a cross-section of 84.6 pb with a total uncertainty of 4.6 %, while for s-channel production, a cross-section of 5.2 pb with a total uncertainty of 4.2 % is predicted.

Diboson

The production of vector boson pairs, i.e. WW, WZ and ZZ is a small background for $t\bar{t}$. Two examples of the WW production are shown in Fig. 3.4. Leptonic decay of one of the vector bosons and hadronic decay of the other can lead to similar final states as $t\bar{t}$ in the lepton+jets channel. In case of the ZZ process, one of the two leptons from the leptonic decay of the Z boson would be undetected to mimic the lepton+jets signature of $t\bar{t}$.

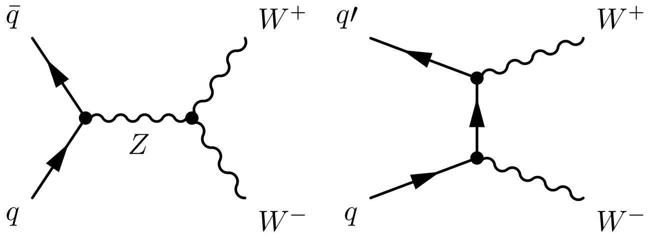

Figure 3.4: *Examples of Feynman diagrams for WW pair production.*

Simulated diboson events were produced using the SHERPA event generator with the CT10 PDF set with up to three additional partons in the ME and PS. The processes are normalised using the inclusive NLO cross-sections provided by MCFM [99], which are 56.8 pb for WW, 7.36 pb for ZZ, and 21.5 pb for WZ production. The total uncertainty for each of the three processes, including scale variations and uncertainties in the PDF, is estimated to be 5 %.

Multijet

The production of multijet events is an important background because of the very large cross-section of this process. Examples of the production of multijet events are shown in Fig. 3.5. Multijet events can be a background to $t\bar{t}$ events in the lepton+jets channel, if one jet in an event is mis-reconstructed as an isolated lepton or if the event has a non-prompt lepton that appears isolated and if there is enough $E_{\mathrm{T}}^{\mathrm{miss}}$ in the event. The $E_{\mathrm{T}}^{\mathrm{miss}}$ arises from the limited energy resolution of the detector. The probability of mis-reconstructing a jet as a lepton is low. However, this is countered by the large cross-section.

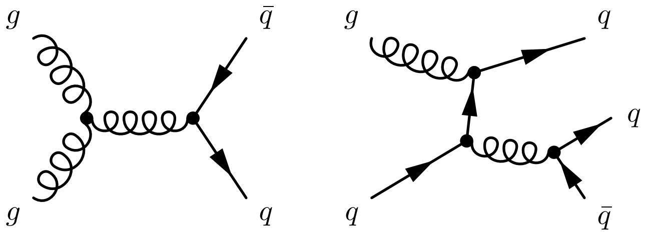

Figure 3.5: *Feynman diagrams for multijet production*

The multijet process is difficult to model with enough statistics in simulation. Therefore, in this analysis it is modelled using different methods in the electron and muon channels, one of which is data-driven. These methods are explained later in Sect. 5.5.1, where the rates of the multijet process are extracted using control regions.

4

Objects reconstruction, identification and selection

Physics objects are reconstructed from signals recorded by the various detector parts. These signals are produced by the interaction of particles with the active detector material. Particles of different types produce signals in different detector parts, which allows to distinguish them. This analysis depends on reconstructed physics objects, thus it is necessary to translate these signals into tracks, energy clusters and momenta of objects. The performance of algorithms used in the reconstruction and identification affects the precision of the $t\bar{t}$ cross-section measurement.

Only objects needed in the reconstruction of $t\bar{t}$ events will be discussed in this chapter. The signature of a semi-leptonic $t\bar{t}$ event comprises charged leptons, jets, including b-quark jets, and missing transverse momentum $E_{\mathrm{T}}^{\mathrm{miss}}$.

4.1 Tracks and vertices

All charged particles leave hits in the ID components and these hits are reconstructed as tracks. The challenge in building tracks is the large number of hits caused by thousands of particles leaving signals in the ID. The main reconstruction algorithm for tracking is the inside-out algorithm where tracks are built from seeds [100]. A seed is constructed from at least three 3D space-points created from hits in the pixel detector and the SCT. A track candidate is then extrapolated from the seed and associated with hits from the outer layers of the SCT and the TRT using the Kalman filter algorithm [101]. A pattern recognition algorithm [102] is utilised in order to resolve ambiguities of tracks sharing one hit or more and to decide whether a track candidate comes from a real particle trajectory.

Track candidates are ranked depending on the number of hits and holes[4] associated with the track, where hits increase the track ranking and holes reduce it. Track candidates are then either selected, rejected or merged with other tracks. Each selected track is required to have a minimum transverse momentum of 400 MeV in order to suppress low p_T tracks. Track parameters d_0 and z_0 are defined to measure the distance of tracks to the IP, termed impact parameters. The d_0 is defined in the transverse plane (x–y plane) and the z_0 is the impact parameter in the longitudinal plane (R–z plane), see Fig. 4.1.

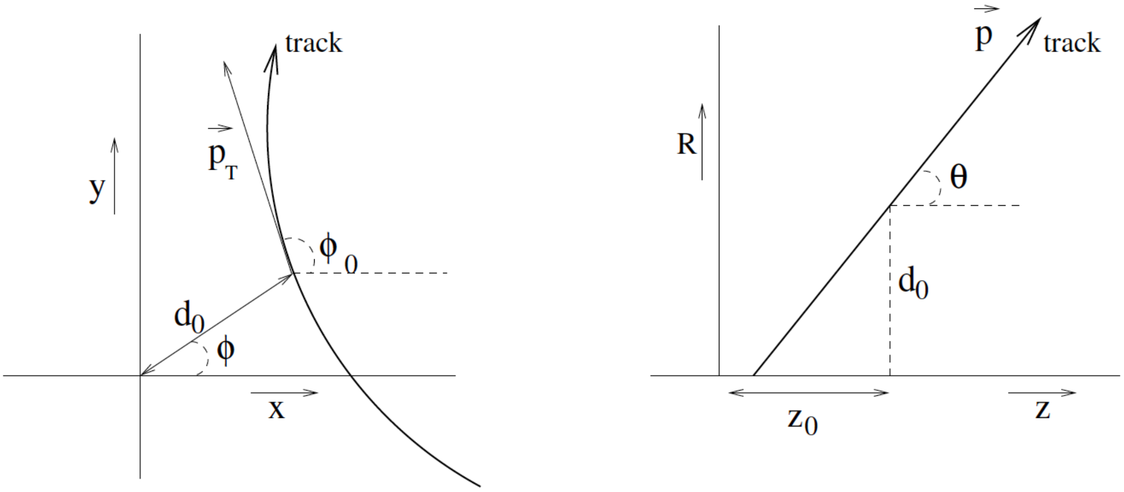

Figure 4.1: *Illustration of the track parametrisation (left) in the x–y plane and (right) in the R–z plane [104].*

The primary vertex is the space point where the hard inelastic pp collision occurred. Due to the high luminosity of the LHC, multiple additional soft inelastic pp interactions take place, referred to as pile-up. The mean number of interactions per bunch crossing for the 2012 dataset with integrated luminosity of 20.2 fb^{-1} is 20.7 [68]. The existence of pile-up makes the reconstruction of the hard-scatter primary vertex challenging. The reconstruction procedure is done using an iterative vertex finding algorithm [105, 106] and adaptive vertex fitting [107]. A vertex seed is determined from the beam spot and the selected tracks. The χ^2 minimisation is then performed to find the vertex position. Tracks are weighted according to their compatibility with the vertex candidate. Tracks with low weights are iteratively removed and used for a new vertex finding. The procedure is repeated until all tracks are associated with vertices. At the end, vertices with at least five tracks are considered. The vertex with the largest sum of p_T^2 of the associated tracks is picked to be the primary vertex of the event. These requirements avoid selecting vertices from pile-up events, which are mostly soft.

---

[4] A hole is defined when the prediction of a track trajectory passes through a sensitive detector element without producing a hit, where inactive modules are excluded from the definition [103].

Secondary vertices may be present as well due to decays of long-lived particles contained within jets, such as, heavy flavour hadrons or K_s^0 and Λ^0 or due to photon conversions. These vertices are displaced from the IP, hence tracks associated to them have higher impact parameters compared to those associated to primary vertices. This feature is utilised in the identification of b-quark jets.

4.2 Electrons

Electrons are charged particles and therefore leave hits in the ID. In the electromagnetic calorimeter, they form narrow showers and are fully stopped. Electron reconstruction is realised by matching tracks reconstructed in the ID with energy deposits (clusters) in the electromagnetic calorimeter [108]. The electromagnetic calorimeter is split into a grid with a unit size of $\Delta\eta \times \Delta\phi = 0.025 \times 0.025$. A seed cluster is found utilising a sliding-window algorithm [109] by searching for energy deposits within a window size of 3×5 cell units. The transverse energy of the cluster[5], $E_{\mathrm{T}}^{\mathrm{cluster}}$, is required to be larger than 2.5 GeV. Tracks are extrapolated to the middle layer of the EM calorimeter and associated to seed clusters. To perform the matching, the distance between the tracks and the clusters has to be small (within 0.05 in η and 0.1 in ϕ). An electron candidate is reconstructed if at least one track is matched to the seed cluster [108]. If more than one track is matched to the seed cluster, the decision is made by demanding track hits in the pixel detector and preferring the smallest distance to the seed cluster. Electron clusters are then formed by adjusting the size of the cells to 3×7 (5×5) in the barrel (endcaps) in all EM layers. Clusters are built within $|\eta^{\mathrm{cluster}}| < 2.47$ excluding the barrel–endcap overlap region between $1.37 < |\eta^{\mathrm{cluster}}| < 1.52$.

The cluster energy does not exactly correspond to the energy of the electron candidate, since some of the energy is lost in the material upstream of the calorimeter or deposited in the neighboring cells of the cluster. Hence, the cluster energy is calibrated in simulated MC samples using multivariate techniques, where correction factors are computed and applied to the cluster energy [110]. Additionally, an overall electron energy calibration is performed using a sample of $Z \to e^+e^-$ events, where scale factors are applied to the energy of the electron candidate in data by comparing to the simulation. The calibration of the energy scale is then validated using $J/\psi \to e^+e^-$ events in data.

The reconstruction efficiency is defined as the ratio of the number of clusters associated to tracks, passing the quality cuts, to the number of all clusters. Fig. 4.2 shows the efficiency comparison of 2011 and 2012 data sets as a function of E_{T} and η. Very good agreement between data and simulation is observed. The efficiency is higher for the 2012 data by $\sim 5\%$. The improvement is due to a new tracking algorithm that enhanced the reconstruction of electrons with high bremsstrahlung [108].

---

[5] $E_{\mathrm{T}}^{\mathrm{cluster}} = E^{\mathrm{cluster}}/\cosh\eta^{\mathrm{track}}$, where the direction η is the direction of the associated track

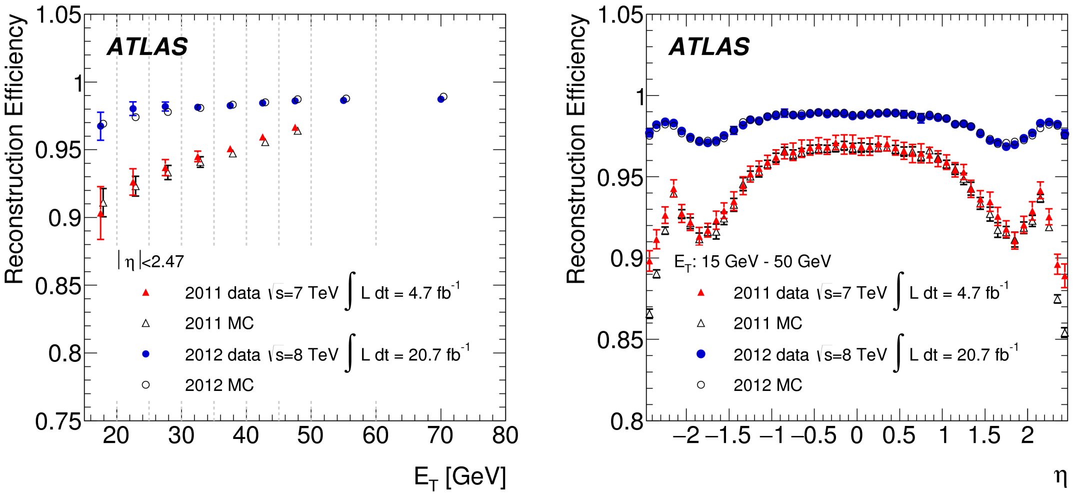

(a)

(b)

Figure 4.2: *Measured reconstruction efficiencies as a function of E_T (left) and as a function of η (right) for the 2011 and the 2012 datasets [108].*

After reconstructing an electron candidate, further requirements are applied to identify signal electrons and reject backgrounds, for example, hadrons, electrons from heavy-flavour decays or from photon conversions. Electron identification in ATLAS employs cut-based selection and multivariate techniques using variables that correspond to the shower shape, track properties and matching quality between tracks and clusters, which are discriminating variables. There are three main groups of cuts: *loose*, *medium* and *tight*. As the names suggest, *loose* selection yields the lowest background rejection while *tight* has the highest rejection rate. Details about these selections and the multivariate likelihood selections can be found in [108].

In this analysis, electron candidates are required to satisfy the *tight* selection. Beside its stricter requirements on the discriminating variables, it adds a selection on the ratio of the cluster energy to the track momentum E/p and rejects electron candidates matched to reconstructed photon conversions. The combined efficiency to reconstruct and identify an electron from $Z \to e^+e^-$ with $E_\mathrm{T} \sim 25\,\mathrm{GeV}$ is around 68 % for the tight criteria [108].

An electron coming from a top-quark decay is expected to be isolated, thus electron isolation is required in addition to the previous identification cuts to reject further backgrounds. Two isolation variables are defined: the calorimeter isolation $\sum E_\mathrm{T}^\mathrm{cluster}$ which is the sum of the calorimeter transverse energy within a cone size of $\Delta R = 0.2$ excluding the electron contribution ($\Delta\eta \times \Delta\phi = 0.125 \times 0.175$) and the track isolation $\sum p_\mathrm{T}^\mathrm{track}$ which is the scalar sum of the transverse momenta of tracks within a cone size of $\Delta R = 0.3$ excluding the associated track. The isolation cuts require minimum calorimeter activity and a small sum of track p_{T} in an η–ϕ cone around the electron. The cuts are optimised to achieve a uniform selection efficiency of $90\,\%$ across electron transverse energy E_{T} and pseudorapidity η.

In this analysis, the transverse momentum of the reconstructed electron is required to be $p_{\mathrm{T}} > 25\,\mathrm{GeV}$.

4.3 Muons

Muons are charged particles leaving hits in the ID, depositing small amount of energy in the electromagnetic and hadronic calorimeters and leaving signals in the muon system. Thus, muons are reconstructed using information from the muon spectrometer as well as the ID [111, 112]. In addition, information from the calorimeter system helps excluding hadrons and achieving high purity of muons at the MS [113]. The procedure starts with reconstructing tracks segments in the muon spectrometer using the *Moore* software package [114]. First, local track segments are formed on each MS layer. Then, segments from all layers are combined. In the next step, the *Muid* algorithm [115] is employed to extrapolate the tracks from the MS to the primary vertex in order to extract track parameters at the interaction point. The *MuidCombined* algorithm combines MS tracks and ID tracks using a global χ^2 fit with five degrees of freedom and builds muon candidates.

The reconstruction efficiency is measured using the tag-and-probe method [112] with $Z \to \mu^+\mu^-$ and $J/\psi \to \mu^+\mu^-$ events. It is shown in Fig. 4.3 as a function of the muon p_{T}. The efficiency is above $98\,\%$ for the whole muon's p_{T} range with $0.1 < |\eta| < 2.5$.

The muon momentum scale and resolution are determined using large samples of $Z \to \mu^+\mu^-$, $J/\psi \to \mu^+\mu^-$ and $\Upsilon \to \mu^+\mu^-$. A template fit of the di-muon invariant mass distribution is performed in data and MC simulation. Corrections are extracted from data and applied to the muon momentum of the simulated events.

Tracks of muon candidates have to satisfy selection requirements on the number of hits in the ID subdetectors. These requirements assist to reject ID tracks from pile-up interactions. Muon candidates are required to have at least one hit in the pixel detector, at least five hits at the SCT, less than three holes in the pixel and SCT detectors and in the region of $0.1 < |\eta| < 1.9$, at least six hits in the TRT are needed and the number of outlier hits [6] in the TRT has to be small $(n_{\mathrm{outliers}}/(n_{\mathrm{hits}} + n_{\mathrm{outliers}}) < 0.9)$. Furthermore, an isolation variable is defined as the scalar sum of the transverse momenta of all tracks originating from the primary vertex with $p_{\mathrm{T}} > 1\,\mathrm{GeV}$, except the track matched to the muon, within a cone of size $R_{\mathrm{iso}} = 10\ \mathrm{GeV}/p_{\mathrm{T}}(\mu)$. Muons are accepted if the isolation divided by the transverse momentum of the muon $p_{\mathrm{T}}(\mu)$ is smaller than 0.05. Similar to electrons, muons coming from top-quark decays are expected to be isolated. Additionally, requiring isolation criteria helps rejecting background muons, like muons from hadronic jets.

---

[6] Outlier hits are hits far away from the associated track

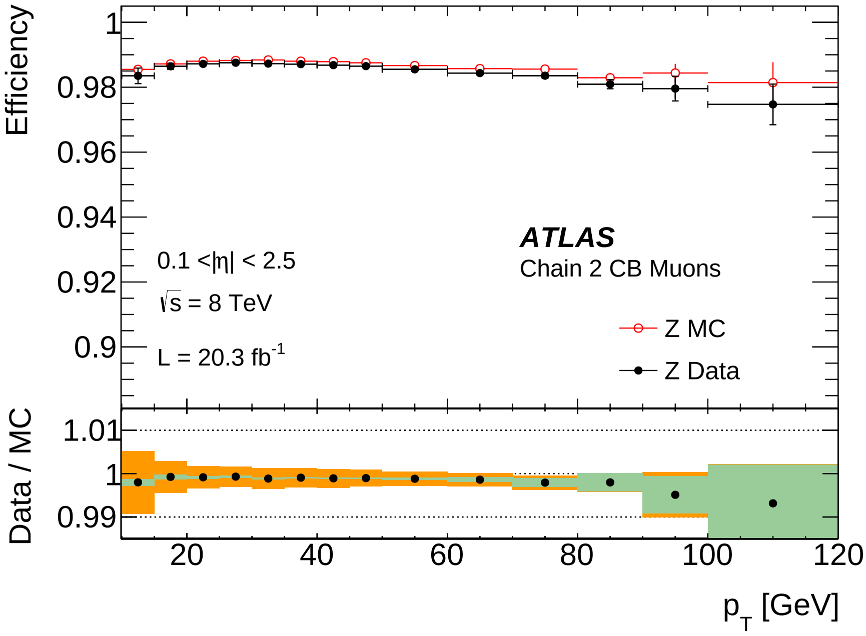

Figure 4.3: *The muon reconstruction efficiency as a function of the* p_T *of the muon measured in* $Z \rightarrow \mu^+\mu^-$ *events for muons with* $p_T > 10\,\text{GeV}$ *in the range* $0.1 < |\eta| < 2.5$ *[112].*

Muons used in this analysis are selected with $p_{\mathrm{T}} > 25\,\mathrm{GeV}$ and in the region of $|\eta| < 2.5$, which is within the acceptance region of the ID. There are acceptance losses in the $\eta \approx 0$ region, where the MS is only partially equipped with muon chambers, and in the region $1.1 < \eta < 1.3$, where some of the chambers were not yet installed for Run I [112].

4.4 Jets

Partons hadronise to form jets which are observed in the detector in the form of energy deposits in the electromagnetic and hadronic calorimeters. The jet reconstruction in this analysis is performed with the so-called anti-k_{T} algorithm [116], which is classified as a sequential recombination algorithm [117]. The inputs to this algorithm are topological clusters in the calorimeter (topo-clusters) [118] constructed from neighbouring cells with high signal to noise ratio. The anti-k_T algorithm defines the distance between the jet candidates i and j as:

$$d_{ij} = \min\left(p_{T,i}^{-2}, p_{T,j}^{-2}\right)\frac{(\Delta R)^2_{ij}}{R^2} \tag{4.1}$$

and the distance between a jet candidate i and the beam (B) as:

$$d_{iB} = p_{T,i}^{-2} \tag{4.2}$$

where $p_{T,i}$ ($p_{T,j}$) is the transverse momentum of the jet candidate i (j), ΔR_{ij} is the angular distance between the jet candidates i and j and R is the radius of the cone, which is set to 0.4 for this analysis.

The algorithm proceeds by defining the smallest among all distances d_{ij} and d_{iB}. In the case of d_{ij}, the two jet candidates i and j are combined by summing the four-momenta of the constituent clusters. If the smallest distance is d_{iB}, the jet candidate i is considered a reconstructed jet and removed from the list of jet candidates. The distances are then recalculated and the same procedure continues until there are no jet candidates left on the list.

The anti-k_T algorithm is simple, infrared and collinear safe. This means that the shape and properties of the reconstructed jets are stable. Soft jet candidates cluster with hard jet candidates before they cluster among themselves, leading to regular jet shapes. Infrared safety implies that soft radiation does not change the jet shape but hard radiation does. Collinear safety means that collinear splitting of hard jets does not alter the reconstructed jet either. Infrared and collinear unsafe is illustrated in Fig. 4.4.

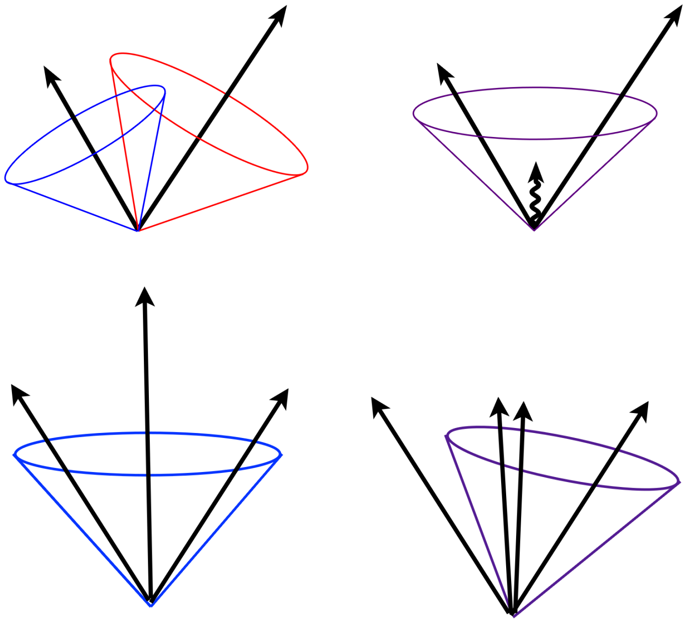

Figure 4.4: *An illustration of (top) infrared unsafe, where soft radiation between two jets may cause merging of the jets and (bottom) collinear unsafe, where splitting of hard jets leads to different jet clustering [119].*

The topological clusters used to reconstruct the jet undergo several steps of energy calibration. At first, the jet energy is calibrated at the EM scale, which accounts correctly for the energy deposited in the calorimeter by electromagnetic showers. However, the response of the ATLAS calorimeter for charged particles and hadrons differs. The local cluster weighting method (LCW) [120] is employed to distinguish electromagnetic and hadronic clusters by the shower's shape and depth. The LCW method applies corrections to hadronic showers based on simulations of charged and neutral pions. Additional corrections are derived to consider the energy loss in inactive material and energy deposits below noise thresholds [121]. The calibrated topo-clusters are then used to reconstruct jets.

Additionally, reconstructed jets using topo-clusters calibrated at the LCW scale go through stages of jet energy scale (JES) calibration (see Fig. 4.5):

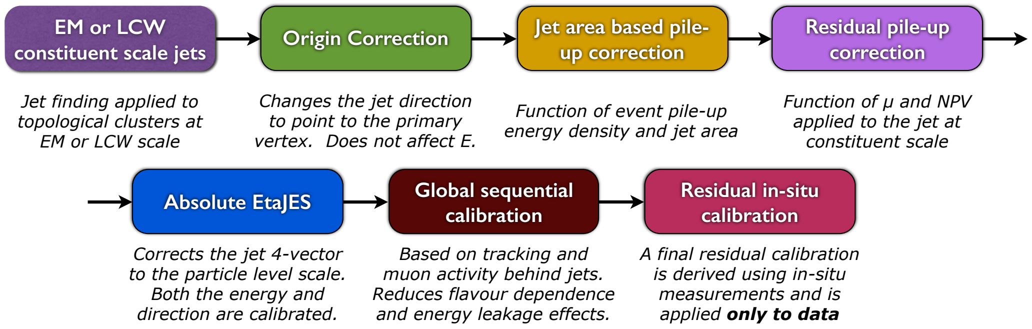

Figure 4.5: *The stages of jet energy scale (JES) calibration [122].*

- Origin correction: The jet direction (η,ϕ) is changed to point to the primary vertex instead of the center of the detector by redefining the direction of the topo-clusters. The jet four-momentum is defined as the sum of the four-momenta of the constituent clusters.
- Pile-up correction: A subtraction method is used to reduce the effect of pile-up based on event pile-up density ρ and jet p_{T}. Additional residual subtraction is done based on the dependence on the number of primary vertices N_{PV} and the average number of interaction per bunch crossing μ [123].
- MC-based jet calibration: A jet energy scale correction is applied to the reconstructed jet energy, derived from the truth jet energy acquired from simulations. Additionally, a small correction is applied to the jet η.
- Global sequential corrections: This correction accounts for the difference of the calorimeter response to quark and gluon initiated jets. It depends on tracking information, energy deposits in the calorimeter as well as muon spectrometer information. Corrections are also applied to consider high p_T jets whose energy is not fully contained within the jet, referred to as 'punch-through' corrections [124].

- In situ energy calibration: A final calibration is applied on data to consider the jet response and resolution difference between simulation and data. Z+jets, γ+jets and multijet events are used to derive these corrections [125].

Jets used in this analysis are selected with $p_{\mathrm{T}} > 25\,\mathrm{GeV}$ and in the region of $|\eta| < 2.5$. To distinguish jets coming from the hard process and pile-up jets, the jet vertex fraction ϵ_{JVF} is defined [126]. It is given by the ratio of the sum of the transverse momenta of all tracks associated to a jet, originating from the primary vertex, to the sum of the transverse momenta of all tracks matched to the jet:

$$\epsilon_{\mathrm{JVF}} = \frac{\sum p_{\mathrm{T},i\in\mathrm{PV}}}{\sum p_{\mathrm{T},i}} \tag{4.3}$$

Only tracks with $p_{\mathrm{T}} > 1\,\mathrm{GeV}$ are considered in the ϵ_{JVF} calculation. To reject pile-up jets, a requirement of $|\epsilon_{\mathrm{JVF}}| > 0.5$ is applied for jets with $|\eta| < 2.4$ and $p_{\mathrm{T}} < 50\,\mathrm{GeV}$.

4.5 Identification of b-quark jets

The identification of jets containing b-hadrons is referred to as b-tagging. It strongly helps suppressing backgrounds with mainly light-flavour jets. Algorithms performing b-tagging make use of the relatively long lifetime of hadrons containing a b-quark, $\tau \approx 1.5\,\mathrm{ps}$, and the decay length of $c\tau \approx 450\,\mu\mathrm{m}$ resulting in a secondary vertex (see Fig. 4.6). Hence, impact parameters of tracks are frequently used in the b-tagging since they are relatively large for tracks stemming from displaced vertices. Other strategies rely on the reconstruction of secondary vertices. Tag weights are given to jets corresponding to their probability of containing a b-hadron.

In this analysis, the MV1 b-tagger [128] is employed. MV1 utilises outputs of other b-taggers and combines them as inputs to a neural network. These algorithms are the IP3D, SV1 and JetFitterCombNN taggers [129]:

- IP3D (Impact parameter 3D): An impact parameter-based algorithm utilising d_0 and z_0 of tracks. In practice, the significances are used instead (d_0/σ_{d_0}, z_0/σ_{z_0}), where σ is the uncertainty on the measurement of the impact parameter. These significances are combined in a likelihood ratio technique, where they are compared to distributions for b- and light-jet hypotheses obtained from MC simulation.
- SV1 (Secondary vertex 1): An algorithm that relies on the reconstruction of inclusive secondary vertices. It also uses a likelihood ratio technique to combine vertex properties such as, the invariant mass and energy fraction of the associated tracks and the number of two-track vertices.
- JetFitterCombNN: This algorithm includes the JetFitter algorithm, which exploits the topological structure of weak b- and c-hadron decays inside the jet. A Kalman

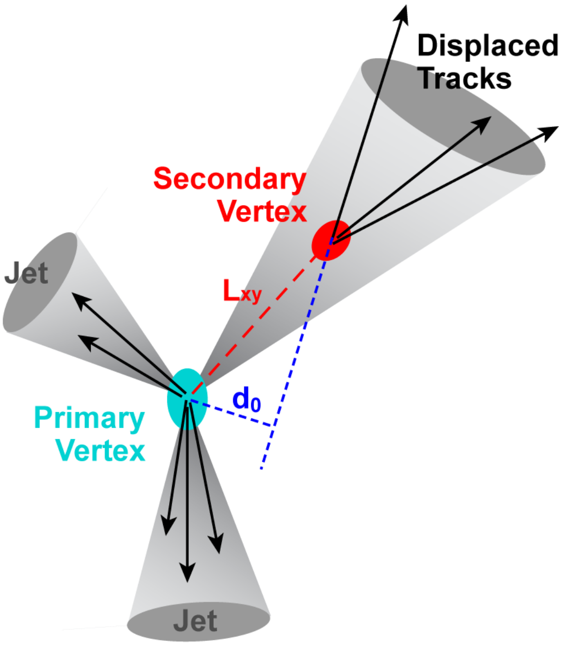

Figure 4.6: *A schematic view of a b-hadron decay, where displaced tracks are stemming from a secondary vertex with a decay length L_{xy} displaced from the primary vertex. The impact parameter d_0 is shown for one of the displaced tracks [127].*

filter is employed to find a common line on which the primary vertex and the b- and c-vertices lie, approximating the b-hadron flight path. Variables describing the decay topology and vertex information are used as inputs to a neural network and the output of the IP3D algorithm is incorporated as additional input variable.

Methods to calibrate the performance of b-tagging algorithms are applied in ATLAS [130, 131]. The performance is defined as the efficiency to tag a jet originating from a b-quark (ϵ_b) and the probability of unintentionally tagging a jet emerging from a c- or a light-quark ($\epsilon_c, \epsilon_{\text{light}}$). ϵ_{light} is referred to as the 'mistag rate'. Working points are defined by applying cuts on the tag weight distribution in simulation. These working points are optimised to achieve a certain b-tagging efficiency for $t\bar{t}$ sample. For the MV1 algorithm, the working points correspond to b-tagging efficiencies of 60 %, 70 % and 80 %.

In this analysis, the 70 % working point is used, with a c-jet rejection factor of 5 and a light-flavour jet rejection factor of 140 [128]. The efficiencies ϵ_b, ϵ_c and ϵ_{light} are measured in data and scale factors of data/simulation difference are derived from these calibrations. The correction for b-jets is derived using $t\bar{t}$ events in the dilepton channel and dijet events. The efficiencies of the MV1 tagger for simulated $t\bar{t}$ events are shown in Figure 4.7 as a function of jet p_{T} and jet η.

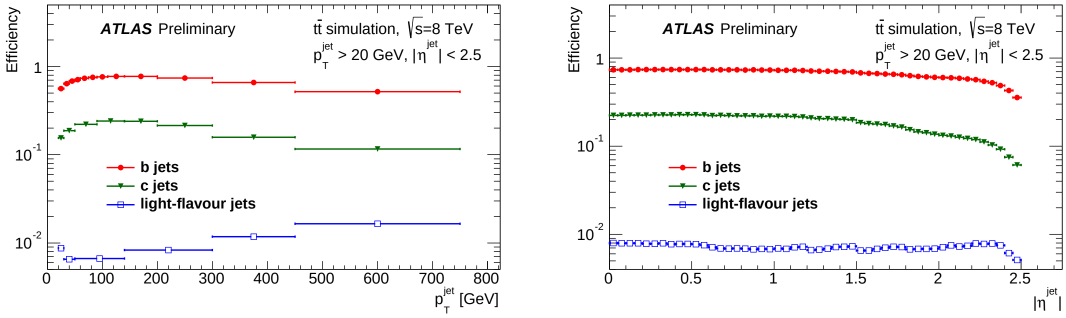

(a)

(b)

Figure 4.7: *The efficiencies of the* MV1 *tagger to tag* b-, c- *and light-jets at a working point of* 70 % *efficiency for* b*-jets as a function of (a) jet* p_T *and (b) jet* η *[131].*

4.6 Missing transverse momentum

Neutrinos do not interact with the detector's material. Their existence can only be assumed indirectly by applying momentum conservation transverse to the beam axis. Since the initial momentum in the transverse plane is zero, any imbalance would indicate the existence of neutrinos. It is referred to as the missing transverse momentum $E_{\text{T}}^{\text{miss}}$.

$$E_{\text{T}}^{\text{miss}} = \sqrt{(E_x^{\text{miss}})^2 + (E_y^{\text{miss}})^2} \tag{4.4}$$

The reconstruction of $E_{\mathrm{T}}^{\mathrm{miss}}$ is based on matching energy deposits in the calorimeter with reconstructed and calibrated physics objects [132, 133]. This is called the 'hard term'. Signals in cells not associated with physics objects form the 'soft term'. The x- and y-components of the $E_{\mathrm{T}}^{\mathrm{miss}}$ are calculated as:

$$E_{x(y)}^{\mathrm{miss}} = E_{x(y)}^{\mathrm{miss},e} + E_{x(y)}^{\mathrm{miss},\gamma} + E_{x(y)}^{\mathrm{miss},\tau} + E_{x(y)}^{\mathrm{miss,jets}} + E_{x(y)}^{\mathrm{miss},\mu} + E_{x(y)}^{\mathrm{miss,soft}} \tag{4.5}$$

where the different terms denote the contributions as the negative vectorial sum of transverse momenta of energy deposits from electrons, photons, hadronically decaying τ, jets and muons, as well as the soft term. Electrons and photons calibrated at the EM scale and with $p_{\mathrm{T}} > 10\,\mathrm{GeV}$ are considered in the $E_{\mathrm{T}}^{\mathrm{miss}}$ reconstruction. Muons have to satisfy the selection criteria of $p_{\mathrm{T}} > 5\,\mathrm{GeV}$. Jets are required to be calibrated at the LCW+JES scale and to have $p_{\mathrm{T}} > 20\,\mathrm{GeV}$. For hadronically decaying τ-leptons, p_{T} has to be larger than 10 GeV with the LCW calibration applied to be included in the $E_{\mathrm{T}}^{\mathrm{miss}}$ reconstruction. For the soft term, energy deposits not matched to high-p_{T} physics objects (which are also calibrated at the LCW scale) are considered in the $E_{\mathrm{T}}^{\mathrm{miss}}$ calculation. Tracks with $p_{\mathrm{T}}^{\mathrm{track}} > 400\,\mathrm{MeV}$ not matched to physics objects are used instead of the calorimeter p_{T} measurements if the track p_{T} resolution is better than the calorimeter resolution and the track is matched to a topo-cluster in the calorimeter using the ΔR significance.

5

Event selection, event reconstruction and backgrounds estimation

After defining and selecting physics objects, cuts on the event topology are still needed to select signal events and at the same time reject a large fraction of background events. The expected number of background events, which remain after these cuts, needs to be estimated.

In the search for observables that discriminate signal from background processes, the reconstruction of the $t\bar{t}$ system is beneficial. Kinematic variables of the top-quarks and the $t\bar{t}$ system add valuable information in addition to those obtained from kinematic variables of selected objects.

In this chapter, Sect. 5.1 explains the event-based selection cuts. The $t\bar{t}$ reconstruction is described in Sect. 5.2. Signal and validation regions are defined in Sect. 5.3. In Sect. 5.4, the reconstruction and selection of particle-level objects is explained. Methods of background estimation are discussed in Sect. 5.5 with emphasis on the multijet background estimation. Finally, the observed data and expected event yields are presented in Sect. 5.6.

5.1 Overlap removal and event selection

The reconstructed and selected physics objects explained in Chapter 4 can overlap with each other. A procedure needs to be applied to remove the overlaps between these objects.

In the overlap removal procedure, muons overlapping with a jet within $\Delta R < 0.4$ are removed from the event, since they are probably muons from heavy-flavour decays. The jet with $\Delta R < 0.2$ closest to an electron is dropped from the event, as they are likely to correspond to the same physics object. To ensure the selection of only isolated electrons, if electrons are still present within $\Delta R < 0.4$ distance to a jet, the electron is removed from the event.

After that, event-based selections are performed. These selection cuts utilise the ℓ+jets topology of $t\bar{t}$ events, which consists of an isolated electron or muon, sizeable missing transverse momentum and at least four jets, two of which are b-quark jets. The aim of these cuts is to reduce the fraction of background processes and reject events failing data quality criteria. Events involving $W \rightarrow \tau\nu$ decays with a subsequent decay of the τ lepton to either $e\nu_e\nu_\tau$ or $\mu\nu_\mu\nu_\tau$ are included.

The datasets used in this analysis are obtained from single-electron or single-muon triggers. The single-electron trigger requires an electron trigger object with $E_\mathrm{T} > 24$ GeV including additional isolation requirements or $E_\mathrm{T} > 60$ GeV [74]. For the single-muon trigger, an isolated muon with a transverse momentum threshold of 24 GeV is required or a muon with $p_\mathrm{T} > 36$ GeV [75].

Events are required to have a reconstructed primary vertex with at least five tracks associated to the vertex, where the p_T of each track is above 400 MeV. Events should contain one reconstructed electron or muon with $p_\mathrm{T} > 25$ GeV. Trigger matching is performed by demanding $\Delta R < 0.15$ between the reconstructed lepton and the trigger-lepton. Events containing an electron and a muon sharing an ID track are discarded. Events which include jets with $p_\mathrm{T} > 20$ GeV with the *looseBad* jet quality defined in Ref. [121] are dropped. Discarding those jets suppress backgrounds from beam–gas and beam-halo interactions, cosmic rays and calorimeter noise.

Furthermore, events must contain at least four jets, where each reconstructed jet is required to have $p_\mathrm{T} > 25$ GeV and $\eta < 2.5$ and at least one of the jets is needed to be b-tagged at a working point corresponding to 70 % b-tagging efficiency. The missing transverse momentum of the event is required to be $E_\mathrm{T}^\mathrm{miss} > 25$ GeV. This requirement helps to reject multijet background. In addition, the transverse mass of the lepton - $E_\mathrm{T}^\mathrm{miss}$ pair, $m_\mathrm{T}(W)$, is required to be

$$m_\mathrm{T}(W) = \sqrt{2p_\mathrm{T}(\ell) \cdot E_\mathrm{T}^\mathrm{miss}\left[1 - \cos\left(\Delta\phi\left(\vec{\ell}, \vec{E}_\mathrm{T}^\mathrm{miss}\right)\right)\right]} \;>\; 30 \text{ GeV}, \tag{5.1}$$

with $p_\mathrm{T}(\ell)$ the transverse momentum of the charged lepton and $\Delta\phi$ the angle in the transverse plane between the charged lepton and the $\vec{E}_\mathrm{T}^\mathrm{miss}$.

In total 335 784 data events pass the selection cuts above. The signal acceptance[7] using the nominal $t\bar{t}$ simulated sample is 9.8 %.

---

[7] Acceptance = number of selected events / number of total generated events

5.2 $t\bar{t}$ reconstruction

The reconstruction of a semi-leptonic $t\bar{t}$ event involves the reconstruction of the leptonically decaying top-quark ($t \rightarrow Wb \rightarrow \ell\nu b$) and the hadronically decaying top-quark ($t \rightarrow Wb \rightarrow bjj$).

The reconstruction of the leptonically decaying top-quark requires the reconstruction of the decay products, which are a W boson and a jet originating from a b-quark. The W boson decays into a charged lepton e or μ and a neutrino. The four-momentum of the W boson is given by $P_W = P_\nu + P_{e,\mu}$. The reconstruction of charged leptons as well as jets was explained in Chapter 4. For the neutrino, the missing transverse momentum is measured in the transverse plane (x–y plane). The z component $p_z(\nu)$ is determined by imposing the W boson pole mass constraint, $m(W) = 80.4\,\text{GeV}$, which can be calculated by solving the quadratic equation [134]:

$$p_z^2(\nu) - 2 \cdot \frac{\mu \cdot p_z(\ell)}{E^2(\ell) - p_z^2(\ell)} \cdot p_z(\nu) + \frac{E^2(\ell) \cdot p_\text{T}^2(\nu) - \mu^2}{E^2(\ell) - p_z^2(\ell)} = 0, \tag{5.2}$$

$$\text{with} \quad \mu = \frac{m_W^2}{2} + \cos\left(\Delta\phi\left(\vec{\ell}, \vec{E}_\text{T}^\text{miss}\right)\right) \cdot p_\text{T}(\ell) \cdot p_\text{T}(\nu) \tag{5.3}$$

Two solutions exist for a quadratic equation. Real solutions are obtained if the transverse mass of the W boson, $m_\text{T}(W)$, is smaller or equal to the W boson pole mass, $m(W)$, while if $m_\text{T}(W)$ is larger than $m(W)$ then the solutions are imaginary. This case can happen due to inaccurate E_T^miss measurement. The $m_\text{T}(W)$ can be rewritten in a different way than Eq. (5.1) as:

$$m_\text{T}(W) = \sqrt{(p_\text{T}(\ell) + p_\text{T}(\nu))^2 - (p_x(\ell) + p_x(\nu))^2 - (p_y(\ell) + p_y(\nu))^2} \tag{5.4}$$

In the case of two real solutions, the smaller solution for p_z is chosen. For the imaginary solutions, $m_\text{T}(W)$ is modified to be equal to $m(W)$ in order to obtain a real solution for p_z and the components p_x and p_y are adjusted such that Eq. (5.2) is still fulfilled. The adjustment is implemented by minimising the distance between the transverse momentum of the neutrino, $p_\text{T}(\nu)$, and the E_T^miss. The modified $p_x(\nu)$ and $p_y(\nu)$ are then used to calculate a real solution for $p_z(\nu)$. The four-momentum of the W boson is then calculated by adding the four-momenta of the neutrino and the charged lepton.

In order to associate jets to the corresponding top-quarks, only the four highest p_T jets in the event are used. For the reconstruction of the jet coming from the leptonically decaying top-quark, the one with smallest angular distance ΔR to the lepton is chosen. Finally, the leptonically decaying top-quark is reconstructed by adding the four-momenta of the W boson and the chosen jet.

The remaining three selected jets are assigned as the ones coming from the hadronically decaying top-quark, two of which are the decay products of the hadronically decaying W and the third is the jet originating from a b-quark. The hadronically decaying top-quark is reconstructed by adding the four-momenta of these three jets.

Performance study

The quality of the reconstruction of the $t\bar{t}$ system is studied using a simulated $t\bar{t}$ sample. A definition of the best possible reconstruction is set using parton-level information about the decay products of the top-quark pair. At the detector-level, all possible permutations of objects are considered to reconstruct the top-quarks. The angular distance between the reconstructed top-quark pair in each permutation and the true hadronically and leptonically decaying top-quarks is calculated. The permutation of objects, where the sum of the distances ΔR between the reconstructed top-quarks and the true ones is the smallest, is considered to be the 'best possible' reconstruction.

For each event, it is checked whether the $t\bar{t}$ reconstruction explained above matches the best possible reconstruction. The reconstruction efficiency is defined as the fraction of events reconstructed using the best possible permutation, which is calculated for this method to be 44 %.

Other $t\bar{t}$ reconstruction methods exist, some of the established methods are explained in Ref. [135]. The reconstruction varies from 21 % using a $p_{\mathrm{T}}^{\mathrm{max}}$ method, where a set of three jets out of four, with the largest transverse momentum is associated to the hadronically decaying top-quark and the remaining jet is associated to the leptonically decay top-quark, 48 % using a χ^2 minimisation method and 52 % using a likelihood method to find the best permutation. Improved versions of some of these method can increase the reconstruction efficiency to about 70 %. The reconstruction method used in this analysis was not optimised to increase the reconstruction efficiency since it does not have an important impact on the analysis.

Fig. 5.1 shows distributions of the mass of the reconstructed hadronically decaying top-quark and the reconstructed leptonically decaying top-quark comparing the shapes for the reconstruction method used here with the shapes for the best possible reconstruction. These distributions are fairly similar and for the purpose of this analysis, having exactly the correct shapes of the masses of the reconstructed top-quarks is not crucial.

5.3 Signal and validation regions

The cross-section measurement is carried out in three disjoint signal regions. This configuration improves the sensitivity to the systematic uncertainties that affect the $t\bar{t}$ cross

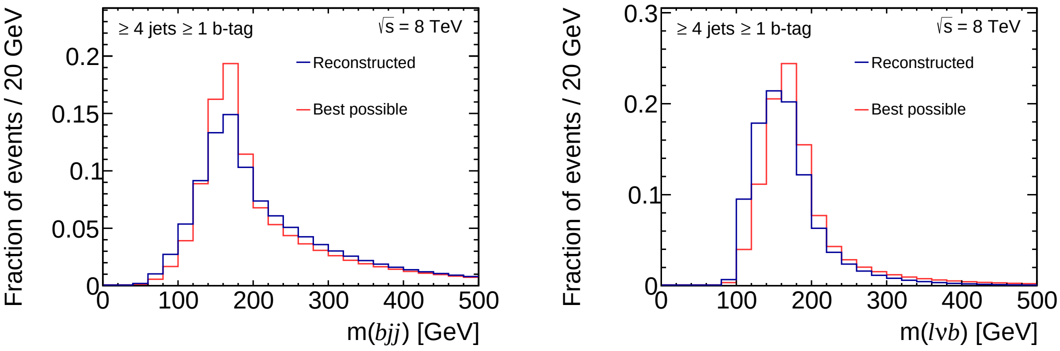

(a) (b)

Figure 5.1: *Probability densities of the (a) mass of the reconstructed hadronically decaying top-quark and (b) mass of the reconstructed leptonically decaying top-quark, for the simulated $t\bar{t}$ signal process. The reconstructed shapes are shown in blue while the best possible reconstruction shapes are shown in red. Distributions are normalised to unit area.*

section measurement. A validation region is defined to check the modelling of kinematic distributions of the main background process W+jets.

5.3.1 Signal regions

The selected events are split into three disjoint signal regions SR1, SR2 and SR3. Fig. 5.2 illustrates the splitting of the three signal regions in relation to the jet multiplicity and the number of b-tagged jets.

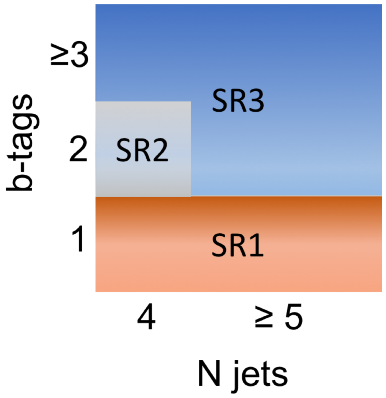

Figure 5.2: *An illustration of the three signal regions.*

SR1 : $\geqslant 4$ jets, 1 b-tag

In this signal region, at least four jets are required to be included in the event. One of these jets has to be b-tagged. This region has the highest number of background events compared with the other two signal regions, along with the highest number of selected $t\bar{t}$ events.

SR2 : 4 jets, 2 b-tags

Four jets are selected in this signal region, two of which need to be b-tagged. This selection provides a clear association of the reconstructed objects to the $t\bar{t}$ decay products. Requiring exactly four jets, two of which are b-tagged, leads to a small expected number of background events. In this signal region, the mass of the hadronically decaying W boson, $m(jj)$, is exploited, where the W-boson decay-products, i.e. the two light jets in the event, are clearly determined through the b-tagging requirement. The mass of the reconstructed W boson is particularly sensitive to variations of the jet energy scale and to additional radiation.

SR3 : $\geqslant 4$ jets, $\geqslant 2$ b-tags (excluding 4 jets, 2 b-tags)

In the third signal region, events need to contain at least four jets, at least two of which are b-tagged jets, excluding events passing the selection of SR2 (with exactly four jets, where two of them are b-tagged). This signal region has the smallest background fractions of the three regions. It includes events with additional jet radiation and mis-tagged jets, i.e. non b-jets (c-jets and light-jets) falsely labeled as b-tagged jets, with the probability of mis-tagging c-jets being the highest.

5.3.2 Validation region

The validation region is defined using the same event selection presented in Sect. 5.1 except the b-tagging requirement for the jets. Events in the validation region are termed as 'pre-tag' events. Discarding the b-tagging enriches the selection with backgrounds, in particular W+jets events. Thus, this region is suitable for verifying the modelling of the kinematic distributions for this background.

5.4 Particle-level object reconstruction and selection

Selections on particle-level objects in simulation are needed to perform the fiducial cross-section measurement. These selections are chosen to match the requirements on the reconstructed objects as close as possible. Particle-level leptons and jets are reconstructed from stable particles with a mean lifetime greater than $0.3 \cdot 10^{-10}$ s. Electrons, muons and neutrinos that originate from the W-boson decay are selected, whereas those originating from hadrons either directly or via a τ decay are rejected. A procedure called 'lepton dressing' is implemented to add any soft photon radiation within $\Delta R < 0.1$ to the four-momentum vector of the electron or muon. The selected electron or muon is required to have $p_{\mathrm{T}} > 25\,\mathrm{GeV}$ and $|\eta| < 2.5$. The reconstruction of particle-level jets is performed using all stable particles excluding the selected leptons and the photons used in the lepton dressing procedure. Similar to the detector-level jets, the anti-k_t algorithm with a radius parameter of $R = 0.4$ is used. Each jet is required to have $p_{\mathrm{T}} > 25\,\mathrm{GeV}$ and $|\eta| < 2.5$.

An overlap removal approach is employed, where events are excluded if a selected lepton is within $\Delta R < 0.4$ to a selected jet. The fiducial volume is defined by selecting exactly one electron or muon and at least three particle-level jets.

In the particle-level selection, the minimum number of jets is three, while in the detector-level selection it is four. This difference was encouraged by studying the fraction of events which are selected on detector-level in one of the three signal regions, but rejected in the particle-level fiducial volume. Table 5.1 shows this fraction selecting at least three jets in the particle-level compared to at least four particle-level jets. Requiring $\geqslant 4$ particle-level jets leads to about one fourth of the selected events not being included in the fiducial volume. On the other hand, selecting $\geqslant 3$ particle-level jets reduces this fraction to the order of 10 %. This way the extrapolation uncertainty is minimised.

Table 5.1: *The fraction of events selected in the detector-level and not selected in the particle-level fiducial volume in the three signal regions.*

Number of particle-level jets	SR1	SR2	SR3
$\geqslant 3$ jets	13 %	11 %	13 %
$\geqslant 4$ jets	24 %	26 %	16 %

Table 5.2 shows the fiducial acceptance, A_{fid}, for various event generators. The fiducial acceptance includes the branching ratio ($\mathcal{B} = 0.543$) for non-allhadronic decays, i.e. at least one of two W bosons decay leptonically.

Comparisons between reconstructed objects and particle-level objects are performed for simulated $t\bar{t}$ events passing both the selection cuts presented in Sect. 5.1 and the particle-level selection cuts presented in this section. The residual distributions are shown in Fig. 5.3 and Fig. 5.4 for the p_{T} and the η of the reconstructed electrons, muons, highest-p_{T} jet and second highest-p_{T} jet, in addition to the $E_{\mathrm{T}}^{\mathrm{miss}}$. The resolution of reconstructed electrons is 1.48 GeV for the transverse momentum and 0.0006 for the pseudorapidity. For

Table 5.2: *The fiducial acceptance A_{fid} for various generators*

Generator	A_{fid}
POWHEG + PYTHIA	19.6 %
POWHEG + HERWIG	19.9 %
MC@NLO + HERWIG	20.0 %
POWHEG + PYTHIA radHi	19.5 %
POWHEG + PYTHIA radLo	20.0 %

reconstructed muons, the resolution is 1.74 GeV in p_{T} and 0.0005 in η. The resolution of $E_{\mathrm{T}}^{\mathrm{miss}}$ is 20 GeV, where the difference between the mean value of the reconstructed $E_{\mathrm{T}}^{\mathrm{miss}}$ distribution and the mean value of the particle-level $E_{\mathrm{T}}^{\mathrm{miss}}$ distribution is about 12 GeV. For the reconstructed jets, a resolution of about 11 GeV is reached in p_{T} and about 0.02 in η.

5.5 Backgrounds estimation

Background processes with similar final states as the $t\bar{t}$ semi-leptonic events that get accepted in the event selection were presented in Sect. 3.2. The expected number of events for these backgrounds and kinematic variables are obtained as follows:

- Z+jets, single-top and diboson production: The expected number of events of these backgrounds are calculated using their theoretical cross-sections and the acceptance from the simulated samples. The shapes of kinematic distributions are obtained as well from the event generators.
- W+jets production: The normalisation of the W+jets process is determined together with the $t\bar{t}$ cross section in the final fit procedure. A data driven method is utilised to derive shapes of distributions for this background, which is based on using Z+jets events from data. This method is explained in details in chapter 6. The pre-fit expected number of events is obtained using the acceptance acquired from the ALPGEN +PYTHIA simulated sample and the theoretical prediction.
- Multijet production: Two methods are utilised to derive a sample for the multijet process. The expected number of events is estimated using a maximum-likelihood fit. The methods and procedure are described below.

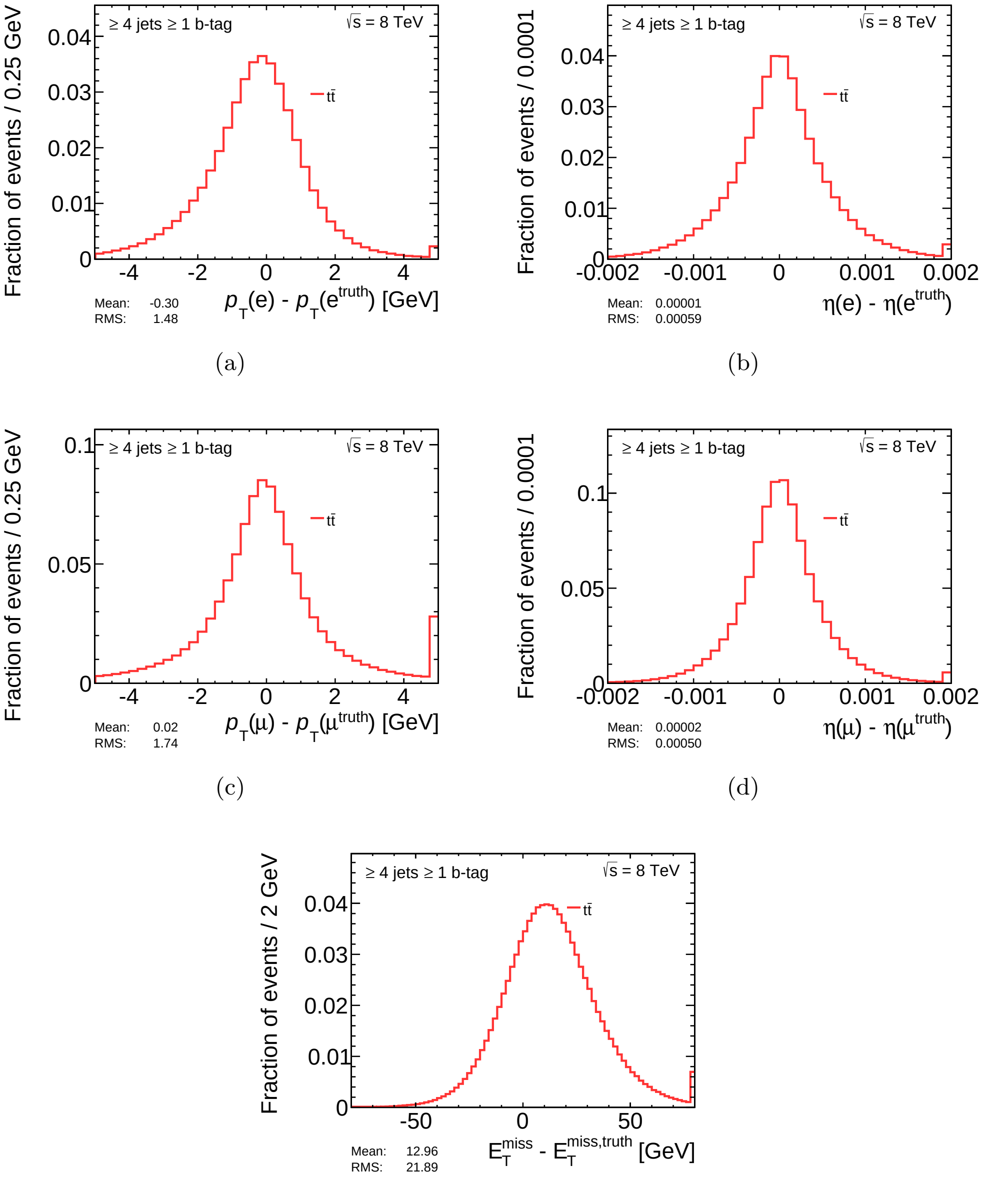

(a)

(b)

(c)

(d)

(e)

Figure 5.3: *Residual distributions of reconstructed electrons, muons and* E_T^{miss} *for simulated* $t\bar{t}$ *events. Distributions are normalised to unit area. The mean value represents the difference between the measured value and the truth value. The RMS indicates the resolution of the measured value. The distributions are: (a)* p_T *of the reconstructed electron, (b)* η *of the reconstructed electron, (c)* p_T *of the reconstructed muon, (d)* η *of the reconstructed muon and (e) the reconstructed* E_T^{miss}*.*

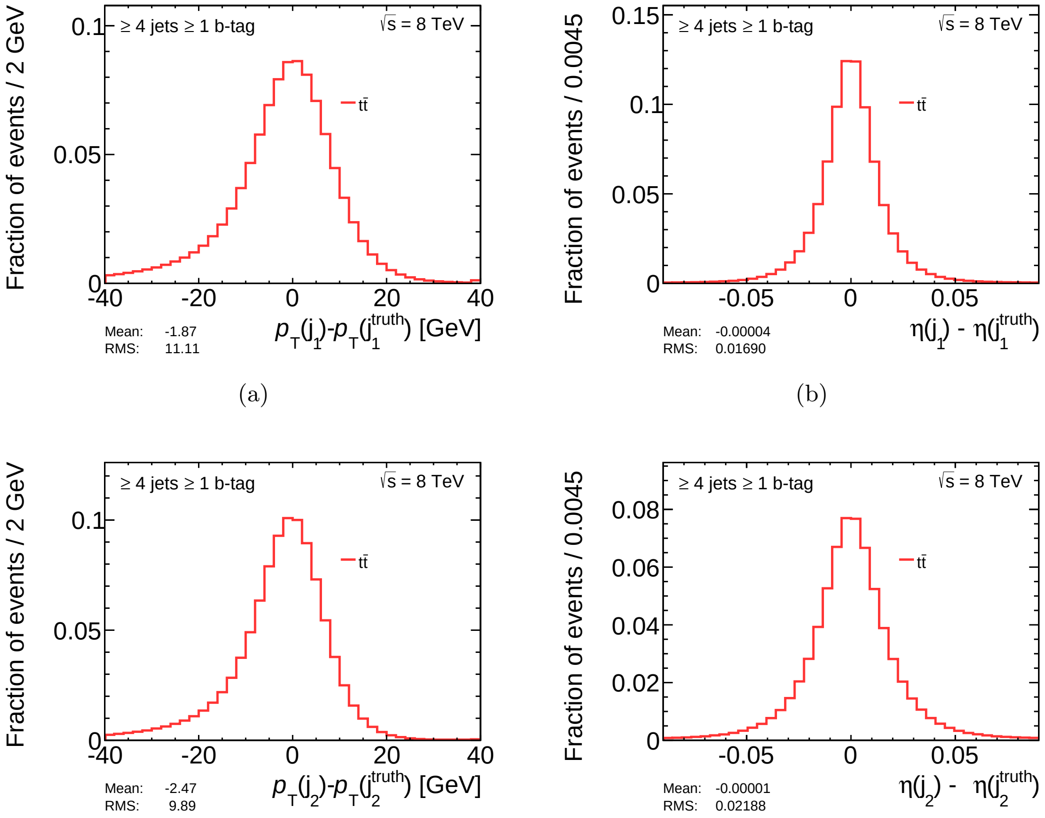

(a) (b)

(c) (d)

Figure 5.4: *Residual distributions of reconstructed jets for simulated $t\bar{t}$ events. Distributions are normalised to unit area. The mean value represents the difference between the measured value and the truth value. The RMS indicates the resolution of the measured value. The distributions are: (a) p_T of the reconstructed highest-p_T jet, (b) η of the reconstructed highest-p_T jet, (c) p_T of the reconstructed second highest-p_T jet, and (d) η of reconstructed second highest-p_T jet.*

5.5.1 Multijet background

Simulation and data driven techniques are implemented to derive a sample for the multijet background in electron and muon channels respectively. In this analysis, the jet-lepton method is employed in the electron channel, while the anti-muon method is utilised in the muon channel. Estimation of the normalisation for the multijet background is achieved using a binned maximum-likelihood fit to data on a discriminating variable.

The jet-lepton model

The jet-lepton method obtains a sample for the multijet background from simulated dijet events [136]. It selects a jet that resembles an electron by requiring the jet kinematics to be similar to those of a signal electron. The selection cuts are summarised in Table 5.3. The transverse momentum for the jet needs to be at least 25 GeV, the pseudorapidity $|\eta| < 2.47$ excluding the barrel–endcap overlap region ($1.37 \leqslant \eta \leqslant 1.52$), the fraction of the jet energy deposited in the electromagnetic calorimeter, f_{EM}, is required to be between 80 % and 95 % and at least 4 tracks need to be found in the jet in order to reject converted photons. To accept an event with this method, one 'jet-lepton' is required to be found. Events passing this selection do not need to fulfil any specific trigger requirement.

Table 5.3: *Selection cuts to obtain a multijet sample using the jet-lepton method.*

Kinematic	Selection cut
Transverse energy of jet	$E_{\mathrm{T}} > 25$ GeV
η of jet	$|\eta| < 2.47$, except $1.37 \leqslant \eta \leqslant 1.52$
EM fraction	$80\,\% < f_{\mathrm{EM}} < 95\,\%$
Number of tracks in jet	$N_{\mathrm{tracks}} \geqslant 4$

The anti-muon model

The anti-muon method uses data instead of simulation to derive a sample for the multijet events [136]. It inverts or alters some identification cuts for muons to obtain a sample enriched with non-isolated muons. The changed cuts are listed in Table 5.4. No cuts are applied on the longitudinal impact parameter z_0. The cut on the track isolation variable, I, (defined in Sect. 4.3) is changed to be $I/p_{\mathrm{T}}(\mu) < 0.1$ and the transverse energy deposited in the calorimeter within a cone of size $\Delta R < 0.2$ around the muon, eTcone20, is required to be larger than 0.03 times $p_{\mathrm{T}}(\mu)$. To further select non-isolated muons, the energy loss in the calorimeter is of type 'not isolated', which means that there are energy deposits from other particles close to the muon. This requirement enriches the sample with muons from heavy-flavour decays. To reject fake muons, the energy loss in the calorimeter is needed to be < 6 GeV.

Table 5.4: *Modified or inverted cuts for muon identification applied to data to extract a multijet sample using the anti-muon method.*

Variable	Selection cut
Impact parameter z_0	No cut
Isolation	eTcone20/$p_{\mathrm{T}}(\mu) > 0.03, I/p_{\mathrm{T}}(\mu) < 0.1$
Energy loss type	Not Isolated (energyLossType == 1)
Energy loss	energyLoss < 6 GeV

For both, the jet-lepton and the anti-muon method, events are required to pass the standard selection presented in Sect. 5.1 except for the changed cuts for electrons and muons listed in Table 5.3 and Table 5.4. Events with additional leptons are not accepted in the selection in order to reject undesired W+jets and Z+jets events.

Estimation of the multijet background normalisation

Samples obtained using the methods explained above provide shapes of distributions for the multijet background. However, the expected number of events of this background in the signal and validation regions needs to be estimated from data. This determination of the normalisation is performed using a binned maximum-likelihood fit on a variable that shows discriminating shapes between the multijet process and other processes. The fit is carried out separately for electrons and muons in each of the three signal regions and in the validation region. The discriminating variable is the $E_{\mathrm{T}}^{\mathrm{miss}}$ distribution for electrons and the $m_{\mathrm{T}}(W)$ distribution for muons. The $m_{\mathrm{T}}(W)$ distribution is utilised in the muon channel, since it provides a better modelling of the multijet background than the $E_{\mathrm{T}}^{\mathrm{miss}}$ observable used in the electron channel. Derived shapes of $E_{\mathrm{T}}^{\mathrm{miss}}$ for electrons comparing multijet, W+jets and $t\bar{t}$ processes are shown in Fig. 5.5, while shapes of the $m_{\mathrm{T}}(W)$ distribution for muons can be found in Fig. 5.6. As expected, distributions show smaller $E_{\mathrm{T}}^{\mathrm{miss}}$ and $m_{\mathrm{T}}(W)$ values for the multijet process, which makes these variables suitable for performing the fit. The fit is done after applying all selection cuts except the cut on $E_{\mathrm{T}}^{\mathrm{miss}}$ in case of electrons, and except the cut on $m_{\mathrm{T}}(W)$ for muons. Since the $\eta(\ell)$ distribution is not well described by the jet-lepton model, the fit in the electron channel is done separately in the barrel ($|\eta| \leqslant 1.5$) and endcaps ($|\eta| > 1.5$) regions. The separation is only relevant in SR1, which has a sizable multijet contribution and the $\eta(\ell)$ distribution in the jet-lepton method does not follow the expected distribution.

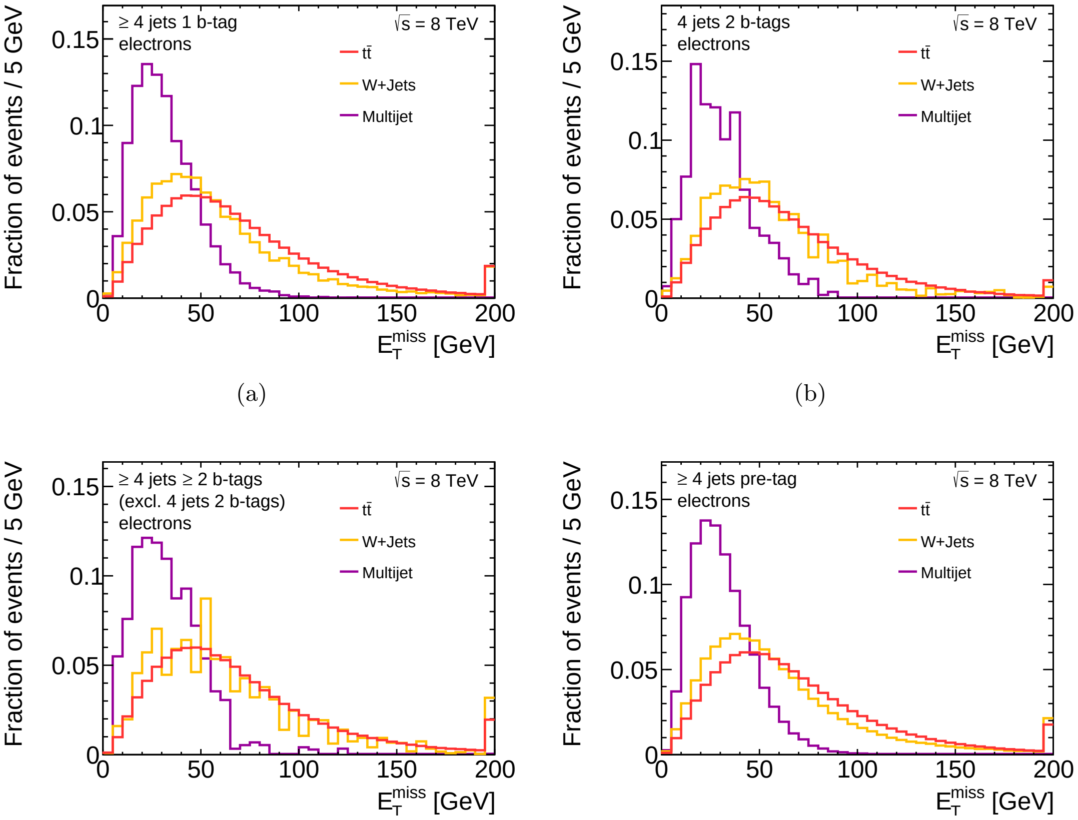

(a) (b)

(c) (d)

Figure 5.5: *Probability densities of the E_T^{miss} distribution for the simulated $t\bar{t}$ signal process, the W+jets process and the multijet process in the electron channel for (a) SR1, (b) SR2, (c) SR3 and (d) the validation region.*

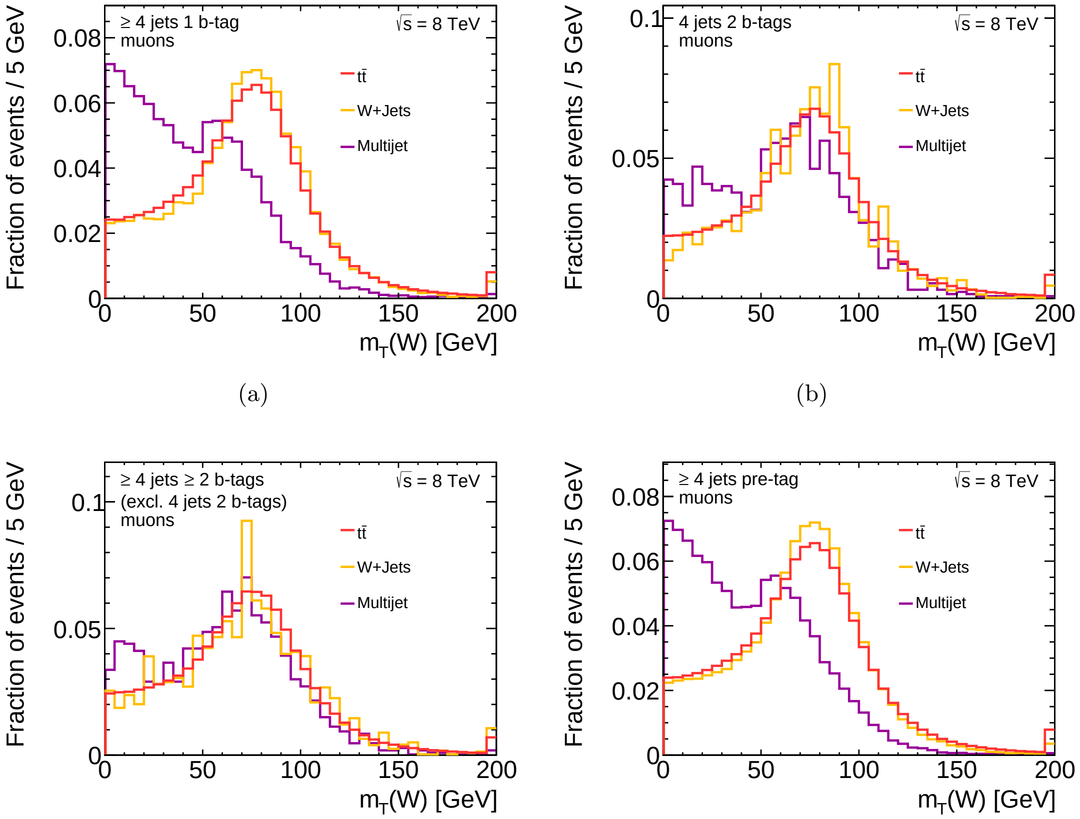

(a)

(b)

(c)

(d)

Figure 5.6: *Probability densities of the $m_T(W)$ distribution for the simulated $t\bar{t}$ signal process, the W+jets process and the multijet process in the electron channel for (a) SR1, (b) SR2, (c) SR3 and (d) the validation region.*

Other background processes are derived from simulation. The expected number of events for Z+jets, single-top and diboson processes are fixed to their theoretical prediction and are not fitted in the procedure, while $t\bar{t}$ and W+jets are fitted together with the multijet process. Distributions normalised to the fit results are shown in Fig. 5.7 for electrons and Fig. 5.8 for muons. The uncertainty band includes the MC statistical uncertainty and normalisation uncertainties for the simulated processes (Z+jets, single-top, diboson, $t\bar{t}$ and W+jets).

The fraction of events of the multijet process after applying $E_{\mathrm{T}}^{\mathrm{miss}} > 25$ GeV for electrons and $m_{\mathrm{T}}(W) > 30$ GeV for muons, is listed in Table 5.5 as well as the scale factors of the fitted processes $t\bar{t}$ and W+jets. The fraction of events of the multijet process for electrons and muons together is 5.4 % in SR1, 2.6 % in SR2 and 1.5 % in SR3. The scale factors of the $t\bar{t}$ and W+jets processes obtained in this fit are not used later in the analysis but are only applied in the control plots of kinematic variables.

Table 5.5: *Estimate of the multijet background normalisation in the signal and validation regions using the binned maximum-likelihood fit on the $E_{\mathrm{T}}^{\mathrm{miss}}$ distribution for electrons and on the $m_{\mathrm{T}}(W)$ distribution for muons. The quoted numbers are the expected number of events in each region together with the scale factors of the simultaneously fitted backgrounds. The uncertainties on the scale factor β are only statistical.*

Region	Events	Fraction	$\beta_{t\bar{t}}$	$\beta_{W+\mathrm{jets}}$
		SR1		
electrons, $\eta \leqslant 1.5$	2884	4.28%	1.02 ± 2 %	0.97 ± 9 %
electrons, $\eta > 1.5$	2464	13.59%	1.03 ± 4 %	0.96 ± 9 %
muons	4950	4.63%	1.01 ± 2 %	1.07 ± 9 %
		SR2		
electrons	404	1.23%	1.05 ± 1%	fixed to 1
muons	1539	3.82%	1.00 ± 1%	fixed to 1
		SR3		
electrons	436	1.40%	1.10 ± 1%	fixed to 1
muons	615	1.58%	1.08 ± 2%	fixed to 1
		W+jets validation region		
electrons	30967	10.32%	1.05 ± 3%	0.92 ± 4%
muons	17753	4.95%	0.95 ± 3%	1.08 ± 3%

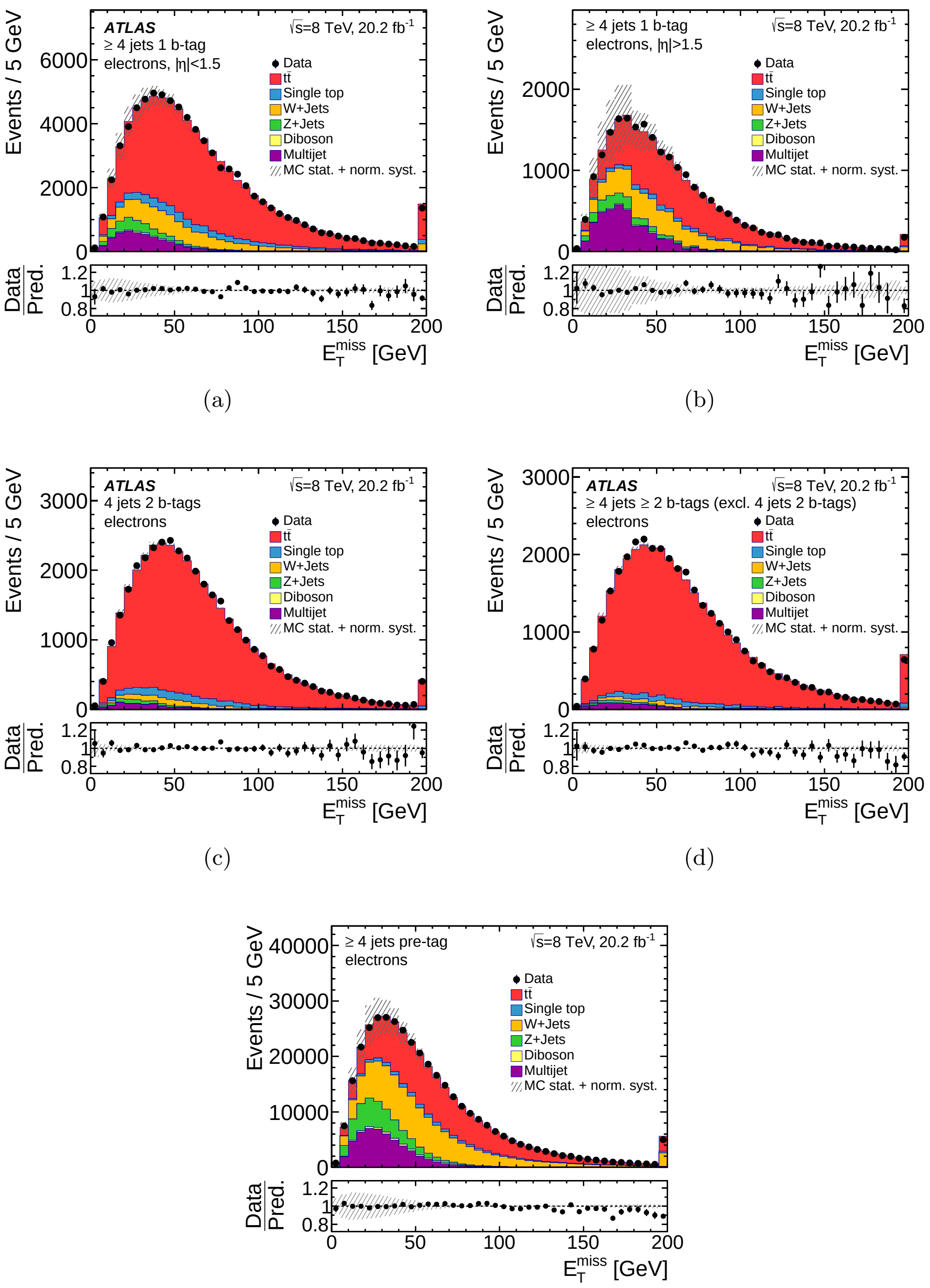

(a)

(b)

(c)

(d)

(e)

Figure 5.7: *The binned maximum-likelihood fit on the E_T^{miss} distribution for the electron channel in (a) SR1 , $\eta \leqslant 1.5$ (b) SR1 , $\eta > 1.5$ (c) SR2 (d) SR3 and (e) the validation region. The uncertainty band includes the MC statistical uncertainty and normalisation uncertainties for all background processes.*

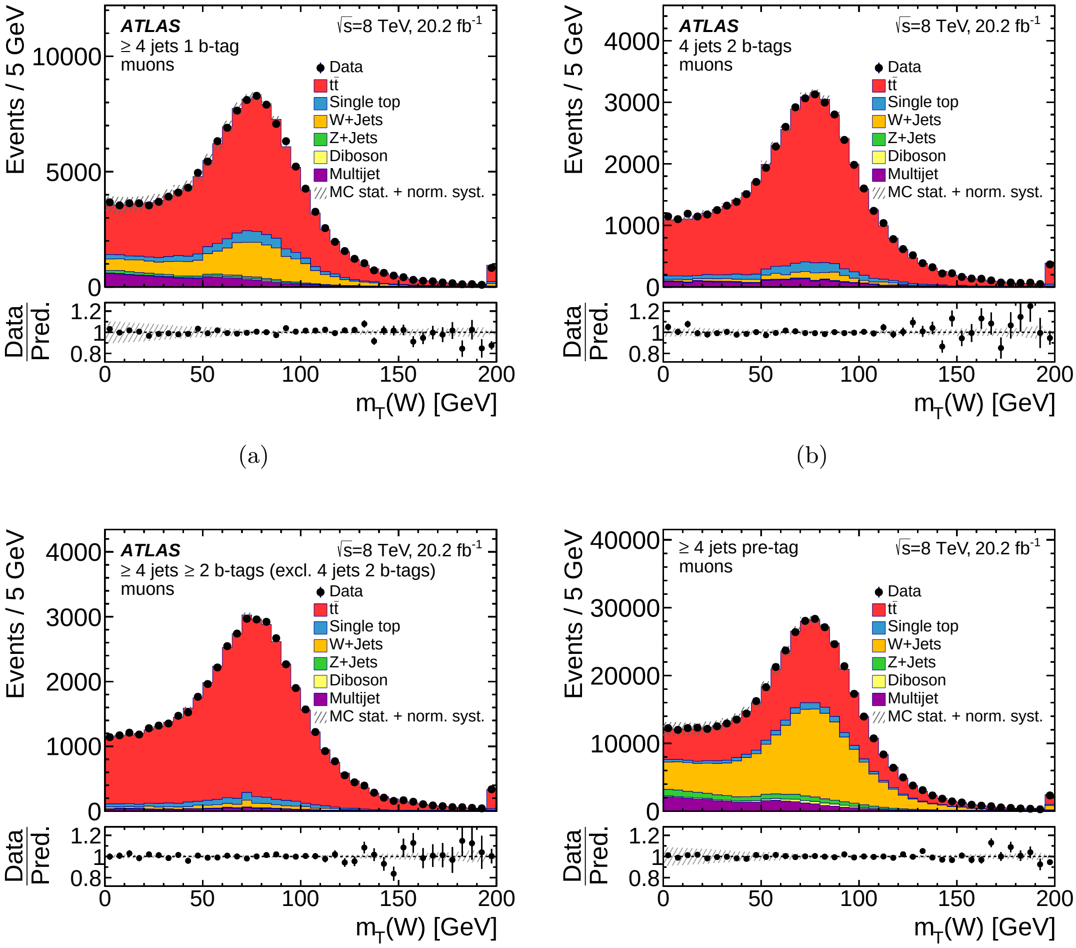

(a) (b)

(c) (d)

Figure 5.8: *The binned maximum-likelihood fit on the $m_T(W)$ distribution for the muon channel in (a) SR1 , $\eta \leqslant 1.5$ (b) SR2 (c) SR3 and (d) the validation region. The uncertainty band includes the MC statistical uncertainty and normalisation uncertainties for all background processes.*

Uncertainty in the multijet estimate

The number of events for the multijet background is small in SR2 and SR3, therefore an uncertainty of 50 % is assigned, based on comparisons of the rates obtained in various phase spaces using alternative methods described in previous analyses [136].

For SR1, an alternative method is used to estimate the systematic uncertainty in the multijet estimate referred to as the 'matrix' method [136]. The method provides template distributions and estimates of the expected number of multijets events. In this method, two samples are defined that differ in the lepton identification criteria. One sample contains a *tight* lepton (same selection as signal lepton). The other sample has a lepton, which satisfies the *loose* identification cuts. The number of selected events in the loose (N^l) or tight selection (N^t) can be written as a linear combination of the number of events with a real lepton ($N_r^{l,t}$) and the number of events with a non-prompt or a fake lepton ($N_f^{l,t}$):

$$\begin{aligned} N^l &= N_r^l + N_f^l, \\ N^t &= \epsilon_r N_r^t + \epsilon_f N_f^t. \end{aligned} \tag{5.5}$$

where ϵ_r is the fraction of the real leptons in the loose selection that also pass the tight selection and ϵ_f is the fraction of fake or non-prompt leptons in the loose selection that also pass the tight one.

The number of multijet events, i.e. fake or non-prompt leptons passing the tight selection can be written as:

$$N_f^t = \frac{\epsilon_f}{\epsilon_r - \epsilon_f}(\epsilon_r N^l - N^t) \tag{5.6}$$

If the efficiencies (ϵ_r and ϵ_f) are known, the number of multijet events can be calculated using Eq. (5.6). The efficiencies are determined from data in control regions. The efficiency of real leptons ϵ_r is determined using the tag-and-probe method from $Z \to e^+e^-$ and $Z \to \mu^+\mu^-$ events. The efficiency of fake leptons ϵ_r is measured using a data sample enriched with fake and non-prompt lepton events.

These efficiencies can also be used to calculate an event weight, which is then used to re-weight collision data to obtain distributions for the multijet process:

$$w_i = \frac{\epsilon_f}{\epsilon_r - \epsilon_f}(\epsilon_r - \delta_i) \tag{5.7}$$

where δ_i equals one if the event i contains a loose lepton that passes the tight selection as well, and zero otherwise. For any variable, the multijet estimate in each bin is determined by the sum of w_i over all events in that bin.

Estimation of the uncertainty in the multijet estimate in SR1 is performed by taking the relative difference between the multijet estimate using the fitting method and the matrix method. This procedure yields a normalisation uncertainty of 67 %.

5.6 Events yield

The numbers of selected events in the three signal regions are compared to the expectation from $t\bar{t}$ and background events in Table 5.6. The uncertainties on the expectations are statistical only for all processes except the multijet events, where the uncertainty on the estimated fraction is calculated as explained in the previous section.

Table 5.6: *Event yield for the three signal regions. The multijet background is estimated from the* $m_T(W)$ *or* E_T^{miss} *fit to data and the uncertainty in the multijet estimate is obtained in SR1 from the comparison between the fitting method and the matrix method. An uncertainty of* 50 % *is used for the other two regions. All the other expectations are derived using theoretical cross-sections, and the corresponding uncertainties arise from Monte Carlo statistics only.*

Process	SR1	SR2	SR3
$t\bar{t}$	133 310 ± 370	63 060 ± 250	59 310 ± 240
Single top	11 020 ± 110	3728 ± 61	2593 ± 51
W+jets	29 870 ± 170	2382 ± 49	1592 ± 40
Z+jets	3569 ± 60	406 ± 20	270 ± 16
Diboson	1339 ± 37	135 ± 12	112 ± 11
Multijet	10 300 ± 6900	1940 ± 970	1050 ± 530
Total expected	189 400 ± 6900	71 700 ± 1000	64 920 ± 580
Observed	192 686	72 978	70 120

6

Data-driven W+jets method

The process of W-boson production in association with jets, referred to as W+jets process, is the main background for the $t\bar{t}$ process in the lepton+jets channel. Fairly precise theoretical predictions of the W+jets production cross-section are available. However, event generators use different methods to simulate the ISR/FSR, parton shower and hadronisation. Furthermore, since the important phase space here is the W-boson production in association with at least four jets, event generators use different methods in the removal of overlapping partons between the matrix element and the parton shower. This causes sizeable differences in the predicted number of events from this background and in the shapes of kinematic distributions and therefore motivates the determination of this background using data. Hence, a data-driven technique is developed to obtain a sample for the W+jets background.

The idea of modelling the W+jets process using Z+jets events is given in Sect. 6.1. The procedure to obtain the sample from data is explained in Sect. 6.2. Control plots in the three signal regions are shown in Sect. 6.3.

6.1 Modelling W+jets with Z+jets events

The theoretical prediction of the production cross-section of a W boson in association with jets is calculated for up to five additional jets at NLO [137–140] and for one additional jet at NNLO [141]. Fig. 6.1(a) shows the production cross-section of the W bosons for different jet multiplicities. The measured cross-section from the ATLAS experiment at $\sqrt{s} = 8\,\mathrm{TeV}$ is compared to various predictions [142]. It can be seen that for high jet multiplicities, the predictions do not agree well with data. At $N_{\mathrm{jets}} \geqslant 4$, the discrepancies between data and predictions are about $20\,\%$. At $N_{\mathrm{jets}} \geqslant 5$, the discrepancies range from $20\,\%$ for predictions by the ALPGEN LO generator to $40\,\%$ for prediction by the SHERPA LO generator. These differences encourage the determination of the W+jets background from data. Thus, the normalisation of this background is determined together with the $t\bar{t}$ cross-section in the final fit procedure.

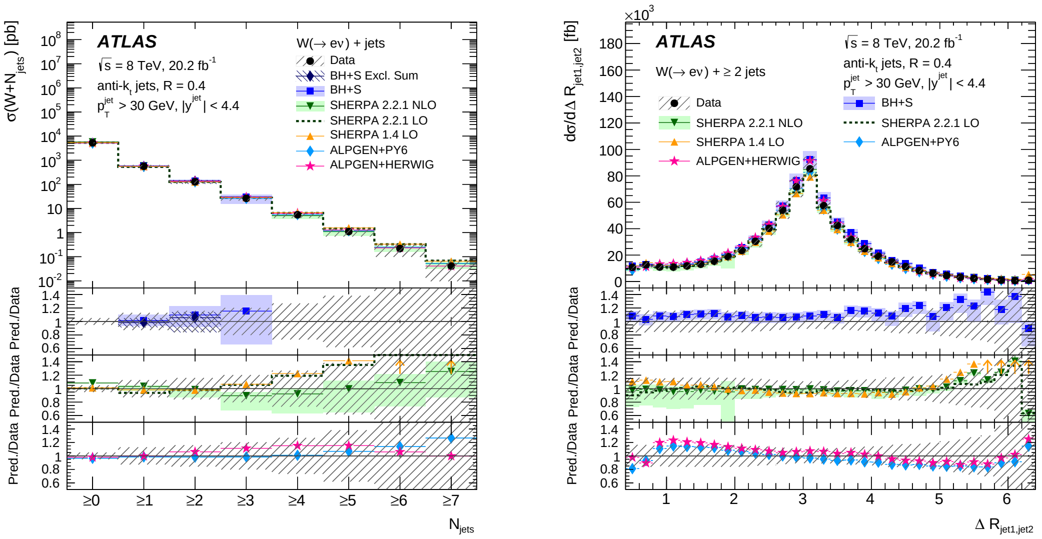

(a)

(b)

Figure 6.1: *(a) Cross-section for the production of W bosons for different inclusive jet multiplicities. (b) Differential cross sections for the production of W+jets as a function of the dijet angular separation, $\Delta R(\text{jet1}, \text{jet2})$, for events with $N_{\text{jets}} \geqslant 2$. The lower panels show the ratios of the predictions to the data [142]*

The differential cross-section for the production of W+jets as a function of the dijet angular separation, $\Delta R(\text{jet1}, \text{jet2})$, is shown in Fig. 6.1(b). As can be seen, all predictions except the one from the Alpgen event generator overestimate the cross sections at large angular separations between the leading two jets, while Alpgen disagrees with data for small and large angular separations. In Ref. [142], the differential cross-section for the production of W+jets is checked as a function of several other distributions. It concludes that no single prediction is able to describe all distributions well. Therefore, obtaining the shapes of kinematic distributions for the W+jets background from a new data-driven technique is encouraged. Using data instead of simulations implies no dependence on uncertainties coming from detector effects, MC modelling and PDFs. This results in a reduction of uncertainties affecting the $t\bar{t}$ cross-section measurements.

The idea of this method is based on the similarity of W+jets and Z+jets events and on the clean signature and low background level of the Z+jets production process. Thus, the sample for the W+jets background is obtained using Z+jets events from data. The development of this method and more studies can be found in Refs. [143, 144].

The W and Z bosons have very similar production modes and decay products, in addition to similar masses. Almost all Feynman diagrams of the W and Z production are identical. Some examples of vector boson production can be seen in Fig. 6.2 with 0,1 or 2 associated partons. Having almost identical production modes leads to similar kinematic properties of W+jets and Z+jets events. Additional partons (more than two) associated with the W and Z bosons are produced through gluon emissions and gluon splitting into $q\bar{q}$. Thus, the production of jets associated to the vector bosons is the same. This means that the kinematic properties of the jets are expected to be alike for W+jets and Z+jets events.

The benefit from using the Z+jets process is that it has a clean signature. Two oppositely charged leptons with invariant mass close to the Z boson mass. Hence, selecting and reconstructing Z+jets events from data produces an almost background-free sample.

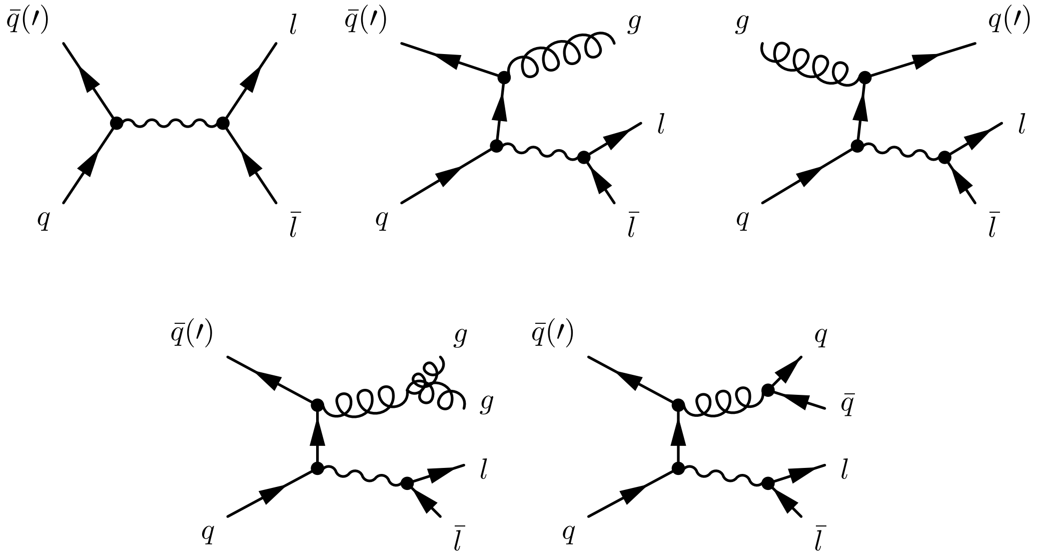

Figure 6.2: *Examples of Feynman diagrams for W and Z production with 0,1 or 2 associated partons.*

Differences between the vector bosons

Despite the many similarities in the production and decay of the W and Z vector bosons, there are some small differences. The main difference is caused by the small difference in the masses of the two bosons. The mass of the W boson is 80.379 ± 0.012 GeV [7], while the Z mass is 91.1876 ± 0.0021 GeV [7]. The higher mass of the Z boson demands higher momentum transfer (Q^2) for the production, which results in a different rapidity distribution and a higher p_{T} of the Z boson. In addition the associated jets in the Z-boson production tend to have on average a higher p_{T}, thus the number of selected jets could be higher for Z+jets events compared to W+jets events.

The LO cross-sections of the on-shell W- and Z-boson production, neglecting the decay width of the gauge boson, are calculated to be [145]:

$$\begin{aligned} \hat{\sigma}^{q\bar{q}'\to W} &= \frac{\pi}{3}\sqrt{2}G_F m_W^2 |V_{qq'}|^2 \delta(\hat{s} - m_W^2), \\ \hat{\sigma}^{q\bar{q}\to Z} &= \frac{\pi}{3}\sqrt{2}G_F m_Z^2 (c_V^2 + c_A^2)\delta(\hat{s} - m_Z^2). \end{aligned} \tag{6.1}$$

where G_F denotes the Fermi constant, m_W and m_Z are the masses of the W and Z bosons respectively, $\hat{s}$ is the squared centre-of-mass energy of the colliding partons, $V_{qq'}$ is the Cabibbo–Kobayashi–Maskawa matrix element and c_V and c_A are the vector and axial-vector couplings to fermions, defined as:

$$\begin{aligned} c_V &= I_{3L}^f + I_{3R}^f - 2e_f \sin^2\theta_W, \\ c_A &= I_{3L}^f - I_{3R}^f. \end{aligned} \tag{6.2}$$

I_{3L}^f and I_{3R}^f are the left-handed and right-handed third isospin component of fermion f, respectively, e_f is the charge of fermion f and θ_W is the weak mixing angle (Weinberg angle).

From Eq. (6.1), the differences in the formulas of W- and Z-boson production are only the masses of the bosons and the couplings to fermions. The coupling strength is given by the CKM matrix element for the W-boson production, while for the Z-boson production, the coupling strength is determined by the vector and axial-vector couplings c_V and c_A. The differences in the couplings to fermions are well understood and described by the theory. These differences lead to different angular distributions of final state objects for W+jets and Z+jets events.

Additionally, there are differences between the helicity[8] structures of the bosons' decay vertices Wff and Zff. NLO calculations show that the left-handed nature of the W-boson coupling leads to a large left-handed polarisation for both W^+ and W^- bosons at high p_{T} [146]. A left-handed W^+ boson tends to decay to a left-handed neutrino along the boson's flight direction and a right-handed ℓ^+ in the opposite direction. For a left-handed W^- boson, it is the opposite: it tends to decay to a left-handed ℓ^- along its flight direction and a right-handed anti-neutrino in the opposite direction. This implies that the charged lepton has a relatively higher p_{T} coming from the W^--boson decay and the neutrino has a relatively lower p_{T}. This is reversed for the W^+-boson decay. Measurements agree with these predictions [147]. The Z boson is less polarised and its decay into two charged leptons is fairly symmetrical. Thus, this difference between the W boson and the Z boson, leads to small differences in the p_{T} distributions of the leptons.

---

[8] The helicity is the spin component along the momentum direction.

In the leptonic decay, the Z boson decays into two charged leptons ($Z \rightarrow \ell^+\ell^-$) while the W boson decays into one charged lepton and a neutrino ($W \rightarrow \ell\nu$). Furthermore, the additional heavy flavour is different in Z+jets and W+jets events. The Zbb coupling is strong while the Wbc coupling is suppressed since the CKM matrix element V_{cb} is small. This difference is not dominant for events with at least four jets, where the main production mode of heavy flavour comes from gluon splitting into $b\bar{b}$.

In general, the W+jets and Z+jets events have strong similarities and all these differences are minor and have a very small effect on the analysis. In this method, some of these differences are accounted for, which will be explained in the following.

6.2 W+jets background sample from data

In order to obtain a data-driven sample to model the W+jets background, Z+jets events are selected from data. After that, a conversion algorithm is applied on the selected sample to account for the major differences between Z+jets and W+jets events. Shapes of kinematic distributions are then checked to validate the usability of the obtained sample.

Selection and conversion procedure

The selection of Z+jets events from data is implemented as follows:

- Requiring exactly two oppositely charged leptons with the same flavour
- The invariant mass of the two leptons has to be: $80\ \text{GeV} \leqslant m(\ell\ell) \leqslant 102\ \text{GeV}$

In order to consider the mass difference of W and Z bosons and the variation of the decay products ($W \rightarrow \ell\nu$ and $Z \rightarrow \ell^+\ell^-$), a conversion method is applied to make Z+jets events more similar to W+jets. The resulting sample is denoted as $Z$to$W$.

First, the two leptons of the Z boson decay are boosted into the Z boson rest frame, with the relativistic transforms:

$$\gamma_Z \; = \; \frac{E_Z}{m_Z}, \quad \vec{\beta}_Z \; = \; \frac{-\vec{p}_Z}{E_Z} \tag{6.3}$$

The momentum vector of the Z boson is the sum of the four momenta of the two leptons. Then, the momenta of the two leptons are scaled down with the ratio of the bosons' masses:

$$\vec{p'}_\ell(i) = \frac{m_W}{m_Z}\vec{p}_\ell(i) \tag{6.4}$$

After that, the momenta of the leptons are boosted back to the laboratory system assuming the momenta of the Z and W bosons are identical. The energy of the W boson is then defined as:

$$E_W \; = \; \sqrt{m_W^2 \; + \; p_Z^2}, \quad \vec{p}_W \; = \; \vec{p}_Z \tag{6.5}$$

and the boost is given by:

$$\gamma_W = \frac{E_W}{m_W}, \quad \vec{\beta} = \frac{-\vec{p}_Z}{E_W} \tag{6.6}$$

At the end of the conversion algorithm, one of the two leptons is chosen randomly and dropped from the event. In a final step, the missing transverse momentum of the event $E_{\mathrm{T}}^{\mathrm{miss}}$ is re-calculated, in order to take into account the removed lepton and the rescaled one. Events have to pass the $t\bar{t}$ event selection explained in section 5.1 except the b-tagging requirement.

Applying this procedure produces a sample that resembles W+jets events using Z+jets events selected from collision data, termed '$Z$to$W$ data' for the rest of this thesis. For some studies, a simulated Z+jets sample is used instead of data and then converted using the above algorithm. In this case, the sample is referred to as 'ZtoW'.

Kinematic distributions

Relevant kinematic distributions, which are used in the validation of the $Z$to$W$ method, are:

- The transverse momentum of the reconstructed charged lepton, $p_T(\ell)$.
- The missing transverse momentum, $E_{\mathrm{T}}^{\mathrm{miss}}$.
- The transverse mass of the W boson, $m_{\mathrm{T}}(W)$.
- The transverse momentum of the reconstructed leading jet (the jet with the highest p_{T}), $p_{\mathrm{T}}(j_1)$.
- The transverse momentum of the reconstructed second-leading jet, $p_{\mathrm{T}}(j_2)$.
- The cosine of the angle θ^*, which is between the momentum of the reconstructed hadronically decaying top-quark and the beam direction in the $t\bar{t}$ rest system, $\cos\theta^*$
- The event shape parameter aplanarity, A, which measures the transverse momentum component pointing out of the event plane. The aplanarity is given by:

  $$A = \frac{3}{2}\lambda_3 \tag{6.7}$$

  where λ_3 is the smallest eigenvalue of the sphericity tensor:

  $$S^{\alpha\beta} = \frac{\sum_i p_i^{\alpha} p_i^{\beta}}{\sum_i \mid p_i \mid^2} \tag{6.8}$$

  Here α, β correspond to the x,y and z momentum components of final state objects in the event, i.e. the jets, the charged lepton and the reconstructed neutrino.
- The mass of the reconstructed hadronically decaying top-quark, $m(bjj)$.

- The mass of the reconstructed leptonically decaying top-quark, $m(l\nu b)$.
- The smallest invariant mass between jet pairs, m_{12}.
- The second smallest invariant mass between jet pairs, m_{23}.
- The smallest invariant mass between the charged lepton and a jet, $m_{\ell 1}$.

A comparison of these kinematic distributions of simulated W+jets against simulated $Z$to$W$ events is performed, shown in Figs. 6.3 and 6.4. This check is done in the three signal regions together ($\geqslant$ 4 jets, $\geqslant$ 1 b-tag) but no b-tagging requirement is applied for the $Z$to$W$ sample.

Distributions show a fairly good agreement between W+jets and $Z$to$W$ events except for the $E_{\mathrm{T}}^{\mathrm{miss}}$ distribution, which shows the largest discrepancies. The $Z$to$W$ events tend to have a higher $E_{\mathrm{T}}^{\mathrm{miss}}$ than the W+jets events. The differences in the $E_{\mathrm{T}}^{\mathrm{miss}}$ distributions is expected to be related to the different W- and Z-boson couplings. Variables with large discrepancies between W+jets and $Z$to$W$ events, like the $E_{\mathrm{T}}^{\mathrm{miss}}$, are not used later in the analysis. A small discrepancy between W+jets and $Z$to$W$ events is visible in all plots. The differences are within 20 %, excluding the region of low statistics.

The idea of this method is to derive kinematic distributions from data. The differences shown are expected and the $Z$to$W$ events are not supposed to reproduce the simulated W+jets events, since the $Z$to$W$ method is designed to have a better modelling, avoiding mis-modellings from simulation.

Comparisons in data in a validation region

Comparisons in data are needed to verify this method. However, in the signal region, the $t\bar{t}$ process is dominant, which makes it unusable for a validation of the W+jets process. Therefore, a different region, which is dominated by the W+jets process, is used. Furthermore, since this method can be considered a general method, it is encouraged to test it in different phase spaces.

In order to find a suitable region, the number of expected events of the different processes for different number of selected jets is investigated. The corresponding distribution is shown in Fig. 6.5. The multijet process is neglected in this plot and the predictions are obtained using the theoretically calculated cross sections and the acceptance from MC simulation. As can be seen, the expected number of events for the W+jets process is the highest in the two jet bin and the contribution from the $t\bar{t}$ process is much smaller. Thus, the 2 jets, $\geqslant$ 1 b-tag region is used to validate the method in data.

The expected number of events of each process in the 2 jets, $\geqslant$ 1 b-tag region can be found in Table 6.1. All values are taken from the theoretical predictions, except for the multijet process. The expected number of multijet events is estimated the same way as explained in Sect. 5.5.

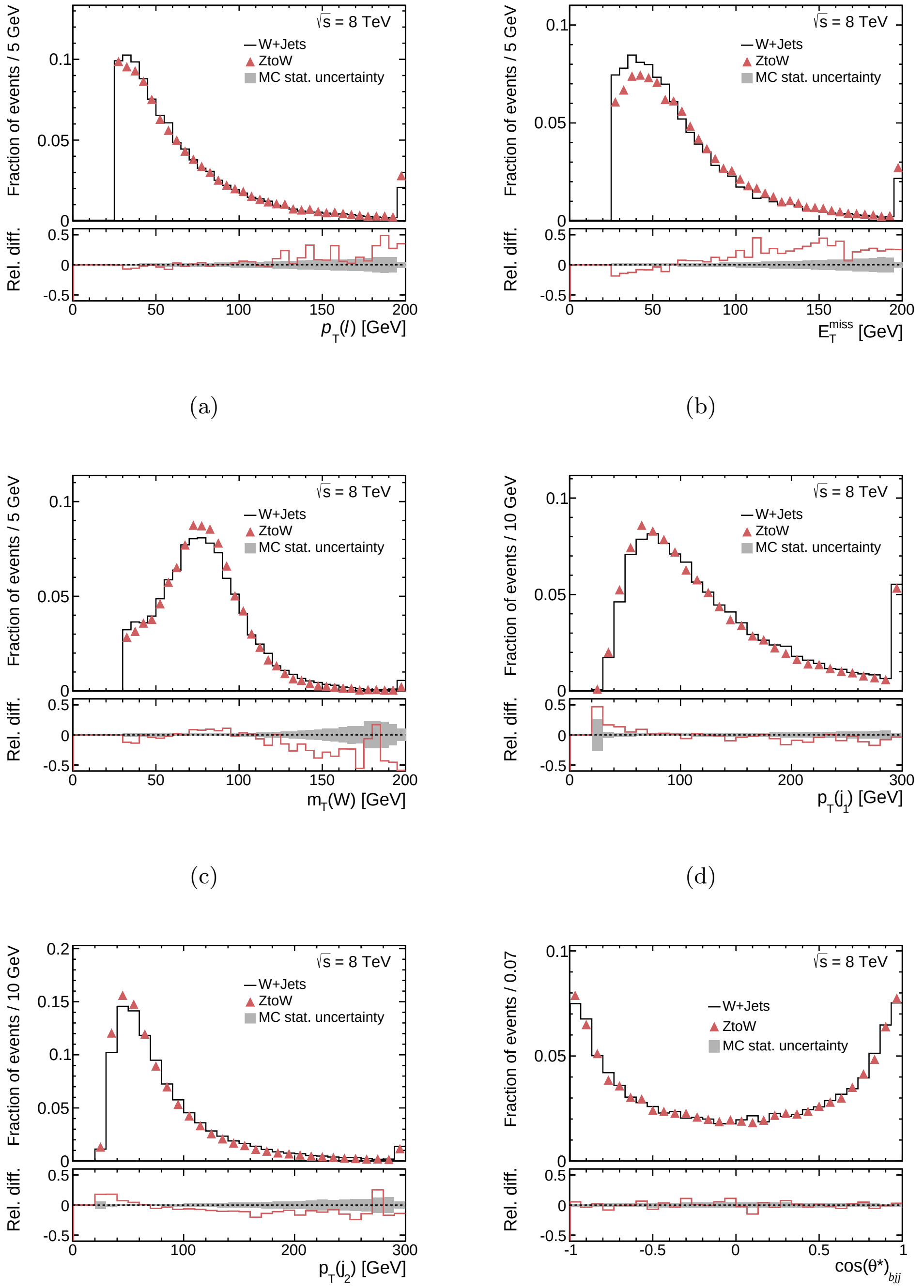

(a) (b)

(c) (d)

(e) (f)

Figure 6.3: *Comparison of distributions for simulated W+jets events and simulated $Z to W$ events in the three signal regions together ($\geqslant$ 4 jets, $\geqslant$ 1 b-tag). No b-tagging requirement is used for $Z to W$ events.*

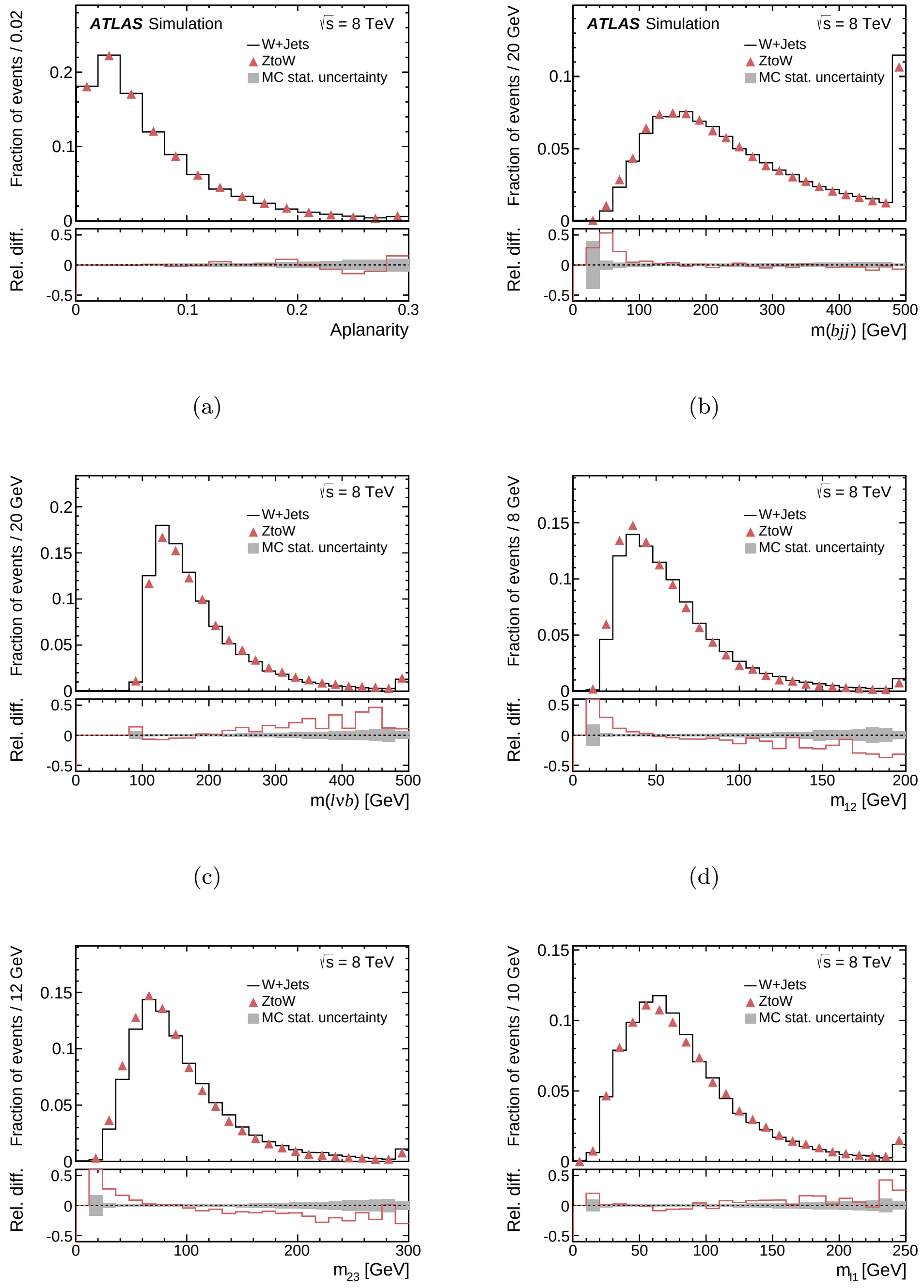

(a) (b)

(c) (d)

(e) (f)

Figure 6.4: *Comparison of distributions for simulated W+jets events and simulated $Z$to$W$ events in the three signal regions together ($\geqslant 4$ jets, $\geqslant 1$ b-tag). No b-tagging requirement is used for $Z$to$W$ events.*

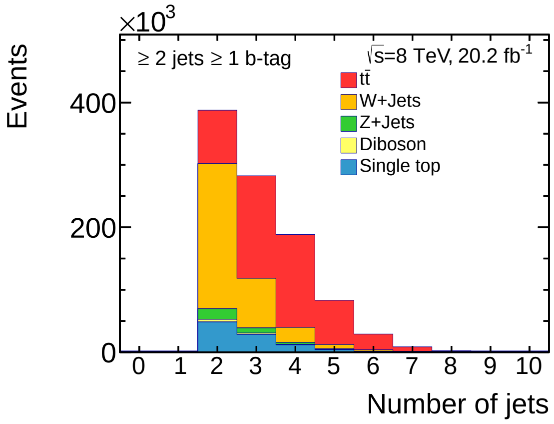

Figure 6.5: *Number of expected events of all processes apart from the multijet process normalised using the theoretically calculated cross section and acceptance from simulation for different number of selected jets.*

Table 6.1: *Event yield for the 2 jets, $\geqslant 1$ b-tag region. The multijet background is estimated from the $m_T(W)$ or E_T^{miss} fit to data and 50 % uncertainty is assumed on the estimate. All the other expectations are derived using theoretical cross-sections, and the corresponding uncertainties arise from Monte Carlo statistics only.*

Process	2 jets, $\geqslant 1$ b-tag
W+jets	232 280 ± 480
$t\bar{t}$	81 270 ± 290
Single top	48 460 ± 220
Z+jets	17 070 ± 130
Diboson	4188 ± 65
Multijet	86 700 ± 43 000
Total expected	470 000 ± 43 000
Observed	489 702

The comparison between W+jets events in the 2 jets, $\geqslant 1$ b-tag validation region and ZtoW data is performed by subtracting templates normalised to the expected number of events of all other processes, i.e. $t\bar{t}$, single top, dibosons, Z+jets and multijet, from the data. Some kinematic distributions are given in Fig. 6.6. All figures show a very good agreement between the $Z$to$W$ data events and the W+jets events, labeled as 'Data-bg'.

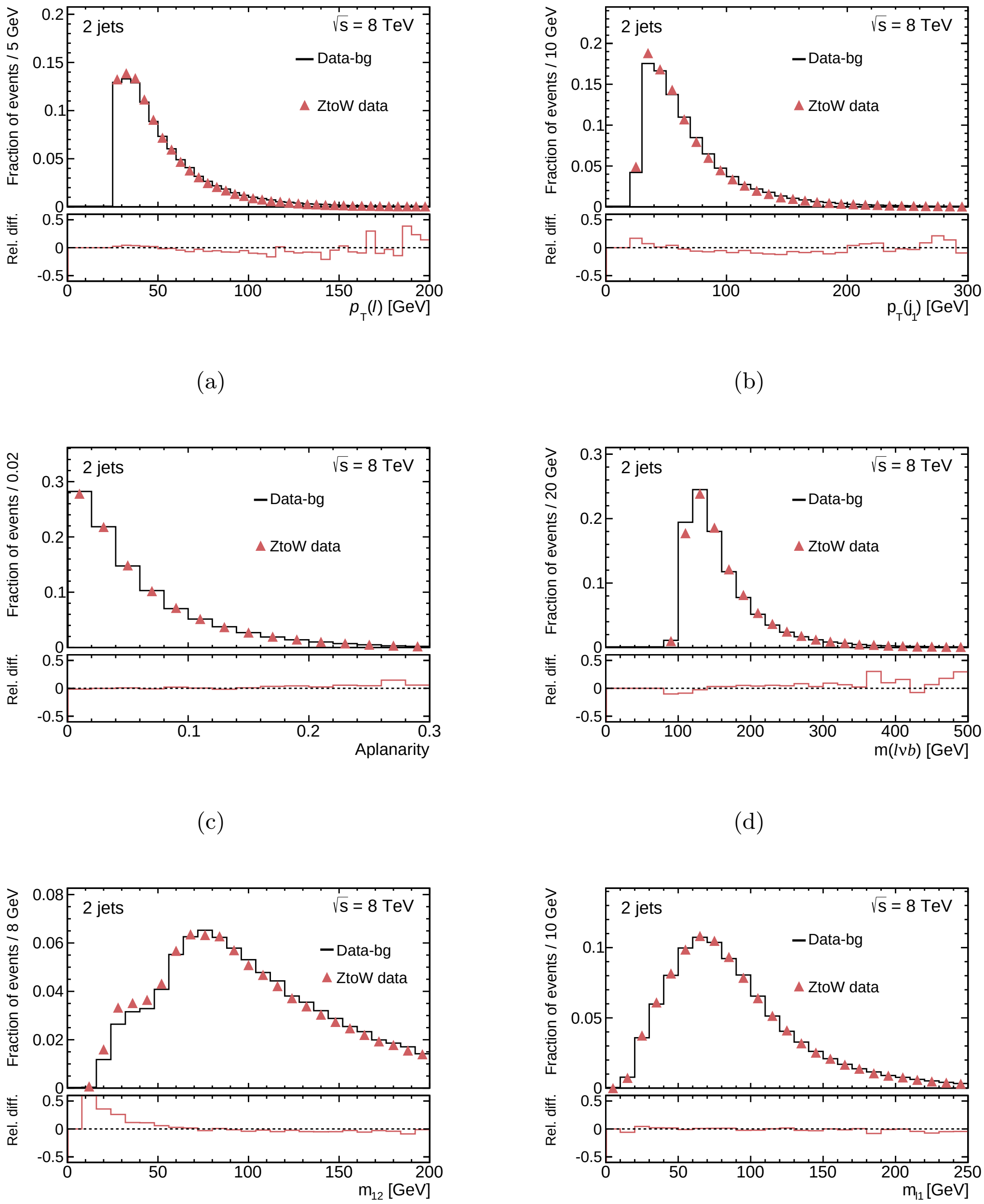

(a) (b)

(c) (d)

(e) (f)

Figure 6.6: *Comparison of distributions for W+jets events in the data ('Data-bg') and ZtoW data events in the 2 jets, $\geqslant 1$ b-tag region. No b-tagging requirement is used for ZtoW events.*

6.3 Control plots

After describing the methods used to estimate and model the multijet and W+jets backgrounds, Kinematic distributions are examined in the three signal regions.

Distributions are presented in Figs. 6.7 and 6.8 for SR1, Figs. 6.9 and 6.10 in SR2 and Figs. 6.11 and 6.12 in SR3. In all figures, the left-hand side plots are for the electron channel and plots on the right-hand side are for the muon channel. Plots are normalised to the result of the maximum likelihood fit on the $E_{\mathrm{T}}^{\mathrm{miss}}$ or $m_{\mathrm{T}}(W)$ distributions presented in Table 5.5. The uncertainty shown includes the statistical uncertainty and the normalisation uncertainty of all processes.

Figs. 6.7, 6.9 and 6.11 show the $E_{\mathrm{T}}^{\mathrm{miss}}$, the $m_{\mathrm{T}}(W)$ and the $p_{\mathrm{T}}(l)$ distributions, while Figs. 6.8, 6.10 and 6.12 show the $p_{\mathrm{T}}(j_1)$, the $p_{\mathrm{T}}(j_2)$ and the $p_{\mathrm{T}}(j_3)$ distributions. In all figures, a good agreement between data and predictions is visible. Differences are within the uncertainties in most bins.

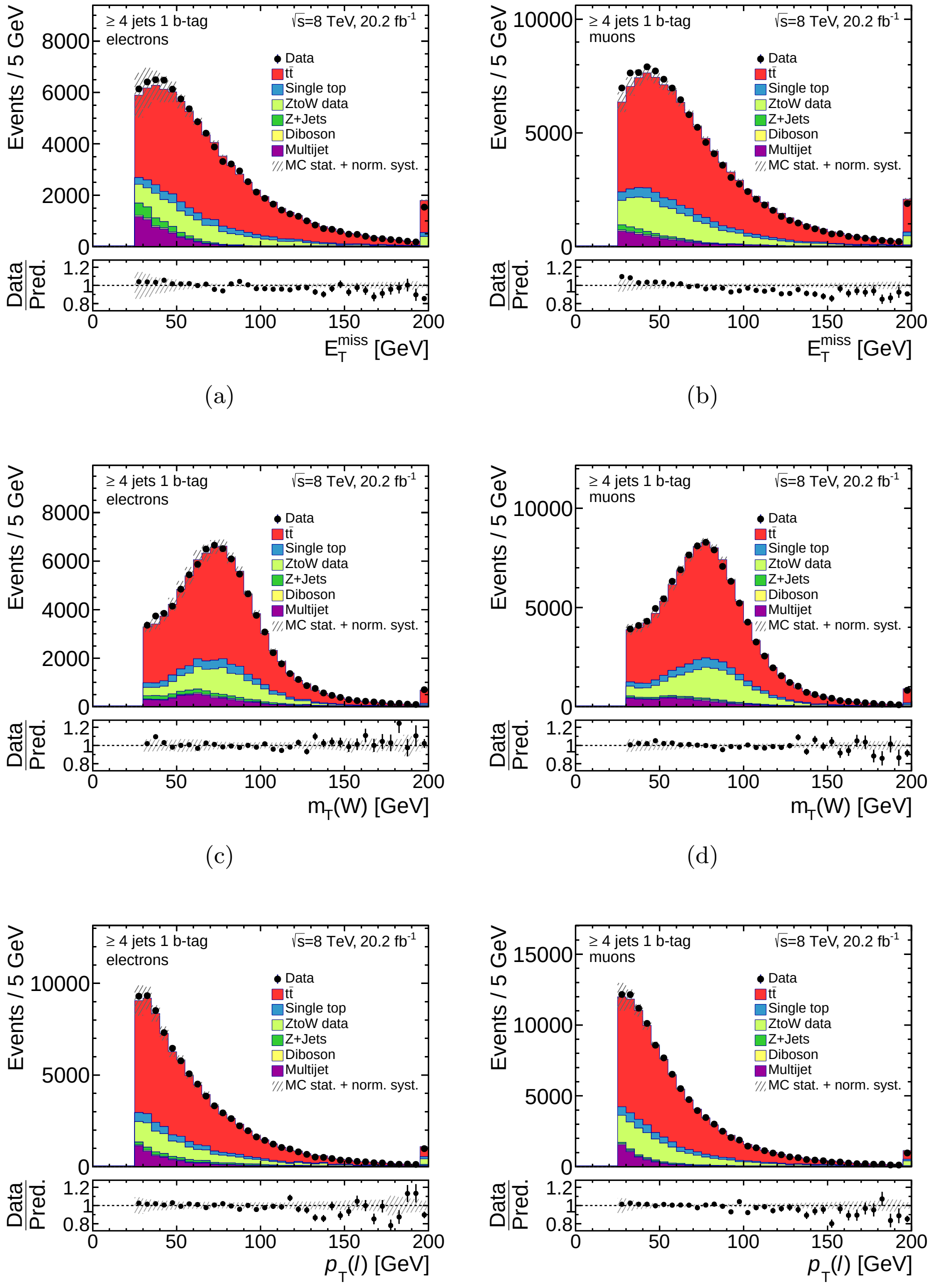

(a) (b)

(c) (d)

(e) (f)

Figure 6.7: *Distributions normalised to the estimates of the multijet fits for the (left) electron channel, (right) muon channel in SR1. The hatched error bands represent the MC statistical uncertainty and the normalisation uncertainty of all processes. The ratio of observed to predicted (Pred.) number of events in each bin is shown in the lower histogram.*

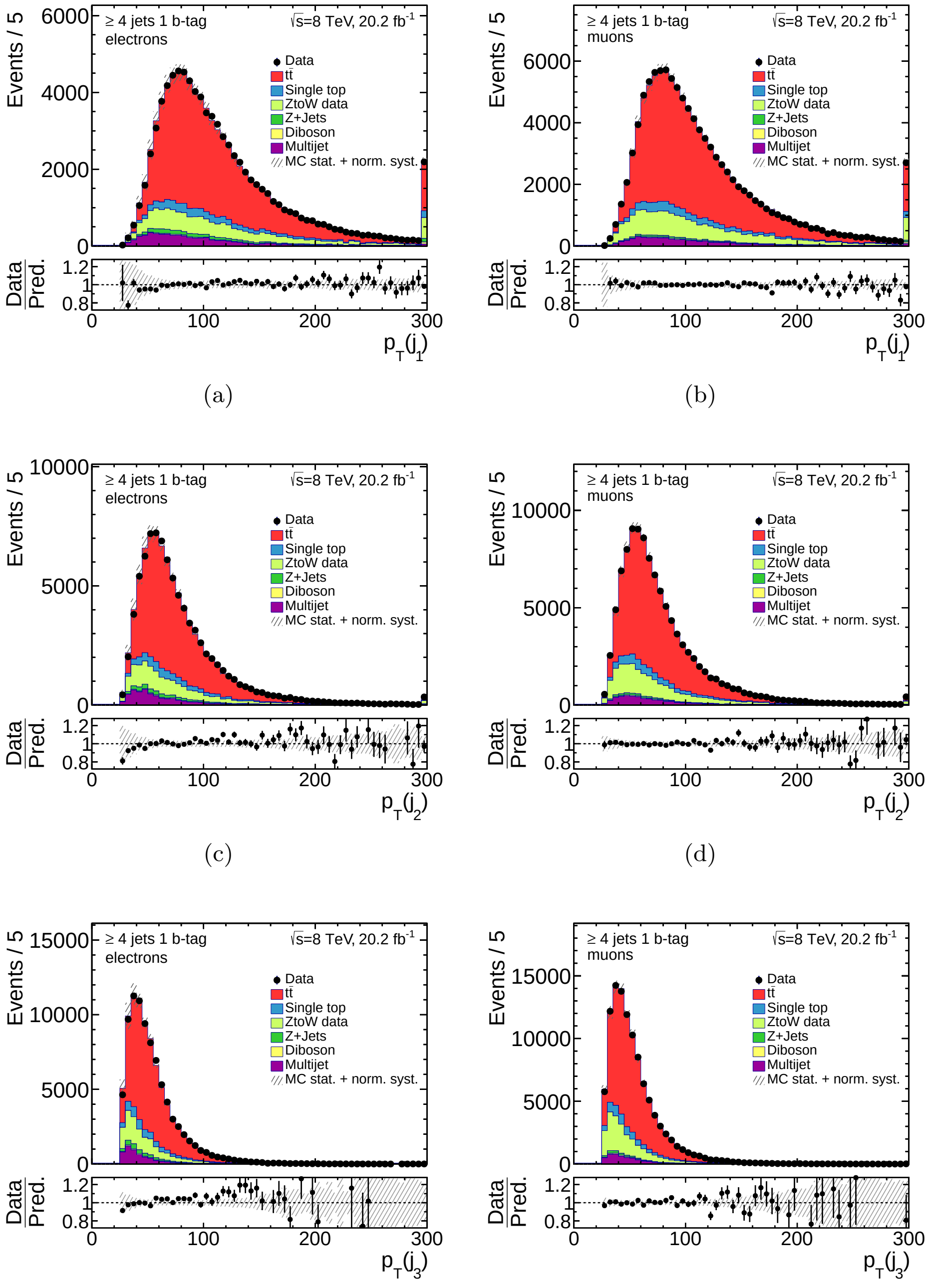

(a) (b)

(c) (d)

(e) (f)

Figure 6.8: *Distributions normalised to the estimates of the multijet fits for the (left) electron channel, (right) muon channel in SR1. The hatched error bands represent the MC statistical uncertainty and the normalisation uncertainty of all processes. The ratio of observed to predicted (Pred.) number of events in each bin is shown in the lower histogram.*

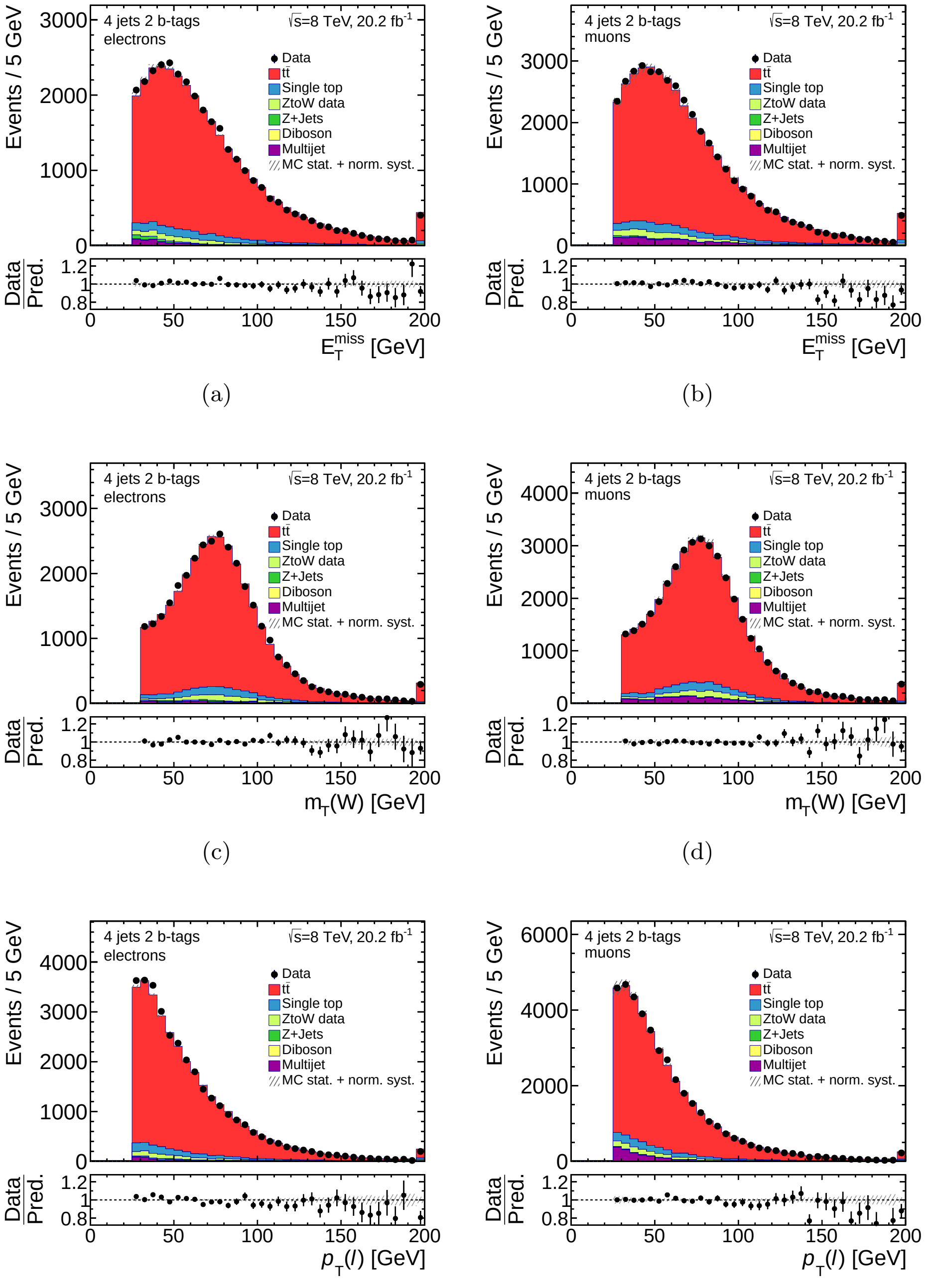

(a) (b)

(c) (d)

(e) (f)

Figure 6.9: *Distributions normalised to the estimates of the multijet fits for the (left) electron channel, (right) muon channel in SR2. The hatched error bands represent the MC statistical uncertainty and the normalisation uncertainty of all processes. The ratio of observed to predicted (Pred.) number of events in each bin is shown in the lower histogram.*

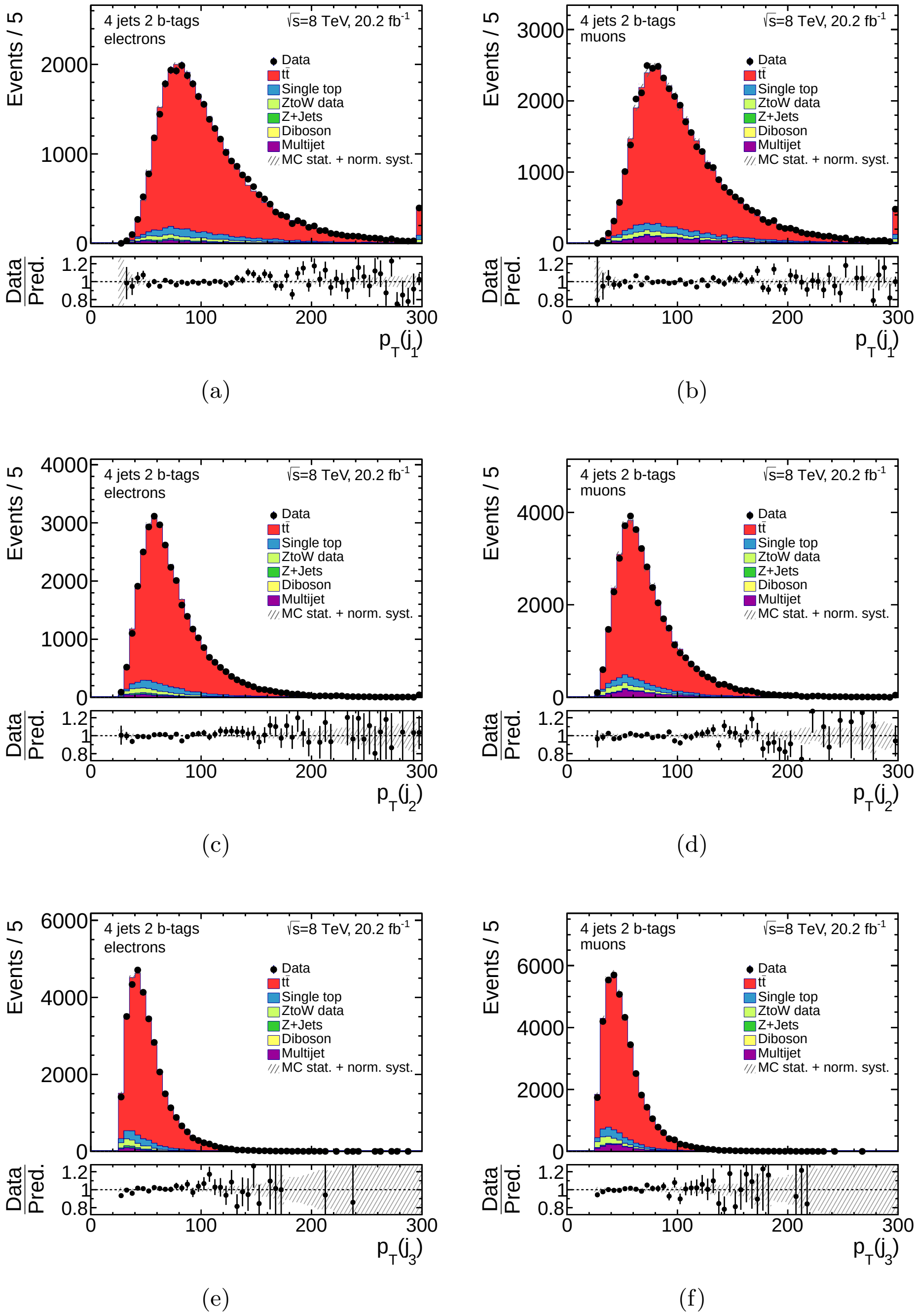

Figure 6.10: *Distributions normalised to the estimates of the multijet fits for the (left) electron channel, (right) muon channel in SR2. The hatched error bands represent the MC statistical uncertainty and the normalisation uncertainty of all processes. The ratio of observed to predicted (Pred.) number of events in each bin is shown in the lower histogram.*

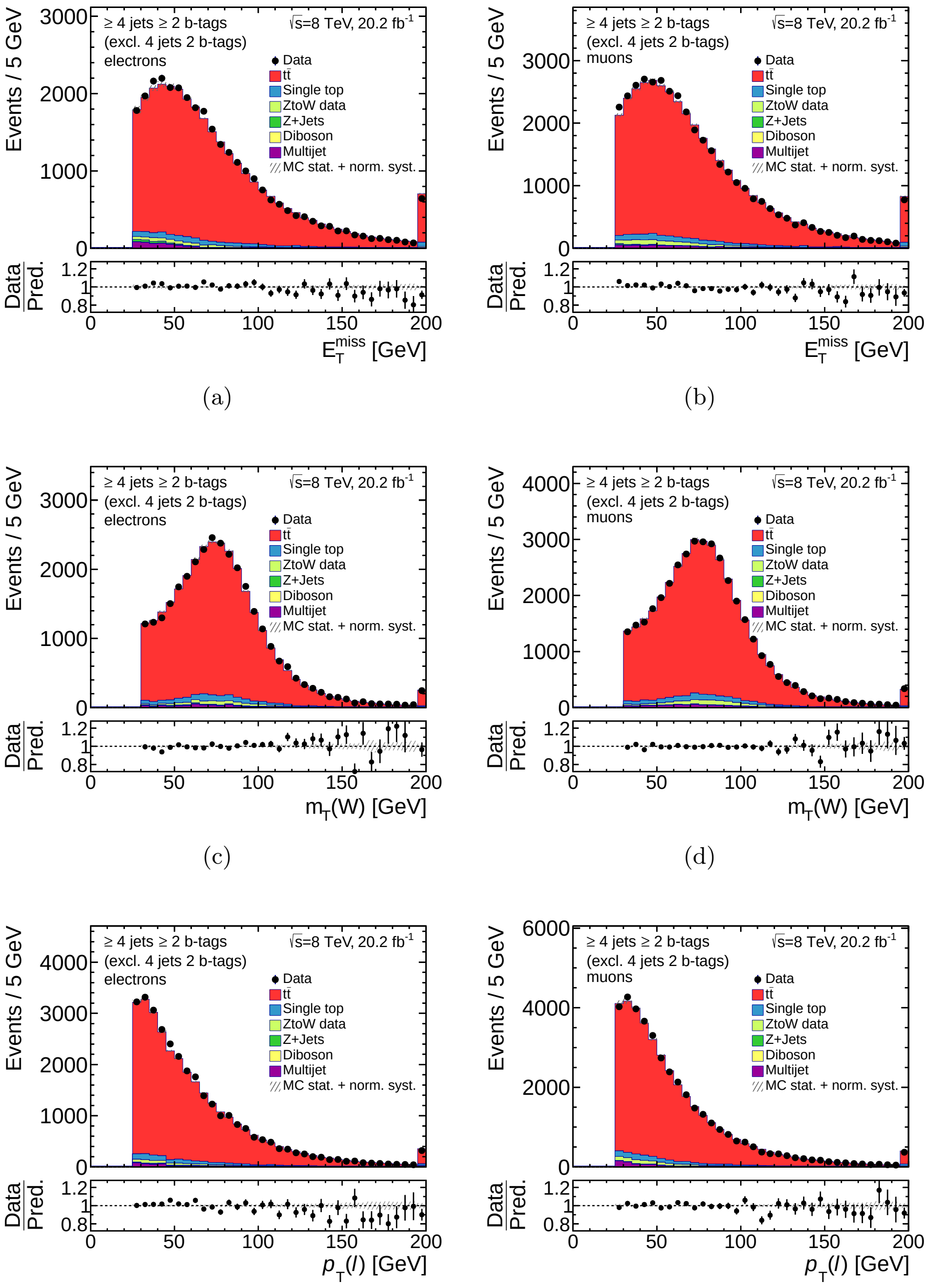

(a) (b)

(c) (d)

(e) (f)

Figure 6.11: *Distributions normalised to the estimates of the multijet fits for the (left) electron channel, (right) muon channel in SR3. The hatched error bands represent the MC statistical uncertainty and the normalisation uncertainty of all processes. The ratio of observed to predicted (Pred.) number of events in each bin is shown in the lower histogram.*

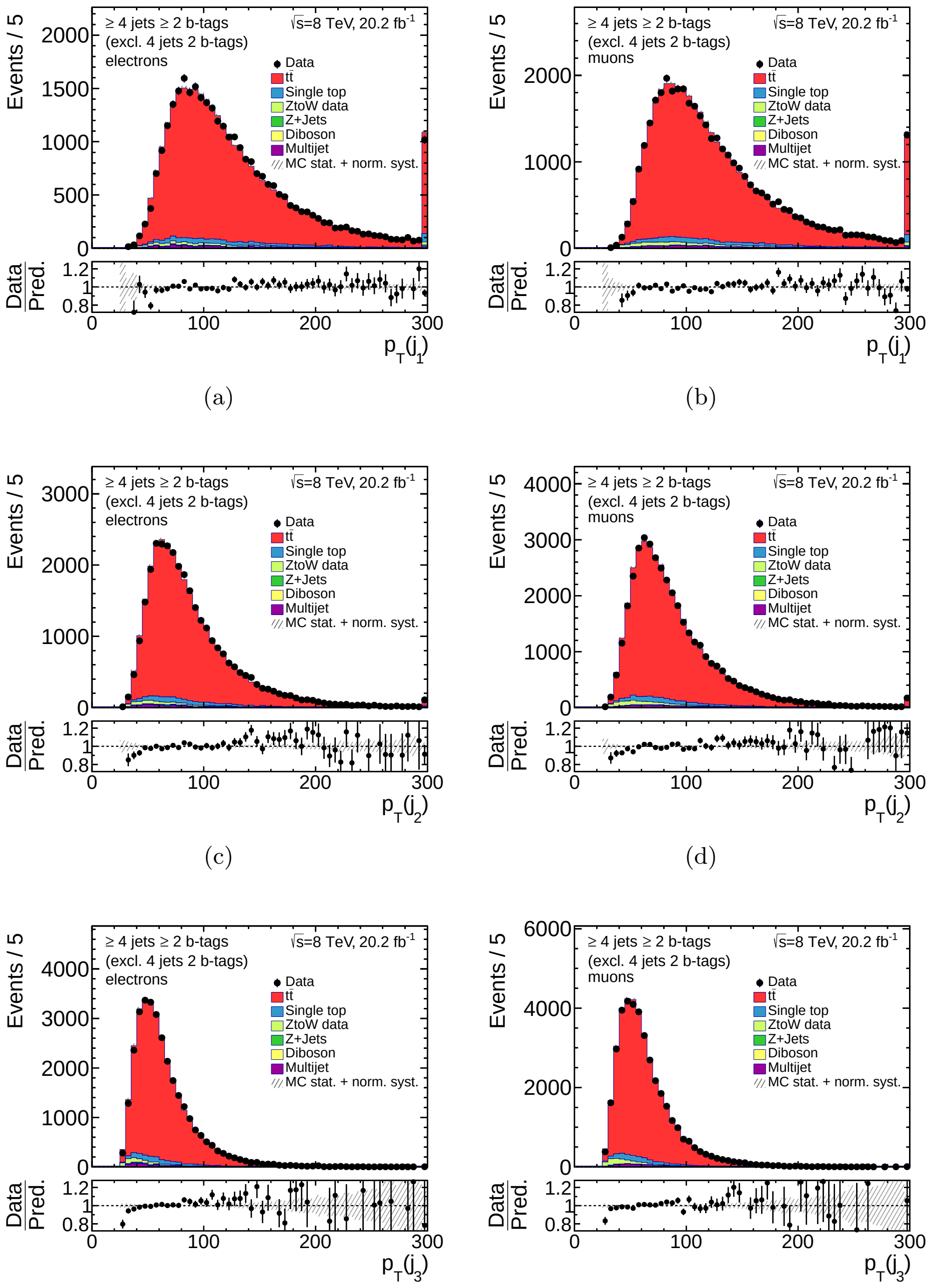

(a) (b)

(c) (d)

(e) (f)

Figure 6.12: *Distributions normalised to the estimates of the multijet fits for the (left) electron channel, (right) muon channel in SR3. The hatched error bands represent the MC statistical uncertainty and the normalisation uncertainty of all processes. The ratio of observed to predicted (Pred.) number of events in each bin is shown in the lower histogram.*

7

Discriminating observables

In the presented analysis, a binned maximum likelihood fit is performed in the three signal regions to extract the $t\bar{t}$ cross-section. A neural network is employed to achieve good separation between $t\bar{t}$ and W+jets events in SR1 and SR3, where the neural network output distribution is used in the fit. In SR2 the invariant mass of the two untagged jets $m(jj)$ is used instead.

An explanation of artificial neural networks as multivariate classifiers and their application to this analysis is given in Sect. 7.1. Sect. 7.2 describes the usage of the reconstructed mass of the hadronically decaying W boson.

7.1 Neural networks

Neural networks are a widely used multivariate technique that can be employed as an event classifier. They allow the combination of information from different event attributes into a single discriminant output value. The event properties are fed to the network in the form of input variables. Neural networks learn the differences of the inputs between signal and background events before the trained network is applied to data. An output distribution in the interval $[0, 1]$ is obtained, that represents the probability for an event to be signal-like. A neural network consists of nodes and connections between those nodes. Different kinds of networks exist, which differ mainly in the way the nodes are connected. In a feed-forward network, the nodes are arranged in layers and each node in one layer has directed connections to the nodes of the next layer. The first layer is called input layer, the intermediate layers are referred to as hidden layers and the last layer is called output layer.

7.1.1 The utilised neural network

The Neurobayes package [148, 149] provides the neural network algorithm for this analysis. In the following, the network architecture, the preprocessing of the input variables and the training procedure including over-training checks are discussed.

Architecture

Neurobayes uses a three-layered feed-forward network with one hidden layer. A schematic of the neural network is illustrated in Fig. 7.1.

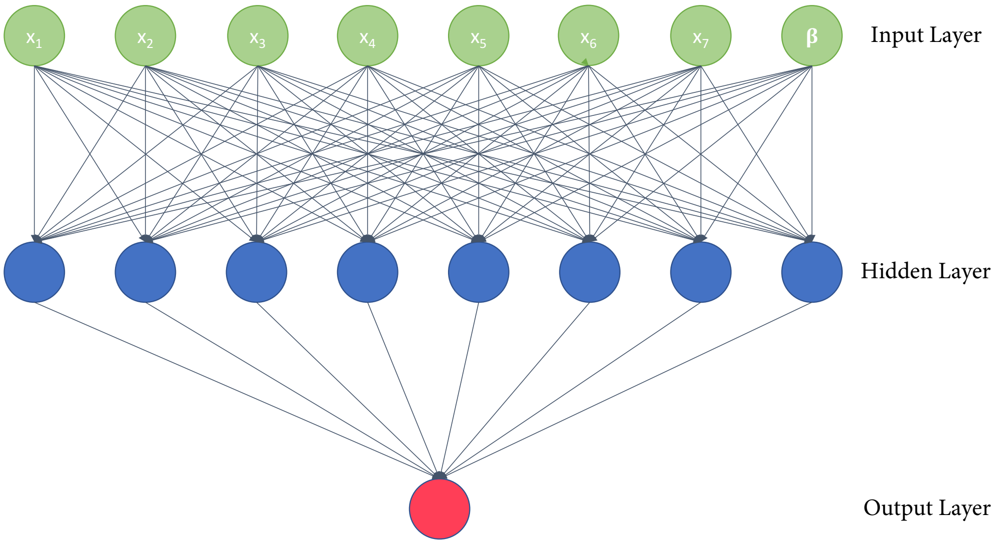

Figure 7.1: *A schematic of the neural network used in the analysis. Shown are the input, hidden and output layers.*

In this analysis, the input layer consists of seven input variables, $x_1, \ldots, x_7$, plus one bias node, β, set to a fixed value. The number of hidden nodes is chosen to be 8. The output layer consists of one node that provides a continuous output in the interval $[-1, 1]$.

The output of the three-layered neural network is given by:

$$o = g\left(\sum_k w_k \cdot g\left(\sum_j w_{jk} \cdot x_j + \beta_k\right)\right) \tag{7.1}$$

where j iterates over the input nodes and k iterates over the hidden nodes. w_{jk} are the weights of the connections between the input nodes x_j and the hidden nodes. w_k are the weights of the connections between the hidden nodes and the output node. β_k are the weights of the connections between the bias node and the hidden nodes. g is a sigmoid function which is used as an activation function:

$$g(z) = \frac{2}{1 + e^{-z}} - 1 \tag{7.2}$$

The activation function is used to transform the input of each hidden and output node into the output. The usage of a sigmoid function is very common. It maps the interval $(-\infty, \infty)$ to the interval $[-1, 1]$, as shown in Fig. 7.2.

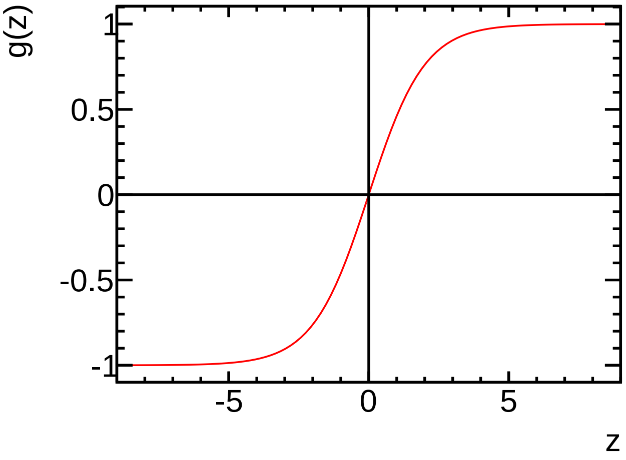

Figure 7.2: *The sigmoid function used as the activation function.*

The weights of the bias node β_k shift the activation function to the sensitive region around zero, which enhances the performance of the network.

Preprocessing of input variables

Neurobayes preprocesses the input variables before the training procedure starts. The preprocessing helps increasing the training speed by providing an appropriate starting point. First, all variables are equalised into a flat distribution between -1 and 1 by a non-linear transformation using the cumulative probability density of the input distribution. In each bin of the flat distribution, the signal purity is calculated. The purity distribution is then fitted with a spline curve. This procedure has the advantage of reducing the effect of statistical fluctuations. The fitted purity distribution is converted into a Gaussian with a mean of zero and a standard deviation of one. The usage of input variables in the same range is beneficial for numerical stability.

In the next step, a ranking of the input variables is performed. The importance of each variable is calculated as the loss in the total correlation to the training target occurring when removing it from the list of input variables. The target has a value of one for signal events and zero for background events. The ranking is done as follows [150]:

1. The correlation matrix of the input variables and the total correlation of input variables to the target is computed.
2. One variable is removed from the list of variables at a time and the total correlation to the target is recalculated each time.
3. Variables are sorted according to the loss in the total correlation to the target occurring by their exclusion.
4. The variable with the least importance is removed from the list of variables.

The steps $1-4$ are repeated using $k-1$, $k-2$,... variables until one variable is left in the list of variables, which is the one with the highest importance.

The additional significance of each variable is defined as the loss of correlation to the target calculated by the iterative procedure above multiplied by $\sqrt{n}$, where n is the sample size used for training.

In the final step, de-correlation of input variables is performed by calculating the covariance matrix of the transformed input variables. The covariance matrix is diagonalised using iterative Jacobian rotations. To transform the covariance matrix into a unit matrix, the rotated input vectors are divided by the square root of the corresponding eigenvalues [148].

Training procedure

The training of the neural network is achieved by iteratively adjusting the weights between the nodes. This procedure utilises a training sample that consists of 50 % simulated signal events ($t\bar{t}$) and 50 % background events ($Z$to$W$ data). The desired output of the neural network (the target value) is 1 for signal events and -1 for the background. In each training iteration, the deviation between the current output of the network and the desired output is minimised through minimising the loss function. The cross entropy function is employed as the loss function [148]:

$$E = \sum_i \log\left(\frac{1}{2}\left(1 + T_i \cdot o_i + \epsilon\right)\right) \tag{7.3}$$

where T_i is the target value of the output node for event i in the training sample, o_i is the network output and ϵ is a small regularisation constant added to prevent numerical issues. The value of ϵ is reduced in each iteration and becomes zero after a few iterations [148].

The gradient descent method is used for the minimisation process. The gradient of the training error is computed in order to first adjust the weights between the output node and the hidden nodes, and then the weights between the hidden and input nodes. This approach is called back-propagation algorithm, which was introduced in [151].

The network output o_i is scaled to the interval $[0, 1]$, which defines the network output as the purity P_i, the probability of event i to be signal-like:

$$P_i = \frac{o_i + 1}{2} \tag{7.4}$$

Over-training checks

Regularisation techniques are applied during training to enhance the performance of the network and prevent over-training. Those techniques are based on Bayesian statistics [149], which include pruning away connections of insignificant weights (i.e. setting them to zero). Over-training is a state in multivariate methods where the classifier has learned statistical fluctuations. It leads to a bias when applying the network to data. Neurobayes evaluates the performance of the training and checks for over-training during the procedure using part of the training sample as a test sample (20 %). The values of the loss function for training and test samples are shown in Figure 7.3 in each iteration. The existence of over-training increases the value of the loss function on the test sample for an iteration. As Figure 7.3 shows, the training is finished after 10 iterations since the value of the loss function becomes zero. Additionally, the values of the loss function for the test sample agree with the values for the training sample, which indicates that over-training did not take place.

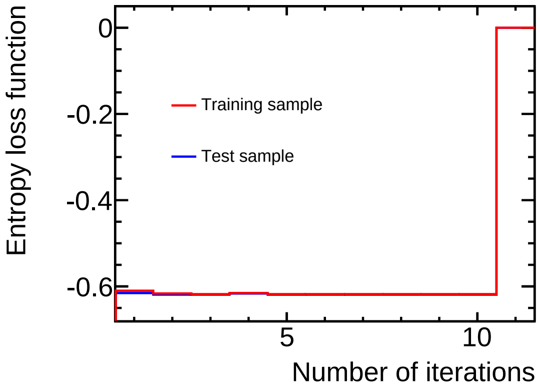

Figure 7.3: *Entropy loss function used during the training of the neural network. The training sample is shown in red, the test sample in blue.*

7.1.2 Input variables

Many variables were studied in terms of discrimination power between $t\bar{t}$ and W+jets and modelling using the $Z$to$W$ method. The studied variables are classified into categories: masses between final state objects, angular distances between final state objects, top-quark properties and global event properties. At the beginning, a large number of variables (≈ 30) were considered. Variables that provide a small additional separation power between the $t\bar{t}$ process and the W+jets process were excluded. Correlations between variables were studied using the preprocessing feature of the neurobayes package and only variables with small correlations to others were kept. The modelling of variables using the $Z$to$W$ method was checked as well. After this optimisation process, seven observables were chosen to be the inputs to the neural network:

1. The smallest invariant mass between jet pairs, m_{12}.
2. The second smallest invariant mass between jet pairs, m_{23}.
3. The smallest invariant mass between the charged lepton and a jet, $m_{\ell 1}$.
4. The mass of the reconstructed leptonically decaying top-quark, $m(l\nu b)$.
5. The mass of the reconstructed hadronically decaying top-quark, $m(bjj)$.
6. The cosine of the angle θ^*, which is between the momentum of the reconstructed hadronically decaying top-quark and the beam direction in the $t\bar{t}$ rest system, $\cos\theta^*$.
7. The aplanarity, A, which was defined in Eq. (6.7).

These input variables are classified into three categories: masses between final state objects (m_{12}, m_{23} and $m_{\ell 1}$), top-quark properties ($m(l\nu b)$, $m(bjj)$ and $\cos\theta^*$) and global event properties (aplanarity). Distributions normalised to unity (probability densities) of input variables are shown in Figs. 7.4 and 7.5 for SR1 and Figs. 7.6 and 7.7 for SR3, comparing distributions for simulated $t\bar{t}$ events and $Z$to$W$ data. These distributions show a good separation power between the $t\bar{t}$ process and the $Z$to$W$ data template used for the W+jets process.

As it can be seen in Figs. 7.4(d) and 7.6(d), the aplanarity distribution for $t\bar{t}$ events tend to be not planar due to the high mass of the $t\bar{t}$ system. The values of the aplanarity are higher for $t\bar{t}$ events compared to W+jets events. For the $\cos\theta^*$ (Figs. 7.4(b) and 7.6(b)), the normalised distribution show differences for $t\bar{t}$ and W+jets events. The distribution for $t\bar{t}$ events is flat, since in the $t\bar{t}$ rest frame, the probability for the decay is equal in all directions. The distributions of the $m(l\nu b)$ (Figs. 7.4(c) and 7.6(c)) and the $m(bjj)$ (Figs. 7.5(a) and 7.7(a)) for $t\bar{t}$ events peak between $140 - 180\,\text{GeV}$, which is close to the top-quark mass. It does not show a sharp peak around the top-quark mass due to the wrong assignment of the top-quark decay products in the reconstruction of the $t\bar{t}$ system for some events. Thus, the top-quark mass distributions for $t\bar{t}$ events are less broad than

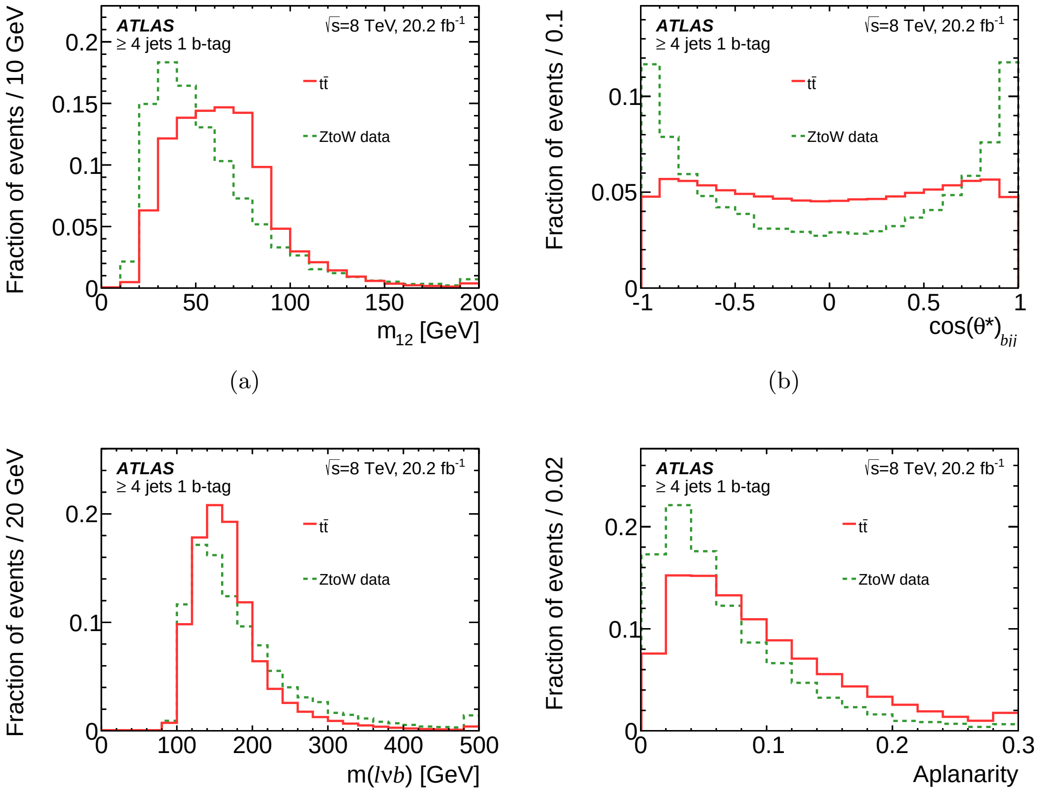

(a) (b)

(c) (d)

Figure 7.4: *Probability densities of four input variables to the neural network for the simulated $t\bar{t}$ signal process and the W+jets background process derived from data using converted Z+jets events ($ZtoW$ data). The distributions are shown for SR1: (a) smallest invariant mass between jet pairs, (b) cosine of the angle between the hadronic-top-quark momentum and the beam direction in the $t\bar{t}$ rest frame, (c) mass of the reconstructed leptonically decaying top-quark, and (d) aplanarity. Events beyond the x-axis range are included in the last bin.*

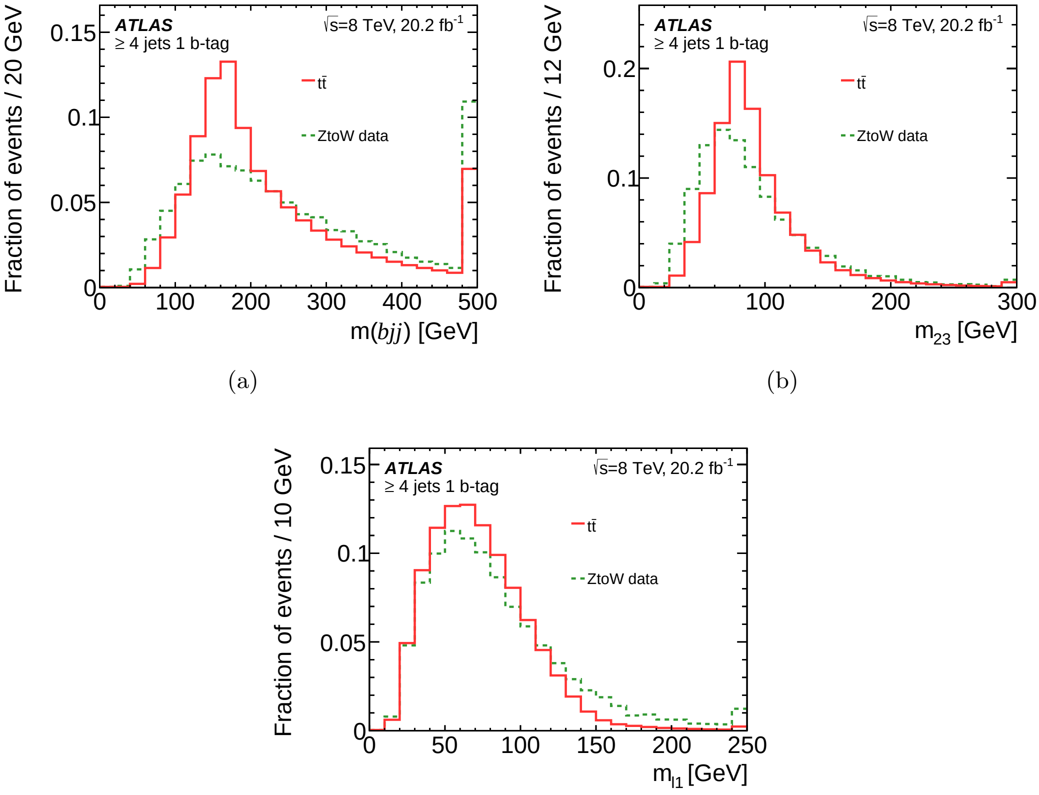

(a)

(b)

(c)

Figure 7.5: *Probability densities of three input variables to the neural network for the simulated $t\bar{t}$ signal process and the W+jets background process derived from data using converted Z+jets events (ZtoW data). The distributions are shown for SR1: (a) mass of the reconstructed hadronically decaying top-quark, (b) second smallest invariant mass between jet pairs, and (c) smallest invariant mass between the charged lepton and a jet. Events beyond the x-axis range are included in the last bin.*

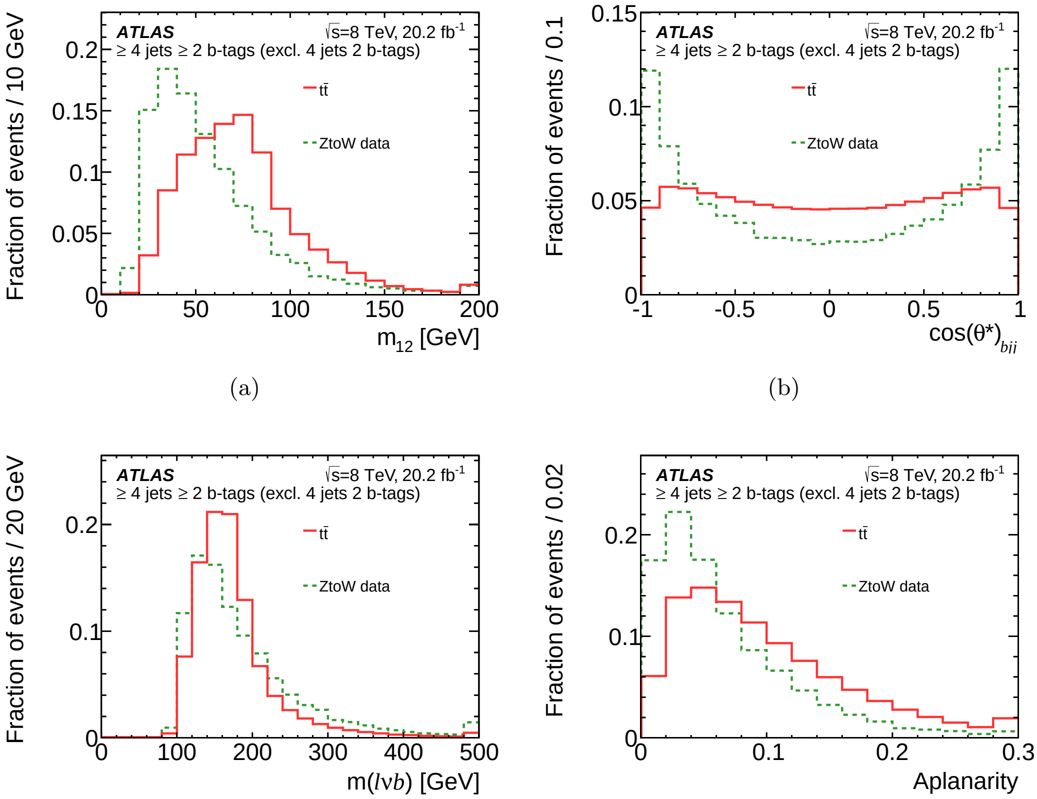

(a) (b)

(c) (d)

Figure 7.6: *Probability densities of four input variables to the neural network for the simulated $t\bar{t}$ signal process and the W+jets background process derived from data using converted Z+jets events ($ZtoW$ data). The distributions are shown for SR3: (a) smallest invariant mass between jet pairs, (b) cosine of the angle between the hadronic-top-quark momentum and the beam direction in the $t\bar{t}$ rest frame, (c) mass of the reconstructed leptonically decaying top-quark, and (d) aplanarity. Events beyond the x-axis range are included in the last bin.*

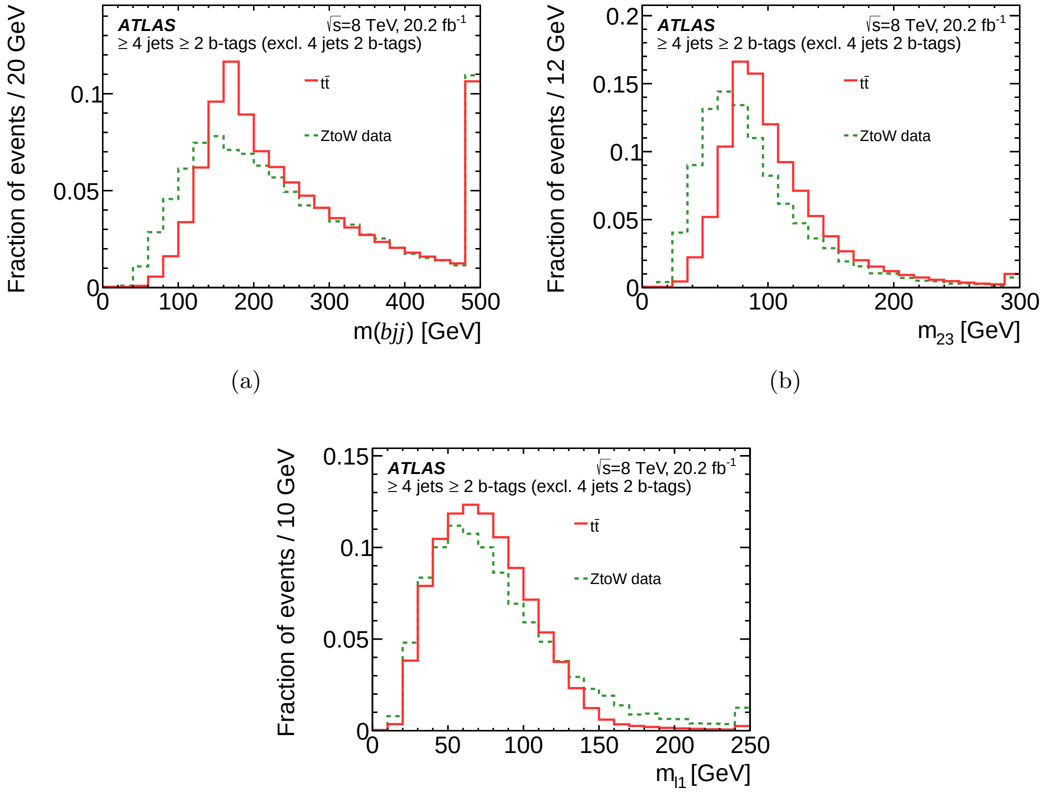

(a)

(b)

(c)

Figure 7.7: *Probability densities of three input variables to the neural network for the simulated $t\bar{t}$ signal process and the W+jets background process derived from data using converted Z+jets events (ZtoW data). The distributions are shown for SR3: (a) mass of the reconstructed hadronically decaying top-quark, (b) second smallest invariant mass between jet pairs, and (c) smallest invariant mass between the charged lepton and a jet. Events beyond the x-axis range are included in the last bin.*

those for W+jets events. The m_{12}, m_{23} and $m_{\ell 1}$ distributions shown in Figs. 7.4(a) and 7.6(a), Figs. 7.5(b) and 7.7(b) and Figs. 7.5(c) and 7.7(c) respectively, are chosen as input variables because they are Lorentz-invariant. For $t\bar{t}$ events, m_{12} and m_{23} peak around 80 GeV, which corresponds to the mass of the W boson. This happens in events where the two jets are coming from the hadronic decay of a W boson. As expected, the mass distributions have higher values for $t\bar{t}$ events compared to W+jets events.

Correlation and significance of input variables

The correlation matrix between input variables is shown in Figure 7.8. The highest correlations exist between the smallest invariant mass between jet pairs (m_{12}) and the second smallest invariant mass between jet pairs (m_{23}). Nevertheless, correlations of input variables are small (< 0.5). Table 7.1 shows the variables sorted by the loss of correlation to the target calculated by the iterative procedure and the additional significance. The most important variables are m_{12} and $\cos(\theta^*)$.

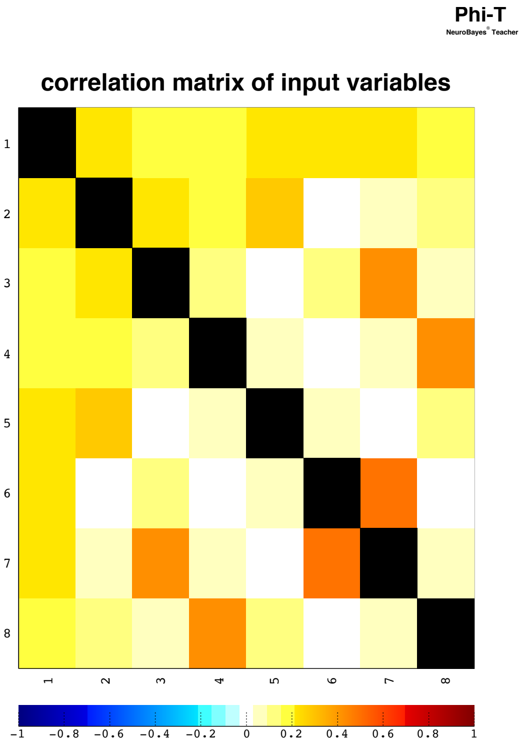

Figure 7.8: *Correlation matrix between the different input nodes / variables used in the network and their correlation to the target. 1. the target, 2. Aplanarity, 3. $m(bjj)$, 4. $m(l\nu b)$, 5. $\cos(\theta^*)$, 6. m_{12}, 7. m_{23}, 8. $m_{\ell 1}$.*

Table 7.1: *The seven variables used in the training of the neural network ordered by their importance. The correlation loss of each variable is the loss of correlation to the target calculated by the iterative procedure described in the previous section. The additional significance is the correlation loss multiplied by* $\sqrt{n}$.

Variable	Corr. loss	Add. significance
m_{12}	25.8 %	57.8
$\cos(\theta^{*})$	23.5 %	52.7
$m(l\nu b)$	18.5 %	41.4
Aplanarity	15.4 %	34.4
$m(bjj)$	10.7 %	23.8
$m_{\ell 1}$	7.0 %	15.7
m_{23}	4.1 %	9.2

The neural network output

The normalised neural network output distributions are shown in Fig. 7.9 for the signal process and the $Z$to$W$ data process in SR1 and SR3. A good discriminating power is observed between the $t\bar{t}$ and the $Z$to$W$ distributions. Bins close to one are dominated by signal events, while bins close to zero contain higher fraction of background events.

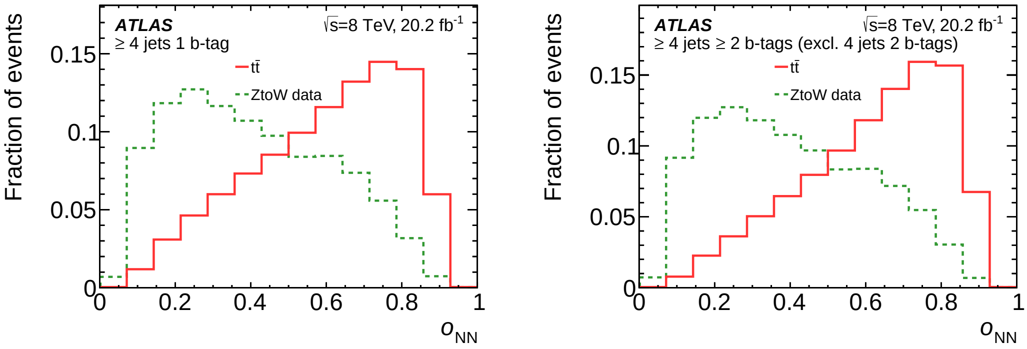

(a) (b)

Figure 7.9: *Probability densities of the neural-network discriminant* o_{NN} *for the simulated* $t\bar{t}$ *signal process and the* W*+jets background process derived from data using converted* Z*+jets events (*$Z$to$W$ *data) (a) for SR1 and (b) for SR3.*

Neural network variables in the validation region

Distributions of the input variables and the neural network output in the validation region ($\geqslant 4$ jets and pre-tag) are shown in Figs. 7.10 and 7.11 for the electron channel and in Figs. 7.12 and 7.13 for the muon channel. Since there is no b tagging requirement, this region is enriched with W+jets events and is used to check the modelling of these variables for this main background. The signal and background processes are normalised to the result of the maximum-likelihood fit presented in Table 5.5. It can be seen that the distributions are well modelled. The ratio of the observed to the predicted number of events is shown in the lower histogram for each plot. The ratio is within the uncertainties in most bins for all plots. Uncertainties include the normalisation uncertainty for all processes as well as the statistical uncertainty.

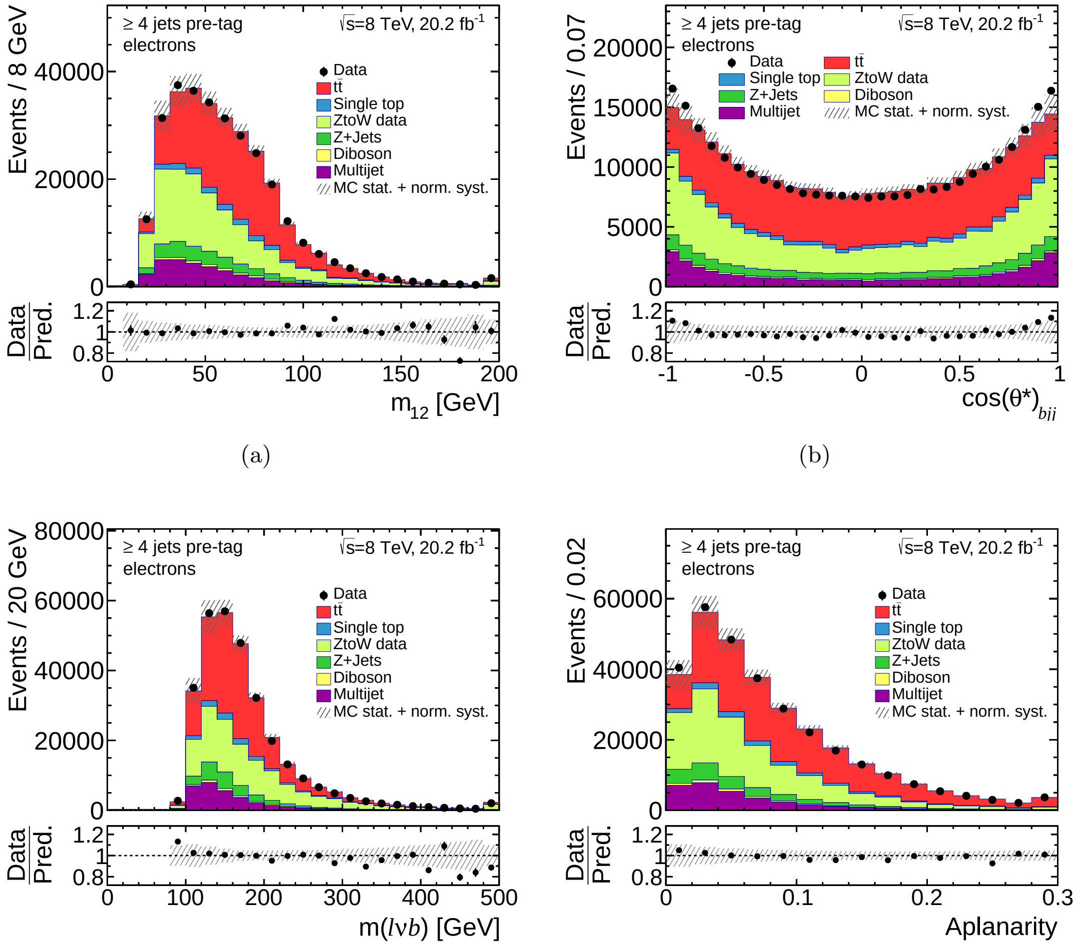

(a)

(b)

(c)

(d)

Figure 7.10: *Distributions of four neural network input variables in the W+jets validation region for the electron channel. The signal and backgrounds are normalised to the result of the maximum-likelihood fit presented in Table 5.5. The hatched error bands represent the normalisation uncertainty for all processes as well as the statistical uncertainty. The ratio of the observed to the predicted (Pred.) number of events in each bin is shown in the lower histogram. Events beyond the x-axis range are included in the last bin.*

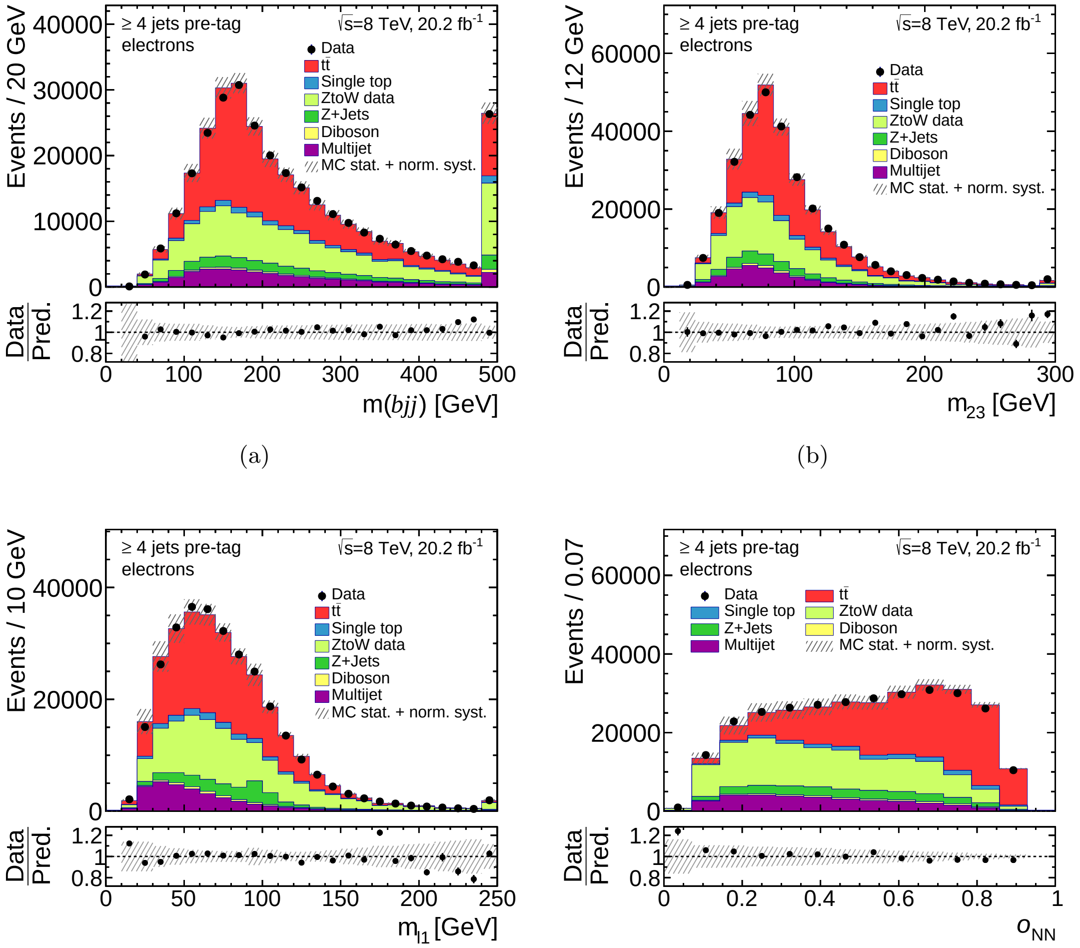

(a) (b)

(c) (d)

Figure 7.11: *Distributions of three neural network input variables and the neural network output in the W+jets validation region for the electron channel. The signal and backgrounds are normalised to the result of the maximum-likelihood fit presented in Table 5.5. The hatched error bands represent the normalisation uncertainty for all processes as well as the statistical uncertainty. The ratio of the observed to the predicted (Pred.) number of events in each bin is shown in the lower histogram. Events beyond the x-axis range are included in the last bin.*

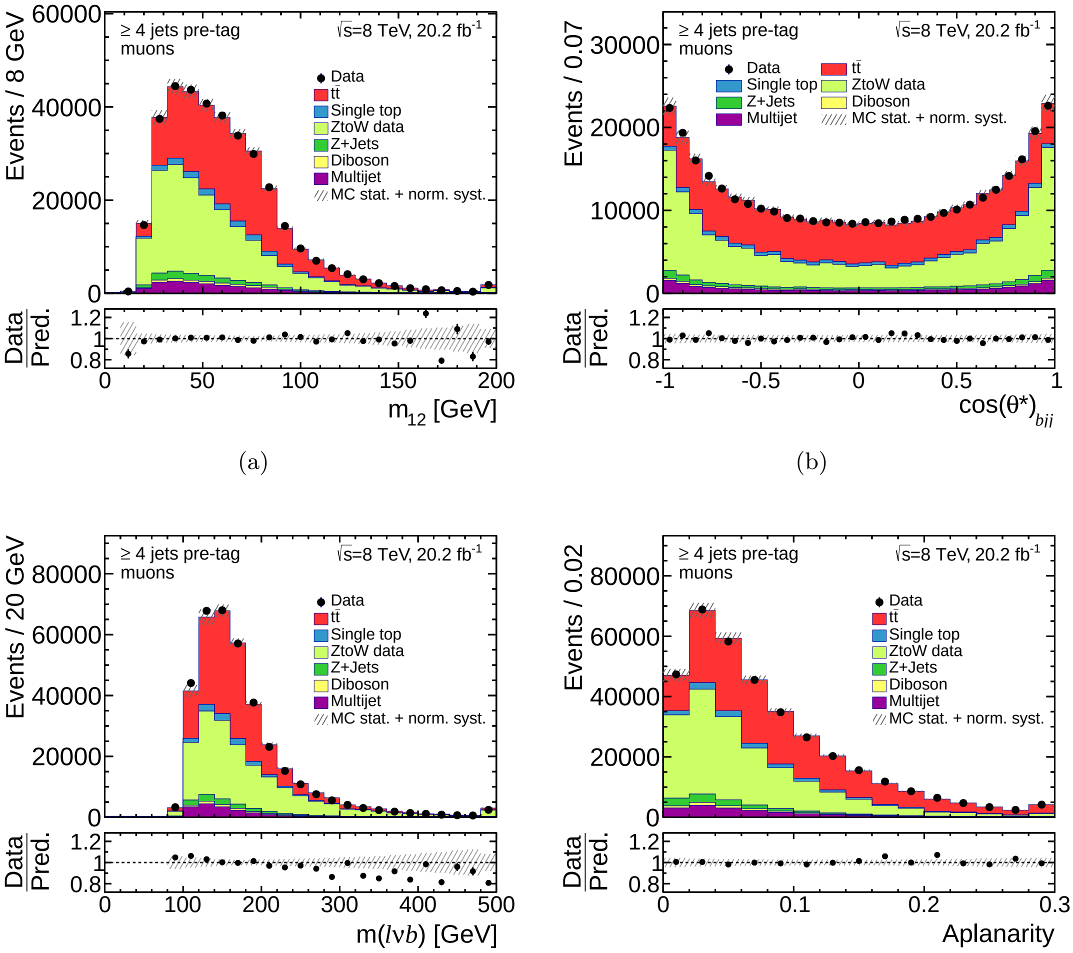

(a) (b)

(c) (d)

Figure 7.12: *Distributions of four neural network input variables in the W+jets validation region for the muon channel. The signal and backgrounds are normalised to the result of the maximum-likelihood fit presented in Table 5.5. The hatched error bands represent the normalisation uncertainty for all process as well as the statistical uncertainty. The ratio of the observed to the predicted (Pred.) number of events in each bin is shown in the lower histogram. Events beyond the x-axis range are included in the last bin.*

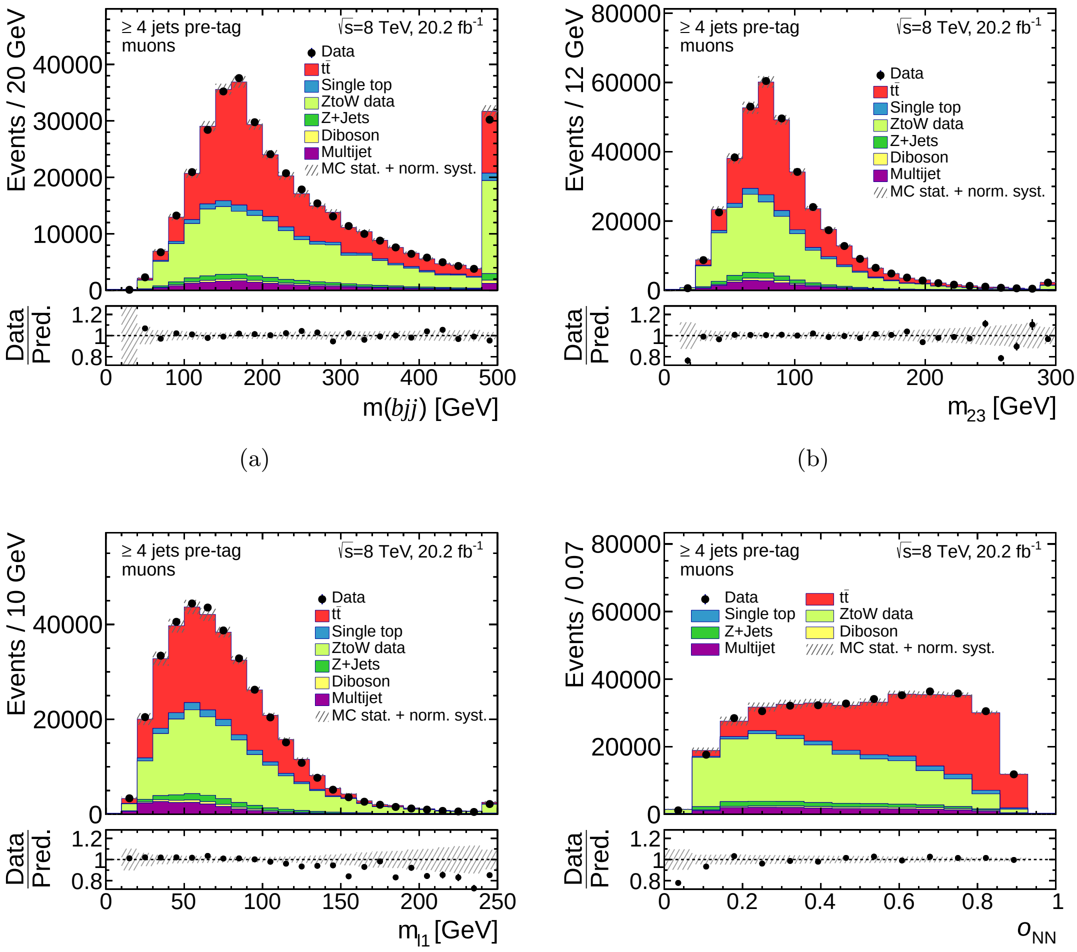

(a) (b)

(c) (d)

Figure 7.13: *Distributions of three neural network input variables and the neural network output in the W+jets validation region for the muon channel. The signal and backgrounds are normalised to the result of the maximum-likelihood fit presented in Table 5.5. The hatched error bands represent the normalisation uncertainty for all process as well as the statistical uncertainty. The ratio of the observed to the predicted (Pred.) number of events in each bin is shown in the lower histogram. Events beyond the x-axis range are included in the last bin.*

7.2 The reconstructed mass of the hadronically decaying W boson

The reconstructed mass of the hadronically decaying W boson is already used in some top mass measurements to reduce the impact of the jet energy scale uncertainty (JES) on the measurement [152–155]. For the same reason, the $m(jj)$ distribution is utilised in this analysis as the discriminating observable in SR2. The reconstruction of the W boson in SR2 is simple because of the b-tagging requirement of two of the four jets in this signal region. It implies that the two light jets in the event are coming from the the two light-quark partons, which are the decay products of the W boson.

A parton-level study is performed to check the association of the light jets to the light-quark partons, where the light-quark partons from the W-boson decay are associated to the untagged jets by requiring $\Delta R < 0.4$ between the parton and the jet. Fig. 7.14 shows distributions of events, where zero, one, or two partons are matched to the untagged jets. In case of two jets matched to the light-quark partons, the peak of the distribution is located around 80 GeV, which corresponds to the mass of the W boson. In case of only one or zero jets matched to the light-quark partons, a flat distribution is observed.

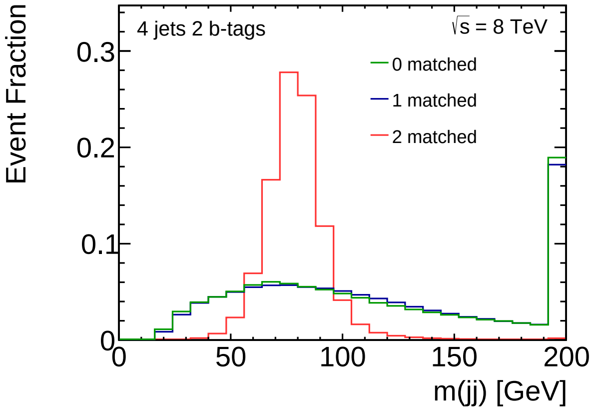

Figure 7.14: *$m(jj)$ of truth matched jets. The distribution is shown for the cases of two, only one, or none of the jets matched to the partons from the W boson decay.*

Table 7.2 lists the fraction of events, where two, one or zero partons are matched to the untagged jets. About 62 % of the events have the two partons matched to the untagged jets. In 25 % of the events, only one of the partons is matched to one of the untagged jets used to reconstruct $m(jj)$.

The dependence of $m(jj)$ on the JES is studied by producing $t\bar{t}$ simulated samples with the jet energy scaled by a constant scale factor of ±2 % and ±4 %. Fig. 7.15(a) shows the peak of the $m(jj)$ distribution for the $t\bar{t}$ signal process for three different values of the scale

Table 7.2: *The fraction of events, where two, one or zero partons are matched to the untagged jets.*

Number of partons	Fraction of events
0	12.4 %
1	25.1 %
2	62.5 %

factors. As expected, a shift of the peak of the $m(jj)$ distribution for different scale factors is observed. The mean values of a Gaussian distribution fitted to the $m(jj)$ distributions show a linear dependence on the scale factors (JSF) as shown in Fig. 7.15(b). A comparison of the mean values of a Gaussian distribution fitted to the $m(jj)$ distribution in the range of 60 GeV $< m(jj) <$ 100 GeV for different generator set-ups is presented in Fig. 7.16. It can be seen that the mean value is consistent for the different event generators, but varies for different settings of the parameters controlling the initial- and final-state radiation.

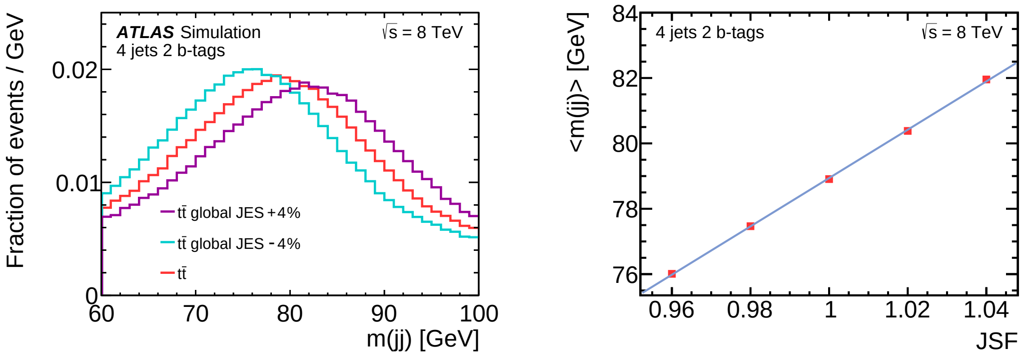

(a) (b)

Figure 7.15: *(a) Probability densities for the $t\bar{t}$ signal process of the $m(jj)$ distribution for three different values of the JES, where events beyond the x-axis range are not shown and the range is restricted to show the peak. (b) Mean value of a fit to the $m(jj)$ distribution using a Gaussian distribution for different JSF values. The uncertainties shown are statistical only.*

Given the linearity of the peak position of the $m(jj)$ distribution with the JSF and the independence of the peak position with respect to different event generators, the $m(jj)$ is suitable to constrain the uncertainty in the JES and the amount of initial- and final-state radiation.

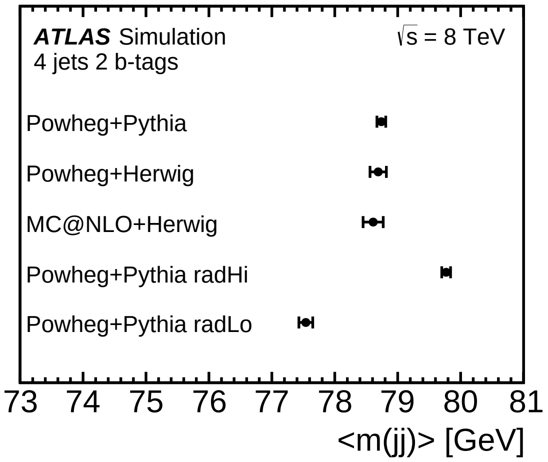

Figure 7.16: *Mean value of a fit to the $m(jj)$ distribution using a Gaussian distribution for different signal generator setups. The uncertainties shown are statistical only.*

8

Sources of systematic uncertainties

Systematic uncertainties are uncertainties related to the acceptance of the detector, the reconstruction of measured signals and imperfection of the models used to describe the data. Many sources of systematic uncertainties affect the $t\bar{t}$ cross-section measurement. Some occur from the measurement of detector signals and the reconstruction of physics objects, others are associated with the modelling of the signal and background processes. The estimation of the systematic uncertainties includes the effect on both the yields of the physics processes and the effect on the shapes of distributions used as discriminating observables in this analysis. The sources of systematic uncertainties can be grouped in these categories: physics objects modelling, signal modelling, and background modelling and normalisation. In addition, the uncertainty in the luminosity determination is considered.

8.1 Physics objects modelling

Uncertainties in this category come from the modelling of reconstructed physics objects, i.e. electrons, muons, jets and $E_{\mathrm{T}}^{\mathrm{miss}}$. In order to obtain correction factors, kinematic distributions of these objects from simulation are scaled to match those distributions in data. Uncertainties on the derived correction factors are taken into account in addition to residual differences between data and simulation.

8.1.1 Charged leptons: electrons and muons

The lepton trigger, identification and reconstruction efficiencies in simulation are different than in observed data. Correction factors have been derived to correct these differences as explained briefly in Sect. 4.2 and Sect. 4.3. The uncertainties on the corrections are evaluated by applying a variation of one standard deviation ($\pm 1\sigma$) to these correction factors [110, 112]. Uncertainties in the electron energy scale and the muon momentum scale are also estimated by scaling the energy or momentum of the lepton by $\pm 1\sigma$. For the electron energy resolution and the muon momentum resolution, the uncertainties are estimated by smearing the energy according to a Gaussian distribution with a width of one standard deviation.

8.1.2 Jets

In the reconstruction of jets and the calibration of their energies, systematic uncertainties arise. These uncertainties are in the jet energy scale (JES), the jet energy resolution (JER) and the jet reconstruction efficiency.

Jet energy scale

A major source of systematic uncertainty in this analysis is the JES. It comes from the uncertainties in the jet energy calibrations mentioned in Sect. 4.4. The JES uncertainty is derived using information from test-beam data, collision data and simulation [125]. It is obtained as a function of the jet p_{T} and η and split into 25 components considered separately. These components originate from different sources of uncertainties related to the different stages of calibration and are divided into several categories. Some arise in the in situ measurements performed on data using the Z+jets, γ+jets and multijet p_{T}-balance methods. Other categories originate in the pile-up correction, the jet energy and η calibration from simulation or the global sequential correction stage.

Fig. 8.1 shows the total JES uncertainty for simulated dijet events as a function of the jet p_{T} and η. The absolute in situ JES refers to the uncertainty coming from the $V+$jets and multijet measurements. The relative in situ JES refers to the uncertainty arising from the dijet η-intercalibration. Furthermore, the flavour composition and response uncertainties are shown, where the gluon fraction is determined from simulation and the uncertainty in the gluon fraction is evaluated by comparing different event generators. The pileup and punch-through uncertainties are also shown. The total JES uncertainty is about 3.5 % for central jets with $p_{\mathrm{T}} = 25\,\mathrm{GeV}$ and it drops to about 2.5 % for jets with $p_{\mathrm{T}} = 40\,\mathrm{GeV}$ and 1.5 % for jets with $p_{\mathrm{T}} = 100\,\mathrm{GeV}$. The bulk of events selected in this analysis contains jets in the p_{T} region of 40 GeV to 100 GeV. As visible in Fig. 8.1(b), the JES uncertainty is almost flat (2.5 % to 3 %) for jets with $p_{\mathrm{T}} = 40\,\mathrm{GeV}$ and $|\eta| < 2.5$.

The different categories of the JES uncertainty are explained here [122]:

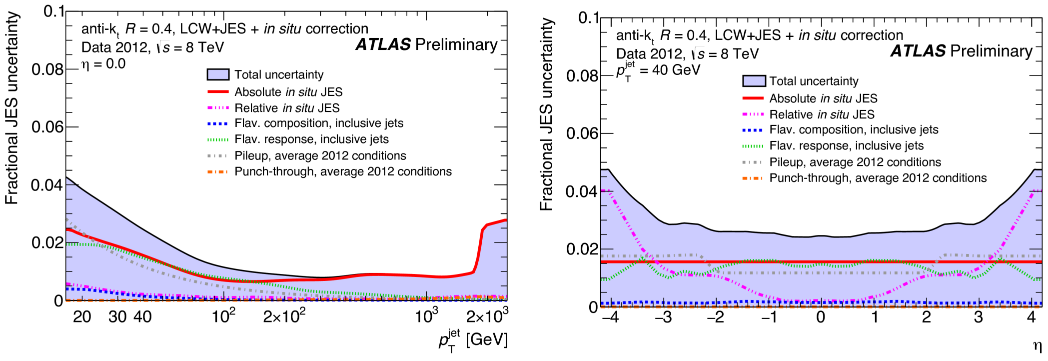

(a) (b)

Figure 8.1: *The total JES uncertainty (a) as a function of p_T for central jets and (b) as a function of $|\eta|$ for jets with $p_T = 40\,\text{GeV}$ for simulated dijet events. The quark/gluon fraction is determined from simulation and the uncertainty is evaluated using comparisons between event generators [122].*

In situ measurements:

- η-intercalibration: In the dijet method [156], dijet events are employed to apply an η-intercalibration in which the average p_T for forward jets ($0.8 < |\eta| < 4.5$) is equalised to the p_T of balancing jets in the central region ($|\eta| < 0.8$). Uncertainties due to physics modelling and additional radiations are taken into account by comparing the event generators, Sherpa and Powheg + Pythia8.

- Detector: An uncertainty arises from the electron and photon energy scale and smearing, and from the muon energy scale and muon momentum smearing in the in situ measurements. Additionally, the uncertainty in the sample purity in γ+jets events is considered.

- Physics modelling: An uncertainty arises from differences between event generators, in the modelling of particles outside the jet cone and variations in the sub-leading jet veto in the Z+jets and γ+jets methods [157]. Additionally, uncertainties in the extrapolation in $\Delta\phi$ between the jet and the Z boson in the Z+jets method and the asymmetry selection between the leading and sub-leading jet in the multijet balance method are taken into account.

- Mixed detector and modelling: Uncertainties due to the choice of the JVF cut in the Z+jets balance method, differences between event generators in the jet fragmentation and the jet p_T threshold in the multijet balance method are considered.

- Statistical: An uncertainty arises from the limited size of datasets used in the in situ calibrations.

Pile-up: An uncertainty arises from the pile-up subtraction and suppression method used for jets [123]. The uncertainty is in the $\langle \mu \rangle$ and N_{PV} dependence of the reconstructed jet p_{T}, where $\langle \mu \rangle$ is the mean number of inelastic pp interactions per bunch crossing and N_{PV} is the total number of reconstructed primary vertices with two or more tracks. In addition, there is an uncertainty in the p_{T} dependence and potential mis-modelling by the use of the median p_{T} density, ρ, for pile-up subtraction.

Flavour composition and response: Uncertainties due to differences in the fraction of jets initiated by quarks versus gluons between the signal events and events used in the calibrations are considered. The calorimeter response to gluon-induced jets was found to be different for different shower generators, due to the differences in the jet fragmentation. In this analysis, the actual fraction of gluon-induced jets is estimated and used as input to the estimation of the uncertainty for signal events in the three signal regions separately. The procedure starts with matching jets at detector-level to truth jets at particle-level by requiring $\Delta R < 0.3$. Then, the truth jet is matched to the highest-energetic parton-level particle within a distance of $\Delta R < 0.4$. The flavour of the matched parton-level particle is used to calculate the gluon fraction f_g as a function of p_T and η of the reconstructed jet. The gluon fraction f_g is defined as follows:

$$f_g = \frac{N_g^{\mathrm{jets}}}{N_g^{\mathrm{jets}} + N_{\mathrm{light\ quarks}}^{\mathrm{jets}} + N_{\mathrm{c\text{-}quarks}}^{\mathrm{jets}}} \tag{8.1}$$

where N_g^{jets} is the number of gluon-induced jets, $N_{\mathrm{light\ quarks}}^{\mathrm{jets}}$ is the number of jets initiated by light-quarks and $N_{\mathrm{c\text{-}quarks}}^{\mathrm{jets}}$ is the number of jet initiated by c-quarks. The jets initiated by b-quarks are excluded from the definition.

The uncertainty in f_g is estimated by using different $t\bar{t}$ samples. For the matrix element generator, the absolute difference of f_g obtained with MC@NLO + HERWIG and POWHEG + HERWIG is used. The absolute difference in f_g between samples generated with POWHEG + HERWIG and POWHEG + PYTHIA is considered to account for the uncertainty due to the parton shower and hadronisation. For the scale variations, half of the absolute difference of f_g obtained with POWHEG + PYTHIA radHi and POWHEG + PYTHIA radLo is considered. The total uncertainty in f_g is estimated as the quadratic sum of the three effects.

Fig. 8.2 shows the gluon fraction as a function of the p_{T} of the jets for events with different jet multiplicities in the three signal regions. The dependence of the gluon fraction on the number of jets is visible. Fig. 8.3 shows the gluon fraction and the uncertainty in the gluon fraction as a function of p_{T} and η of the jets for the three signal regions. As shown in the figures, the fraction of gluon-induced jets is found to be between 15 ± 10% and 30 ± 20% depending on the p_{T} and η of the jet. Since it is irrelevant for backgrounds, an unknown flavour composition of 50 ± 50% is assumed.

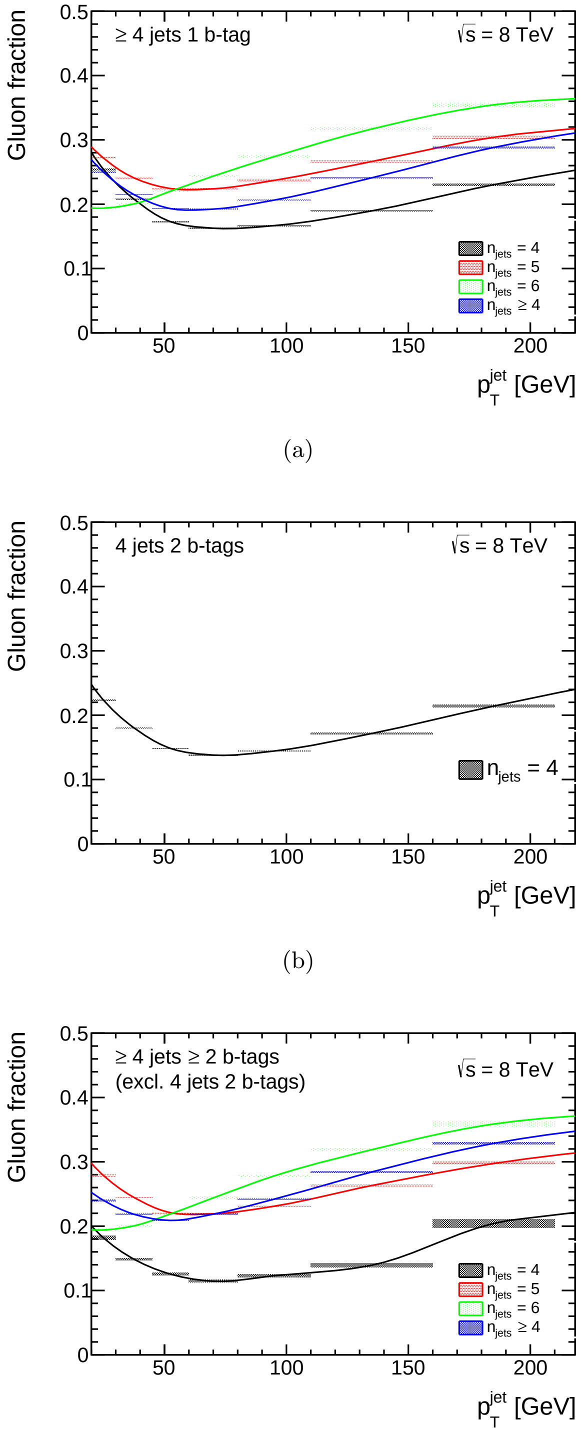

(a)

(b)

(c)

Figure 8.2: *The gluon fraction as a function of jet p_T for events with different jet multiplicities in (a) SR1, (b) SR2 and (c) SR3.*

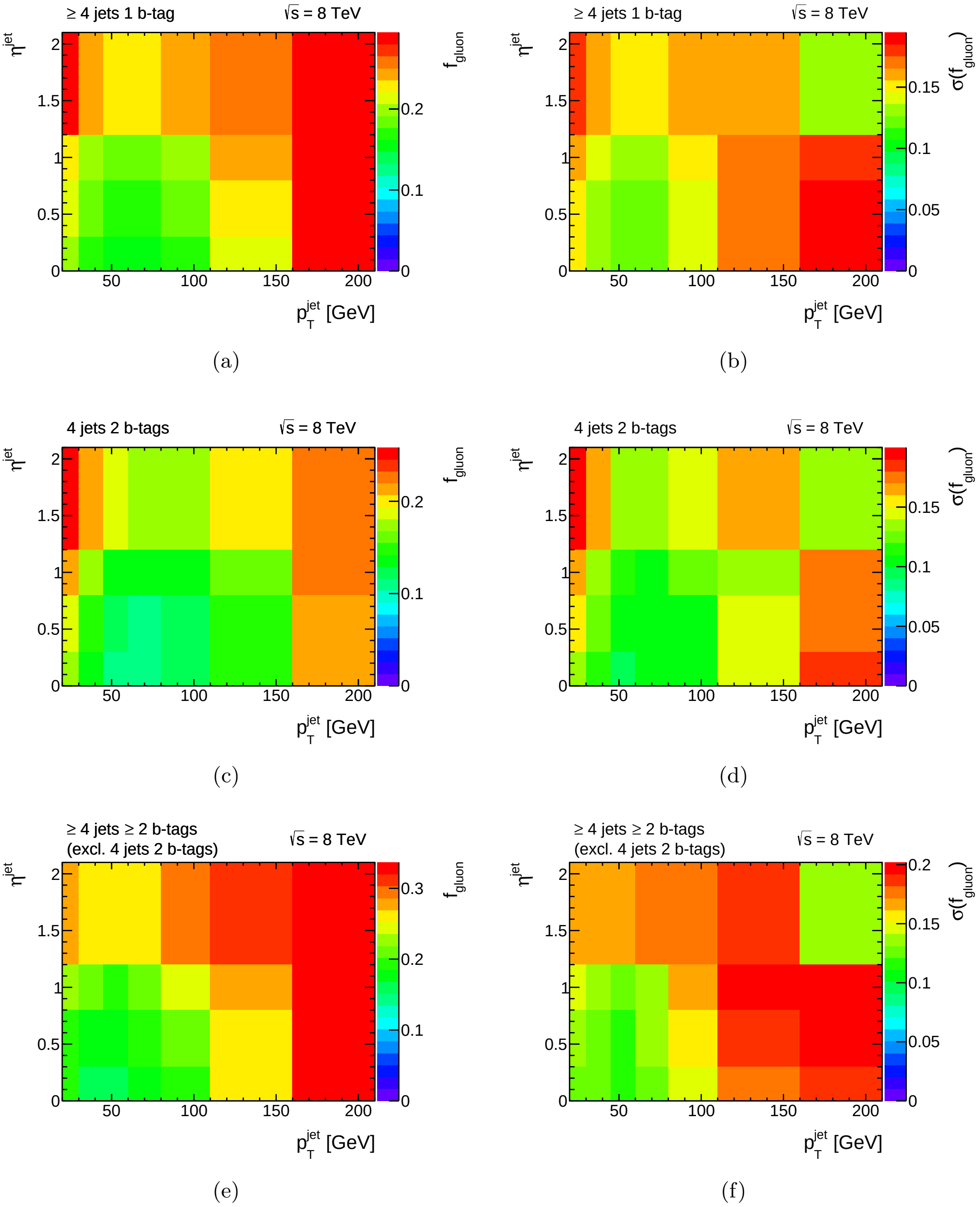

(a) (b) (c) (d) (e) (f)

Figure 8.3: *(left) The gluon fraction as function of p_T and η of the jets for (a) SR1, (c) SR2 and (e) SR3. (right) The uncertainty on the gluon fraction as a function of p_T and η for (b) SR1, (d) SR2 and (f) SR3.*

b-jet energy scale: An uncertainty arises from the calorimeter response to b-jets, which is estimated using a combination of different simulations.

Punch-through: An uncertainty arises from the calorimeter response to high p_T jets, whose energy is not fully contained within the jet. The calorimeter response to such jets is correlated with the amount of activity in the muon spectrometer. Corrections for these jets are derived in the global sequential correction stage.

Jet energy resolution

An additional smaller source of uncertainty besides the JES is the jet energy resolution (JER). To measure the resolution, the width of the p_T distribution of events where a jet recoils off a Z/γ boson and of dijet events is used [122].

Jet reconstruction efficiency

The jet reconstruction efficiency is studied using dijet events. It is measured by matching calorimeter jets to track jets, where the matching efficiency is found to be consistent between data and simulation [158]. Hence, the uncertainty in the jet reconstruction efficiency is negligible in this measurement.

Flavour tagging efficiency of jets

As mentioned in Sect. 4.5, the b-taggging efficiency and the mis-tag rate of c-jets and light-jets are calibrated by deriving correction factors from data to correct the efficiencies in simulated events [130, 131]. The uncertainties in these correction factors are taken into account and propagated to the analysis. The corrections for b-jets are derived using $t\bar{t}$ events in the dilepton channel and dijet events. Uncertainties in the b-jets calibration have the highest impact on this analysis compared to those of light-jets and c-jets calibrations. The main systematic uncertainties in the b-jets calibration are related to the modelling of the signal and background processes. In addition, uncertainties due to physics objects modelling are considered. All uncertainties are summed in quadrature to obtain the final uncertainty in the b-jets calibration.

8.1.3 Missing transverse momentum

As explained in Sect. 4.6, the E_T^{miss} is reconstructed using calibrated physics objects, i.e. electrons, photons, hadronically decaying taus, jets and muons. The uncertainties in the energy scale and momentum resolution of these objects are propagated to the E_T^{miss}.

Additionally, the uncertainty from the soft term is taken into account, which includes effects from pileup and the impact of the generator and underlying-event modelling [133].

8.2 Signal modelling

Uncertainties in the modelling of the signal process ($t\bar{t}$) are considered, which include uncertainties coming from the choice of the event generator, parton shower and hadronisation models and scale variations. These uncertainties are estimated by changing the event generators for the signal process or changing parameters in the nominal event generator. In addition, systematic uncertainties related to the parton distribution function (PDF) set are taken into account. Variations of shapes of discriminating observables due to the signal modelling uncertainties are given in App. B.

8.2.1 NLO matrix element

This systematic uncertainty accounts for the choice of the matrix element generator and the matching to the parton shower. It is estimated by comparing events generated using the POWHEG event generator interfaced to HERWIG with events generated by the MC@NLO event generator showered with the same parton shower generator HERWIG.

8.2.2 Parton shower and hadronisation

For the parton shower modelling, hadronisation effects and underlying-event, predictions from PYTHIA and HERWIG are compared. The uncertainty is estimated by comparing events generated using the matrix element generator POWHEG and showered by PYTHIA or interfaced to HERWIG.

8.2.3 Scale variations

This uncertainty is estimated by varying the renormalisation and factorisation scales in the matrix element simultaneously with the scales in the parton shower. The nominal sample POWHEG + PYTHIA is used, with two variations of the tuning parameters: a variation of the renormalisation and factorisation scales by a factor of 2 together with the Perugia2012radLo parameters in the parton shower. In the second variation, the scales are varied by a factor of 0.5 together with the Perugia2012radHi parameters [92] and the h_{damp} parameter is set to twice the top-quark mass [159]. These two variations are compared and half of the full difference is considered as the uncertainty.

8.2.4 Parton distribution functions

A specific PDF set is used in the generation of the simulated samples. Each PDF set provides a central value and an error set of uncertainty eigenvectors. The evaluation of the uncertainty is performed according to the recommendation of the PDF4LHC group [160] using the PDF4LHC15 PDF set, which is a combination of the CT14 [161], MMHT14 [162] and NNPDF3.0 [38] PDF sets. The $t\bar{t}$ simulated sample generated with MC@NLO + Herwig is used, where events are re-weighted using the PDF4LHC15 PDF set central value and the 30 eigenvectors of the error sets. In calculating a new weight w, the partonic momentum fraction x_1 and x_2, the energy scale of the interaction Q^2 and the incoming parton flavours f_1 and f_2 are needed:

$$w = \frac{\mathrm{V}_2(x_1, Q^2, f_1) \cdot \mathrm{V}_2(x_2, Q^2, f_2)}{\mathrm{V}_1(x_1, Q^2, f_1) \cdot \mathrm{V}_1(x_2, Q^2, f_2)}$$

where V_2 stands for the value of the PDF using the central value of the PDF4LHC15 PDF set or one of the uncertainty eigenvectors. V_1 refers to the value of the PDF according to the CT10 PDF set.

The uncertainty using the error eigenvectors of the PDF4LHC15 is referred to as the ‘intra’-PDF of the PDF4LHC15 PDF set. Additionally, the relative difference between the central value of the PDF4LHC15 PDF set and the central value of the CT10 PDF set is also considered. Since this uncertainty is higher than the ‘intra’-PDF uncertainty of the PDF4LHC15, it is taken as the final uncertainty.

For the inclusive measurement, the acceptance is determined for each signal region. For the fiducial measurement, both the selected events and the events passing the fiducial volume are re-weighted and the uncertainty is taken on $N_{\mathrm{sel}}/N_{\mathrm{fid}}$ for each signal region. The acceptance uncertainty is shown in Fig. 8.4, the figures on the left are for the inclusive measurement and the figures on the right are for the fiducial measurement. The ‘intra’-PDF uncertainty and the relative difference to the CT10 PDF set are given in Table 8.1 for each signal region. For the fiducial measurement, the acceptance uncertainty is much reduced since the PDF uncertainty is largest for events which are produced in the forward direction, i.e. one initial gluon has a high momentum fraction value x. The PDFs for high-x gluons have large uncertainties in all current PDF sets. Selecting events in the fiducial volume reduces the fraction of such events significantly and therefore the uncertainty is reduced significantly as well.

Shape uncertainties on the fitted distributions are considered by comparing the shapes of the distributions for the $t\bar{t}$ sample using the PDF4LHC15 PDF set and using the CT10 PDF set. Fig. 8.5 shows the shape uncertainty on the NN output distribution in SR1.

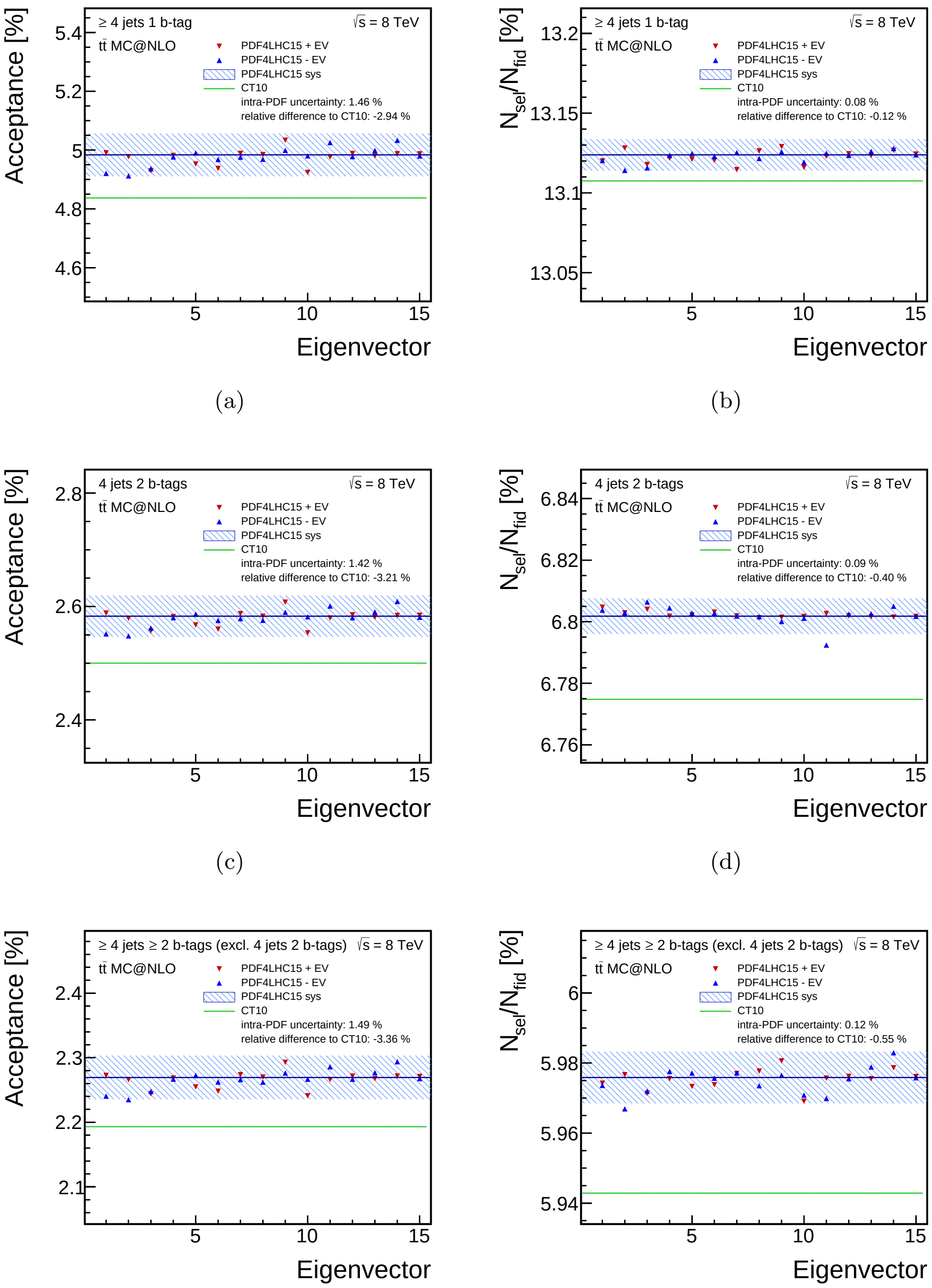

(a) (b)

(c) (d)

(e) (f)

Figure 8.4: *The acceptance (left)/ N_{sel}/N_{fid} (right), using the central value of the* CT10 *PDF set and the central value of the* PDF4LHC15 *PDF set and the corresponding uncertainty eigenvectors for (a)-(b) SR1 , (c)-(d) SR2 and (e)-(f) SR3.*

Table 8.1: *The PDF acceptance uncertainty in the three signal regions for the inclusive and the fiducial measurement.*

Signal region	‘intra’-PDF uncertainty	Relative difference to CT10 PDF set
	Inclusive	
SR1	1.5 %	−2.9 %
SR2	1.4 %	−3.2 %
SR3	1.5 %	−3.4 %
	Fiducial	
SR1	0.1 %	−0.1 %
SR2	0.1 %	−0.4 %
SR3	0.1 %	−0.6 %

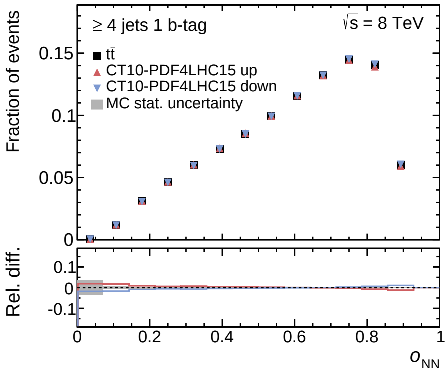

Figure 8.5: *The normalised shape variation of the* o_{NN} *distribution by comparing the* CT10 *PDF set and the* PDF4LHC15 *PDF set in SR1.*

8.3 Background modelling and normalisation

Uncertainties in this category include the background normalisation for non-fitted backgrounds, the modelling of the $Z$to$W$ data-driven method used to derive shapes for the W+jets background and the multijet background modelling and normalisation.

8.3.1 Background normalisation for non-fitted backgrounds

The normalisation uncertainties of the non-fitted background processes, i.e. single top-quark production, Z+jets and diboson, are estimated using the uncertainties on their theoretical cross-section predictions. For the Wt-, s- and t-channel processes, the predicted production cross-section is calculated with an uncertainty of 7.6 %, 4.2 % and 4.6 %, respectively, including uncertainties in the scales and the PDF. A normalisation uncertainty of 6 % is used for the single top-quark production process, which is calculated according to the individual uncertainties of the predicted cross-sections of the three processes. In the case of the Z+jets process, the uncertainty of the inclusive cross-section is 4 % including the contributions from the PDF and scale variations. For the diboson process, the total uncertainty of each of the three processes, WW, WZ and ZZ, is estimated to be 5 %. Additionally for both Z+jets and diboson, an uncertainty of 24 % per additional jet is added to the inclusive uncertainty in quadrature leading to a total uncertainty of 48 % for events with four jets. The normalisation uncertainties are summarized in Table 8.2.

Table 8.2: *Uncertainties in the normalisation of the non-fitted background processes.*

Process	Uncertainty
Single top	6 %
Z+jets, diboson	48 %

8.3.2 W+jets modelling

A data-driven method is employed to extract a shape for the W+jets background using Z+jets events as explained in Chapter 6. Although the production mode of Z-bosons and W-bosons is very similar, differences exist in the details of the production and decay. There are differences in heavy-flavour production and in the helicity structures of the decay vertices. These differences are taken into account by introducing a shape uncertainty, that is obtained by comparing the shapes of the discriminating observables in simulated W+jets events with those in simulated $Z$to$W$ events. The simulated $Z$to$W$ events are obtained using a simulated Z+jets sample and converting the events to $Z$to$W$ events according to the algorithm explained in Sect. 6.2. Fig. 8.6(a) shows the shape uncertainty in SR1, where the fraction of W+jets events is considerably larger than in the other two signal regions.

8.3.3 Multijet background modelling and normalisation

The multijet background estimate has an uncertainty of 67 % in SR1 obtained by comparing the rates with those given by the matrix method. Additionally, the difference in shapes to

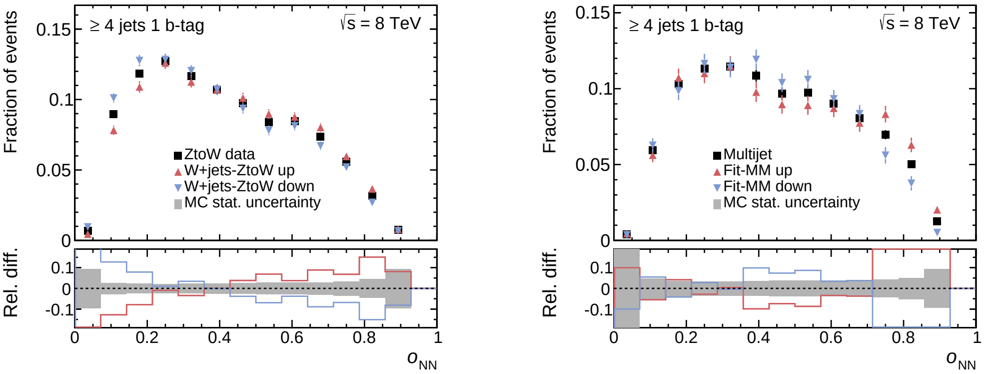

(a)

(b)

Figure 8.6: *(a) The normalised shape variation of the* o_{NN} *distribution by comparing simulated* Z*toW and* W*+jets in SR1. (b) The normalised shape variation of the* o_{NN} *distribution by comparing the fit method and the matrix method in SR1.*

the matrix method is added as a shape uncertainty, see Fig. 8.6(b). For SR2 and SR3, the multijet estimate is small, therefore 50 % uncertainty is assumed based on comparisons of the rates obtained using alternative methods in previous analyses [136].

8.4 Luminosity

The ATLAS luminosity scale for the 2012 LHC run has been calibrated using data from dedicated beam-separation scans, also known as van der Meer scans. The final uncertainty in the luminosity is 1.9 % [71].

The acceptance uncertainties in the three signal regions of physics objects modelling and signal modelling systematic sources are given in App. C.

9

Statistical analysis

This chapter explains the statistical details of the maximum-likelihood fit performed to extract the $t\bar{t}$ cross-section. In this procedure, parameters can be added in the likelihood fit to parameterise sources of systematic uncertainties. This approach, referred to as ‘profiling’, is followed here to constrain the effect of some uncertainties. Constraining systematic uncertainties using this method is only possible if there is sensitivity to measure them in the used observables, which will be discussed here as well.

The maximum-likelihood method is explained in Sect. 9.1. The procedure to evaluate the effect of the systematic uncertainties on the cross-section measurement is described in Sect. 9.2. Constraining the effect of some large uncertainties is explained in Sect. 9.3. Sect. 9.4 presents the extraction of the $t\bar{t}$ cross-section and the observed number of $t\bar{t}$ events, then the total and individual systematic uncertainties affecting this measurement are shown in Sect. 9.5.

9.1 Maximum likelihood method

A binned maximum-likelihood fit is done in three signal regions simultaneously. The fitted observables are the neural-network output-distribution, o_{NN}, in both SR1 and SR3 and the $m(jj)$ distribution in SR2. Free parameters in the fit procedure are:

- A scale factor for the $t\bar{t}$ process, $\beta_{t\bar{t}}$. This is the parameter of interest that is applied to the theoretical prediction of the $t\bar{t}$ cross-section to obtain the measured value of the cross-section.
- Two scale factors for the W+jets process, β_{W_1} and β_{W_2}. One scale factor is used for SR1, while the other is used for SR2 and SR3. Using two scale factors takes into

account the differences in the flavour composition for single-tagged events versus double-tagged events of this background.

- A nuisance parameter for the b-tagging-efficiency correction-factor, $\delta_{b-\text{tag}}$.
- A nuisance parameter for the JES correction factor, δ_{JES}. This parameter corresponds to the overall (global) JES, which is one parameter that combines all the JES components.

Here, the scale factor β_j for a process j describes the ratio of the measured cross-section to the predicted one:

$$\beta_j = \frac{\sigma_{\text{obs}}}{\sigma_{\text{pred}}},$$

and the correction factor δ_i for a systematic uncertainty i describes a factor of the a-priori one sigma systematic deviation.

The likelihood function is given by the product of the Poisson likelihoods for each bin of the o_{NN} and $m(jj)$ histograms times a Gaussian prior constraint on $\delta_{b-\text{tag}}$:

$$L(\beta_{t\bar{t}}, \beta_{W_1}, \beta_{W_2}, \delta_{b\text{-tag}}, \delta_{\text{JES}}) = \prod_{k=1}^{M} \mathcal{P}(n_k, \mu_k) \cdot \mathcal{G}(\delta_{b\text{-tag}}; 0, 1) \tag{9.1}$$

with

$$\begin{aligned} \mathcal{P}(n_k, \mu_k) &= \frac{\mathrm{e}^{-\mu_k} \cdot \mu_k^{n_k}}{n_k!}, \\ \mathcal{G}(\delta_{b\text{-tag}}; 0, 1) &= \frac{1}{\sqrt{2\pi}} \exp\left\{ -\frac{1}{2} \delta_{b\text{-tag}}^2 \right\}. \end{aligned}$$

where k iterates over the number of bins M, n_k is the number of events observed in bin k and μ_k is the expected number of events in bin k for all processes, which is given by:

$$\mu_k = \beta_s \cdot \nu_s \cdot \alpha_k^s + \sum_{j=1}^{2} \beta_{W_j} \cdot \nu_{W_j} \cdot \alpha_k^{W_j} + \sum_{b=1}^{4} \nu_b \cdot \alpha_k^b$$

The index s denotes the signal, W_j stands for the W+jets background and b represents the other processes that are not varied in the fit. The ν_s, ν_{W_j} and ν_b are the predicted number of events of the processes, α_k^s, $\alpha_k^{W_j}$ and α_k^b are the fractions of events in bin k of the normalised distribution for the processes, that fulfil the normalisation condition $\sum_{k=1}^{M} \alpha_k^{s,W_j,b} = 1$. The signal scale factor, β_s, is further given by the product of $\beta_{t\bar{t}}$ and the variation of the signal fraction with respect to variations of the nuisance parameters δ_i:

$$\beta_s = \beta_{t\bar{t}} \left\{ 1 + \sum_{i=1}^{2} |\delta_i| \cdot (H(\delta_i) \cdot \epsilon_{i+} + H(-\delta_i) \cdot \epsilon_{i-}) \right\}$$

where ϵ_{i+} and ϵ_{i-} are the positive and negative variations of the acceptance uncertainties of the two profiled systematic uncertainties. The symbol H denotes the Heaviside function,[9]

---

[9] The Heaviside function is a unit step function whose value is zero for negative argument and one for positive argument.

which determines the usage of either the positive or the negative variation of the uncertainty depending on the sign of δ_i. The shape uncertainties of the two profiled systematic uncertainties are included in the calculation of α_k^s, which represents the signal template distribution. The α_k^s are calculated by interpolating in each bin k between the nominal template α_k and the systematically altered templates $\alpha_{ki}^{\pm}$ using the nuisance parameter δ_i as a weight:

$$\alpha_k^s = \alpha_k^{t\bar{t}} \sum_{i=1}^{2} |\delta_i| \cdot \left\{(\alpha_{ki}^{+} - \alpha_k) \cdot H(\delta_i) + (\alpha_{ki}^{-} - \alpha_k) \cdot H(-\delta_i)\right\}.$$

9.2 Evaluation of uncertainties using pseudo-experiments

In this analysis, a frequentist approach is employed to estimate the systematic uncertainties in the measured cross-section. The method relies on repeating the experiment and obtaining an estimator of the probability density of all possible outcomes of the measurement. Sets of 100 000 pseudo-experiments are used for the evaluation. To estimate the total uncertainty in each pseudo-experiment, all the systematic effects explained in Chapter 8 are varied together within their systematic uncertainties. These systematic effects impact the yields of the processes and the shapes of the discriminating observables used in the fit in the three signal regions. In this approach, correlations between acceptance and shape uncertainties for a certain effect is taken into account.

In each pseudo-experiment, a random number following a Gaussian distribution with a mean of zero and a width of one, δ_i, is thrown. The δ_i is used as a weight in considering the acceptance and shape uncertainties for the systematic uncertainty i. To evaluate the acceptance uncertainties ϵ_{ij+} and ϵ_{ij-} for a process j, the predicted number of events, ν_j, is varied according to all systematic uncertainties, S, as:

$$\nu_j^{\text{gen}} = \nu_j \cdot \left\{1 + \sum_{i=1}^{S} |\delta_i| \cdot (H(\delta_i) \cdot \epsilon_{ij+} + H(-\delta_i) \cdot \epsilon_{ij-})\right\} . \tag{9.2}$$

where ν_j^{gen} is the expected number of events for process j in a pseudo-experiment. The number of events n_j^{gen} is then drawn from a Poisson distribution with mean ν_j^{gen}. The shape uncertainties on the o_{NN} and the $m(jj)$ distributions are considered using the altered template distributions α_{jki}^{+} and α_{jki}^{-} according to a $\pm 1\sigma$ variation of systematic effect i in process j and bin k in a similar way like the profiled systematic uncertainties. The generated template distribution in each pseudo-experiment is given by:

$$\alpha_{jk}^{\text{gen}} = \alpha_{jk} + \sum_{i=1}^{S} |\delta_i| \cdot \left\{(\alpha_{jki}^{+} - \alpha_{jk}) \cdot H(\delta_i) + (\alpha_{jki}^{-} - \alpha_{jk}) \cdot H(-\delta_i)\right\} \tag{9.3}$$

For both acceptance and shape uncertainties, the magnitude $|\delta_i|$ controls the amount of the shift due to the uncertainty $(0\sigma, 1\sigma)$. The o_{NN} and $m(jj)$ distributions for all processes are then set for a given pseudo-experiment by drawing n^{gen} from the template distributions α_k^{gen}. The sum of the generated distributions using ν^{gen}, n^{gen} and α_k^{gen} for all processes represents one pseudo-experiment, where the fit is redone according to Eq. (9.1) and a value for β_s is extracted as described later in this chapter. The standard deviation of the β_s distribution from all the 100 000 pseudo-experiments is an estimator of the total uncertainty on the measurement. To estimate the impact of one or a subset of systematic uncertainties, the same procedure is done while changing the set of systematics considered in the sum in Eqs. 9.2 and 9.3. More details about the procedure of generating pseudo-experiments can be found in [163, 164].

Closure and linearity

Fig. 9.1 shows the $\hat{\beta}_{t\bar{t}}$ distribution for the 100 000 pseudo-experiments. The mean value of the distribution is one, which is consistent with $\beta_{t\bar{t}}^{\mathrm{gen}}$. The RMS of the estimator $\hat{\beta}_{t\bar{t}}$ is a measure of the total uncertainty in the measurement.

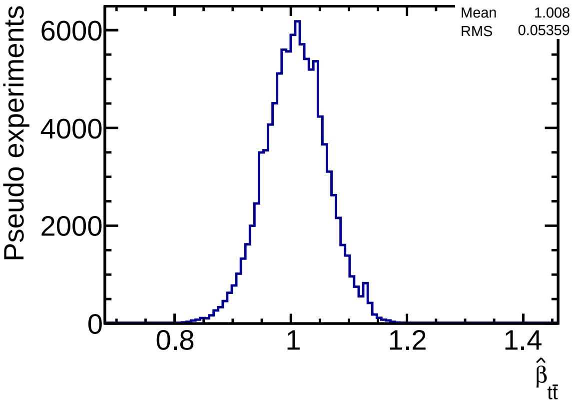

Figure 9.1: Distribution of the estimator $\hat{\beta}_{t\bar{t}}$ of the signal $t\bar{t}$ process for 100 000 pseudo-experiments.

The linearity of the signal fit parameter is tested using pseudo-experiments. The generated signal fit parameter, $\beta_{t\bar{t}}^{\mathrm{gen}}$, which is set to one in the default configuration, is varied by ±0.2, ±0.45 and ±0.6 and the estimator is observed for each value, see Fig. 9.2. As expected, the measured value of $\hat{\beta}_{t\bar{t}}$ is consistent with $\beta_{t\bar{t}}^{\mathrm{gen}}$. The points are fitted using a linear function to describe the relation between $\beta_{t\bar{t}}^{\mathrm{gen}}$ and $\hat{\beta}_{t\bar{t}}$.

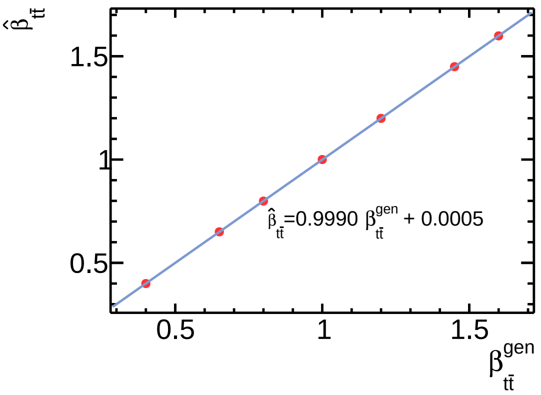

Figure 9.2: *The estimator $\hat{\beta}_{t\bar{t}}$ of the signal $t\bar{t}$ process for different values of the generated one $\beta^{\text{gen}}_{t\bar{t}}$ using* 100 000 *pseudo-experiments for each value of $\beta^{\text{gen}}_{t\bar{t}}$.*

9.3 Systematic uncertainties paramterised in the likelihood fit

The JES and the b-tagging efficiency are systematic sources with high uncertainties in the $t\bar{t}$ cross-section measurement. In this analysis, the effects of these two sources are parameterised with nuisance parameters in the likelihood fit in order to constrain these effects by measuring them in data. The ability to constrain the effects of these sources comes from the sensitivity introduced by separating the selected events into three disjoint regions and by using the $m(jj)$ distribution as a fit variable in SR2, which is sensitive to JES variations.

Jet energy scale

The dependence of $m(jj)$ on the JES was already discussed in Sect. 7.2. This dependence is the key idea for constraining the JES uncertainty. Fig. 9.3 shows the change of the shape of the fitted distributions due to $\pm 1\sigma$ variations of the overall JES. The dependence of $m(jj)$ on the JES is clearly visible in Fig. 9.3(b).

Variations in the JES affect the acceptance of events in the signal regions. Some events could get rejected or additional events could get accepted. Furthermore, events could migrate from one signal region to another due to the migration to a different jet bin.

The acceptance uncertainty of the overall JES is presented in Table 9.1, where the overall JES scale factor (JSF) is varied by $\pm 1\sigma$. The acceptance uncertainty is the highest in SR3. The differences of the acceptance uncertainties between the signal regions give additional sensitivity to constrain the JES.

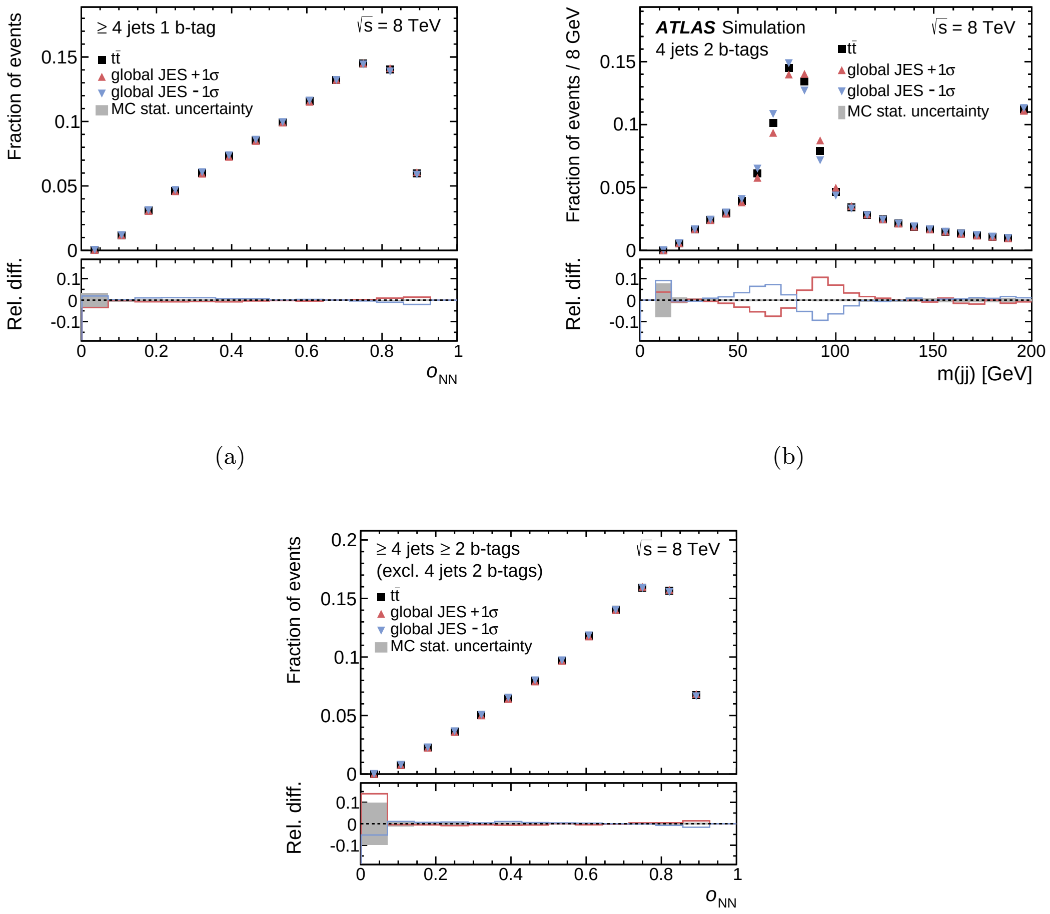

(a)

(b)

(c)

Figure 9.3: *The normalised shape variation due to the uncertainty in the overall JES for the simulated $t\bar{t}$ events of the (a) NN output distribution in SR1, (b) $m(jj)$ distribution in SR2 and (c) NN output distribution in SR3. The lower histogram in each of the plots shows the relative difference between the numbers of events in each bin with respect to the nominal sample. The grey error band represents the MC statistical uncertainty.*

Table 9.1: *The acceptance uncertainty ($\pm 1\sigma$) of the overall JES in each signal region.*

JES	$+1\sigma$ [%]	-1σ [%]
SR1	4.3	−4.3
SR2	1.8	−2.0
SR3	6.4	−6.1

A sensitive variable to the variation in the JES for the acceptance of events in the selection is the minumum p_{T} of the jets in the event, $p_{\mathrm{T}}^{\mathrm{min}}(j_n)$. A ratio can be defined as:

$$R(p_{\mathrm{T}}^{\mathrm{min}})^x = \frac{\mathcal{D}(p_{\mathrm{T}}^{\mathrm{min}})^{\mathrm{JSF}=x}}{\mathcal{D}(p_{\mathrm{T}}^{\mathrm{min}})^{\mathrm{JSF}=1}} \tag{9.4}$$

The function $\mathcal{D}(p_{\mathrm{T}}^{\mathrm{min}})^{\mathrm{JSF}=x}$ is the expected number of events as a function of $p_{\mathrm{T}}^{\mathrm{min}}(j_n)$ for a certain JSF. Fig. 9.4 shows the $p_{\mathrm{T}}^{\mathrm{min}}(j_n)$ distributions in the three signal regions for a simulated $t\bar{t}$ sample with JSF = 1 and for the variations of the JSF by ±2 %. Only the low range of $p_{\mathrm{T}}^{\mathrm{min}}(j_n)$ is shown, since this is the sensitive region for acceptance differences. As it can be seen, the slope of the $p_{\mathrm{T}}^{\mathrm{min}}(j_n)$ distribution is steepest for SR3, less steep in SR1 and least steep in SR2. The migration of events due to the variation of JSF is larger, the steeper the slope is. The ratios shown in the lower panel of each plot reflect the steepness of the p_{T} distributions. This observation is consistent with the acceptance uncertainties in the three signal regions shown in Table 9.1.

The parameterisation of the JES in the likelihood fit corresponds to a correction factor of the overall JES, which is one parameter that combines all the JES components. In evaluating the systematic uncertainty due to the JES, all components are considered separately and the overall JES is not included in the generation of the pseudo-experiments. Nevertheless, the impact of the various components is highly reduced due to the inclusion of the correction factor of the overall JES in the likelihood function.

b-tagging efficiency

The splitting of selected events into three signal regions allows constraining the uncertainty in the b-tagging efficiency by parameterising the effect of this uncertainty with a nuisance parameter in the likelihood fit. The sensitivity originates from the separation of one b-tagged events and two b-tagged events. The ratio is given by:

$$R_b = \frac{\nu(2b\text{-tagged})}{\nu(1b\text{-tagged})} \tag{9.5}$$

which roughly corresponds to the ratio of the sum of events in SR2 and SR3 to the events in SR1.

The expected number of events that have two b-tagged jets and one b-tagged jet are:

$$\begin{aligned} \nu(1b\text{-tagged}) &= \quad 2 \cdot \epsilon_b \cdot (1-\epsilon_b) \cdot \nu_{t\bar{t}} \\ \nu(2b\text{-tagged}) &= \qquad\qquad\qquad \epsilon_b^2 \cdot \nu_{t\bar{t}} \end{aligned} \tag{9.6}$$

where $\nu_{t\bar{t}}$ is the expected number of $t\bar{t}$ events in the three signal regions and ϵ_b is the average b-tagging efficiency for b-jets from top-quark decays.

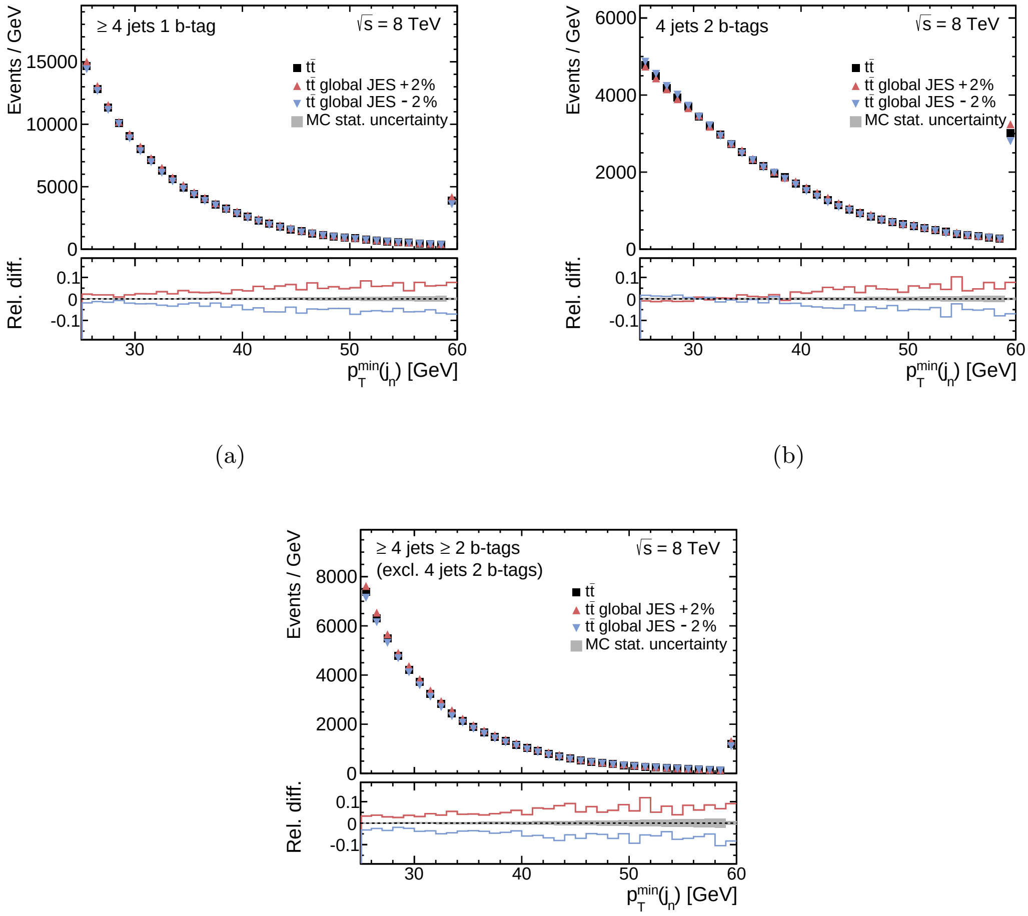

(a)

(b)

(c)

Figure 9.4: *The variation on the $p_T^{\text{min}}(j_n)$ due to variation of the JSF by 2 % for the simulated $t\bar{t}$ events in (a) SR1, (b) SR2 and (c) SR3. Plots are normalised to predictions. The lower histogram in each of the plots shows the relative difference between the numbers of events in each bin with respect to the nominal sample. The grey error band represents the MC statistical uncertainty.*

Solving Eq. (9.6) using Eq. (9.5) leads to:

$$\epsilon_b = \frac{2R_b}{1 + 2R_b} \tag{9.7}$$

Thus, the b-tagging efficiency is independent of $\nu_{t\bar{t}}$ but depends only on R_b. This shows that there is sensitivity to the b-tagging efficiency from the separation of events with two and one b-tagged jets in the signal regions. In addition, the measured $t\bar{t}$ cross-section does not depend on the b-tagging efficiency nuisance parameter. The assumption given in Eq. (9.7) is distorted by the fact that events with three b-tagged jets are also selected in SR3 and the formulas given above do not take into account the efficiency to tag c-quarks. However, the aim of this study is not to measure the b-tagging efficiency, but merely to assess the sensitivity to it.

The differences in the acceptance between the signal regions for this uncertainty are presented in Table 9.2. Since the uncertainty comes from applying a correction factor, no variation on the shapes of distributions is expected, as seen in Fig. 9.5.

Table 9.2: *The acceptance uncertainty ($\pm 1\sigma$) of the b-tagging efficiency in each signal region.*

b-tagging efficiency	up [%]	down [%]
SR1	−1.6	1.4
SR2	4.3	−4.2
SR3	4.3	−4.2

The b-tagging efficiency correction factor is parameterised by one parameter in the likelihood fit. The same parameter is included in the generation of the pseudo-experiments to evaluate the effect of this uncertainty in the cross-section measurement. Additionally, a study was done to check the effect of this uncertainty using the eigenvector variation method, where each source of uncertainty is varied by ±1σ, and the effect of each source on the calibration of the correction factor is considered. This method was tested for the uncertainty due to the b-tagging efficiency and also the c-tagging efficiency and the mistag rate. The total uncertainty using the eigenvector method did not differ from the one-component-per-uncertainty method which is the default one. The breakdown of the various components of these uncertainties will be shown later in this chapter.

Profiling checks

The effect on the measured $t\bar{t}$ cross-section of including nuisance parameters in the likelihood fit to parameterise the JES and the b-tagging efficiency uncertainties is studied here. Fig. 9.6

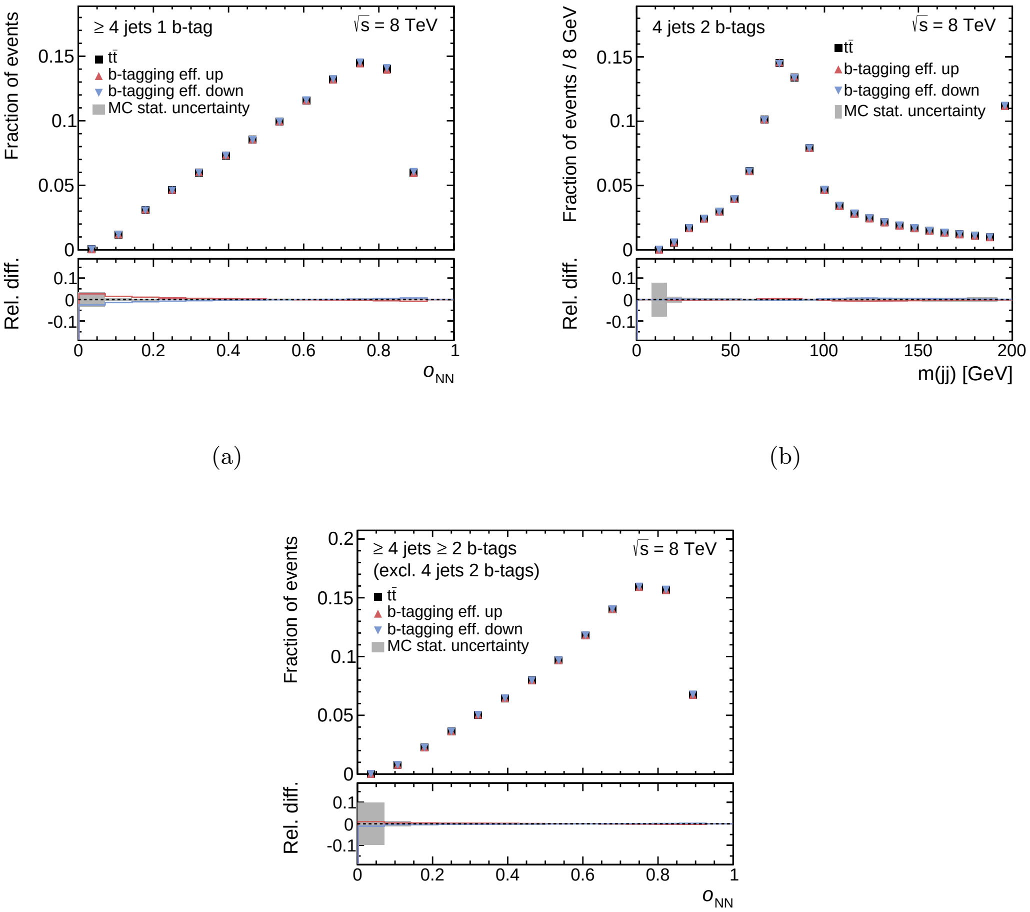

(a)

(b)

(c)

Figure 9.5: *The normalised shape variation due to the uncertainty in the b-tagging efficiency for the simulated $t\bar{t}$ events of the (a) NN output distribution in SR1, (b) $m(jj)$ distribution in SR2 and (c) NN output distribution in SR3. The lower histogram in each of the plots shows the relative difference between the numbers of events in each bin with respect to the nominal sample. The grey error band represents the MC statistical uncertainty.*

shows the profile of the estimator of the scale factor of the signal process $\hat{\beta}_{t\bar{t}}$ versus $\delta^{\mathrm{gen}}_{\mathrm{JES}}$ or $\delta^{\mathrm{gen}}_{b-\mathrm{tag}}$ for the pseudo-experiments. In the case of not fitting any nuisance parameter, there is a clear dependence of the signal estimator on δ^{gen}, while when fitting the two parameters, no dependence is visible. This means that the signal estimator is not biased by including the nuisance parameters.

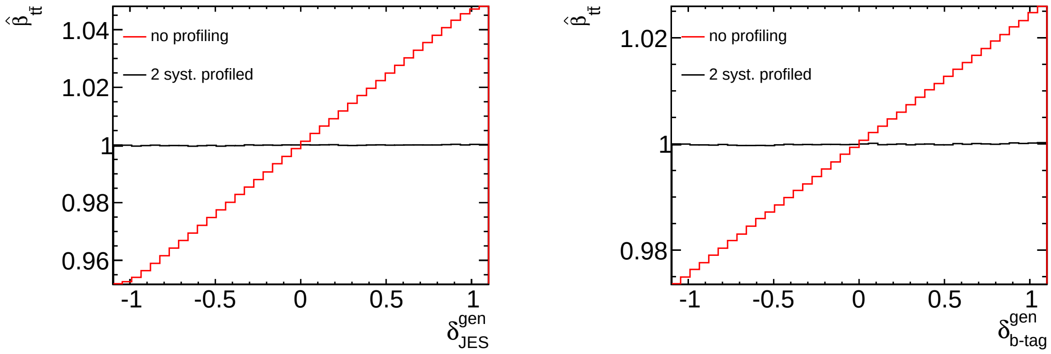

(a) (b)

Figure 9.6: *A profile of the signal estimator $\hat{\beta}_{t\bar{t}}$ (a) versus the generated correction factor for the JES $\delta^{\mathrm{gen}}_{\mathrm{JES}}$ and (b) versus the generated correction factor for the b-tagging efficiency $\delta^{\mathrm{gen}}_{b-\mathrm{tag}}$. Two configurations are considered, once with two nuisance parameters included in the fit and once without nuisance parameters.*

The linearity of the nuisance parameters is verified in Fig. 9.7, where the generated parameters δ^{gen} are varied in each pseudo-experiment and the estimators $\hat{\delta}$ are observed.

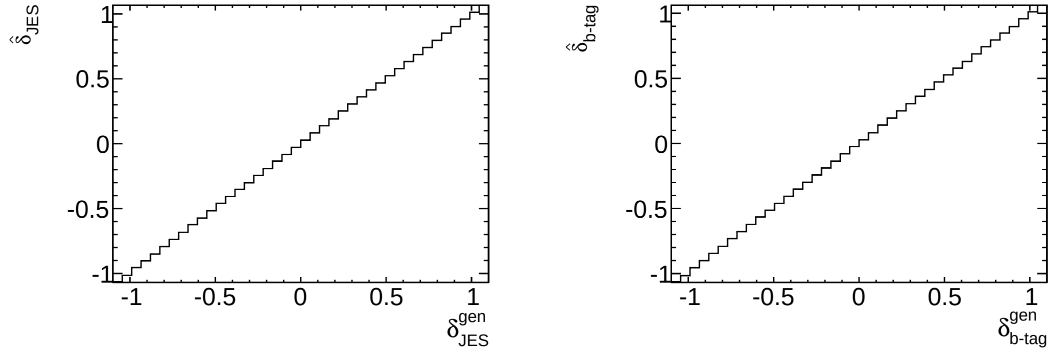

(a) (b)

Figure 9.7: *The fitted nuisance parameter $\hat{\delta}$ versus the generated one δ^{gen} for (a) the JES and (b) the b-tagging efficiency.*

Fig. 9.8 shows the residual of the nuisance parameters, i.e. $\hat{\delta} - \delta^{\mathrm{gen}}$. The RMS of this distribution represents the reduction in the uncertainty of these systematic sources by including the nuisance parameters in the likelihood fit. For both uncertainties, JES and b-tagging efficiency, the uncertainty is reduced to about 10 % of its original value without fitting parameters. However, the actual reduction in the JES uncertainty is lower (75 %), since the various components of the JES uncertainty are varied in the pseudo-experiments and not only one global parameter.

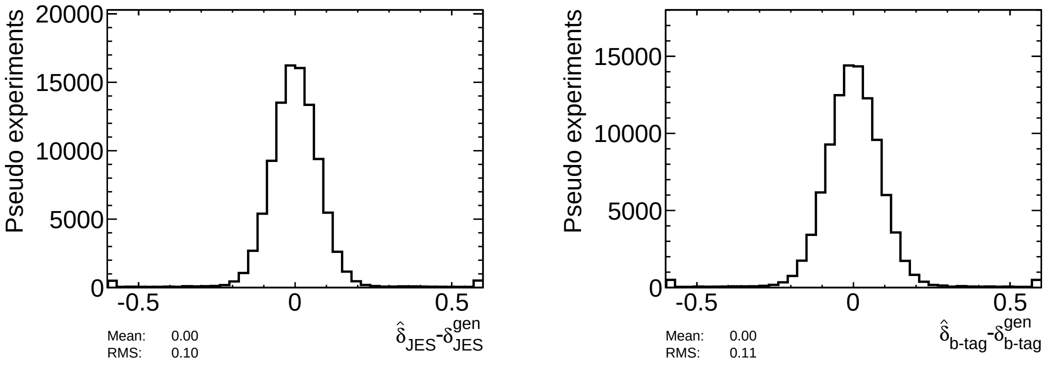

(a) (b)

Figure 9.8: *The residual distribution of (a) the nuisance parameter for the JES and (b) the nuisance parameter for the b-tagging efficiency.*

Separate signal regions

Additional studies are performed to achieve a better understanding of the systematic uncertainties in the inclusive $t\bar{t}$ cross-section measurement and the effect of adding nuisance parameters for the JES and b-tagging efficiency correction factors. This study is done by evaluating the systematic uncertainties due to JES and the b-tagging efficiency for different configurations. The aim of this study is to understand where the constraints come from for these two systematic sources. One or a subset of the signal regions is used and a likelihood with or without the JES and b-tagging efficiency nuisance parameters is used. The latter case is referred to as 'No profiling'.

The result can be found in Table 9.3. As can be seen, very little sensitivity to the b-tagging correction factor comes from single individual signal regions while the uncertainty is reduced when using at least two signal regions with different numbers of b-tags applied, i.e. SR1 and SR2 or SR1 and SR3. For JES, there is some sensitivity from all signal regions but mostly from SR2. A general small reduction in all configurations can be attributed to the fact, that introducing an additional free parameter in the fit can compensate small differences.

The sensitivity to a given systematic variation is given by the independence of the signal

Table 9.3: *Evaluation of the systematic uncertainties using pseudo-experiments without profiling and with profiling for one or a subset of the signal regions. Only the profiled systematic uncertainty is varied in the pseudo experiment. The statistical uncertainty in the pseudo-experiments is* 0.3 %.

	No profiling	Profiling
Signal regions	b-tagging eff [%]	b-tagging eff [%]
	JES [%]	JES [%]
SR1	2.0	1.7
	4.8	3.9
SR2	4.6	3.8
	2.2	1.2
SR3	4.3	4.2
	6.2	5.2
SR1 + SR2	1.3	0.2
	3.3	1.0
SR1 + SR3	1.3	0.2
	5.3	5.5
SR2 + SR3	4.5	3.4
	4.3	1.5
SR1 + SR2 + SR3	2.4	0.3
	4.1	1.1

estimator $\hat{\beta}_{t\bar{t}}$ on the input value of the systematic parameter δ_i^{gen}. If a dependence is observed, i.e. there are correlations between $\hat{\beta}_{t\bar{t}}$ and δ_i^{gen}, then there is no sensitivity to a given systematic variation and the measured cross-section depends on the input value of the systematic variation.

The result of this study for the *b*-tagging correction factor is shown in Figure 9.9. It can be seen that using only one signal region (Figs. 9.9(a) - 9.9(c)) does provide either no or only low sensitivity, whereas using SR1 and SR2 or SR1 and SR3 increases the sensitivity. For the JES correction factor shown in Fig. 9.10, almost all combinations provide at least some sensitivity, while SR2 and all combinations including it provide the highest sensitivity.

Correlations with signal modelling uncertainties

Including two nuisance parameters in the likelihood fit, which parameterise the effect of the JES and the *b*-tagging efficiency correction factors can have an effect on other uncertainties. Studies have shown that these uncertainties are the ones related to the signal modelling. This effect was checked by evaluating the signal modelling uncertainties in the inclusive measurement using a likelihood without any nuisance parameter and a likelihood with one or both nuisance parameters.

Correlations with the estimators are observed. The results can be found in Table 9.4. It can be seen, that the uncertainty from the NLO matching is reduced when including the JES parameter, whereas the scale variation uncertainty is reduced by including the parameter for the *b*-tagging efficiency. In the case of the uncertainty from the parton shower, it seems to be reduced from including both parameters. To validate this result, the profile of $\hat{\delta}_{\text{JES}}$ and $\hat{\delta}_{b-\text{tag}}$ is shown versus the δ^{gen} for each of these uncertainties in Fig. 9.11. These figures show correlations between the estimators and δ^{gen}, which explains the reduction in these uncertainties.

Table 9.4: *The effect of including nuisance parameters in the likelihood fit on the $t\bar{t}$ modelling uncertainties. The statistical uncertainty in the pseudo-experiments is* 0.3 %.

Systematic	No par. [%]	par. for JES [%]	par. for *b*-tag [%]	par. for JES and *b*-tag [%]
NLO matching	3.9	1.8	3.7	1.1
Parton shower	3.7	3.0	2.4	1.3
Scale variation	6.9	5.9	2.5	2.2

Differences in the acceptance between various event generators used in the evaluation of the signal modelling uncertainties can be due to jets from additional radiations, which cause a change in the jet multiplicity. Thus, events can get accepted or rejected in the

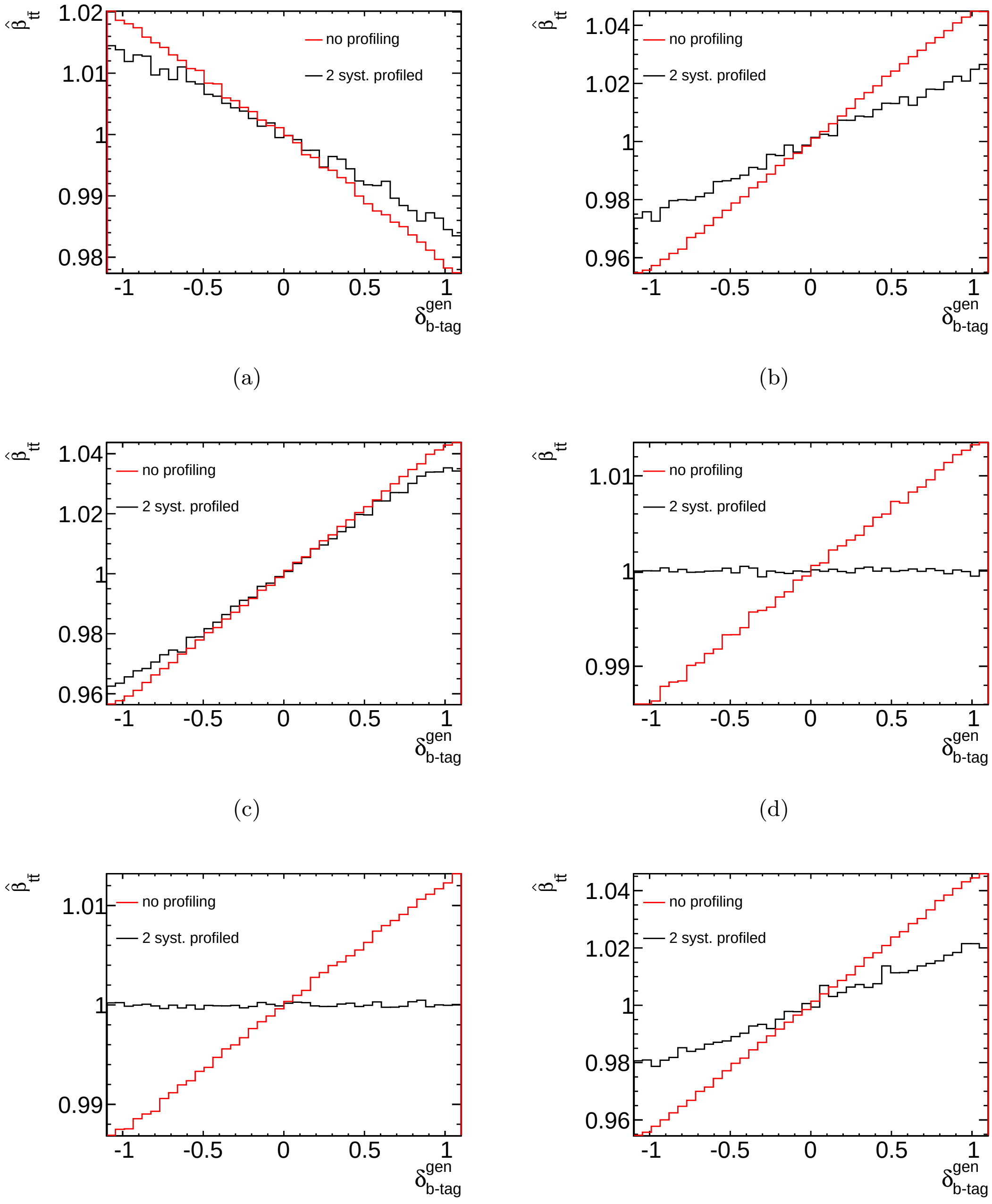

(a) (b)

(c) (d)

(e) (f)

Figure 9.9: *The estimator of the $t\bar{t}$ parameter $\hat{\beta}_{t\bar{t}}$ versus $\delta^{\mathrm{gen}}_{b-\mathrm{tag}}$ using (a) SR1, (b) SR2, (c) SR3, (d) SR1 + SR2, (e) SR1 + SR3, (f) SR2 + SR3. Two configurations are considered, once with two nuisance parameters included in the fit and once with no parameters used in the fit.*

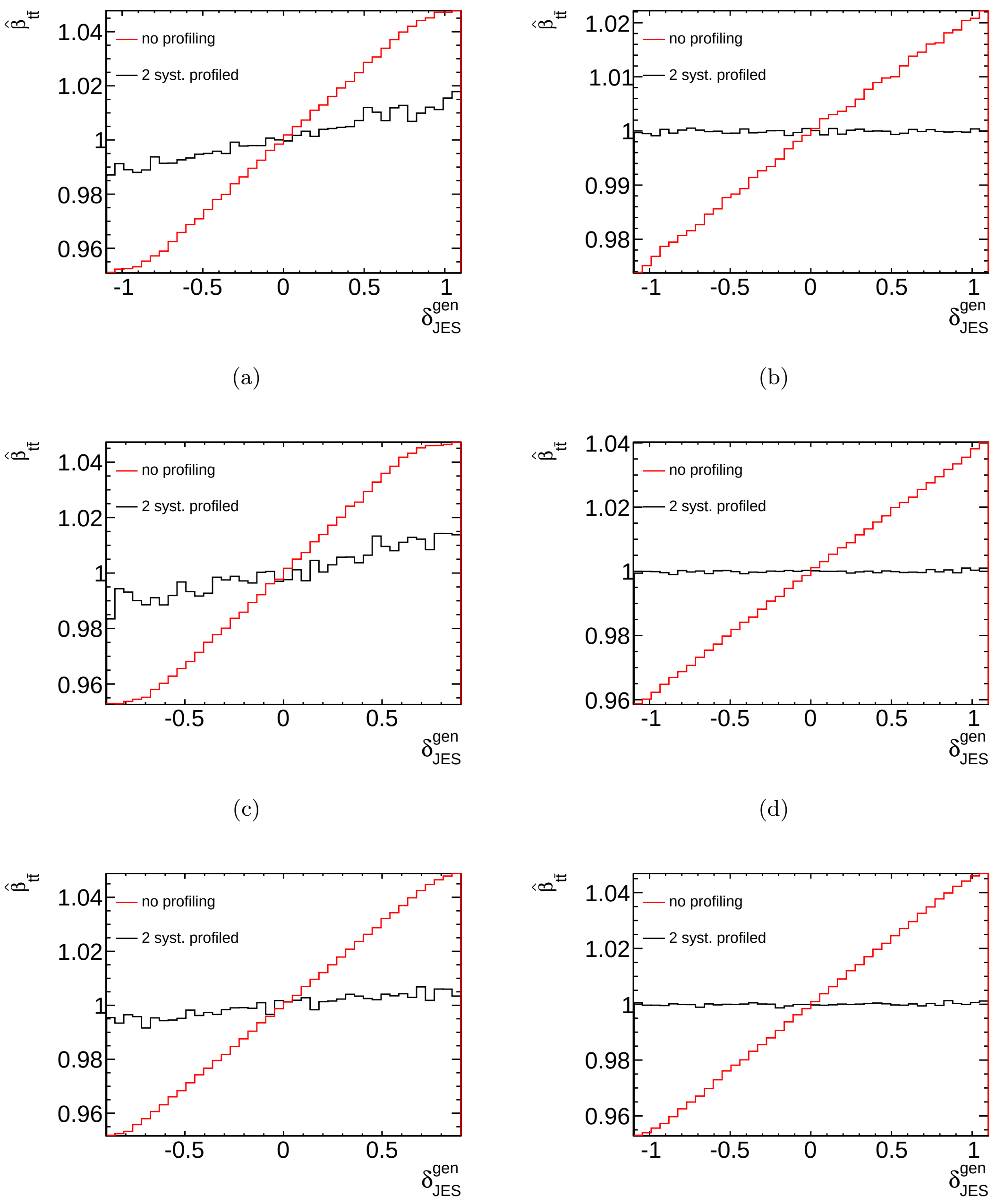

(a) (b)

(c) (d)

(e) (f)

Figure 9.10: *The estimator of the $t\bar{t}$ parameter $\hat{\beta}_{t\bar{t}}$ versus $\delta_{\mathrm{JES}}^{\mathrm{gen}}$ using (a) SR1, (b) SR2, (c) SR3, (d) SR1 + SR2, (e) SR1 + SR3, (f) SR2 + SR3. Two configurations are considered, once with two nuisance parameters included in the fit and once with no parameters used in the fit.*

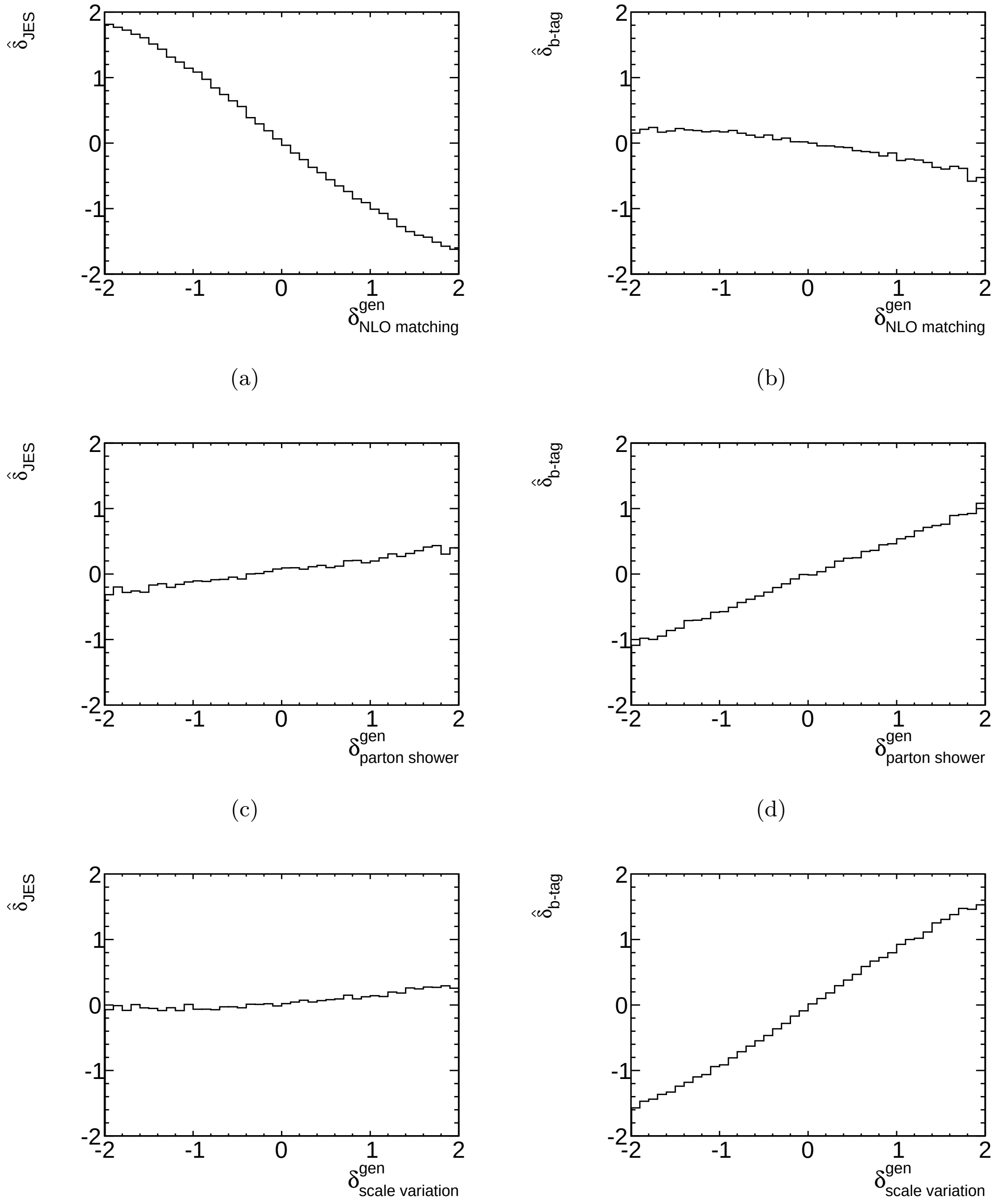

(a) (b)

(c) (d)

(e) (f)

Figure 9.11: *Correlations of the estimators* $\hat{\delta}$ *with* δ^{gen}*: (a)* $\hat{\delta}_{\mathrm{JES}}$ *versus* δ^{gen} *for the NLO matching, (b)* $\hat{\delta}_{b-\mathrm{tag}}$ *versus* δ^{gen} *for the NLO matching, (c)* $\hat{\delta}_{\mathrm{JES}}$ *versus* δ^{gen} *for the parton shower, (d)* $\hat{\delta}_{b-\mathrm{tag}}$ *versus* δ^{gen} *for the parton shower, (e)* $\hat{\delta}_{\mathrm{JES}}$ *versus* δ^{gen} *for the scale variation and (f)* $\hat{\delta}_{b-\mathrm{tag}}$ *versus* δ^{gen} *for the scale variation.*

selection. The contribution of additional radiation can be estimated from the ratio of events in SR3 to SR2:

$$R_{2,3} = \frac{\nu(SR3)}{\nu(SR2)} \tag{9.8}$$

Table 9.5 shows the value of $R_{2,3}$ for the various generators.

Table 9.5: *The value of $R_{2,3}$ for various generators.*

Generator	$R_{2,3}$
Powheg + Pythia	0.949 ± 0.006
Powheg + Herwig	1.056 ± 0.005
MC@NLO + Herwig	0.882 ± 0.006
Powheg + Pythia radHi	1.067 ± 0.006
Powheg + Pythia radLo	1.015 ± 0.005

As can be seen, the value of $R_{2,3}$ varies among the event generators, which explains differences in the acceptance by the differences in the jets from additional radiations.

9.4 Extraction of the $t\bar{t}$ cross-section

The measured $t\bar{t}$ cross-section is obtained by applying the likelihood function on collision data. Technically, the negative log-likelihood is minimised using the MINUIT framework [165]. The estimators of the scale factor parameters of the likelihood function for the processes, $\hat{\beta}_j$, are presented in Table 9.6, along with the estimated number of events in each signal region for all processes, $\hat{\nu}_j$. The estimator of the scale factor of the signal process, $\hat{\beta}_{\mathrm{t\bar{t}}}$ is measured to be 0.982 ± 0.005, where 0.005 represents the statistical uncertainty.

The estimator of the scale factor of the W+jets process in SR2 and SR3 yields a value significantly higher than the one predicted, but consistent with previous measurements. This indicates an underestimate of heavy-flavour production in the simulation as seen in Ref. [166]. In this table only statistical uncertainties obtained from the maximum-likelihood fit are shown for $t\bar{t}$ and W+jets, while the normalisation uncertainties are quoted for the other processes.

The estimators of the nuisance parameters for the systematic uncertainties, which parameterise their optimal shift relative to the default value 0 in terms of their uncertainty, are given in Table 9.7. The deviation of the b-tagging efficiency correction factor from the nominal value of the simulated sample corresponds to a shift of the acceptance in SR1 of

Table 9.6: *Result of the maximum-likelihood fit to data. Estimators of the parameters of the likelihood function, the scale factor $\hat{\beta}$ for $t\bar{t}$ and the two W+jets channels and the derived contributions of the various processes to the three signal regions are listed. Only the statistical uncertainties obtained from the maximum-likelihood fit are shown for $t\bar{t}$ and W+jets, while the normalisation uncertainties are quoted for the other processes.*

Process	$\hat{\beta}$	SR1	SR2	SR3
$t\bar{t}$	0.982 ± 0.005	$133\,390 \pm 630$	$64\,360 \pm 300$	$62\,380 \pm 280$
W+jets 1 b-tag	1.08 ± 0.02	$32\,150 \pm 480$	–	–
W+jets $\geqslant 2$ b-tags	1.41 ± 0.08	–	3370 ± 190	2250 ± 130
Single top	–	$11\,020 \pm 660$	3730 ± 220	2590 ± 160
Z+jets	–	3600 ± 1700	410 ± 200	270 ± 130
Diboson	–	1300 ± 640	135 ± 65	112 ± 54
Multijet	–	$10\,300 \pm 6900$	1940 ± 970	1050 ± 530
Total sum	–	$191\,700 \pm 7200$	$73\,900 \pm 1100$	$68\,660 \pm 650$
Total observed	–	192 686	72 978	70 120

1 % and 2.6 % in SR2 and SR3. The deviation for the JES correction factor corresponds to a shift of the acceptance of 2.9 % in SR1, of 1.4 % in SR2, and of 4.4 % in SR3. The deviation of the JES correction factor also potentially accounts for differences in the modelling of additional radiation between the different event generator set-ups, which was discussed in Sect. 7.2 in the dependence on the $m(jj)$ distribution.

Table 9.7: *Estimators of the nuisance parameters of the likelihood function. The quoted uncertainties are statistical only.*

Systematic uncertainty	$\hat{\delta}$
b-tagging efficiency	0.62 ± 0.09
JES	0.68 ± 0.07

The signal and background templates scaled and morphed to the fitted values of the fit parameters are compared to the observed distributions of the NN discriminant in SR1 and SR3 and the $m(jj)$ distribution in SR2 as shown in Fig. 9.12. Distributions of the input variables of the NN normalised to the fit result can be seen in Figs. 9.13 and 9.14 for SR1 and in Figs. 9.15 and 9.16 for SR3. The lower histogram in each plot shows the ratio of the observed to the predicted number of events in each bin. The distributions are well modelled and the ratio in each bin is within the uncertainty. The uncertainties included in the plots are the post-fit uncertainties, which are taken from pseudo-experiments as

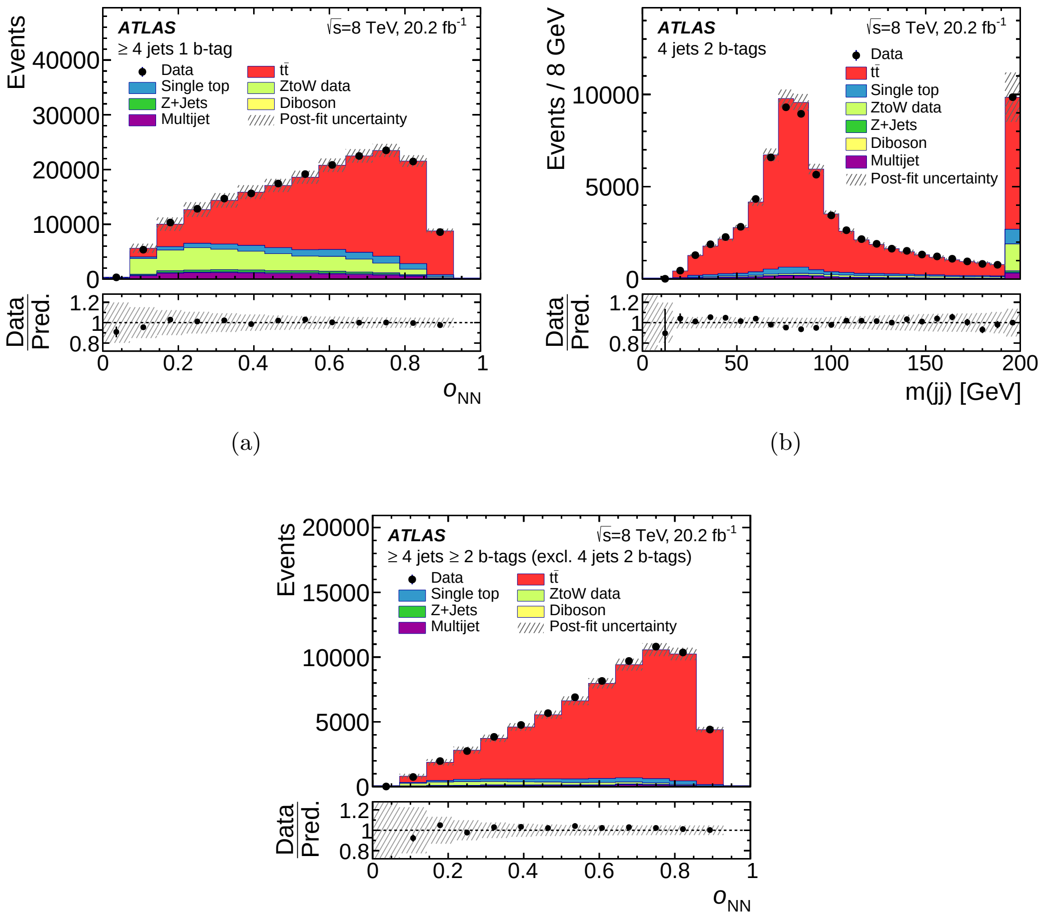

(a)

(b)

(c)

Figure 9.12: *Neural network discriminant o_{NN} or the $m(jj)$ distribution normalised to the result of the maximum-likelihood fit for (a) SR1, (b) SR2, and (c) SR3. The hatched error bands represent the post-fit uncertainty. The ratio of observed to predicted (Pred.) number of events in each bin is shown in the lower histogram. Events beyond the x-axis range are included in the last bin.*

the RMS of the $\hat{\beta}$ distribution. For the backgrounds, which are fixed in the fit, the normalisation uncertainties are added in quadrature.

9.5 Uncertainties in the inclusive and fiducial measurement

The total uncertainty in both the inclusive and the fiducial $t\bar{t}$ cross-section is presented in Table 9.8 and is estimated to be 5.7 % for the inclusive measurement and 4.5 % for the

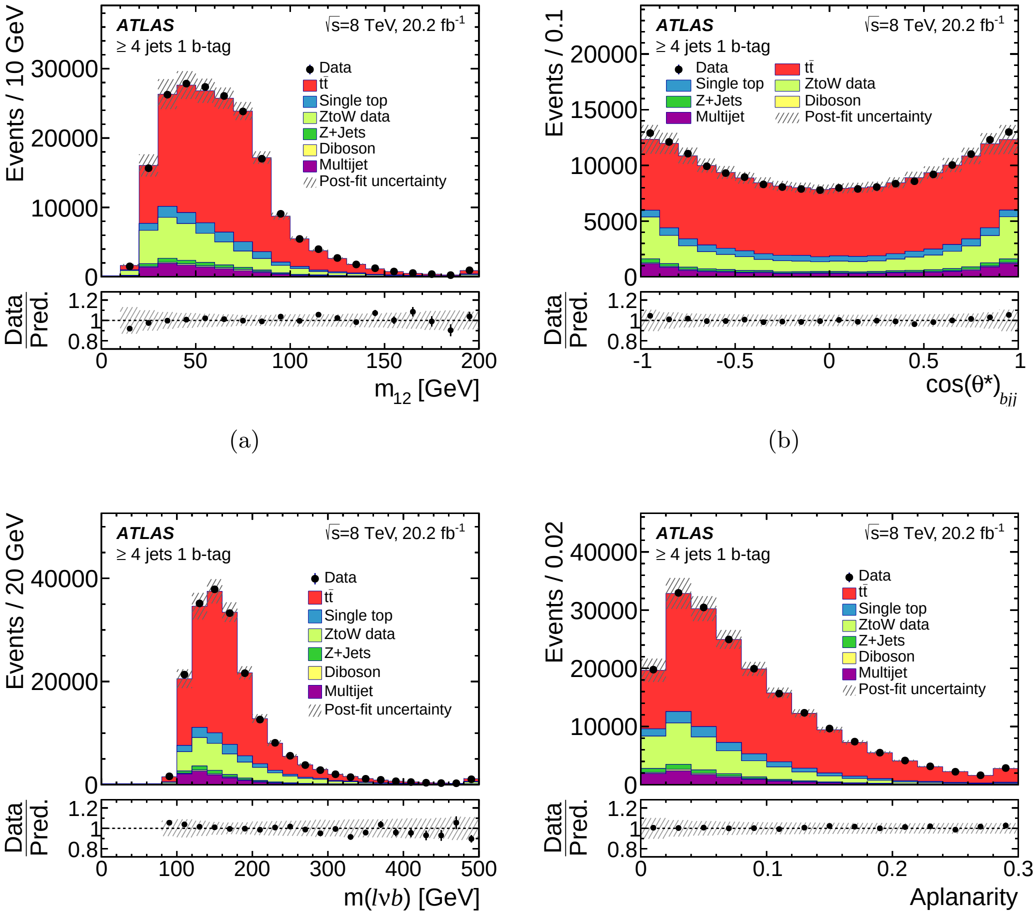

(a)

(b)

(c)

(d)

Figure 9.13: *Distributions four NN input variables for SR1 . The signal and backgrounds are normalised to the result of the maximum-likelihood fit: (a) smallest invariant mass between jet pairs, (b) cosine of the angle between the hadronic-top-quark momentum and the beam direction in the* $t\bar{t}$ *rest frame, and (c) mass of the reconstructed semileptonically decaying top quark, and (d) aplanarity. The hatched error bands represent the post-fit uncertainty. The ratio of observed to predicted (Pred.) number of events in each bin is shown in the lower histogram. Events beyond the* x*-axis range are included in the last bin.*

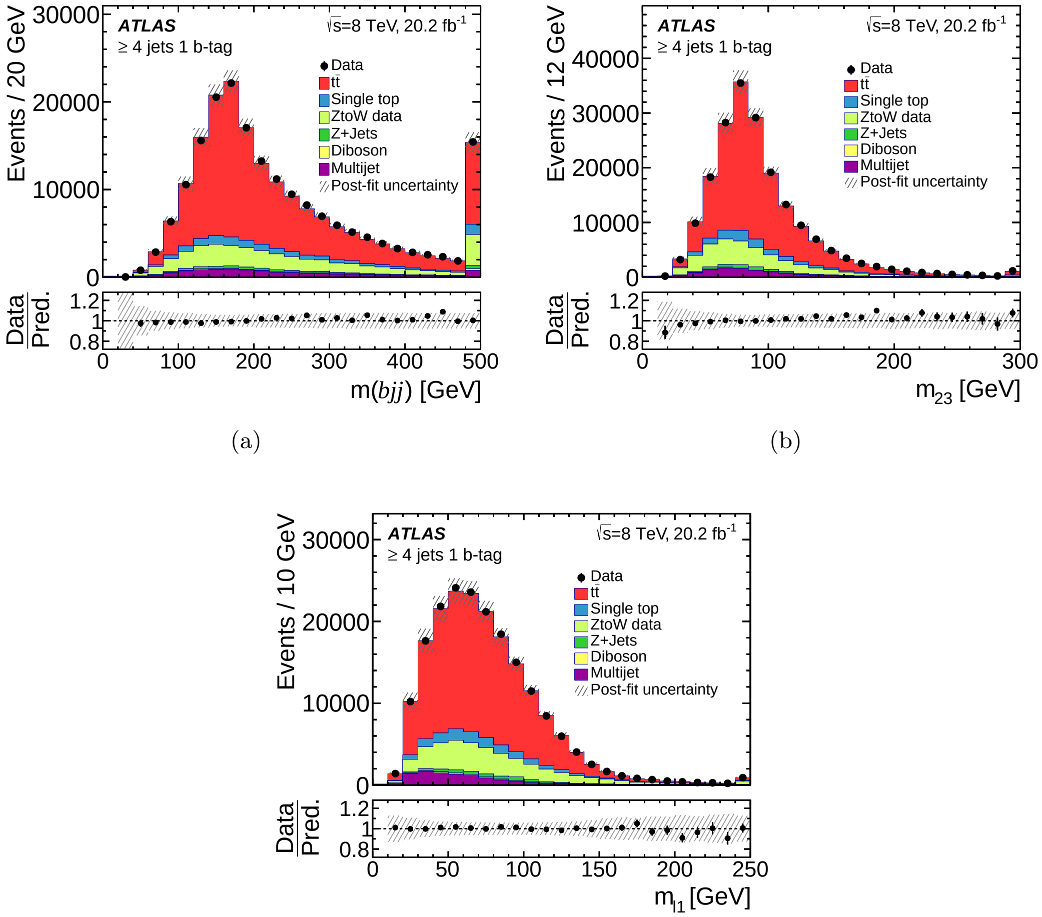

(a)

(b)

(c)

Figure 9.14: *Distribution of three NN input variables. The signal and backgrounds are normalised to the result of the maximum-likelihood fit for SR1: (a) mass of the reconstructed hadronically decaying top-quark, (b) second smallest invariant mass between jet pairs, and (c) smallest invariant mass between the charged lepton and a jet. The hatched error bands represent the post-fit uncertainty. The ratio of observed to predicted (Pred.) number of events in each bin is shown in the lower histogram. Events beyond the x-axis range are included in the last bin.*

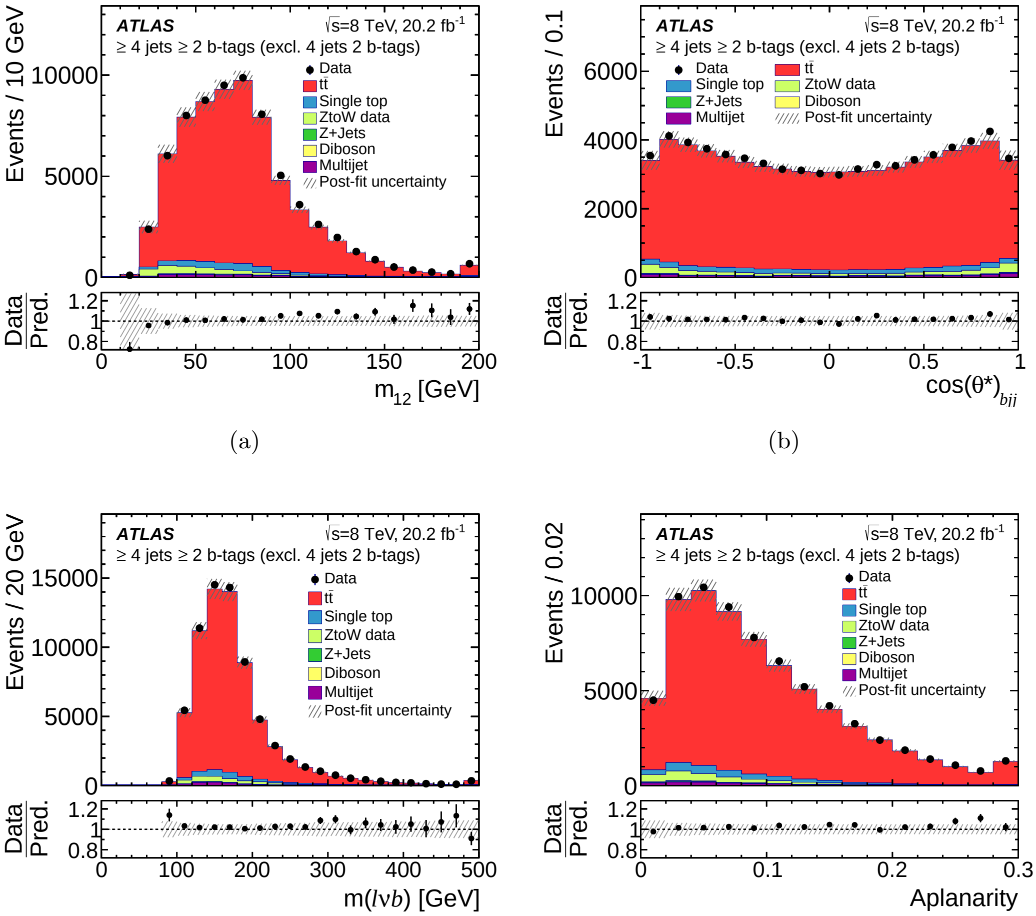

(a) (b)

(c) (d)

Figure 9.15: *Distributions of four NN input variables for SR3. The signal and backgrounds are normalised to the result of the maximum-likelihood fit: (a) smallest invariant mass between jet pairs, (b) cosine of the angle between the hadronic-top-quark momentum and the beam direction in the $t\bar{t}$ rest frame, and (c) mass of the reconstructed semileptonically decaying top quark, and (d) aplanarity. The hatched error bands represent the post-fit uncertainty. The ratio of observed to predicted (Pred.) number of events in each bin is shown in the lower histogram. Events beyond the x-axis range are included in the last bin.*

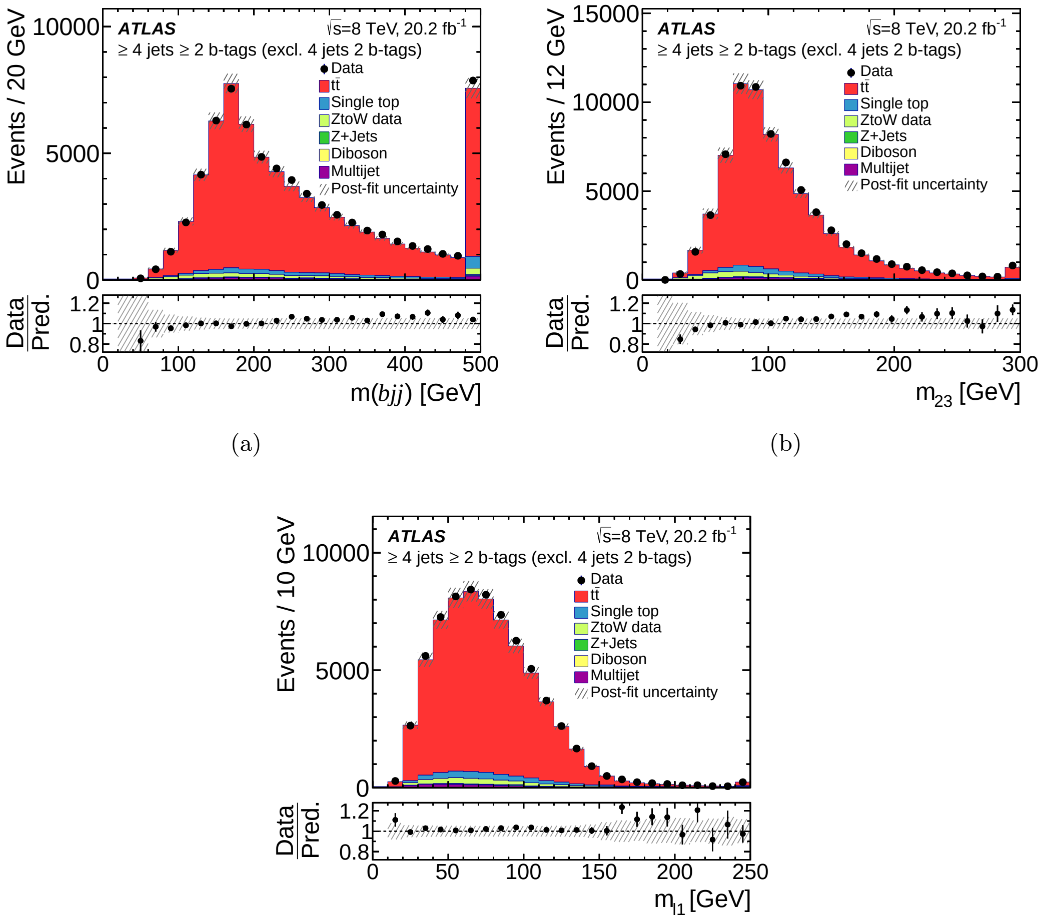

(a)

(b)

(c)

Figure 9.16: *Distribution of three NN input variables. The signal and backgrounds are normalised to the result of the maximum-likelihood fit for SR3: (a) mass of the reconstructed hadronically decaying top-quark, (b) second smallest invariant mass between jet pairs, and (c) smallest invariant mass between the charged lepton and a jet. The hatched error bands represent the post-fit uncertainty. The ratio of observed to predicted (Pred.) number of events in each bin is shown in the lower histogram. Events beyond the x-axis range are included in the last bin.*

fiducial measurement. The individual uncertainties from the various systematic sources are also shown. They are estimated in the same way as the total uncertainty but by only including the considered uncertainty in the generation of the pseudo-experiments.

The breakdown of the various components of the JES uncertainty in the $t\bar{t}$ cross-section measurement is shown in Table 9.9.

The breakdown of the various components of the uncertainty due to the b-tagging efficiency, the c-tagging efficiency and the mistag rate are listed in Table 9.10.

Uncertainties in the inclusive and fiducial measurements are identical except for the $t\bar{t}$ modelling and PDF uncertainties, since only these uncertaintes are affected by the difference between the fiducial volume and the full phase space. The effects of uncertainties in the JES and the b-tagging efficiency have been significantly reduced by including them as nuisance parameters in the likelihood fit. The uncertainty in the JES is reduced from 4.2 % to 1.1 %. The uncertainty in the b-tagging efficiency is reduced from 2.4 % to 0.3 %. The largest uncertainties in the inclusive measurement are due to the uncertainty in the PDF sets and the signal modelling.

For the fiducial cross-section measurement, the uncertainties in the signal modelling and PDF sets are reduced. In case of the signal modelling, the uncertainty due to additional radiation is reduced more than the parton-shower and NLO-matching uncertainties, since varying the amount of radiation leads to similar changes in the selection efficiencies of the fiducial and reconstructed volumes and therefore to smaller uncertainties in the $t\bar{t}$ cross-section. The reduction in the PDF uncertainty is due to the high reduction in the PDF acceptance uncertainty as explained in Sect. 8.2.4.

Acceptance and shape uncertainties

Uncertainties originating from acceptance and shape variation are studied separately in order to assess their different impacts in the total uncertainty. Only uncertainties that have high contributions in the inclusive $t\bar{t}$ cross-section measurement are studied. A likelihood without the JES and b-tagging efficiency nuisance parameters is used. This is done to avoid correlations between different sources of uncertainties.

The result is shown in Table 9.11. It can be seen, that for most systematic sources the shape variation is negligible and within the statistical uncertainty of the pseudo-experiments. For the scale variation uncertainty, the shape variation has a small effect. Nevertheless, the systematic uncertainty from all systematic sources are dominated by the acceptance uncertainty.

Table 9.8: *Breakdown of relative uncertainties in the measured inclusive and fiducial $t\bar{t}$ cross-sections. The total uncertainties contain all considered uncertainties.*

Source	$\frac{\Delta\sigma_{\text{inc}}}{\sigma_{\text{inc}}}$ [%]	$\frac{\Delta\sigma_{\text{fid}}}{\sigma_{\text{fid}}}$ [%]
Statistical uncertainty	0.3	0.3
Physics object modelling		
Jet energy scale	1.1	1.1
Jet energy resolution	0.1	0.1
Jet reconstruction efficiency	<0.1	<0.1
$E_{\mathrm{T}}^{\mathrm{miss}}$ scale	0.1	0.1
$E_{\mathrm{T}}^{\mathrm{miss}}$ resolution	<0.1	<0.1
Muon momentum scale	<0.1	<0.1
Muon momentum resolution	<0.1	<0.1
Electron energy scale	0.1	0.1
Electron energy resolution	<0.1	<0.1
Lepton identification	1.4	1.4
Lepton reconstruction	0.3	0.3
Lepton trigger	1.3	1.3
b-tagging efficiency	0.3	0.3
c-tagging efficiency	0.5	0.5
Mistag rate	0.3	0.3
Signal Monte Carlo modelling and parton distribution functions		
NLO matching	1.1	0.9
Scale variations	2.2	1.0
Parton shower	1.3	0.9
PDF	3.0	0.1
Background normalisation for non-fitted backgrounds		
Single top	0.3	0.3
Z+jets	0.2	0.2
Diboson	0.1	0.1
Background modelling		
$Z$to$W$ modelling	1.1	1.1
Multijet	0.6	0.6
Luminosity	1.9	1.9
Total (syst.)	5.7	4.5
Total (syst.+stat.)	5.7	4.5

Table 9.9: *Breakdown of the various components of the jet energy scale systematic uncertainty on the observed values for the inclusive and fiducial $t\bar{t}$ cross-section. Uncertainties contributing less than* $0.10\,\%$ *are marked with "< 0.1"*

Source	$\frac{\Delta\sigma}{\sigma}$ [%]
b-jet energy scale	0.6
JES η intercal. statistical	<0.1
JES η intercal. modelling	0.1
JES detector 1	0.4
JES detector 2	<0.1
JES detector 3	<0.1
JES flavour composition	<0.1
JES flavour response	0.2
JES mixed detector and modelling 1	0.3
JES mixed detector and modelling 2	0.1
JES mixed detector and modelling 3	0.2
JES mixed detector and modelling 4	<0.1
JES physics modelling 1	<0.1
JES physics modelling 2	<0.1
JES physics modelling 3	0.4
JES physics modelling 4	<0.1
JES pile-up μ	<0.1
JES pile-up p_T	<0.1
JES pile-up N_{PV}	0.1
JES pile-up ρ	0.2
JES statistical 1	0.4
JES statistical 2	<0.1
JES statistical 3	0.3
JES statistical 4	<0.1
Punch-through	<0.1

Table 9.10: *Breakdown of the various components of the b-tagging efficiency, c-tagging efficiency and mistag rate systematic uncertainties on the observed values for the inclusive and fiducial $t\bar{t}$ cross-section. Uncertainties contributing less than* 0.10 % *are marked with* "< 0.1"

Source	$\frac{\Delta\sigma}{\sigma}$ [%]
b-tagging efficiency EV0	<0.1
b-tagging efficiency EV1	<0.1
b-tagging efficiency EV2	<0.1
b-tagging efficiency EV3	<0.1
b-tagging efficiency EV4	<0.1
b-tagging efficiency EV5	0.1
c-tagging efficiency EV0	<0.1
c-tagging efficiency EV1	0.2
c-tagging efficiency EV2	<0.1
c-tagging efficiency EV3	0.3
Mistag rate EV0	<0.1
Mistag rate EV1	<0.1
Mistag rate EV2	<0.1
Mistag rate EV3	<0.1
Mistag rate EV4	<0.1
Mistag rate EV5	<0.1
Mistag rate EV6	<0.1
Mistag rate EV7	<0.1
Mistag rate EV8	<0.1
Mistag rate EV9	<0.1
Mistag rate EV10	<0.1
Mistag rate EV11	0.3

Table 9.11: *The acceptance and shape uncertainties for systematic variations with large contributions in the measurement. The statistical uncertainty in the pseudo-experiments is* 0.3 %.

Systematic	Both [%]	Only shape [%]	Only rate [%]
JES	4.1	0.3	4.0
b-tagging efficiency	2.4	0.1	2.4
NLO matching	3.9	0.3	3.7
Parton shower	3.7	0.6	3.1
Scale variation	6.9	1.1	6.2
PDF	3.0	0.2	3.0

Summary

As discussed in this chapter, splitting the selected events into three disjoint signal regions and using the $m(jj)$ distribution as the fit observable in SR2 provides sensitivity to constrain some systematic uncertainties. In the likelihood fit, two nuisance parameters are used to parameterise the JES and b-tagging efficiency correction factor. Including the $m(jj)$ in SR2 helps constraining the JES uncertainty. Including signal regions with different numbers of b-tagged jets, leads to a high sensitivity to reduce the uncertainty in the b-tagging efficiency. Additionally, correlations of the fitted nuisance parameters with uncertainties related to the signal modelling are observed, which explains the reduction in these uncertainties.

10

Results

A summary of the measured cross-section together with a dependence of the result on the top-quark mass is presented in this chapter. The measured cross-section is extracted for the full phase space and for a fiducial phase space close to the selected dataset. The systematic uncertainties affecting the measurements are estimated as given in the previous chapter.

10.1 Inclusive $t\bar{t}$ cross-section

Here, the measured inclusive $t\bar{t}$ cross-section is presented. In addition, the top-quark mass is extracted from the cross-section dependence using a simplified method.

10.1.1 Result

The estimator of the $t\bar{t}$ scale factor, obtained using the simultaneous binned maximum-likelihood fit to the NN discriminant distributions in SR1 and SR3 and the $m(jj)$ distribution in SR2, is used to extract the inclusive cross-section. The inclusive cross-section is then calculated using Eq. (1.13).

Thus, the inclusive $t\bar{t}$ cross-section is measured to be:

$$\sigma_{\text{inc}}(t\bar{t}) = 248.3 \pm 0.7\,(\text{stat.}) \pm 13.4\,(\text{syst.}) \pm 4.7\,(\text{lumi.})\ \text{pb}$$

assuming a top-quark mass of $m_{\text{top}} = 172.5\ \text{GeV}$.

Fig. 10.1 compares this measurement with other $t\bar{t}$ cross-section measurements from the ATLAS and CMS collaborations and with the NNLO+NNLL theoretical prediction at a

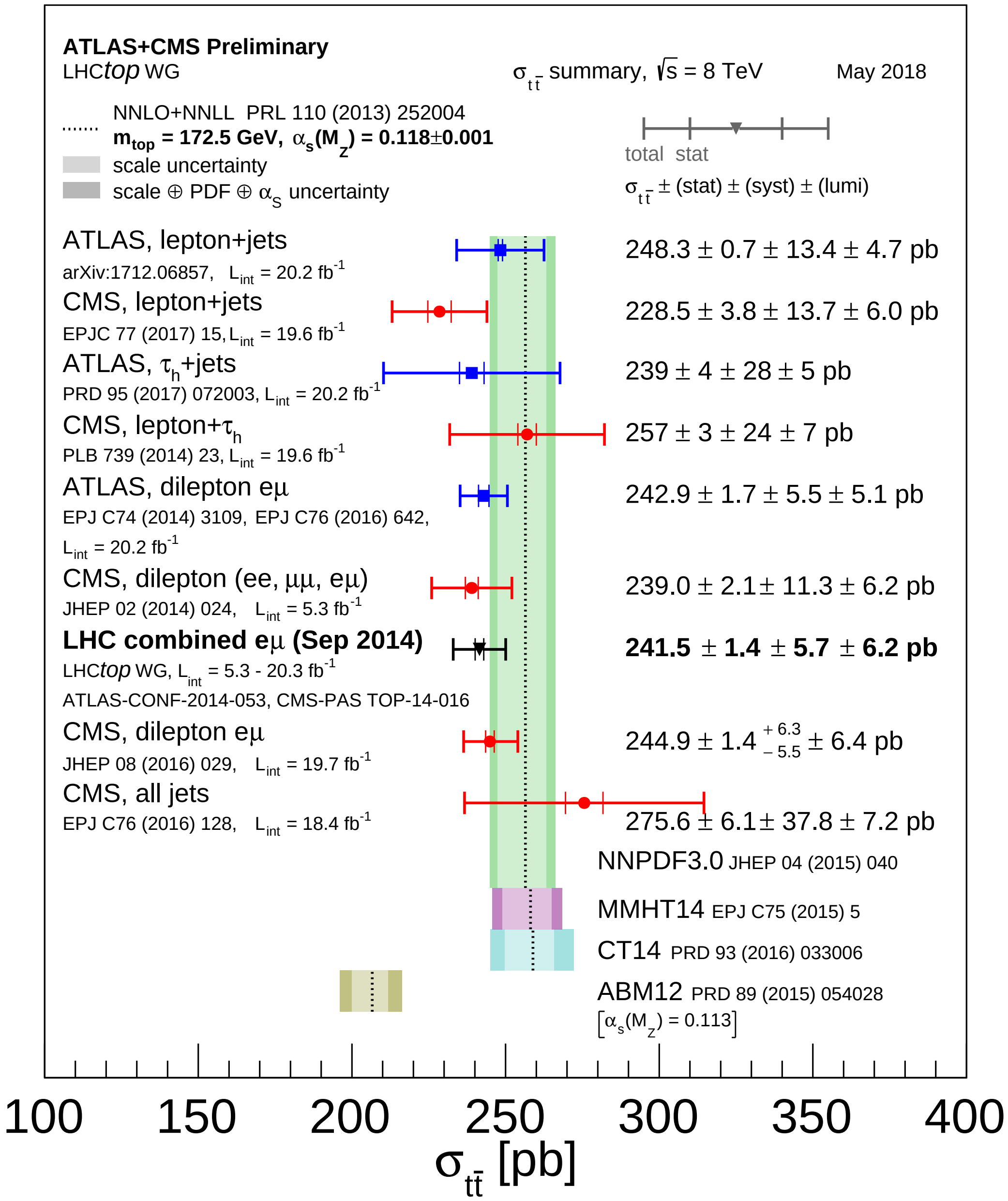

Figure 10.1: *Summary of measurements of the top-pair production cross-section at 8 TeV compared to the exact NNLO QCD calculation complemented with NNLL resummation (top++2.0) using four different PDF sets. The theory bands represent uncertainties due to renormalisation and factorisation scale, parton density functions and the strong coupling constant. The measurements and the theory calculation are quoted at* m_{top} = 172.5 GeV *[50].*

centre-of-mass energy of 8 TeV. This result is consistent with the theoretical predictions and with results obtained from other measurements. The presented measurement is the most precise one in the lepton+jets channel and has been recently published in Ref. [167].

10.1.2 Cross-section dependence on the top-quark mass

The dependence of the inclusive $t\bar{t}$ cross-section measurement on the assumed value of m_{top} is mainly due to acceptance effects. This dependence can be expressed by a quadratic function:

$$\sigma_{t\bar{t}}(m_{\text{top}}) = \sigma_{t\bar{t}}(172.5\ \text{GeV}) + p_1 \cdot \Delta m_{\text{top}} + p_2 \cdot \Delta m_{\text{top}}^2 \ ,$$

with $\Delta m_{\text{top}} = m_{\text{top}} - 172.5\,\text{GeV}$. The parameters p_1 and p_2 are determined using dedicated signal samples with different m_{top} values. The m_{top} values used are: 165, 167.5, 170, 175, 177.5 and 180 GeV. Signal template distributions are obtained from the alternative samples and the fit to data is repeated for each of these samples.

Fig. 10.2 shows the measured cross-section at each of the m_{top} values and the fit result. The parameters are determined to be: $p_1 = -2.07 \pm 0.07\,\text{pb/GeV}$ and $p_2 = 0.07 \pm 0.02\,\text{pb/GeV}^2$. The dependence of the theoretical prediction on m_{top} is also shown using the parameterisation proposed in Ref. [32], which is much stronger than the measured one.

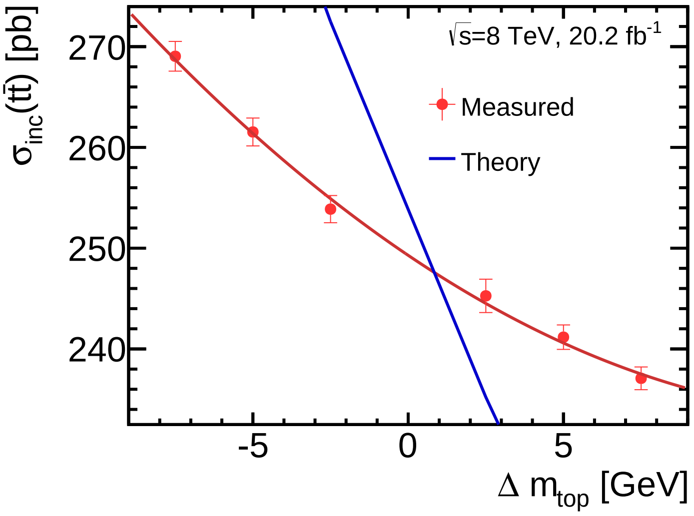

Figure 10.2: *Cross section dependence on the top-quark mass. Error bars include statistical uncertainty only.*

In this channel, the extraction of the top-quark mass from the cross-section measurement will not be as precise as in the dilepton channel (see Ref. [52]), since the dependence of the $t\bar{t}$ cross-section on the top-quark mass is much stronger here. The reason comes from the fact that the event topology of the lepton+jets channel has at least four jets. Thus, there is a higher dependence of the signal acceptance on the assumed m_{top} value used to generate the simulated samples. However, using a simplified method, the top-quark mass is extracted. The measured top-quark mass value corresponds to the intersection between the fitted curve of the dependence of the measured cross-section on m_{top} and the curve for the dependence of the theoretical prediction on m_{top}, as shown in Fig. 10.2. To calculate the uncertainty on the measured m_{top}, the uncertainty in the theoretical prediction and the uncertainty in the measured cross-section are added in quadrature, which corresponds to a precision of 8.2 %. The measured value of the top-quark mass is $m_{\mathrm{top}} = 173.3 \pm 14.2$ GeV. This result is consistent with the world average value of the top-quark mass.

10.2 Fiducial $t\bar{t}$ cross-section

The fiducial cross-section measured in the fiducial volume is extracted using Eq. (1.14). The fiducial acceptance, A_{fid}, is about 20 %. In case of the POWHEG-BOX + PYTHIA generator setup it is $A_{\mathrm{fid}} = 19.6\,\%$.

The fiducial cross-section is measured to be:

$$\sigma_{\mathrm{fid}}(t\bar{t}) = 48.8 \pm 0.1\,(\mathrm{stat.}) \pm 2.0\,(\mathrm{syst.}) \pm 0.9\,(\mathrm{lumi.})\ \mathrm{pb}.$$

Fig. 10.3 shows the measured fiducial cross-section compared with the predictions from various event generators. The measured value agrees with the predictions within the statistical and systematic uncertainties.

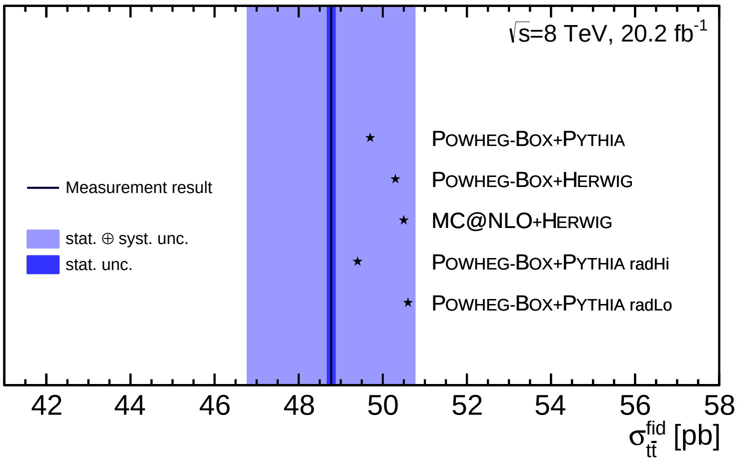

Figure 10.3: *The measured fiducial cross section and predictions from various event generators. The statistical and systematic uncertainties of the measurement are shown.*

Conclusion and outlook

This dissertation presents a measurement of the inclusive and fiducial $t\bar{t}$ cross-sections in the lepton+jets channel using $20.2\,\mathrm{fb}^{-1}$ of data collected in pp collisions at a centre-of-mass energy of $\sqrt{s} = 8\,\mathrm{TeV}$ in 2012 with the ATLAS experiment at the LHC.

An event selection is applied based on the lepton+jets topology of the $t\bar{t}$ process, which consists of an isolated electron or muon, sizeable missing transverse momentum and at least four jets, two of which are b-quarks jets. The expected number of events of background processes with similar final states as the signal is estimated. The most important background, the W+jets process, is modelled using Z+jets events in a data-driven approach. Here, Z+jets candidate events selected from collision data are converted into a W+jets sample, thus reducing modelling uncertainties significantly.

The selected events are separated into three disjoint regions with different numbers of b-tagged jets and different jet multiplicities. An artificial neural network is trained to improve the separation between the $t\bar{t}$ signal and the main background, W+jets process. The neural network output distribution is used as the discriminant in two signal regions while the mass of the hadronically decaying top-quark is used in the third one. This configuration improves the sensitivity to systematic uncertainties affecting the $t\bar{t}$ measurement. In particular, systematic uncertainties due to the modelling of the jet energy scale and b-tagging efficiency are constrained and thus the impact on the $t\bar{t}$ cross section measurement is reduced. The dependence of the reconstructed mass of the hadronically decaying W boson on the jet energy scale helps to reduce the impact of this uncertainty. The sensitivity to the b-tagging efficiency originates from the separation of one b-tagged and two b-tagged events.

A simultaneous binned maximum-likelihood fit is performed in the three signal regions to determine the $t\bar{t}$ cross-section. Correction factors for the jet energy scale and the b-tagging efficiency are parameterised in the fit as nuisance parameters.

The inclusive $t\bar{t}$ cross-section is measured with an unprecedented precision of 5.7 % to be:

$$\sigma_{\mathrm{inc}}(t\bar{t}) = 248.3 \pm 0.7\,(\mathrm{stat.}) \pm 13.4\,(\mathrm{syst.}) \pm 4.7\,(\mathrm{lumi.})\ \mathrm{pb}$$

assuming a top-quark mass of $m_{\mathrm{top}} = 172.5\ \mathrm{GeV}$.

The $t\bar{t}$ cross-section measurement is also performed in a fiducial volume close to the selected dataset, which is advantageous in reducing MC modelling uncertainties. The fiducial cross-section is measured with a precision of 4.5 % to be:

$$\sigma_{\text{fid}}(t\bar{t}) = 48.8 \pm 0.1\,(\text{stat.}) \pm 2.0\,(\text{syst.}) \pm 0.9\,(\text{lumi.})\ \text{pb}.$$

This result is in good agreement with the theoretical prediction at NNLO+NNLL accuracy and with other measurements performed with the ATLAS and CMS experiments. The inclusive $t\bar{t}$ cross-section determined in this thesis is the most precise measurement in the lepton+jets channel by the ATLAS collaboration and more precise than the CMS measurement, which achieved a total uncertainty of 6.8 %. Previous ATLAS measurement reached an uncertainty of 9.4 %.

Furthermore, a simplified method is used to determine the top-quark mass from the dependence of the measured cross-section and the theoretical prediction on the mass. The measured value of the top-quark mass is $m_{\text{top}} = 173.3 \pm 14.2$ GeV, which is consistent with the world average value of the top-quark mass.

This measurement can be repeated at a centre-of-mass energy of $\sqrt{s} = 13\,\text{TeV}$, where a larger dataset is available. Additionally, this result can be interpreted as a search for new physics, with particles decaying into top-quark pairs. A search for such events can be performed by looking for an excess in the measured cross-section with respect to the SM prediction. For example, a limit can be set on the pair production of supersymmetric top squarks using this measurement, where the top squarks decay into a top-quark and a neutralino producing final states very similar to the one from SM $t\bar{t}$ production.

A

Simulated samples

Lists of simulated samples used in the analysis are given in Table A.1 for the $t\bar{t}$ process, in Table A.2 for the W+jets process, in Table A.3 for the single-top process, in Table A.4 for the Z+jets process and in Table A.5 for the diboson process.

Table A.1: *List of the simulated samples used for the $t\bar{t}$ process (no fully hadronic). The production cross-section, the k-factor and the event generator for each sample are given.*

Event generator	Cross-section [pb]	k-factor	Parameters
POWHEG-BOX +PYTHIA (nominal)	114.5	1.20	$h_{\text{damp}} = m_{\text{top}}$
POWHEG-BOX +PYTHIA	114.5	1.20	$h_{\text{damp}} = \infty$
POWHEG-BOX +HERWIG	115.6	1.19	
MC@NLO +HERWIG	112.9	1.22	
POWHEG-BOX +PYTHIA	137.32	1.00	$2 \times \mu$, $h_{\text{damp}} = m_{\text{top}}$, radLo
POWHEG-BOX +PYTHIA	137.32	1.00	$0.5 \times \mu$, $h_{\text{damp}} = 2 \times m_{\text{top}}$, radHi

Table A.2: *List of the simulated samples used for the W+jets process, generated with the* Alpgen *+* Pythia *event generators. ℓ refers to the three lepton flavours, e, μ and τ. The production cross-section and the k-factor for each sample are given.*

Process	Cross-section [pb]	k-factor
$W \to \ell\nu$ + 0 partons	8127	1.13
$W \to \ell\nu$ + 1 parton	1792	1.13
$W \to \ell\nu$ + 2 partons	542	1.13
$W \to \ell\nu$ + 3 partons	147	1.13
$W \to \ell\nu$ + 4 partons	37.7	1.13
$W \to \ell\nu$ + 5 partons	11.9	1.13
$W \to \ell\nu + b\bar{b}$ + 0 partons	52.2	1.13
$W \to \ell\nu + b\bar{b}$ + 1 parton	45.6	1.13
$W \to \ell\nu + b\bar{b}$ + 2 partons	23.9	1.13
$W \to \ell\nu + b\bar{b}$ + 3 partons	13.6	1.13
$W \to \ell\nu + c\bar{c}$ + 0 partons	149.4	1.13
$W \to \ell\nu + c\bar{c}$ + 1 parton	143.9	1.13
$W \to \ell\nu + c\bar{c}$ + 2 partons	84.2	1.13
$W \to \ell\nu + c\bar{c}$ + 3 partons	44.3	1.13
$W \to \ell\nu + c$ + 0 partons	758.9	1.13
$W \to \ell\nu + c$ + 1 parton	274.5	1.13
$W \to \ell\nu + c$ + 2 partons	71.6	1.13
$W \to \ell\nu + c$ + 3 partons	16.5	1.13
$W \to \ell\nu + c$ + 4 partons	4.8	1.13

Table A.3: *List of the simulated samples used for the single-top process, generated with the* Powheg-Box + Pythia *event generator. The production cross-section and the k-factor for each sample are given.*

Process	Cross-section [pb]	k-factor
t-channel (leptonic top)	17.5	1.05
t-channel (leptonic anti-top)	9.4	1.06
s-channel (leptonic)	1.6	1.11
Wt-channel (inclusive)	20.5	1.09

Table A.4: *List of the simulated samples used for the Z+jets process, generated with the* Alpgen + Pythia *event generator. ℓ refers to the three lepton flavours, e, μ and τ. The production cross-section and the k-factor for each sample are given.*

Process	Cross-section [pb]	k-factor
$Z \to \ell\ell + 0$ partons	719	1.18
$Z \to \ell\ell + 1$ parton	175.7	1.18
$Z \to \ell\ell + 2$ partons	58.9	1.18
$Z \to \ell\ell + 3$ partons	15.7	1.18
$Z \to \ell\ell + 4$ partons	4.0	1.18
$Z \to \ell\ell + 5$ partons	1.3	1.18
$Z \to \ell\ell + b\bar{b} + 0$ partons	6.5	1.18
$Z \to \ell\ell + b\bar{b} + 1$ parton	3.3	1.18
$Z \to \ell\ell + b\bar{b} + 2$ partons	1.3	1.18
$Z \to \ell\ell + b\bar{b} + 3$ partons	0.6	1.18
$Z \to \ell\ell + c\bar{c} + 0$ partons	11.8	1.18
$Z \to \ell\ell + c\bar{c} + 1$ parton	7.1	1.18
$Z \to \ell\ell + c\bar{c} + 2$ partons	3.4	1.18
$Z \to \ell\ell + c\bar{c} + 3$ partons	1.7	1.18

Table A.5: *List of the simulated samples used for the diboson process, generated with the* SHERPA *event generator. ℓ refers to the three lepton flavours, e, μ and τ. The production cross-section and the k-factor for each sample are given.*

Process	Cross-section [pb]	k-factor
$WW \to \ell\ell\nu\nu$	5.3	1.06
$WW \to e\nu q\bar{q}$	7.3	1.06
$WW \to \mu\nu q\bar{q}$	7.3	1.06
$WW \to \tau\nu q\bar{q}$	7.3	1.06
$ZZ \to llll$	8.6	1.00
$ZZ \to e^+e^-q\bar{q}$	0.2	1.00
$ZZ \to \mu^+\mu^-q\bar{q}$	0.2	1.00
$ZZ \to \tau\tau q\bar{q}$	0.2	1.00
$WZ \to \ell\ell\ell\nu$	2.6	1.27
$WZ \to \ell\nu\nu\nu$	1.4	1.05
$WZ \to e\nu q\bar{q}$	1.9	1.05
$WZ \to \mu\nu q\bar{q}$	1.9	1.05
$WZ \to \tau\nu q\bar{q}$	1.9	1.05
$ZW \to e^+e^-q\bar{q}$	1.5	1.05
$ZW \to \mu^+\mu^-q\bar{q}$	1.5	1.05
$ZW \to \tau^+\tau^-q\bar{q}$	1.5	1.05

B

Shape uncertainties

Variations of the shapes of discriminating observables due to signal modelling uncertainties are shown in Fig. B.1 for the NLO matching uncertainty, Fig. B.2 for the scale variations uncertainty and Fig. B.3 for the parton shower uncertainty.

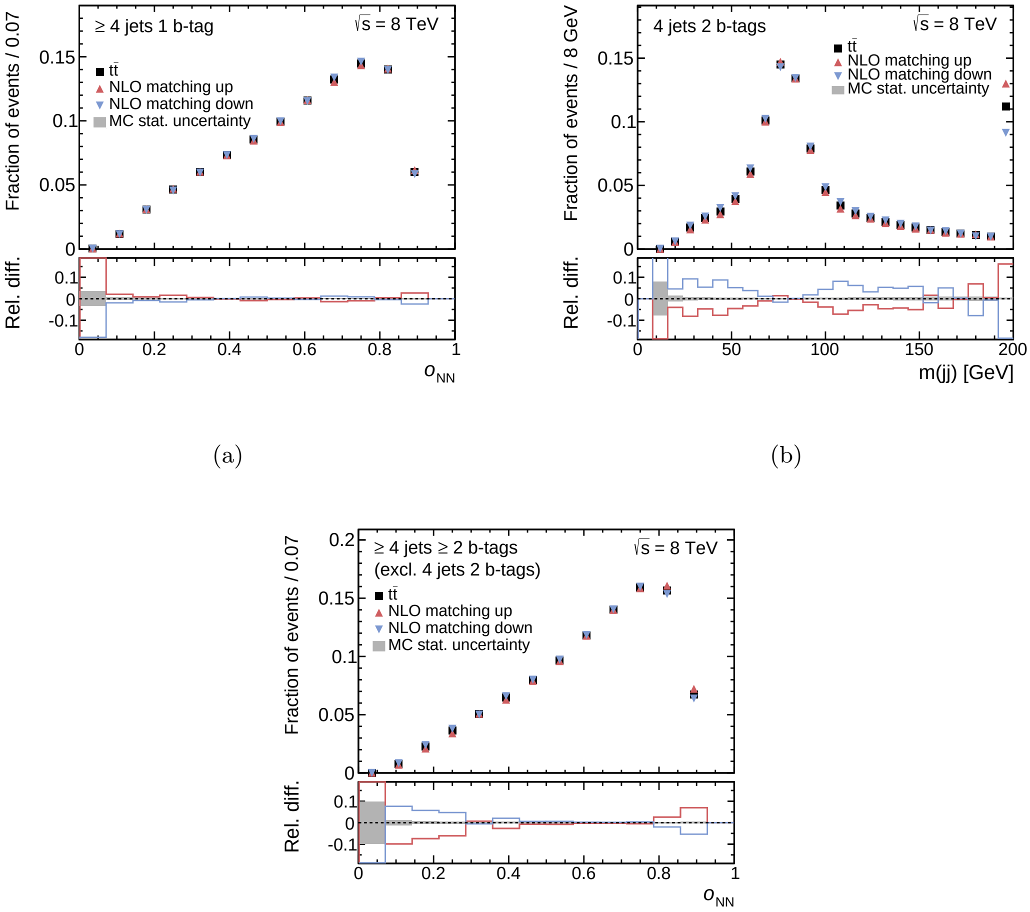

(a)

(b)

(c)

Figure B.1: *The normalised shape variation due to the uncertainty in the NLO matching for the simulated $t\bar{t}$ events of the (a) NN output distribution in SR1, (b) $m(jj)$ distribution in SR2 and (c) NN output distribution in SR3. The lower histogram shows the relative difference between the numbers of events in each bin with respect to the nominal sample. The grey error band represents the MC statistical uncertainty.*

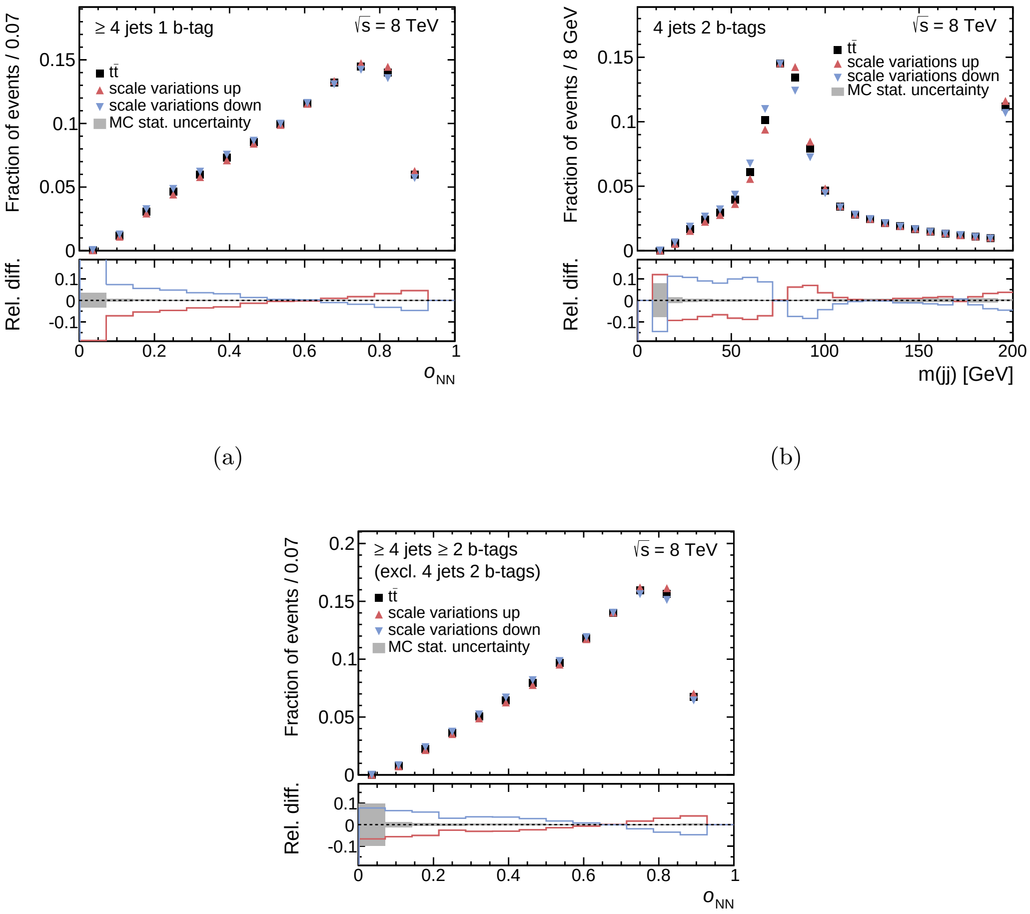

(a)

(b)

(c)

Figure B.2: *The normalised shape variation due to the uncertainty in the scale variations for the simulated $t\bar{t}$ events of the (a) NN output distribution in SR1, (b) $m(jj)$ distribution in SR2 and (c) NN output distribution in SR3. The lower histogram shows the relative difference between the numbers of events in each bin with respect to the nominal sample. The grey error band represents the MC statistical uncertainty.*

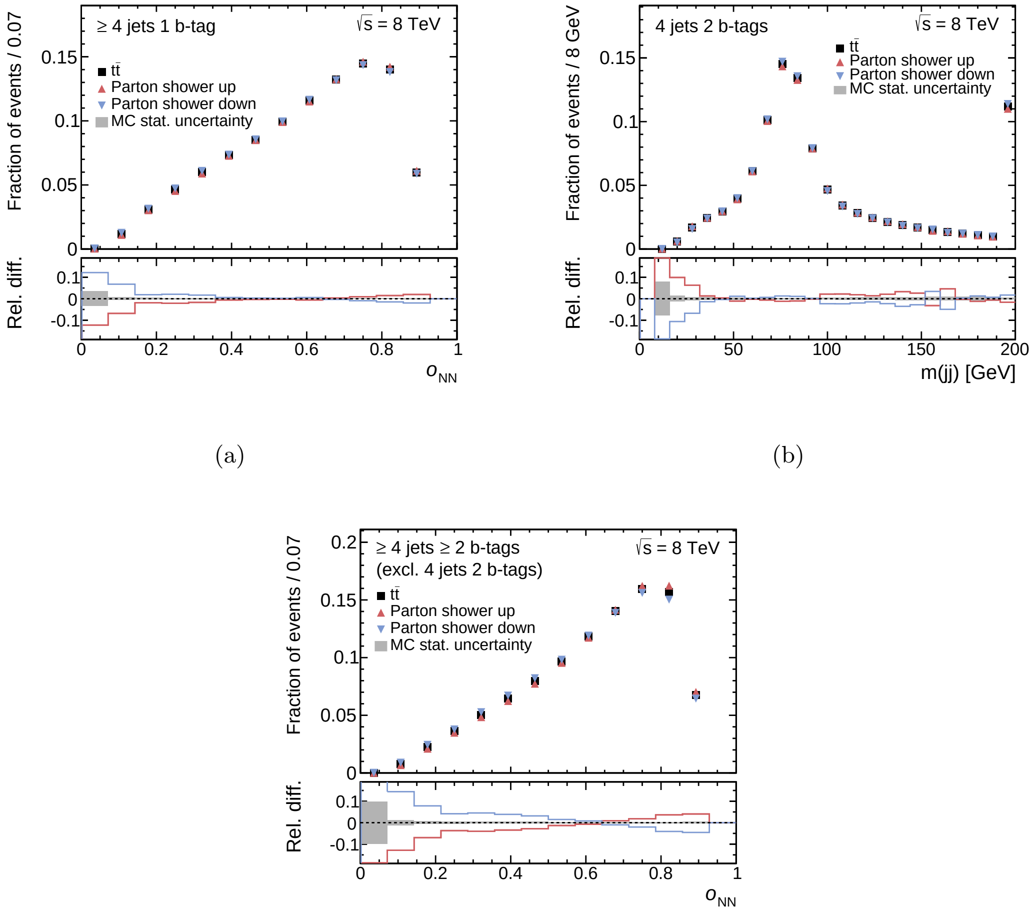

(a)

(b)

(c)

Figure B.3: *The normalised shape variation due to the uncertainty in the parton shower for the simulated $t\bar{t}$ events of the (a) NN output distribution in SR1, (b) $m(jj)$ distribution in SR2 and (c) NN output distribution in SR3. The lower histogram shows the relative difference between the numbers of events in each bin with respect to the nominal sample. The grey error band represents the MC statistical uncertainty.*

C

Acceptance uncertainties

The acceptance uncertainties due to the $t\bar{t}$ modelling in the three signal regions are given in Table C.1 for the inclusive and fiducial measurements. The acceptance uncertainties from all other systematic sources are listed in Table C.2 for SR1, in Table C.3 for SR2 and in Table C.4 for SR3.

Table C.1: *The relative acceptance uncertainty of the $t\bar{t}$ modelling (up, down) in the three signal regions for the inclusive and the fiducial measurement.*

Signal region	NLO matching [%]	Scale variations [%]	Parton shower [%]
		Inclusive	
SR1	−4.3, +4.3	+1.4, −1.4	−0.4, +0.4
SR2	+6.4, −6.4	+9.3, −9.3	+3.4, −3.4
SR3	−13.0, −13.0	+7.6, −7.6	+5.9, −5.9
		Fiducial	
SR1	−4.6, +4.6	+0.1, −0.1	−0.8, +0.8
SR2	+5.8, +5.8	+8.0, −8.0	+3.0, −3.0
SR3	−13.3, +13.3	+6.2, −6.2	+5.4, −5.4

Table C.2: *The relative acceptance uncertainties (up,down) for each process in SR1.*

Source	$t\bar{t}$ [%]	Single-top [%]	Z+jets [%]	Diboson [%]
b-jet energy scale	+0.3, −0.4	+0.5, −0.4	+0.3, −0.2	+0.1, −0.1
JES η intercal. statistical	+0.6, −0.6	+1.0, −1.0	+1.3, −1.2	+1.1, −0.8
JES η intercal. modelling	+0.5, −0.5	+0.9, −0.7	+1.1, −1.0	+0.8, −0.5
JES detector 1	+0.2, −0.2	+0.4, −0.3	+0.3, −0.3	+0.4, −0.2
JES detector 2	+0.2, −0.2	+0.3, −0.2	+0.4, −0.3	+0.3, −0.3
JES detector 3	+0.0, −0.0	+0.1, −0.0	+0.1, −0.0	+0.0, −0.1
JES flavour composition	+0.8, −0.8	+5.0, −4.8	+7.1, −6.7	+5.2, −4.0
JES flavour response	−0.8, +0.8	−2.5, +2.4	−3.9, +4.1	−2.4, +3.0
JES mixed detector and modeling 1	+0.4, −0.4	+0.6, −0.6	+0.6, −0.5	+0.5, −0.5
JES mixed detector and modeling 2	−0.4, +0.4	−0.7, +0.6	−0.7, +0.8	−0.7, +0.6
JES mixed detector and modeling 3	+0.1, −0.1	+0.1, −0.1	+0.3, −0.1	+0.1, −0.2
JES mixed detector and modeling 4	+0.0, −0.0	+0.0, +0.0	+0.0, +0.0	−0.0, +0.0
JES physics modeling 1	+2.5, −2.5	+3.9, −3.9	+5.6, −5.5	+4.1, −3.1
JES physics modeling 2	−0.1, +0.1	−0.1, +0.1	−0.0, +0.2	−0.1, +0.2
JES physics modeling 3	+0.1, −0.1	+0.2, −0.1	+0.5, −0.3	+0.2, −0.3
JES physics modeling 4	+0.0, −0.0	+0.1, −0.0	+0.1, +0.0	+0.0, +0.0
JES pile-up μ	−0.2, +0.2	−0.3, +0.4	−0.5, +0.3	−0.2, +0.3
JES pile-up p_T	+0.0, −0.0	+0.0, +0.1	+0.0, +0.2	+0.0, +0.0
JES pile-up N_{PV}	−0.6, +0.6	−0.8, +0.9	+0.2, −0.0	−0.5, +0.8
JES pile-up ρ	+1.9, −1.9	+2.9, −2.8	+4.1, −4.1	+3.0, −2.3
JES statistical 1	+1.0, −1.0	+1.5, −1.4	+2.1, −1.9	+1.5, −1.2
JES statistical 2	−0.1, +0.1	−0.1, +0.1	−0.1, +0.2	−0.1, +0.1
JES statistical 3	−0.1, +0.1	−0.1, +0.1	+0.1, +0.1	−0.0, +0.1
JES statistical 4	+0.2, −0.2	+0.2, −0.2	+0.2, −0.2	+0.2, −0.3
Punch-through	+0.0, +0.0	−0.0, −0.0	−0.0, +0.0	+0.0, −0.0
Jet energy resolution	+0.4, −0.4	+1.6, −1.6	+6.9, −6.9	+1.9, −1.9
Jet reconstruction efficiency	−0.0, +0.0	−0.0, +0.0	−0.0, +0.0	−0.0, +0.0
$E_{\mathrm{T}}^{\mathrm{miss}}$ scale	+0.0, −0.0	+0.1, −0.0	+1.3, −0.8	+0.3, −0.2
$E_{\mathrm{T}}^{\mathrm{miss}}$ resolution	+0.0, +0.0	−0.0, +0.0	+0.9, +0.8	−0.0, +0.1
Muon momentum scale	+0.0, −0.0	+0.0, −0.0	+0.0, +0.0	+0.0, −0.1
Muon momentum resolution	+0.0, −0.0	+0.0, −0.0	+0.1, −0.1	−0.0, +0.0
Electron energy scale	+0.1, −0.1	+0.1, −0.1	+0.7, −0.4	+0.3, −0.2
Electron energy resolution	−0.0, +0.0	−0.0, +0.0	+0.1, +0.3	+0.0, +0.1
Lepton identification	+1.3, −1.3	+1.3, −1.3	+1.7, −1.7	+10.2, +7.1
Lepton reconstruction	+0.2, −0.2	+0.3, −0.3	+0.3, −0.3	+0.3, −0.3
Lepton trigger	+1.3, −1.3	+1.3, −1.3	+1.2, −1.2	+1.3, −1.3
b-tagging efficiency	−1.6, +1.4	−0.3, +0.1	+0.4, −0.5	+0.0, −0.0
c-tagging efficiency	−0.5, +0.5	−0.4, +0.4	+2.4, −2.5	+4.6, −4.6
Mistag rate	−0.3, +0.3	−0.3, +0.3	+5.2, −5.2	+3.3, −3.3

Table C.3: *The relative acceptance uncertainties (up,down) for each process in SR2.*

Source	$t\bar{t}$ [%]	Single-top [%]	Z+jets [%]	Diboson [%]
b-jet energy scale	+0.5, −0.5	+0.6, −0.7	+0.6, −0.9	+0.3, −1.3
JES η intercal. statistical	+0.3, −0.3	+0.8, −0.7	+0.9, −1.4	0.1, −2.1
JES η intercal. modelling	+0.2, −0.2	+0.6, −0.4	+0.7, −1.0	0.4, −1.5
JES detector 1	+0.1, −0.1	+0.4, −0.4	+0.1, −0.1	−0.2, −0.5
JES detector 2	+0.1, −0.1	+0.3, −0.3	+0.3, −0.1	−0.1, −0.4
JES detector 3	+0.0, −0.0	+0.0, −0.1	+0.1, +0.0	+0.0, +0.0
JES flavour composition	+0.1, −0.2	+3.2, −3.2	+7.0, −5.9	+2.9, −3.0
JES flavour response	−0.1, +0.1	−1.3, +1.3	−2.4, +2.6	−2.5, +0.3
JES mixed detector and modeling 1	+0.2, −0.1	+0.4, −0.4	+0.3, −0.7	−0.3, −0.6
JES mixed detector and modeling 2	−0.2, +0.2	−0.5, +0.5	−1.0, +0.9	−1.5, +0.1
JES mixed detector and modeling 3	+0.1, −0.0	+0.3, −0.2	+0.2, −0.1	−0.3, −0.2
JES mixed detector and modeling 4	+0.0, −0.0	+0.0, +0.0	+0.0, −0.2	+0.0, −0.0
JES physics modeling 1	+1.1, −1.2	+2.6, −2.7	+4.6, −4.8	+2.0, −3.4
JES physics modeling 2	−0.0, +0.0	−0.1, +0.1	−0.2, +0.2	−0.2, −0.3
JES physics modeling 3	+0.1, −0.1	+0.3, −0.2	+0.6, −0.3	−0.4, −0.4
JES physics modeling 4	+0.0, −0.0	+0.1, −0.0	+0.0, −0.2	−0.0, +0.0
JES pile-up μ	−0.1, +0.1	−0.4, +0.3	−0.0, +0.1	−0.7, −0.8
JES pile-up p_T	−0.0, −0.0	+0.0, −0.0	+0.0, −0.1	+0.0, +0.2
JES pile-up N_{PV}	−0.3, +0.2	−0.4, +0.6	+0.4, +0.5	−1.0, −0.2
JES pile-up ρ	+0.8, −0.8	+2.1, −2.1	+3.2, −2.8	+0.9, −3.2
JES statistical 1	+0.4, −0.4	+1.2, −1.3	+1.3, −1.8	+0.7, −2.7
JES statistical 2	−0.0, +0.0	−0.1, +0.1	−0.1, +0.2	−0.1, −0.3
JES statistical 3	−0.0, +0.0	−0.1, +0.1	+0.1, −0.2	+0.0, −0.1
JES statistical 4	+0.1, −0.1	+0.3, −0.3	+0.1, −0.0	−0.2, −0.4
Punch-through	+0.0, −0.0	+0.0, +0.0	+0.0, +0.0	−0.0, +0.0
Jet energy resolution	−0.7, +0.7	+1.2, −1.2	+6.1, −6.1	+1.5, −1.5
Jet reconstruction efficiency	−0.0, +0.0	−0.0, +0.0	−0.0, +0.0	+0.3, −0.3
$E_{\mathrm{T}}^{\mathrm{miss}}$ scale	+0.1, −0.1	+0.0, +0.2	+1.2, −1.2	+0.5, +0.2
$E_{\mathrm{T}}^{\mathrm{miss}}$ resolution	+0.0, +0.0	+0.3, +0.1	+0.4, −0.8	−0.7, −0.4
Muon momentum scale	+0.0, −0.0	+0.0, −0.0	+0.0, −0.0	+0.0, −0.1
Muon momentum resolution	−0.0, +0.0	+0.0, −0.0	+0.1, −0.1	+0.0, −0.0
Electron energy scale	+0.1, −0.1	+0.2, −0.1	+0.3, −0.2	+0.2, −0.1
Electron energy resolution	−0.0, +0.0	+0.0, +0.0	−0.0, −0.1	−0.0, +0.3
Lepton identification	+1.3, −1.3	+1.3, −1.3	+1.7, −1.7	+1.4, −1.4
Lepton reconstruction	+0.2, −0.2	+0.2, −0.2	+0.3, −0.3	+0.3, −0.3
Lepton trigger	+1.3, −1.3	+1.3, −1.3	+1.1, −1.1	+1.3, −1.3
b-tagging efficiency	+4.3, −4.2	+4.6, −4.5	+4.1, −4.0	+3.4, −3.3
c-tagging efficiency	+0.3, −0.3	+0.9, −0.9	+2.5, −2.4	+4.0, −3.8
Mistag rate	+0.2, −0.2	+0.5, −0.5	+4.1, −3.7	+3.4, −3.3

Table C.4: *The relative acceptance uncertainties (up,down) for each process in SR3.*

Source	$t\bar{t}$ [%]	Single-top [%]	Z+jets [%]	Diboson [%]
b-jet energy scale	+0.6, −0.6	+0.5, −0.9	+0.8, −1.6	+1.4, −0.7
JES η intercal. statistical	+0.9, −0.9	+0.8, −1.2	+1.4, −1.6	+1.9, −0.7
JES η intercal. modelling	+0.7, −0.7	+0.7, −1.0	+1.1, −1.1	+1.3, +0.1
JES detector 1	+0.3, −0.3	+0.1, −0.4	+0.1, −0.3	+1.1, +0.3
JES detector 2	+0.3, −0.3	+0.2, −0.2	+0.5, −0.8	+1.3, +0.0
JES detector 3	+0.1, −0.0	+0.0, −0.0	+0.1, −0.0	+0.6, −0.0
JES flavour composition	+1.2, −1.2	+5.0, −5.4	+7.4, −7.1	+7.2, −5.5
JES flavour response	−0.9, +1.0	−2.6, +2.1	−3.5, +3.1	−2.0, +3.7
JES mixed detector and modeling 1	+0.5, −0.5	+0.3, −0.5	+0.5, −0.7	+1.8, −0.0
JES mixed detector and modeling 2	−0.6, +0.6	−0.7, +0.5	−1.4, +0.8	−0.6, +1.9
JES mixed detector and modeling 3	+0.2, −0.2	+0.1, −0.1	+0.5, −0.6	+0.9, +0.4
JES mixed detector and modeling 4	+0.0, −0.0	+0.0, −0.0	−0.0, +0.1	+0.4, −0.0
JES physics modeling 1	+3.7, −3.7	+3.8, −4.4	+5.6, −6.1	+6.8, −4.7
JES physics modeling 2	−0.1, +0.1	−0.1, +0.1	−0.7, +0.2	−0.2, +0.9
JES physics modeling 3	+0.2, −0.2	+0.2, −0.2	+0.1, −0.5	+1.2, +0.0
JES physics modeling 4	+0.0, −0.0	−0.0, −0.0	−0.1, −0.0	+0.5, −0.0
JES pile-up μ	−0.3, +0.3	−0.3, +0.1	−1.1, +0.4	−0.2, +1.7
JES pile-up p_T	+0.0, +0.0	−0.0, +0.1	+0.0, +0.0	+0.2, +0.2
JES pile-up N_{PV}	−1.0, +1.1	−0.9, +0.6	+0.6, +0.0	−0.6, +2.6
JES pile-up ρ	+2.8, −2.7	+2.8, −3.2	+4.5, −4.9	+5.3, −3.2
JES statistical 1	+1.4, −1.4	+1.3, −1.6	+2.7, −2.7	+3.1, −1.8
JES statistical 2	−0.1, +0.1	−0.1, +0.1	−0.5, +0.2	+0.2, +0.7
JES statistical 3	−0.0, +0.1	−0.0, +0.1	−0.3, +0.0	+0.0, +0.4
JES statistical 4	+0.2, −0.2	+0.1, −0.2	+0.3, −0.5	+1.5, +0.0
Punch-through	+0.0, +0.0	−0.0, −0.0	+0.0, −0.0	−0.0, +0.0
Jet energy resolution	+0.6, −0.6	+1.4, −1.4	+6.0, −6.0	+0.5, −0.5
Jet reconstruction efficiency	−0.0, +0.0	−0.0, +0.0	+0.2, −0.2	+0.1, −0.1
$E_{\mathrm{T}}^{\mathrm{miss}}$ scale	+0.1, −0.0	−0.1, +0.0	+0.7, −0.9	+0.8, −0.2
$E_{\mathrm{T}}^{\mathrm{miss}}$ resolution	+0.0, +0.0	−0.0, −0.2	−0.5, −1.1	+0.2, +0.5
Muon momentum scale	+0.0, −0.0	+0.0, −0.0	+0.0, −0.0	−0.0, −0.0
Muon momentum resolution	+0.0, −0.0	+0.0, −0.0	−0.0, +0.0	−0.1, +0.1
Electron energy scale	+0.1, −0.1	+0.2, −0.2	+0.5, −0.8	+0.5, +0.1
Electron energy resolution	−0.0, +0.0	+0.1, −0.0	+0.1, −0.2	+0.0, +0.7
Lepton identification	+1.3, −1.3	+1.3, −1.3	+1.7, −1.7	+1.5, −1.5
Lepton reconstruction	+0.2, −0.2	+0.3, −0.3	+0.3, −0.3	+0.3, −0.3
Lepton trigger	+1.5, −1.1	+1.3, −1.3	+1.1, −1.1	+1.2, −1.2
b-tagging efficiency	+4.3, −4.2	+4.7, −4.6	+4.1, −4.0	+3.0, −3.0
c-tagging efficiency	+1.5, −1.5	+1.5, −1.5	+2.9, −2.8	+5.6, −5.3
Mistag rate	+0.9, −0.9	+1.2, −1.2	+4.6, −4.2	+4.7, −4.5

List of Figures

List of Tables

Bibliography

[1] S. L. Glashow. 'Partial Symmetries of Weak Interactions'. In: *Nucl. Phys.* 22 (1961), pages 579–588. DOI: `10.1016/0029-5582(61)90469-2` (cited on pages 3, 7).

[2] S. Weinberg. 'A Model of Leptons'. In: *Phys. Rev. Lett.* 19 (21 Nov. 1967), pages 1264–1266. DOI: `10.1103/PhysRevLett.19.1264`. URL: `https://link.aps.org/doi/10.1103/PhysRevLett.19.1264` (cited on pages 3, 7).

[3] A. Salam. 'Weak and Electromagnetic Interactions'. In: *Conf. Proc.* C680519 (1968), pages 367–377 (cited on pages 3, 7).

[4] O. W. Greenberg. 'Spin and Unitary Spin Independence in a Paraquark Model of Baryons and Mesons'. In: *Phys. Rev. Lett.* 13 (1964), pages 598–602. DOI: `10.1103/PhysRevLett.13.598` (cited on page 3).

[5] M. Y. Han and Y. Nambu. 'Three Triplet Model with Double SU(3) Symmetry'. In: *Phys. Rev.* 139 (1965). [,187(1965)], B1006–B1010. DOI: `10.1103/PhysRev.139.B1006` (cited on page 3).

[6] H. Fritzsch, M. Gell-Mann and H. Leutwyler. 'Advantages of the Color Octet Gluon Picture'. In: *Phys. Lett.* 47B (1973), pages 365–368. DOI: `10.1016/0370-2693(73)90625-4` (cited on page 3).

[7] M. Tanabashi et al. '2018 Review of Particle Physics'. In: *Phys. Rev.* D 98 (2018), page 030001 (cited on pages 4–6, 75).

[8] ATLAS, CDF, CMS and D0 collaborations. 'First combination of Tevatron and LHC measurements of the top-quark mass'. In: (2014). arXiv: `1403.4427 [hep-ex]` (cited on pages 4, 8, 15).

[9] F. Halzen and A. D. Martin. *QUARKS AND LEPTONS: AN INTRODUCTORY COURSE IN MODERN PARTICLE PHYSICS.* 1984 (cited on page 5).

[10] N. Cabibbo. 'Unitary Symmetry and Leptonic Decays'. In: *Phys. Rev. Lett.* 10 (12 June 1963), pages 531–533. DOI: `10.1103/PhysRevLett.10.531`. URL: `https://link.aps.org/doi/10.1103/PhysRevLett.10.531` (cited on page 6).

[11] M. Kobayashi and T. Maskawa. 'CP Violation in the Renormalizable Theory of Weak Interaction'. In: *Prog. Theor. Phys.* 49 (1973), pages 652–657. DOI: `10.1143/PTP.49.652` (cited on page 6).

[12] P. W. Higgs. ‘Broken Symmetries and the Masses of Gauge Bosons’. In: *Phys. Rev. Lett.* 13 (1964). [,160(1964)], pages 508–509. DOI: `10.1103/PhysRevLett.13.508` (cited on page 7).

[13] F. Englert and R. Brout. ‘Broken Symmetry and the Mass of Gauge Vector Mesons’. In: *Phys. Rev. Lett.* 13 (1964). [,157(1964)], pages 321–323. DOI: `10.1103/PhysRevLett.13.321` (cited on page 7).

[14] CMS Collaboration. ‘Measurement of the weak mixing angle with the Drell-Yan process in proton–proton collisions at the LHC’. In: *Phys. Rev. D* 84 (2011), page 112002. DOI: `10.1103/PhysRevD.84.112002`. arXiv: `1110.2682 [hep-ex]` (cited on page 7).

[15] ATLAS Collaboration. ‘Observation of a new particle in the search for the Standard Model Higgs boson with the ATLAS detector at the LHC’. In: *Phys. Lett. B* 716 (2012), page 1. DOI: `10.1016/j.physletb.2012.08.020`. arXiv: `1207.7214 [hep-ex]` (cited on page 7).

[16] CMS Collaboration. ‘Observation of a new boson at a mass of 125 GeV with the CMS experiment at the LHC’. In: *Phys. Lett. B* 716 (2012), page 30. DOI: `10.1016/j.physletb.2012.08.021`. arXiv: `1207.7235 [hep-ex]` (cited on page 7).

[17] ATLAS and CMS Collaborations. ‘Combined Measurement of the Higgs Boson Mass in pp Collisions at $\sqrt{s} = 7$ and 8 TeV with the ATLAS and CMS Experiments’. In: *Phys. Rev. Lett.* 114 (2015), page 191803. DOI: `10.1103/PhysRevLett.114.191803`. arXiv: `1503.07589 [hep-ex]` (cited on page 7).

[18] CDF collaboration. ‘Observation of top quark production in $\bar{p}p$ collisions’. In: *Phys. Rev. Lett.* 74 (1995), pages 2626–2631. DOI: `10.1103/PhysRevLett.74.2626`. arXiv: `hep-ex/9503002 [hep-ex]` (cited on page 8).

[19] D0 collaboration. ‘Observation of the top quark’. In: *Phys. Rev. Lett.* 74 (1995), pages 2632–2637. DOI: `10.1103/PhysRevLett.74.2632`. arXiv: `hep-ex/9503003 [hep-ex]` (cited on page 8).

[20] W. Wagner. ‘Top quark physics in hadron collisions’. In: *Rept. Prog. Phys.* 68 (2005), pages 2409–2494. DOI: `10.1088/0034-4885/68/10/R03`. arXiv: `hep-ph/0507207 [hep-ph]` (cited on page 8).

[21] A. Quadt. ‘Top quark physics at hadron colliders’. In: *Eur. Phys. J.* C48 (2006), pages 835–1000. DOI: `10.1140/epjc/s2006-02631-6` (cited on page 8).

[22] D. Wicke. ‘Properties of the Top Quark’. In: *Eur. Phys. J.* C71 (2011), page 1627. DOI: `10.1140/epjc/s10052-011-1627-0`. arXiv: `1005.2460 [hep-ex]` (cited on page 8).

[23] F.-P. Schilling. 'Top Quark Physics at the LHC: A Review of the First Two Years'. In: *Int. J. Mod. Phys.* A27 (2012), page 1230016. DOI: `10.1142/S0217751X12300165`. arXiv: `1206.4484 [hep-ex]` (cited on page 8).

[24] A. Giammanco and R. Schwienhorst. 'Single top-quark production at the Tevatron and the LHC'. In: (2017). arXiv: `1710.10699 [hep-ex]` (cited on page 8).

[25] J. C. Collins, D. E. Soper and G. F. Sterman. 'Factorization of Hard Processes in QCD'. In: *Adv. Ser. Direct. High Energy Phys.* 5 (1989), pages 1–91. DOI: `10.1142/9789814503266_0001`. arXiv: `hep-ph/0409313 [hep-ph]` (cited on page 8).

[26] H.-L. Lai et al. 'New parton distributions for collider physics'. In: *Phys. Rev.* D82 (2010), page 074024. DOI: `10.1103/PhysRevD.82.074024`. arXiv: `1007.2241 [hep-ph]` (cited on pages 10–11, 35).

[27] F. Hautmann et al. 'TMDlib and TMDplotter: library and plotting tools for transverse-momentum-dependent parton distributions'. In: *Eur. Phys. J.* C74 (2014), page 3220. DOI: `10.1140/epjc/s10052-014-3220-9`. arXiv: `1408.3015 [hep-ph]` (cited on page 10).

[28] M. Cacciari et al. 'Top-pair production at hadron colliders with next-to-next-to-leading logarithmic soft-gluon resummation'. In: *Phys. Lett. B* 710 (2012), pages 612–622. DOI: `10.1016/j.physletb.2012.03.013`. arXiv: `1111.5869 [hep-ph]` (cited on page 11).

[29] P. Bärnreuther, M. Czakon and A. Mitov. 'Percent Level Precision Physics at the Tevatron: First Genuine NNLO QCD Corrections to $q\bar{q} \to t\bar{t} + X$'. In: *Phys. Rev. Lett.* 109 (2012), page 132001. DOI: `10.1103/PhysRevLett.109.132001`. arXiv: `1204.5201 [hep-ph]` (cited on page 11).

[30] M. Czakon and A. Mitov. 'NNLO corrections to top-pair production at hadron colliders: the all-fermionic scattering channels'. In: *JHEP* 12 (2012), page 054. DOI: `10.1007/JHEP12(2012)054`. arXiv: `1207.0236 [hep-ph]` (cited on page 11).

[31] M. Czakon and A. Mitov. 'NNLO corrections to top pair production at hadron colliders: the quark-gluon reaction'. In: *JHEP* 01 (2013), page 080. DOI: `10.1007/JHEP01(2013)080`. arXiv: `1210.6832 [hep-ph]` (cited on page 11).

[32] M. Czakon, P. Fiedler and A. Mitov. 'The total top quark pair production cross-section at hadron colliders through $O(\alpha_S^4)$'. In: *Phys. Rev. Lett.* 110 (2013), page 252004. DOI: `10.1103/PhysRevLett.110.252004`. arXiv: `1303.6254 [hep-ph]` (cited on pages 11, 157).

[33] M. Czakon and A. Mitov. 'Top++: A program for the calculation of the top-pair cross-section at hadron colliders'. In: *Comput. Phys. Commun.* 185 (2014), page 2930. DOI: `10.1016/j.cpc.2014.06.021`. arXiv: `1112.5675 [hep-ph]` (cited on page 11).

[34] A. D. Martin et al. 'Parton distributions for the LHC'. In: *Eur. Phys. J.* C63 (2009), pages 189–285. DOI: `10.1140/epjc/s10052-009-1072-5`. arXiv: `0901.0002 [hep-ph]` (cited on page 11).

[35] M. Botje et al. *The PDF4LHC Working Group Interim Recommendations.* 2011. arXiv: `1101.0538 [hep-ph]` (cited on page 11).

[36] A. D. Martin et al. 'Uncertainties on α_S in global PDF analyses and implications for predicted hadronic cross sections'. In: *Eur. Phys. J. C* 64 (2009), pages 653–680. DOI: `10.1140/epjc/s10052-009-1164-2`. arXiv: `0905.3531 [hep-ph]` (cited on page 11).

[37] J. Gao et al. 'CT10 next-to-next-to-leading order global analysis of QCD'. In: *Phys. Rev.* D89.3 (2014), page 033009. DOI: `10.1103/PhysRevD.89.033009`. arXiv: `1302.6246 [hep-ph]` (cited on page 11).

[38] R. D. Ball et al. 'Parton distributions with LHC data'. In: *Nucl. Phys.* B867 (2013), pages 244–289. DOI: `10.1016/j.nuclphysb.2012.10.003`. arXiv: `1207.1303 [hep-ph]` (cited on pages 11, 119).

[39] M. Beneke et al. 'Inclusive Top-Pair Production Phenomenology with TOPIXS'. In: *JHEP* 07 (2012), page 194. DOI: `10.1007/JHEP07(2012)194`. arXiv: `1206.2454 [hep-ph]` (cited on page 11).

[40] N. Kidonakis. 'NNNLO soft-gluon corrections for the top-antitop pair production cross section'. In: *Phys. Rev.* D90.1 (2014), page 014006. DOI: `10.1103/PhysRevD.90.014006`. arXiv: `1405.7046 [hep-ph]` (cited on page 11).

[41] C. Muselli et al. 'Top quark pair production beyond NNLO'. In: *JHEP* 08 (2015), page 076. DOI: `10.1007/JHEP08(2015)076`. arXiv: `1505.02006 [hep-ph]` (cited on page 11).

[42] M. Czakon and A. Mitov. 'Inclusive Heavy Flavor Hadroproduction in NLO QCD: The Exact Analytic Result'. In: *Nucl. Phys.* B824 (2010), pages 111–135. DOI: `10.1016/j.nuclphysb.2009.08.020`. arXiv: `0811.4119 [hep-ph]` (cited on page 11).

[43] V. Ahrens et al. 'Renormalization-Group Improved Predictions for Top-Quark Pair Production at Hadron Colliders'. In: *JHEP* 09 (2010), page 097. DOI: `10.1007/JHEP09(2010)097`. arXiv: `1003.5827 [hep-ph]` (cited on page 11).

[44] M. Aliev et al. 'HATHOR: HAdronic Top and Heavy quarks crOss section calculatoR'. In: *Comput. Phys. Commun.* 182 (2011), pages 1034–1046. DOI: `10.1016/j.cpc.2010.12.040`. arXiv: `1007.1327 [hep-ph]` (cited on page 11).

[45] C. Schwinn. *Status of predictions for the total $t\bar{t}$ cross section and measurement of the pole mass.* `https://indico.mpp.mpg.de/event/2644/session/2/contribution/6/material/slides/0.pdf` (cited on page 12).

[46] M. Czakon, D. Heymes and A. Mitov. 'High-precision differential predictions for top-quark pairs at the LHC'. In: *Phys. Rev. Lett.* 116.8 (2016), page 082003. DOI: `10.1103/PhysRevLett.116.082003`. arXiv: `1511.00549 [hep-ph]` (cited on pages 11–12).

[47] M. Czakon et al. 'Top-pair production at the LHC through NNLO QCD and NLO EW'. In: *JHEP* 10 (2017), page 186. DOI: `10.1007/JHEP10(2017)186`. arXiv: `1705.04105 [hep-ph]` (cited on page 13).

[48] M. Jezabek and J. H. Kuhn. 'Semileptonic Decays of Top Quarks'. In: *Phys. Lett.* B207 (1988), pages 91–96. DOI: `10.1016/0370-2693(88)90892-1` (cited on page 13).

[49] M. Jezabek and J. H. Kuhn. 'QCD Corrections to Semileptonic Decays of Heavy Quarks'. In: *Nucl. Phys.* B314 (1989), pages 1–6. DOI: `10.1016/0550-3213(89)90108-9` (cited on page 13).

[50] *Summary plots from the ATLAS Top physics group.* `https://atlas.web.cern.ch/Atlas/GROUPS/PHYSICS/CombinedSummaryPlots/TOP/` (cited on pages 15–16, 156).

[51] CDF and D0 Collaborations. 'Combination of measurements of the top-quark pair production cross section from the Tevatron Collider'. In: *Phys. Rev. D* 89.7 (2014), page 072001. DOI: `10.1103/PhysRevD.89.072001`. arXiv: `1309.7570 [hep-ex]` (cited on page 16).

[52] ATLAS Collaboration. 'Measurement of the $t\bar{t}$ production cross-section using $e\mu$ events with b-tagged jets in pp collisions at $\sqrt{s} = 7$ and 8 TeV with the ATLAS detector'. In: *Eur. Phys. J. C* 74 (2014), page 3109. DOI: `10.1140/epjc/s10052-016-4501-2`. arXiv: `1406.5375 [hep-ex]` (cited on pages 16, 157).

[53] ATLAS Collaboration. 'Measurement of the $t\bar{t}$ production cross-section using $e\mu$ events with b-tagged jets in pp collisions at $\sqrt{s} = 13$ TeV with the ATLAS detector'. In: *Phys. Lett. B* 761 (2016), page 136. DOI: `10.1016/j.physletb.2016.08.019`. arXiv: `1606.02699 [hep-ex]` (cited on page 16).

[54] CMS Collaboration. 'Measurement of the $t\bar{t}$ production cross section in the $e\mu$ channel in proton–proton collisions at $\sqrt{s} = 7$ and 8 TeV'. In: *JHEP* 08 (2016), page 029. DOI: `10.1007/JHEP08(2016)029`. arXiv: `1603.02303 [hep-ex]` (cited on page 16).

[55] CMS Collaboration. 'Measurement of the $t\bar{t}$ production cross section using events in the $e\mu$ final state in pp collisions at $\sqrt{s} = 13$ TeV'. In: *Eur. Phys. J. C* 77 (2017), page 172. DOI: `10.1140/epjc/s10052-017-4718-8`. arXiv: `1611.04040 [hep-ex]` (cited on page 16).

[56] CMS Collaboration. 'Measurements of the $t\bar{t}$ production cross section in lepton+jets final states in pp collisions at 8 TeV and ratio of 8 to 7 TeV cross sections'. In: *Eur. Phys. J. C* 77 (2017), page 15. DOI: `10.1140/epjc/s10052-016-4504-z`. arXiv: `1602.09024 [hep-ex]` (cited on page 16).

[57] ATLAS Collaboration. 'Measurement of the top pair production cross section in 8 TeV proton–proton collisions using kinematic information in the lepton+jets final state with ATLAS'. In: *Phys. Rev. D* 91 (2015), page 112013. DOI: `10.1103/PhysRevD.91.112013`. arXiv: `1504.04251 [hep-ex]` (cited on page 16).

[58] L. Evans and P. Bryant. 'LHC Machine'. In: *Journal of Instrumentation* 3.08 (2008), S08001. URL: `http://stacks.iop.org/1748-0221/3/i=08/a=S08001` (cited on pages 19, 21).

[59] ATLAS Collaboration. 'The ATLAS Experiment at the CERN Large Hadron Collider'. In: *JINST* 3 (2008), S08003. DOI: `10.1088/1748-0221/3/08/S08003` (cited on pages 19, 23, 25–26, 28).

[60] CMS Collaboration. 'The CMS experiment at the CERN LHC'. In: *JINST* 3 (2008), S08004. DOI: `10.1088/1748-0221/3/08/S08004` (cited on page 19).

[61] LHCb Collaboration. 'The LHCb Detector at the LHC'. In: *Journal of Instrumentation* 3.08 (2008), S08005. URL: `http://stacks.iop.org/1748-0221/3/i=08/a=S08005` (cited on page 19).

[62] ALICE Collaboration. 'The ALICE experiment at the CERN LHC'. In: *Journal of Instrumentation* 3.08 (2008), S08002. URL: `http://stacks.iop.org/1748-0221/3/i=08/a=S08002` (cited on page 19).

[63] The LHCf Collaboration. 'The LHCf detector at the CERN Large Hadron Collider'. In: *Journal of Instrumentation* 3.08 (2008), S08006. URL: `http://stacks.iop.org/1748-0221/3/i=08/a=S08006` (cited on page 19).

[64] The TOTEM Collaboration. 'The TOTEM Experiment at the CERN Large Hadron Collider'. In: *Journal of Instrumentation* 3.08 (2008), S08007. URL: `http://stacks.iop.org/1748-0221/3/i=08/a=S08007` (cited on page 20).

[65] MoEDAL Collaboration. *Technical Design Report of the MoEDAL Experiment*. Technical report CERN-LHCC-2009-006. MoEDAL-TDR-001. CERN, June 2009. URL: `http://cds.cern.ch/record/1181486` (cited on page 20).

[66] *The CERN accelerator complex.* `https://cds.cern.ch/record/1621894` (cited on page 20).

[67] M. Lamont. 'Status of the LHC'. In: *Journal of Physics: Conference Series* 455.1 (2013), page 012001. URL: `http://stacks.iop.org/1742-6596/455/i=1/a=012001` (cited on page 21).

[68] *Luminosity Public Results.* `https://twiki.cern.ch/twiki/bin/view/AtlasPublic/LuminosityPublicResults` (cited on pages 22, 42).

[69] ATLAS Collaboration. 'Study of the material of the ATLAS inner detector for Run 2 of the LHC'. In: *JINST* 12 (2017), P12009. DOI: `10.1088/1748-0221/12/12/P12009`. arXiv: `1707.02826 [hep-ex]` (cited on page 27).

[70] ATLAS Collaboration. 'Performance of the ATLAS Trigger System in 2010'. In: *Eur. Phys. J. C* 72 (2012), page 1849. DOI: `10.1140/epjc/s10052-011-1849-1`. arXiv: `1110.1530 [hep-ex]` (cited on page 28).

[71] ATLAS Collaboration. 'Luminosity determination in *pp* collisions at $\sqrt{s} = 8$ TeV using the ATLAS detector at the LHC'. In: *Eur. Phys. J. C* 76 (2016), page 653. DOI: `10.1140/epjc/s10052-016-4466-1`. arXiv: `1608.03953 [hep-ex]` (cited on pages 29, 123).

[72] F. Lasagni Manghi. 'The LUCID detector ATLAS luminosity monitor and its electronic system'. In: *Nucl. Instrum. Meth.* A824 (2016), pages 311–312. DOI: `10.1016/j.nima.2015.11.134` (cited on page 29).

[73] V. Cindro et al. 'The ATLAS beam conditions monitor'. In: *JINST* 3 (2008), P02004. DOI: `10.1088/1748-0221/3/02/P02004` (cited on page 29).

[74] ATLAS Collaboration. *Performance of the ATLAS Electron and Photon Trigger in pp Collisions at $\sqrt{s} = 7$ TeV in 2011.* ATLAS-CONF-2012-048. 2012. URL: `https://cds.cern.ch/record/1450089` (cited on pages 30, 54).

[75] ATLAS Collaboration. 'Performance of the ATLAS muon trigger in *pp* collisions at $\sqrt{s} = 8$ TeV'. In: *Eur. Phys. J. C* 75 (2015), page 120. DOI: `10.1140/epjc/s10052-015-3325-9`. arXiv: `1408.3179 [hep-ex]` (cited on pages 30, 54).

[76] S. Höche. 'Introduction to parton-shower event generators'. In: *Proceedings, Theoretical Advanced Study Institute in Elementary Particle Physics: Journeys Through the Precision Frontier: Amplitudes for Colliders (TASI 2014): Boulder, Colorado, June 2-27, 2014.* 2015, pages 235–295. DOI: `10.1142/9789814678766_0005`. arXiv: `1411.4085 [hep-ph]`. URL: `https://inspirehep.net/record/1328513/files/arXiv:1411.4085.pdf` (cited on page 32).

[77] Z. Marshall. 'Simulation of Pile-up in the ATLAS Experiment'. In: *J. Phys. Conf. Ser.* 513 (2014), page 022024. DOI: `10.1088/1742-6596/513/2/022024` (cited on page 33).

[78] T. Sjöstrand et al. 'An introduction to PYTHIA 8.2'. In: *Comput. Phys. Commun.* 191 (2015), pages 159–177. DOI: `10.1016/j.cpc.2015.01.024`. arXiv: `1410.3012 [hep-ph]` (cited on page 33).

[79] S. Alioli et al. 'A general framework for implementing NLO calculations in shower Monte Carlo programs: the POWHEG BOX'. In: *JHEP* 06 (2010), page 043. DOI: `10.1007/JHEP06(2010)043`. arXiv: `1002.2581 [hep-ph]` (cited on pages 33, 35).

[80] S. Frixione et al. 'A Positive-weight next-to-leading-order Monte Carlo for heavy flavour hadroproduction'. In: *JHEP* 0709 (2007), page 126. DOI: `10.1088/1126-6708/2007/09/126`. arXiv: `0707.3088 [hep-ph]` (cited on pages 33, 35).

[81] S. Frixione and B. R. Webber. 'Matching NLO QCD computations and parton shower simulations'. In: *JHEP* 06 (2002), page 029. DOI: `10.1088/1126-6708/2002/06/029`. arXiv: `hep-ph/0204244 [hep-ph]` (cited on page 33).

[82] S. Frixione, P. Nason and B. R. Webber. 'Matching NLO QCD and parton showers in heavy flavor production'. In: *JHEP* 08 (2003), page 007. DOI: `10.1088/1126-6708/2003/08/007`. arXiv: `hep-ph/0305252 [hep-ph]` (cited on page 33).

[83] M. L. Mangano et al. 'ALPGEN, a generator for hard multiparton processes in hadronic collisions'. In: *JHEP* 07 (2003), page 001. DOI: `10.1088/1126-6708/2003/07/001`. arXiv: `hep-ph/0206293 [hep-ph]` (cited on page 34).

[84] J. Alwall et al. 'Comparative study of various algorithms for the merging of parton showers and matrix elements in hadronic collisions'. In: *Eur. Phys. J. C* 53 (2008), pages 473–500. DOI: `10.1140/epjc/s10052-007-0490-5`. arXiv: `0706.2569 [hep-ph]` (cited on page 34).

[85] T. Gleisberg et al. 'Event generation with SHERPA 1.1'. In: *JHEP* 02 (2009), page 007. DOI: `10.1088/1126-6708/2009/02/007`. arXiv: `0811.4622 [hep-ph]` (cited on page 34).

[86] S. Catani et al. 'QCD matrix elements + parton showers'. In: *JHEP* 11 (2001), page 063. DOI: `10.1088/1126-6708/2001/11/063`. arXiv: `hep-ph/0109231 [hep-ph]` (cited on page 34).

[87] T. Sjostrand, S. Mrenna and P. Z. Skands. 'PYTHIA 6.4 Physics and Manual'. In: *JHEP* 05 (2006), page 026. DOI: `10.1088/1126-6708/2006/05/026`. arXiv: `hep-ph/0603175 [hep-ph]` (cited on page 34).

[88] G. Corcella et al. ‘HERWIG 6: An Event generator for hadron emission reactions with interfering gluons (including supersymmetric processes)’. In: *JHEP* 01 (2001), page 010. DOI: `10.1088/1126-6708/2001/01/010`. arXiv: `hep-ph/0011363 [hep-ph]` (cited on page 34).

[89] J. M. Butterworth, J. R. Forshaw and M. H. Seymour. ‘Multiparton interactions in photoproduction at HERA’. In: *Z. Phys. C* 72 (1996), pages 637–646. DOI: `10.1007/BF02909195,10.1007/s002880050286`. arXiv: `hep-ph/9601371` (cited on page 34).

[90] S. Agostinelli et al. ‘GEANT4: A simulation toolkit’. In: *Nucl. Instrum. Meth. A* 506 (2003), pages 250–303. DOI: `10.1016/S0168-9002(03)01368-8` (cited on page 34).

[91] ATLAS Collaboration. ‘The ATLAS Simulation Infrastructure’. In: *Eur. Phys. J. C* 70 (2010), page 823. DOI: `10.1140/epjc/s10052-010-1429-9`. arXiv: `1005.4568 [physics.ins-det]` (cited on page 34).

[92] P. Z. Skands. ‘Tuning Monte Carlo generators: The Perugia tunes’. In: *Phys. Rev. D* 82 (2010), page 074018. DOI: `10.1103/PhysRevD.82.074018`. arXiv: `1005.3457 [hep-ph]` (cited on pages 35, 118).

[93] J. Pumplin et al. ‘New generation of parton distributions with uncertainties from global QCD analysis’. In: *JHEP* 07 (2002), page 012. DOI: `10.1088/1126-6708/2002/07/012`. arXiv: `hep-ph/0201195` (cited on page 36).

[94] R. Gavin et al. ‘FEWZ 2.0: A code for hadronic Z production at next-to-next-to-leading order’. In: *Comput. Phys. Commun.* 182 (2011), pages 2388–2403. DOI: `10.1016/j.cpc.2011.06.008`. arXiv: `1011.3540 [hep-ph]` (cited on page 37).

[95] R. Gavin et al. ‘W Physics at the LHC with FEWZ 2.1’. In: *Comput. Phys. Commun.* 184 (2013), pages 208–214. DOI: `10.1016/j.cpc.2012.09.005`. arXiv: `1201.5896 [hep-ph]` (cited on page 37).

[96] N. Kidonakis. ‘Two-loop soft anomalous dimensions for single top quark associated production with a W^- or H^-’. In: *Phys. Rev. D* 82 (2010), page 054018. DOI: `10.1103/PhysRevD.82.054018`. arXiv: `1005.4451 [hep-ph]` (cited on page 37).

[97] P. Kant et al. ‘HatHor for single top-quark production: Updated predictions and uncertainty estimates for single top-quark production in hadronic collisions’. In: *Comput. Phys. Commun.* 191 (2015), pages 74–89. DOI: `10.1016/j.cpc.2015.02.001`. arXiv: `1406.4403 [hep-ph]` (cited on page 38).

[98] J. M. Campbell et al. ‘Next-to-Leading-Order Predictions for t-Channel Single-Top Production at Hadron Colliders’. In: *Phys. Rev. Lett.* 102 (2009), page 182003. DOI: `10.1103/PhysRevLett.102.182003`. arXiv: `0903.0005 [hep-ph]` (cited on page 38).

[99] J. M. Campbell, R. K. Ellis and C. Williams. 'Vector boson pair production at the LHC'. In: *JHEP* 07 (2011), page 018. DOI: `10.1007/JHEP07(2011)018`. arXiv: `1105.0020 [hep-ph]` (cited on page 38).

[100] T. Cornelissen et al. *Concepts, Design and Implementation of the ATLAS New Tracking (NEWT)*. Technical report ATL-SOFT-PUB-2007-007. ATL-COM-SOFT-2007-002. Geneva: CERN, Mar. 2007. URL: `https://cds.cern.ch/record/1020106` (cited on page 41).

[101] R. Fruhwirth. 'Application of Kalman filtering to track and vertex fitting'. In: *Nucl. Instrum. Meth.* A262 (1987), pages 444–450. DOI: `10.1016/0168-9002(87)90887-4` (cited on page 41).

[102] ATLAS Collaboration. *Performance of the ATLAS Silicon Pattern Recognition Algorithm in Data and Simulation at* $\sqrt{s} = 7$ *TeV*. ATLAS-CONF-2010-072. 2010. URL: `https://cds.cern.ch/record/1281363` (cited on page 41).

[103] ATLAS Collaboration. *Track Reconstruction Performance of the ATLAS Inner Detector at* $\sqrt{s} = 13$ *TeV*. ATL-PHYS-PUB-2015-018. 2015. URL: `https://cds.cern.ch/record/2037683` (cited on page 42).

[104] M. Limper. 'Track and Vertex Reconstruction in the ATLAS Inner Detector'. PhD thesis. NIKHEF, Amsterdam, 2009. URL: `http://inspirehep.net/record/834028/files/CERN-THESIS-2009-061.pdf` (cited on page 42).

[105] G. Piacquadio, K. Prokofiev and A. Wildauer. 'Primary vertex reconstruction in the ATLAS experiment at LHC'. In: *Journal of Physics: Conference Series* 119.3 (2008), page 032033. URL: `http://stacks.iop.org/1742-6596/119/i=3/a=032033` (cited on page 42).

[106] ATLAS Collaboration. 'Reconstruction of primary vertices at the ATLAS experiment in Run 1 proton-proton collisions at the LHC'. In: (2016). arXiv: `1611.10235 [physics.ins-det]` (cited on page 42).

[107] R. Fruhwirth, W. Waltenberger and P. Vanlaer. 'Adaptive vertex fitting'. In: *J. Phys.* G34 (2007), N343. DOI: `10.1088/0954-3899/34/12/N01` (cited on page 42).

[108] ATLAS Collaboration. 'Electron efficiency measurements with the ATLAS detector using 2012 LHC proton-proton collision data'. In: (2016). arXiv: `1612.01456 [hep-ex]` (cited on pages 43–44).

[109] W. Lampl et al. 'Calorimeter clustering algorithms: Description and performance'. In: (2008) (cited on page 43).

[110] ATLAS Collaboration. 'Electron and photon energy calibration with the ATLAS detector using LHC Run 1 data'. In: *Eur. Phys. J. C* 74 (2014), page 3071. DOI: `10.1140/epjc/s10052-014-3071-4`. arXiv: `1407.5063 [hep-ex]` (cited on pages 43, 112).

[111] ATLAS Collaboration. 'Muon reconstruction efficiency and momentum resolution of the ATLAS experiment in proton–proton collisions at $\sqrt{s} = 7$ TeV in 2010'. In: *Eur. Phys. J. C* 74 (2014), page 3034. DOI: `10.1140/epjc/s10052-014-3034-9`. arXiv: `1404.4562 [hep-ex]` (cited on page 45).

[112] ATLAS Collaboration. 'Measurement of the muon reconstruction performance of the ATLAS detector using 2011 and 2012 LHC proton–proton collision data'. In: *Eur. Phys. J. C* 74 (2014), page 3130. DOI: `10.1140/epjc/s10052-014-3130-x`. arXiv: `1407.3935 [hep-ex]` (cited on pages 45–46, 112).

[113] ATLAS Collaboration. 'ATLAS: Detector and physics performance technical design report. Volume 1'. In: (1999) (cited on page 45).

[114] D. Adams et al. *Track reconstruction in the ATLAS Muon Spectrometer with MOORE 007.* Technical report ATL-SOFT-2003-007. revised version number 1 submitted on 2003-10-13 13:51:39. Geneva: CERN, May 2003. URL: `http://cds.cern.ch/record/685500` (cited on page 45).

[115] T. Lagouri et al. 'A muon identification and combined reconstruction procedure for the ATLAS detector at the LHC at CERN'. In: *2003 IEEE Nuclear Science Symposium. Conference Record (IEEE Cat. No.03CH37515).* Volume 3. Oct. 2003, 1545–1548 Vol.3. DOI: `10.1109/NSSMIC.2003.1352171` (cited on page 45).

[116] M. Cacciari, G. P. Salam and G. Soyez. 'The Anti-k(t) jet clustering algorithm'. In: *JHEP* 04 (2008), page 063. DOI: `10.1088/1126-6708/2008/04/063`. arXiv: `0802.1189 [hep-ph]` (cited on page 46).

[117] J. Tseng and H. Evans. 'Sequential recombination algorithm for jet clustering and background subtraction'. In: *Phys. Rev.* D88 (2013), page 014044. DOI: `10.1103/PhysRevD.88.014044`. arXiv: `1304.1025 [hep-ph]` (cited on page 46).

[118] ATLAS Collaboration. 'Topological cell clustering in the ATLAS calorimeters and its performance in LHC Run 1'. In: *Eur. Phys. J. C* 77 (2017), page 490. DOI: `10.1140/epjc/s10052-017-5004-5`. arXiv: `1603.02934 [hep-ex]` (cited on page 46).

[119] B. Isildak. 'Measurement of the differential dijet production cross section in proton-proton collisions at $\sqrt{s} = 7$ tev'. PhD thesis. Bogazici U., 2011. arXiv: `1308.6064 [hep-ex]`. URL: `http://inspirehep.net/record/1251416/files/arXiv:1308.6064.pdf` (cited on page 47).

[120] T. Barillari et al. *Local Hadronic Calibration.* Technical report ATL-LARG-PUB-2009-001-2. ATL-COM-LARG-2008-006. ATL-LARG-PUB-2009-001. Due to a report-number conflict with another document, the report-number ATL-LARG-PUB-2009-001-2 has been assigned. Geneva: CERN, June 2008. URL: `https://cds.cern.ch/record/1112035` (cited on page 48).

[121] ATLAS Collaboration. 'Jet energy measurement with the ATLAS detector in proton–proton collisions at $\sqrt{s} = 7$ TeV'. In: *Eur. Phys. J. C* 73 (2013), page 2304. DOI: `10.1140/epjc/s10052-013-2304-2`. arXiv: `1112.6426 [hep-ex]` (cited on pages 48, 54).

[122] ATLAS Collaboration. *Monte Carlo Calibration and Combination of In-situ Measurements of Jet Energy Scale, Jet Energy Resolution and Jet Mass in ATLAS.* ATLAS-CONF-2015-037. 2015. URL: `https://cds.cern.ch/record/2044941` (cited on pages 48, 112–113, 117).

[123] ATLAS Collaboration. *Pile-up subtraction and suppression for jets in ATLAS.* ATLAS-CONF-2013-083. 2013. URL: `https://cds.cern.ch/record/1570994` (cited on pages 48, 114).

[124] ATLAS Collaboration. *Jet global sequential corrections with the ATLAS detector in proton–proton collisions at $\sqrt{s} = 8$ TeV.* ATLAS-CONF-2015-002. 2015. URL: `https://cds.cern.ch/record/2001682` (cited on page 48).

[125] ATLAS Collaboration. 'Jet energy measurement and its systematic uncertainty in proton–proton collisions at $\sqrt{s} = 7$ TeV with the ATLAS detector'. In: *Eur. Phys. J. C* 75 (2015), page 17. DOI: `10.1140/epjc/s10052-014-3190-y`. arXiv: `1406.0076 [hep-ex]` (cited on pages 49, 112).

[126] ATLAS Collaboration. 'Performance of pile-up mitigation techniques for jets in *pp* collisions at $\sqrt{s} = 8$ TeV using the ATLAS detector'. In: *Eur. Phys. J. C* 76 (2016), page 581. DOI: `10.1140/epjc/s10052-016-4395-z`. arXiv: `1510.03823 [hep-ex]` (cited on page 49).

[127] *B-jet identification.* `https://www-d0.fnal.gov/Run2Physics/top/singletop_observation/` (cited on page 50).

[128] ATLAS Collaboration. 'Performance of b-jet identification in the ATLAS experiment'. In: *JINST* 11 (2016), P04008. DOI: `10.1088/1748-0221/11/04/P04008`. arXiv: `1512.01094 [hep-ex]` (cited on pages 49, 51).

[129] ATLAS Collaboration. *Commissioning of the ATLAS high performance b-tagging algorithms in the* 7 *TeV collision data.* ATLAS-CONF-2011-102. 2011. URL: `https://cds.cern.ch/record/1369219` (cited on page 49).

[130] ATLAS Collaboration. *Calibration of b-tagging using dileptonic top pair events in a combinatorial likelihood approach with the ATLAS experiment.* ATLAS-CONF-2014-004. 2014. URL: `https://cds.cern.ch/record/1664335` (cited on pages 51, 117).

[131] ATLAS Collaboration. *Calibration of the performance of b-tagging for c and light-flavour jets in the 2012 ATLAS data.* ATLAS-CONF-2014-046. 2014. URL: `https://cds.cern.ch/record/1741020` (cited on pages 51, 117).

[132] ATLAS Collaboration. 'Performance of missing transverse momentum reconstruction in proton–proton collisions at $\sqrt{s} = 7$ TeV with ATLAS'. In: *Eur. Phys. J. C* 72 (2012), page 1844. DOI: `10.1140/epjc/s10052-011-1844-6`. arXiv: `1108.5602 [hep-ex]` (cited on page 52).

[133] ATLAS Collaboration. 'Performance of algorithms that reconstruct missing transverse momentum in $\sqrt{s} = 8$ TeV proton–proton collisions in the ATLAS detector'. In: *Eur. Phys. J. C* 77 (2017), page 241. DOI: `10.1140/epjc/s10052-017-4780-2`. arXiv: `1609.09324 [hep-ex]` (cited on pages 52, 118).

[134] T. Chwalek. 'Measurement of the W boson helicity in top-antitop quark events with the CDF II experiment'. Karlsruhe U., EKP, 2006. DOI: `10.2172/911839`. URL: `http://lss.fnal.gov/archive/thesis/2000/fermilab-thesis-2006-100.pdf` (cited on page 55).

[135] J. Erdmann et al. 'A likelihood-based reconstruction algorithm for top-quark pairs and the KLFitter framework'. In: *Nucl. Instrum. Meth.* A748 (2014), pages 18–25. DOI: `10.1016/j.nima.2014.02.029`. arXiv: `1312.5595 [hep-ex]` (cited on page 56).

[136] ATLAS Collaboration. *Estimation of non-prompt and fake lepton backgrounds in final states with top quarks produced in proton–proton collisions at $\sqrt{s} = 8$ TeV with the ATLAS Detector.* ATLAS-CONF-2014-058. 2014. URL: `https://cds.cern.ch/record/1951336` (cited on pages 63, 70, 123).

[137] C. F. Berger et al. 'Next-to-Leading Order QCD Predictions for W+3-Jet Distributions at Hadron Colliders'. In: *Phys. Rev.* D80 (2009), page 074036. DOI: `10.1103/PhysRevD.80.074036`. arXiv: `0907.1984 [hep-ph]` (cited on page 73).

[138] C. F. Berger et al. 'Precise Predictions for $W + 3$ Jet Production at Hadron Colliders'. In: *Phys. Rev. Lett.* 102 (2009), page 222001. DOI: `10.1103/PhysRevLett.102.222001`. arXiv: `0902.2760 [hep-ph]` (cited on page 73).

[139] C. F. Berger et al. 'Precise Predictions for W + 4 Jet Production at the Large Hadron Collider'. In: *Phys. Rev. Lett.* 106 (2011), page 092001. DOI: `10.1103/PhysRevLett.106.092001`. arXiv: `1009.2338 [hep-ph]` (cited on page 73).

[140] Z. Bern et al. 'Next-to-Leading Order W + 5-Jet Production at the LHC'. In: *Phys. Rev.* D88.1 (2013), page 014025. DOI: `10.1103/PhysRevD.88.014025`. arXiv: `1304.1253 [hep-ph]` (cited on page 73).

[141] R. Boughezal et al. 'W-boson production in association with a jet at next-to-next-to-leading order in perturbative QCD'. In: *Phys. Rev. Lett.* 115.6 (2015), page 062002. DOI: `10.1103/PhysRevLett.115.062002`. arXiv: `1504.02131 [hep-ph]` (cited on page 73).

[142] ATLAS Collaboration. 'Measurement of differential cross sections and W^+/W^- cross-section ratios for W boson production in association with jets at $\sqrt{s} = 8$ TeV with the ATLAS detector'. In: (2017). arXiv: `1711.03296 [hep-ex]` (cited on pages 73–74).

[143] M. Sandhoff. 'Prospects of a cross section ratio measurement of W and Z events as a function of the jet multiplicity with early ATLAS data'. PhD thesis. Wuppertal U., 2011. URL: `http://elpub.bib.uni-wuppertal.de/edocs/dokumente/fbc/physik/diss2010/sandhoff` (cited on page 74).

[144] T. T. Boek. 'Estimation of the W+ jet background in the analysis of semileptonic top quark pair events'. PhD thesis. Wuppertal U., 2013. URL: `http://elpub.bib.uni-wuppertal.de/servlets/DerivateServlet/Derivate-4092/dc1330.pdf` (cited on page 74).

[145] J. M. Campbell, J. W. Huston and W. J. Stirling. 'Hard Interactions of Quarks and Gluons: A Primer for LHC Physics'. In: *Rept. Prog. Phys.* 70 (2007), page 89. DOI: `10.1088/0034-4885/70/1/R02`. arXiv: `hep-ph/0611148 [hep-ph]` (cited on page 76).

[146] Z. Bern et al. 'Left-Handed W Bosons at the LHC'. In: *Phys. Rev.* D84 (2011), page 034008. DOI: `10.1103/PhysRevD.84.034008`. arXiv: `1103.5445 [hep-ph]` (cited on page 76).

[147] CMS Collaboration. 'Measurement of the Polarization of W Bosons with Large Transverse Momenta in W+Jets Events at the LHC'. In: *Phys. Rev. Lett.* 107 (2011), page 021802. DOI: `10.1103/PhysRevLett.107.021802`. arXiv: `1104.3829 [hep-ex]` (cited on page 76).

[148] M. Feindt. 'A Neural Bayesian Estimator for Conditional Probability Densities'. In: (2004). arXiv: `physics/0402093 [physics.data-an]` (cited on pages 92, 94).

[149] M. Feindt and U. Kerzel. 'The NeuroBayes neural network package'. In: *Nuclear Instruments and Methods in Physics Research Section A: Accelerators, Spectrometers, Detectors and Associated Equipment* 559.1 (2006). Proceedings of the X International Workshop on Advanced Computing and Analysis Techniques in Physics ResearchA-CAT 05X International Workshop on Advanced Computing and Analysis Techniques,

pages 190–194. DOI: `https://doi.org/10.1016/j.nima.2005.11.166`. URL: `http://www.sciencedirect.com/science/article/pii/S0168900205022679` (cited on pages 92, 95).

[150] P. I. Technologies. 'The NeuroBayes® User's Guide'. In: *http://neurobayes.phi-t.de/nb_doc/NeuroBayes-HowTo.pdf* (2010) (cited on page 94).

[151] D. E. Rumelhart, G. E. Hinton and R. J. Williams. 'Learning representations by back-propagating errors'. In: *Nature* 323.6088 (Oct. 1986), pages 533–536. URL: `http://dx.doi.org/10.1038/323533a0` (cited on page 95).

[152] ATLAS Collaboration. 'Measurement of the top quark mass in the $t\bar{t} \rightarrow$ lepton+jets and $t\bar{t} \rightarrow$ dilepton channels using $\sqrt{s} = 7$ TeV ATLAS data'. In: *Eur. Phys. J. C* 75 (2015), page 330. DOI: `10.1140/epjc/s10052-015-3544-0`. arXiv: `1503.05427 [hep-ex]` (cited on page 108).

[153] CMS Collaboration. 'Measurement of the top quark mass using proton–proton data at $\sqrt{s} = 7$ and 8 TeV'. In: *Phys. Rev. D* 93 (2016), page 072004. DOI: `10.1103/PhysRevD.93.072004`. arXiv: `1509.04044 [hep-ex]` (cited on page 108).

[154] D0 Collaborations, V. M. Abazov et al. 'Precise measurement of the top quark mass from lepton+jets events at D0'. In: *Phys. Rev. Lett.* 101 (2008), page 182001. DOI: `10.1103/PhysRevLett.101.182001`. arXiv: `0807.2141 [hep-ex]` (cited on page 108).

[155] CDF Collaborations, T. Aaltonen et al. 'Precision Top-Quark Mass Measurements at CDF'. In: *Phys. Rev. Lett.* 109 (2012), page 152003. DOI: `10.1103/PhysRevLett.109.152003`. arXiv: `1207.6758 [hep-ex]` (cited on page 108).

[156] ATLAS Collaboration. *Data-driven determination of the energy scale and resolution of jets reconstructed in the ATLAS calorimeters using dijet and multijet events at* $\sqrt{s} = 8$ *TeV*. ATLAS-CONF-2015-017. 2015. URL: `https://cds.cern.ch/record/2008678` (cited on page 113).

[157] ATLAS Collaboration. *Determination of the jet energy scale and resolution at ATLAS using* Z/γ*-jet events in data at* $\sqrt{s} = 8$ *TeV*. ATLAS-CONF-2015-057. 2015. URL: `https://cds.cern.ch/record/2059846` (cited on page 113).

[158] ATLAS Collaboration. *Jet Energy Resolution and Selection Efficiency Relative to Track Jets from In-situ Techniques with the ATLAS Detector Using Proton–Proton Collisions at a Center of Mass Energy* $\sqrt{s} = 7$ *TeV*. ATLAS-CONF-2010-054. 2010. URL: `https://cds.cern.ch/record/1281311` (cited on page 117).

[159] ATLAS Collaboration. *Comparison of Monte Carlo generator predictions to ATLAS measurements of top pair production at* 7 *TeV*. ATL-PHYS-PUB-2015-002. 2015. URL: `https://cds.cern.ch/record/1981319` (cited on page 118).

[160] J. Butterworth et al. ‘PDF4LHC recommendations for LHC Run II’. In: *J. Phys. G* 43 (2016), page 023001. DOI: `10.1088/0954-3899/43/2/023001`. arXiv: `1510.03865 [hep-ph]` (cited on page 119).

[161] S. Dulat et al. ‘New parton distribution functions from a global analysis of quantum chromodynamics’. In: *Phys. Rev.* D93.3 (2016), page 033006. DOI: `10.1103/PhysRevD.93.033006`. arXiv: `1506.07443 [hep-ph]` (cited on page 119).

[162] L. A. Harland-Lang et al. ‘Parton distributions in the LHC era: MMHT 2014 PDFs’. In: *Eur. Phys. J.* C75.5 (2015), page 204. DOI: `10.1140/epjc/s10052-015-3397-6`. arXiv: `1412.3989 [hep-ph]` (cited on page 119).

[163] G. Sartisohn. ‘Higgs Boson Search in the $\boldsymbol{H \rightarrow WW^{(*)} \rightarrow \ell\nu\ell\nu}$ Channel using Neural Networks with the ATLAS Detector at 7 TeV’. PhD thesis. Wuppertal U., 2012 (cited on page 128).

[164] K. Becker. ‘Inclusive and Differential Cross-Section Measurements of t-channel single top-quark production at $\sqrt{s} = 7$ TeV with the ATLAS detector’. PhD thesis. Wuppertal, Germany: Wuppertal U., 2014-08-13. URL: `http://inspirehep.net/record/1429572/files/fulltext_JJ7r87.pdf` (cited on page 128).

[165] F. James and M. Roos. ‘Minuit: A System for Function Minimization and Analysis of the Parameter Errors and Correlations’. In: *Comput. Phys. Commun.* 10 (1975), pages 343–367. DOI: `10.1016/0010-4655(75)90039-9` (cited on page 142).

[166] ATLAS Collaboration. ‘Measurement of the cross-section for W boson production in association with b-jets in pp collisions at $\sqrt{s} = 7$ TeV with the ATLAS detector’. In: *JHEP* 06 (2013), page 084. DOI: `10.1007/JHEP06(2013)084`. arXiv: `1302.2929 [hep-ex]` (cited on page 142).

[167] ATLAS Collaboration. ‘Measurement of the inclusive and fiducial $t\bar{t}$ production cross-sections in the lepton+jets channel in pp collisions at $\sqrt{s} = 8$ TeV with the ATLAS detector’. In: (2017). arXiv: `1712.06857 [hep-ex]` (cited on page 157).

Acknowledgments

I would like to begin by thanking my supervisor Prof. Dr. Peter Mättig for his continuous help and support during my PhD. Giving me the opportunity to join his research group, made it possible to accomplish this dissertation. His guidance and many ideas led to significant improvements on my research. I would also like to thank Dr. Dominic Hirschbühl for his daily supervision in physics, statistics and technical issues, especially for the close collaboration during the approval procedure of the related paper. Many thanks goes to Dr. Mark Owen for accepting to be my second referee and taking the time to read my dissertation.

I would like to express my appreciation to Prof. Dr. Wolfgang Wagner for his helpful answers to my questions and the fruitful discussions. Many thanks to Prof. Dr. Francesco Knechtli for happily accepting to be a member in my PhD committee and for all his support during my master studies.

I am grateful to all the members of the experimental particle physics group in Wuppertal who provided a warm working environment and useful discussions, especially my office-mates: Gunnar Jäkel, Shayma Wahdan, Dr. Phillipp Tepel and Dr. Kathrin Becker. In addition to Dr. Dominic Hirschbühl, I am thankful to Dr. Marisa Sandhoff and Nicolas Lang for revising several chapters of my dissertation during the writing process. For the joyful coffee breaks and kicker matches, I thank Gunnar, Shayma, Nicolas and Dr. Marcelo Vogel.

The opportunity to be a member of CERN, the ATLAS collaboration, and in particular, a member of the top-quark physics group was of special significance to me. Many Thanks to everyone who expressed interest in my analysis or gave comments and suggestions.

Last but not least, I would like to thank my parents and siblings for their unconditional love. Very special thanks go to my dear husband, companion and my best friend, Saed Abughannam, for his love and endless support.